# Thoracic Magnetic Resonance Imaging

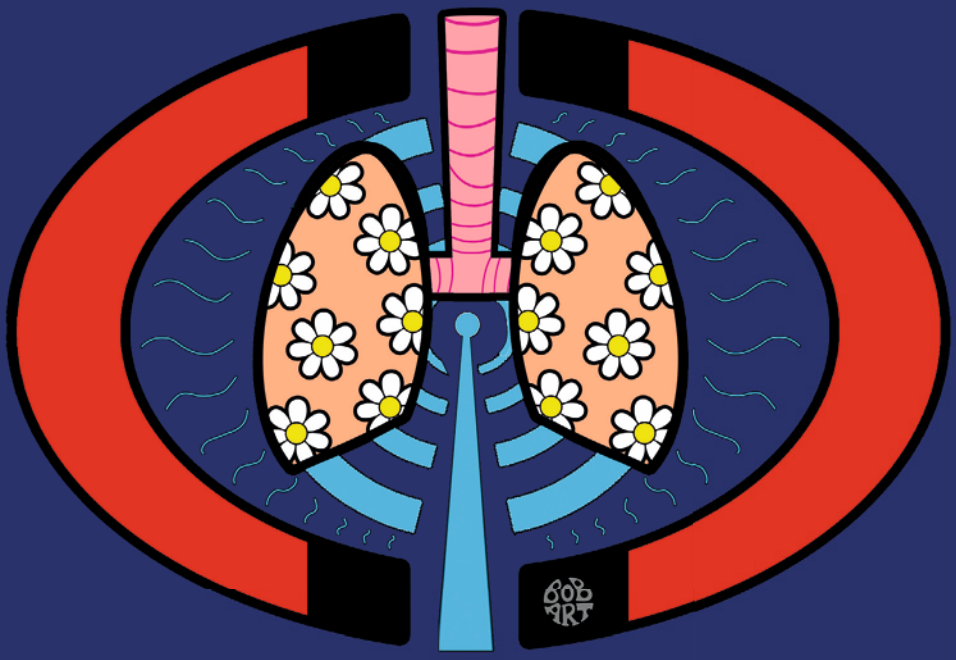

Pierluigi Ciet

# Thoracic Magnetic Resonance Imaging

Pierluigi Ciet

## Acknowledgements

The work presented in this thesis was conducted at the Department of Pediatrics, Division Pediatric Respiratory Medicine and Allergology of the Sophia Children's Hospital, department of Radiology of the Erasmsus Medical Center in Rotterdam, Netherlands, Department of Radiology of the Ca'Foncello General Hospital in Treviso, Italy; and department of Radiology of the Beth Israel Deaconess Medical Center in Boston, USA.
All studies represented in this thesis where in toto or partially funded by the Sophia Children's Hospital Fund (SSWO) through the 2011 Sporten voor Sophia funds raising campaign. Studies represented in chapter 3-5 and were supported in part by the Italian Cystic Fibrosis League (Lega Italiana Fibrosi Cistica, LIFC) and by the Italian Cystic Fibrosis Foundation (Fondazione Fibrosi Cistica, FFC).

The printing of this thesis has been financially supported by the Erasmus University Rotterdam, the Radiology Department of the Erasmus Medical Center and by the foundation Imago.

Cover design: cover was designed by Bob Marongiu (www.bobart.it).
Layout: Legatron Electronic Publishing, Rotterdam
Printed by: Ipskamp Drukkers, Enschede

ISBN/EAN: 978-94-028-0432-4

# Thoracic Magnetic Resonance Imaging

Thesis

To obtaining the degree of Doctor from the Erasmus University Rotterdam
by command of the rector magnificus

Prof. dr. Huibert A.P. Pols

and in accordance with the decision of the Doctorate Board,
The public defence shall be held on
Wednesday 14th December 2016 at 13.30 hours

By
Pierluigi Ciet
Born in Asolo, Italy

Erasmus University Rotterdam

## Doctoral Committee/Promotiecomissie

**Promotors:** Prof. Dr. H. A. W. M. Tiddens
Prof. Dr. G. P. Krestin

**Other members:** Prof. Dr. W.M. Prokop
Prof. Dr. I.K.M. Reiss
Prof. Dr. E.H.H.M. Rings

To my beloved wife Laura and my children Agata and Carlo

# Contents

# Chapter 1

## General Introduction

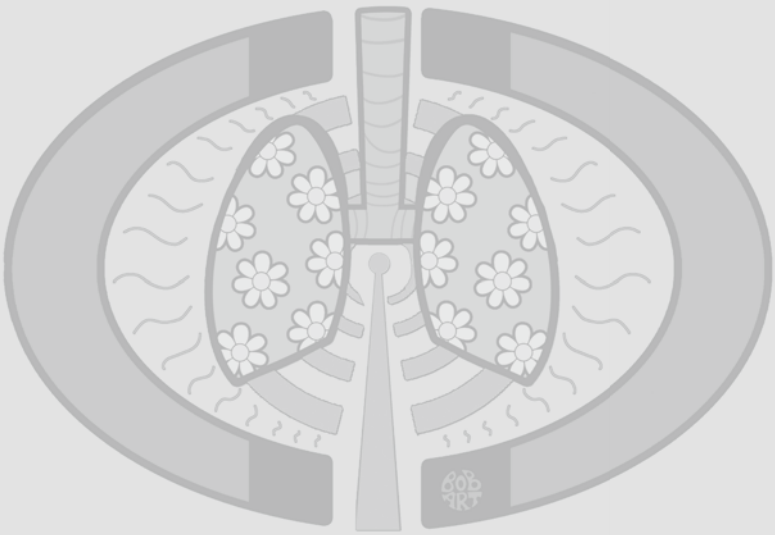

## Thoracic Imaging: from X-RAY to MRI

Chest-x ray (CXR) and computed tomography (CT) [1] are today the most important techniques used for thoracic imaging. Chest CT is fast and offers great anatomical detail. The major limitation of chest CT is related to the use of ionizing radiation [2]. Although, the last generation of CT scanners can perform low or ultra-low dose chest CT protocols [3], the long term risk of developing radiation-related cancer cannot be ignored [4]. This risk is greater in pediatric patients, who are more sensitive to radiation than adults [4]. To reduce radiation exposure in medical imaging, the American College of Radiology has promoted two campaigns both in children (Image Gently) and in adults (Image Wisely) [5,6].

Magnetic Resonance Imaging (MRI) which development has started in the same period as CT in late 1970 is an ionizing radiation free technique based on magnetic fields and radio waves to image the body [7]. MRI has become the most important image modality for high proton density structures such as the brain, liver, and musculoskeletal system. Unfortunately, the lung is not well suited for MRI being a spongious structure with low proton density that results in a low MRI signal [8]. In addition, tissue air interfaces result in proton dephasing with extreme shortening of lung T2* relaxation time and consequent rapid signal loss [8]. Related to the relatively long acquisition times needed for lung MRI the images are sensitive to breathing and heart motions, which further decrease image quality [8]. For these reasons, relatively little research efforts was directed towards the development of lung MRI and CT has remained the preferred method for thoracic imaging [9]. Only in the last two decades lung MRI has regained interest as a radiation free alternative for thoracic imaging [10-12]. This new interest in pulmonary MRI has been mostly driven by the development of fast and high-resolution sequences, which now allows to overcome the challenges related to lung MRI [10]. Further development of MRI as a radiation free alternative for thoracic imaging is highly relevant, especially in children with chronic lung disease [13]. These patients require repeated imaging, so MRI being a radiation free alternative for chest CT could be a very efficient strategy to reduce cumulative radiation exposure [8].

## Chronic lung disease and follow-up imaging: the CF model

Cystic Fibrosis (CF) is a typical example of a congenital chronic lung disease that potentially could benefit greatly from further development of lung MRI [14]. CF is characterized by a defect of the cystic fibrosis transmembrane conductance regulator (CFTR) protein that results in chronic inflammation and progressive structural lung changes that starts in infancy [15]. Regular follow-up of CF lung disease is mandatory to timely detecting progressive lung changes and in order to adjust therapy [16]. Monitoring of CF lung disease can be performed both indirectly with lung function techniques and directly with imaging [17,18]. The former detects the effect of structural lung changes on lung physiology and can include several techniques, which are grouped as pulmonary function tests (PFT). PFT have the advantage of wide availability and low costs, but they suffer from limited sensitivity for

regional structural changes [17]. Patients with CF can have severe localized structural lung changes despite normal spirometry parameters [19]. For this reason imaging techniques are needed to detect structural lung changes. The imaging of CF lung disease has changed considerably in the last two decades, following the technological developments both in chest CT and chest MRI [18]. Although chest x-ray (CXR) is still the most used radiology modality, thanks its large availability and low cost, CT has shown to be the most sensitive technique to detect and monitor CF lung disease [20]. Concerns related to cumulative dose are at the basis for the development of low and ultra-low dose CT protocols and the introduction of pulmonary MRI in clinical practice [14]. To date however, a large number of studies have been conducted to develop and validate chest CT as outcome measure for CF lung disease. For chest MRI these developments have been started only recently.

## Pro and cons of chest MRI

MRI has several advantages over CT for thoracic imaging [11]. The most important one is the absence or ionizing radiation, which makes MRI especially suitable for pediatric and repeated lung imaging. Another advantage of MRI over CT is its higher tissue characterization deriving from multi-parametric (T1, T2, proton density) imaging [8]. Different tissue weighting can provide different information about the target tissue. For example T2 sequences are better suited to detect water, for example in the case of pleural effusion, while T1 sequence are instead preferred for vascular imaging, especially after contrast administration [21].

MRI also has the ability to provide functional information, which are not readily available with CT, except at the expenses of high radiation exposure [11]. For instance, MRI can provide ventilation imaging using hyperpolarized gases or Fourier Decomposition techniques [22,23]. Moreover, MRI can be used to assess pulmonary inflammation using Diffusion Weighted Imaging (DWI). Contrast administration can be used to assess pulmonary vasculature and parenchymal perfusion [24]. Finally, MRI has the advantage to perform dynamic studies to assess "moving" thoracic structures, like central airways and diaphragm[13].

Therefore, chest MRI has the potential to provide in a single scan session information about Ventilation, Inflammation, Perfusion and Structure, which can be summarized by the acronym we coined: VIPS [25]. VIPS information can provide new insight not only in CF lung disease, but also in other chronic lung diseases where structure-function relationship has not been fully unfolded. However, before introducing VIPS techniques in clinical practice, they need to be validated against other established outcome measures.

The studies in this thesis aimed to contribute to the development of chest MRI for pediatric and adult lung diseases.

## Thesis topics

This thesis describes first in a review the challenges, solutions and possible applications of MRI in thoracic imaging. Furthermore it addresses the use of chest MRI for three areas: CF lung disease monitoring (five studies), central airways assessment (two studies) and diaphragm mechanics (one study).

## Chest MRI in CF lung disease monitoring

To further validate chest MRI as outcome measure in CF lung disease we:
- Compared chest MRI to chest CT to assess CF lung disease in a group of stable patients with CF (chapter 3)
- Investigated diffusion-weighted MRI (DW-MRI) as new technique to assess inflammation in CF lung disease (chapter 4)
- Validated DW-MRI as new tool to quantify pulmonary inflammation during CF lung exacerbation (chapter 5)
- Studied the relationship between trapped air and hypoperfusion in CF lung disease using CEMRI (chapter 6)
- Investigated a newly developed three-dimensional (3D) Fourier Decomposition ventilation MRI protocol for patients with CF (chapter 7)

To validate chest MRI as new tools to assess central airways dynamics we:
- Developed a new chest MRI protocol to assess central airways in static and dynamic conditions and tested this protocol in a group of pediatric patients with a clinical suspicion of tracheobronchomalacia (chapter 8)
- Tested the central airways protocol in a group of healthy volunteers and adult patients with a clinical suspicion of saber-sheath tracheomalacia (chapter 9)

To validate chest MRI as new method to assess diaphragm mechanics we:
- Developed a chest MRI protocol to assess diaphragmatic function in patients with Pompe disease (chapter 10).

## Thesis outline

**Chapter 1** General introduction and description of aims and thesis outline

**Chapter 2** State-of-the art review on chest MRI

**Chapter 3** Cross-sectional study comparing chest-MRI with chest-CT to assess CF lung disease

**Chapter 4** Cross-sectional study investigating DW-MRI as possible tool to assess pulmonary inflammation

**Chapter 5** Longitudinal study testing DW-MRI as new tool to quantify inflammation during CF pulmonary exacerbation

**Chapter 6** Cross-sectional study using contrast-enhanced MRI (CEMRI) to investigate the relationship between trapped air and lung perfusion

**Chapter 7** Cross-sectional study describing the results of a newly developed three-dimensional Fourier Decomposition MRI protocol for ventilation imaging

**Chapter 8** Cross-sectional study describing the results of a newly developed chest MRI protocol to assess tracheobronchomalacia in a group of paediatric patients

**Chapter 9** Cross-sectional study using chest MRI to assess tracheal collapsibility in a group of healthy volunteers and adult patients with a clinical suspicion of saber-sheath tracheomalacia

**Chapter 10** Cross-sectional study using a newly developed MRI protocol to assess diaphragmatic function in patients with Pompe disease

**Chapter 11** General discussion on the results of the studies performed in this thesis

## Bibliography


1. Williams H, Levy-domn M, Lawson D, Williams H (1991) Radiologic Exhibit in North including chest family. 325–332.
2. Systems HC, Smith-bindman R, Miglioretti DL, et al. (2012) Use of Diagnostic Imaging Studies and Associated Radiation Exposure for Patients Enrolled in Large Integrated Health Care Systems, 1996-2010. Jama. doi: 10.1001/jama.2012.5960
3. Kim Y, Kim YK, Lee BE, et al. (2015) Ultra-Low-Dose CT of the Thorax Using Iterative Reconstruction: Evaluation of Image Quality and Radiation Dose Reduction. Am J Roentgenol 204:1197–1202. doi: 10.2214/AJR.14.13629
4. Miglioretti DL, Johnson E, Williams A, et al. (2013) The use of computed tomography in pediatrics and the associated radiation exposure and estimated cancer risk. JAMA Pediatr 167:700–7. doi: 10.1001/jamapediatrics.2013.311
5. Don S, Macdougall R, Strauss K, et al. (2013) Image gently campaign back to basics initiative: ten steps to help manage radiation dose in pediatric digital radiography. AJR Am J Roentgenol 200:W431–6. doi: 10.2214/AJR.12.9895
6. Brink J a, Amis ES (2010) Image Wisely: a campaign to increase awareness about adult radiation protection. Radiology 257:601–602. doi: 10.1148/radiol.10101335
7. Geva T (2006) Magnetic Resonance Imaging: Historical Perspective. J Cardiovasc Magn Reson 8:573–580. doi: 10.1080/10976640600755302
8. Ciet P, Tiddens HAWM, Wielopolski PA, et al. (2015) Magnetic resonance imaging in children: common problems and possible solutions for lung and airways imaging. Pediatr Radiol. doi: 10.1007/s00247-015-3420-y
9. Rubin GD (2014) Computed Tomography : Revolutionizing the Practice of Medicine for 40 Years 1. 273:45–74. doi: 10.1148/radiol.14141356
10. Wild JM, Marshall H, Bock M, et al. (2012) MRI of the lung (1/3): methods. Insights Imaging 3:345–53. doi: 10.1007/s13244-012-0176-x
11. Biederer J, Beer M, Hirsch W, et al. (2012) MRI of the lung (2/3). Why … when … how? Insights Imaging 3:355–71. doi: 10.1007/s13244-011-0146-8
12. Biederer J, Mirsadraee S, Beer M, et al. (2012) MRI of the lung (3/3)-current applications and future perspectives. Insights Imaging 3:373–86. doi: 10.1007/s13244-011-0142-z
13. Baez JC, Ciet P, Mulkern R, et al. (2015) Pediatric Chest MR Imaging: Lung and Airways. Magn Reson Imaging Clin N Am 23:337–49. doi: 10.1016/j.mric.2015.01.011
14. Wielpütz MO, Mall MA (2015) Imaging modalities in cystic fibrosis. Curr Opin Pulm Med 21:609–616. doi: 10.1097/MCP.0000000000000213
15. Cohen-Cymberknoh M, Kerem E, Ferkol T, Elizur A (2013) Airway inflammation in cystic fibrosis: molecular mechanisms and clinical implications. Thorax 68:1157–62. doi: 10.1136/thoraxjnl-2013-203204
16. Cohen-Cymberknoh M, Shoseyov D, Kerem E (2011) Managing cystic fibrosis: strategies that increase life expectancy and improve quality of life. Am J Respir Crit Care Med 183:1463–71. doi: 10.1164/rccm.201009-1478CI
17. Bush A, Sly PD (2015) Evolution of cystic fibrosis lung function in the early years. Curr Opin Pulm Med 21:602–8. doi: 10.1097/MCP.0000000000000209
18. Eichinger M, Heussel C-P, Kauczor H-U, et al. (2010) Computed tomography and magnetic resonance imaging in cystic fibrosis lung disease. J Magn Reson Imaging 32:1370–8. doi: 10.1002/jmri.22374
19. de Jong P A, Lindblad A, Rubin L, et al. (2006) Progression of lung disease on computed tomography and pulmonary function tests in children and adults with cystic fibrosis. Thorax 61:80–5. doi: 10.1136/thx.2005.045146

20. Tiddens H A WM, Stick SM, Davis S (2013) Multi-modality monitoring of cystic fibrosis lung disease: The role of chest computed tomography. Paediatr Respir Rev 1–6. doi: 10.1016/j.prrv.2013.05.003

21. Ciet P, Wielopolski P, Manniesing R, et al. (2014) Spirometer-controlled cine magnetic resonance imaging used to diagnose tracheobronchomalacia in paediatric patients. Eur Respir J 43:115–24. doi: 10.1183/09031936.00104512

22. Fain SB, Korosec FR, Holmes JH, et al. (2007) Functional lung imaging using hyperpolarized gas MRI. J Magn Reson Imaging 25:910–23. doi: 10.1002/jmri.20876

23. Bauman G, Puderbach M, Heimann T, et al. (2013) Validation of Fourier decomposition MRI with dynamic contrast-enhanced MRI using visual and automated scoring of pulmonary perfusion in young cystic fibrosis patients. Eur J Radiol 82:2371–7. doi: 10.1016/j.ejrad.2013.08.018

24. Liszewski MC, Hersman FW, Altes T A, et al. (2013) Magnetic resonance imaging of pediatric lung parenchyma, airways, vasculature, ventilation, and perfusion: state of the art. Radiol Clin North Am 51:555–82. doi: 10.1016/j.rcl.2013.04.004

25. Tiddens HAWM, Stick SM, Wild JM, et al. (2015) Respiratory tract exacerbations revisited: Ventilation, inflammation, perfusion, and structure (VIPS) monitoring to redefine treatment. Pediatr Pulmonol 50:S57–S65. doi: 10.1002/ppul.23266

# Part 1

## Cystic Fibrosis (CF) lung monitoring using MRI

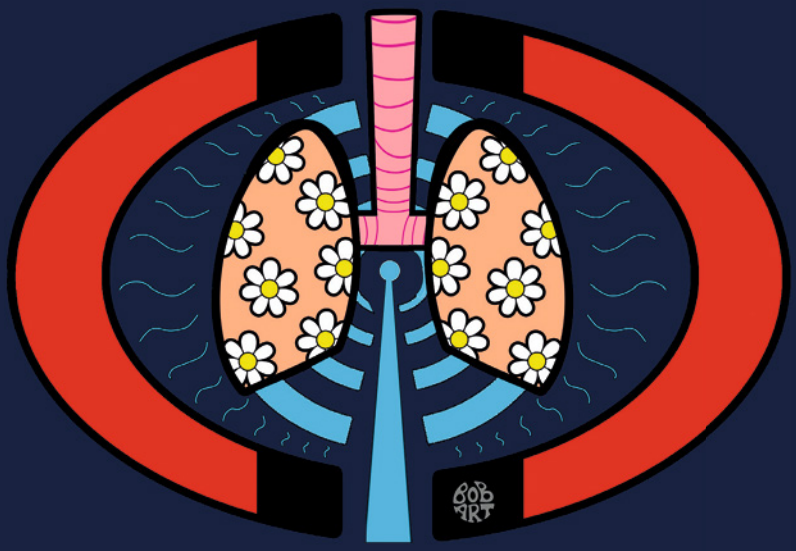

# Chapter 2

## Magnetic Resonance Imaging in Children: Common Problems and Possible Solutions for Lung and Airways Imaging

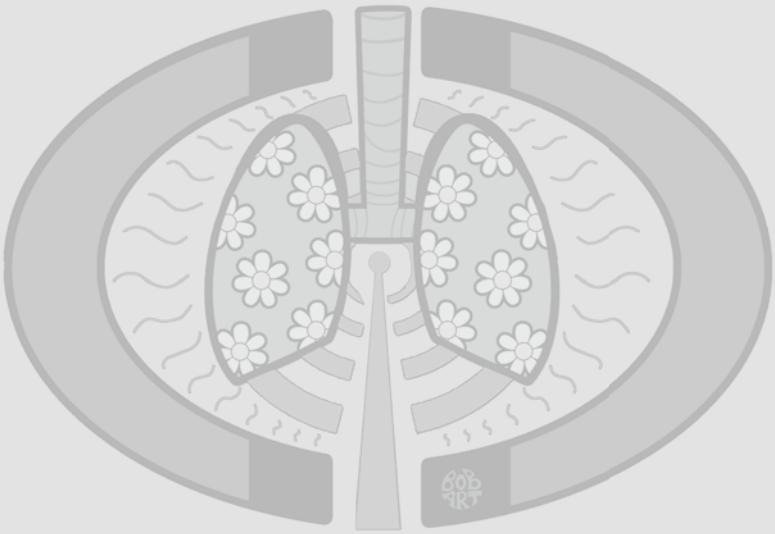

*Ciet P, Tiddens HA, Wielopolski PA, Wild JM, Lee EY, Morana G, Lequin MH*

Based upon Pediatric Radiology. 2015 Dec;45(13):1901-15. (Extended version)

## Abstract

Pediatric chest MRI faces many challenges. High resolution scans of the lungs and airways are compromised by long imaging times, low lung proton density signal and cardiac and respiratory motion. A low lung signal is problematic in imaging relatively normal lung tissue, but less so for diseased lung tissue. Indeed, various pathologic conditions often result in an increased signal from lung parenchyma that can render chest MRI more informative.

One of the most important criteria for successful chest MRI is proper patient cooperation. In fact, relatively long acquisition times of MRI makes patient preparation crucial. Children usually have problems with long breath holds or the concept of quiet breathing. The acquisition of chest MRI in young children is even more challenging because of higher cardiac and respiratory rates, which result in motion and imaging blurring. For these reasons, to date computed tomography (CT) has been preferred over MRI for chest pediatric imaging.

Despite its drawbacks, MRI also has advantages over CT, which justifies its further development and clinical use. The most important advantage is the absence of ionizing radiation, which allows frequent scanning for short and long term follow-up studies of chronic diseases. Moreover, MRI allows the assessment of functional aspects of the chest, such as lung perfusion and ventilation, or airways and diaphragm mechanics. In this review, we describe the most common MRI acquisition techniques on the verge of clinical translation, their problems and the possible solutions to make chest MRI feasible in children.

## Introduction

Lung Magnetic resonance imaging (MRI) is challenging because of the magnetic heterogeneous environment in this region [1]. Lung parenchyma is a spongious structure with a low proton density per voxel and hence a reduced signal-to-noise ratio (SNR) and contrast-to-noise ratio (CNR) [2]. In addition, the numerous air-tissue interfaces within a voxel induce strong localised microscopic magnetic field gradients, which produce extensive MRI signal dephasing leading to extremely short T2-star ($T_2$*, between 1 and 2 ms at 1.5 Tesla) and geometric distortions. These field inhomogeneity effects become stronger at higher magnetic field strengths, such as 3.0 Tesla, which is increasingly used in clinical setting [3]. However, in cases of lung pathology like pneumonia, edema, tumors and atelectasis, the SNR of these diseased regions is higher due to increased proton density of the fluid and/or tissue, so resulting in an improved visualization [4]. Another important reason for the relatively poor spatial resolution of MRI compared to computed tomography (CT) is the relatively long scan times required, which result in artifacts related to respiratory and cardiac motion. Hence, many well established MRI and magnetic resonance angiographic (MRA) techniques used in routine studies of the brain, neck and peripheral vasculature cannot be easily implemented in the lung region due to inconsistent image quality.

To optimize lung MRI protocols the target structure, and the patient's cooperation in following breathing instructions have to be taken into account [5].

The target structure influences the contrast weighting needed, such as that $T_1$ weighting is normally used for vessel visualization, $T_2$ weighting for bronchi, and PD weighting for lung parenchyma [4]. Breath-hold is usually preferred for lung MRI and MRA sequences, because it supplies the best image quality [5]. Unfortunately, many lung diseases result in increased respiratory rates and maintaining breath holds of several seconds may not be possible for patients[5]. This problem is even more prominent for young children, who have a higher respiratory rate compared to adults [5] and where cooperation is poor. To address this problem a MR sequence with high temporal resolution and good SNR is required. MR physicists have worked hard to develop MR acquisition techniques [6] that meet these challenging criteria [7,8]. Breathing instruction has been improved by introducing dedicated patient's training before the examination. Also MRI compatible spirometers have been developed and used for MRI lung imaging [9,10].

The driving force to develop sophisticated MR sequences for lung MRI is that this technique is free of ionizing radiation, which is especially important for pediatric patients or in case of serial imaging. Pediatric patients are more sensitive to ionizing radiation than adults, therefore is crucial to reduce cumulative dose according to the ALARA principle [11]. Similarly adult patients, who need repeated imaging to assess clinical deterioration or response to therapy, might end up with high cumulative radiation dose [12]. For these reasons, dose reduction campaigns were promoted by the American College of Radiology both in pediatric and adult populations [13,14].

Lung MRI fits the aim of these campaigns because it makes it possible to monitor chronic pediatric diseases (i.e. cystic fibrosis, CF) or oncology patients [15] without increasing the lifelong cumulative radiation dose [3]. Moreover, MRI has the advantage of integrating anatomical and physiologic information in a single examination, a possibility not as readily available with other imaging modalities. In fact, MRI can provide information regarding lung perfusion [16] using gadolinium contrast, lung mechanics using dynamic acquisitions [10], and ventilation and gas exchange using inhaled hyperpolarized gases [17], oxygen enhancement or dynamic motion based methods [18]. Furthermore, MRI has shown advantages over CT for imaging the following lung related disorders: 1) Identification of tumor infiltration into the mediastinum or the chest wall [19,20]; 2) differentiation between solid lesions and vascular structures in the hila without intravenous contrast medium injection [21], 3) representation of pathologies of the diaphragm, in particular evidence of tumor penetration of the thorax into the abdomen [22]; 4) evaluation of the mediastinum in patients with treated lymphoma [23].

For all the aforementioned reasons, MRI has been introduced in clinical practice, although use on a large-scale base is still far off. In this introduction, we will review the challenges faced in lung MRI and the most common MRI techniques used for imaging lung and airways diseases.

**Patient preparation**

Image quality in thoracic imaging is highly dependent of patient cooperation, which in turn is related to patient age, mental status and disease status [5]. Patients with dyspnea, younger than 6 years old, mentally impaired or with hearing problems have problems following breathing instructions. In patient with dyspnea, fast imaging or respiratory gated options should be chosen to reduce scan time. These techniques will be discussed in the following chapters. In pediatric patients younger than 6 years old, as some adult subjects, may need sedation for MR imaging because of claustrophobia or other anxiety. In young children, the need of sedation can be reduced by making the child more comfortable during the examination. For instance, the parents can stay in the examination room with the child or it can be used some distraction methods, such as movies or music [24]. When these methods fail, it is frequently necessary to use deep sedation, with airways intubation in collaboration with anesthesiologists [25]. The use of deep anesthesia is anyway controversy, and it should be weighed against the potential risks and benefits of other faster imaging options, such as CT. There is indeed recent evidence that deep sedation in early-developing brain might produce long-term sequelae [26,27].

Sedation in radiology departments can be performed with different anesthetic agents, such as fentanyl, midazolam, pentobarbital, propofol, chlorpromazine, and sevoflurane chloral hydrate [28]. The selection of the most appropriate anesthetic agent should be performed by a dedicated anesthesia team and according to patient's age, duration of examination, comorbidities [29]. During sedation, the anesthesiologist can monitor patient's vital signs and respiration and coordinate with the MR imaging technologist the acquisition of images. For lung MRI, the anesthesiologist can recreate breath-hold conditions in inspiration (25 cm $H_2O$) and at end-expiration (0 cm $H_2O$) in a controlled environment,

while the radiologist and the MR radiographer minimize the imaging time and ensure diagnostic MRI sequences [24]. Finally, lung MRI should be performed in short scan sessions to avoid the development of atelectasis, which can hamper assessment of the underlying disease and be secondary to patient ventilation. After anesthesia, patient should be monitored and evaluated before discharge, being the radiologist responsible for any adverse outcomes that result from the use of sedation, even after the patient leaves the facility [29].

In children of 6 years and above, cooperation can be increased substantially with adequate patient training in a mock scanner and the use of MR-compatible spirometers [9]. Patient training consists of a set of training instructions to rehearse a specific breathing maneuver, ideally before the scan is performed. Training can be performed in the supine position adopted in the MRI scanner on a bed using a MRI-compatible spirometer (Figure 1).

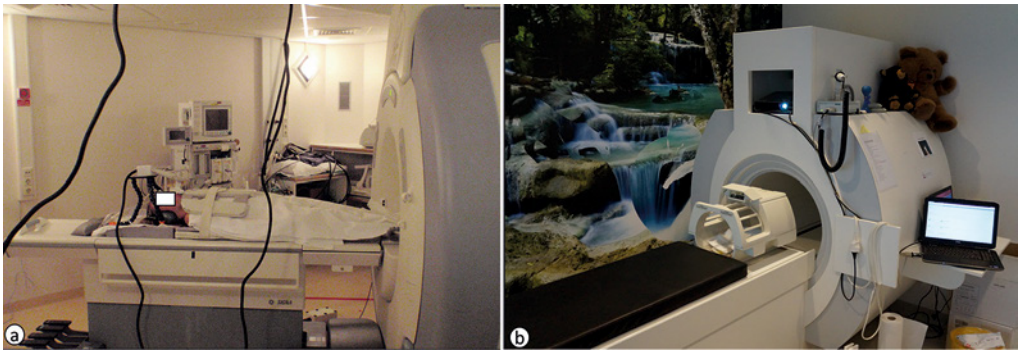

**Figure 1. MRI compatible spirometer set-up.** CF patient in a 1.5 T MRI with MR compatible spirometer setting. (1a) A plastic adjustable tripod holds the mouthpiece that is connected through a plastic black corrugated tube to the control computer at the scanner operator's side. (1b) Mock MRI scanner is used to train the pediatric patient before the actual MRI scan. The mock MRI scanner can reproduce the noises that the patient will hear inside the real MRI environment. The mock scanner also contributes to reduce the anxiety level of the patient before the real examination.

The purpose of the training is: 1) to obtain inspiratory and expiratory capacity in supine position as a point of reference for the actual scanning; 2) to train the subject executing specified breathing maneuvers by using the spirometer during the MRI; 3) to reduce anxiety related to MRI investigations; and 4) to increase the number of successful MRI investigations [9,10]. Commonly used breathing maneuvers are: a breath-hold at maximal inspiration or maximal expiration; quiet free breathing; quiet deep inspiration-expiration; forced expiration after a maximal deep inspiration; or coughing maneuvers. These maneuvers allow the study of anatomical detail of airway and parenchyma or to study the response of the airways to respiratory motion and different air flow situations [10].

Breath-hold acquisitions are the cornerstone of chest MRI and can be acquired comfortably in most pediatric patients without extensive MRI scanning sessions [5]. These acquisitions are in general preferred over free-breathing acquisitions for thoracic imaging as resolution and SNR are lower when compared to gated MRI scans (Figure 2).

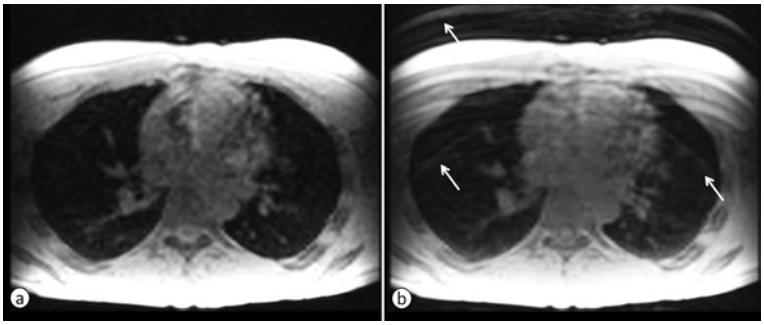


**Figure 2. Breath-hold versus free-breathing acquisition.** Breath-hold (a) versus free-breathing (b) 3D SPGR axial reformats (TR/TE/FA=1.4/0.6/2). Note the motion artifact in the free-breathing acquisition (arrows).

## MR system and coil selection

Selection of the appropriate MR system is of key importance as it strongly influences image quality in lung MRI. Theoretically one could enhance SNR, like in other imaging regions [4], by using higher magnetic field strengths, but in lung MRI higher field strength does not necessarily equate to higher SNR due to the increase in $T_2^*$ dephasing and susceptibility artifacts. For this reason, lower magnetic field systems (i.e. 1.5 Tesla) are currently more suitable for routine clinical lung MRI than 3 T systems, (Figure 3). Given the requirements for higher spatial resolution in children, MR scanners with strong and fast imaging gradients are needed, with values typically between 40-50 mT/m (milliTesla/meter), and slew rates in excess of 200 T/m/s (Tesla/meter/second).

Making the correct coil selection for a given exam is also a critical factor for image quality. For lung MRI close fitting receiver array coils are optimum, which have multiple small coils combined (coil elements in phased array) to record the signal simultaneously [30]. Array coils provide higher SNR by virtue of the closer proximity to the lungs but also allow for shorter acquisition time [30] through the use of parallel imaging [6]. Optimal coil designs differ depending on the anatomy, for thoracic MRI the coils most frequently used are arrays with 4 to 32 channels. Ideally a tailored closely fitting receiver coil suited to the size of the thorax of the child should be used, for enhanced sensitivity and patient comfort. For instance, an 8 channels head-neck-spine coil can provide better SNR than a 32 channels torso coil for dedicated central airways imaging, because of the closer fitting to chest anatomy.

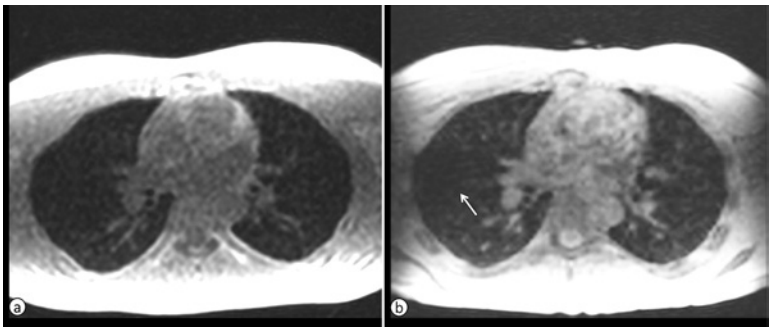

**Figure 3. SNR at 1.5T and 3T.** Same subject scanned with 1.5 T (a) and 3 T (b) systems, and same parameters (TR/TE=1.4/0.6 ms, Acceleration=6, 3 seconds scan). Note the signal decay of the lung parenchyma with 3T system (arrow). Windowing setting is kept constant in both images.

## Lung Morphology and image quality

Multiple problems related to lung structure affect image quality in lung MRI: a) extremely low proton density of normal lung tissue; b) relative large body volume; c) presence of extensive air-tissue interfaces; and motion related signal alterations from breathing and cardiovascular pulsations during data collection. In the sections below, these points are clarified in more detail.

### Low proton density of the lung and optimal SNR selection

Lung MRI has an intrinsic low SNR, for which reason lung MRI images are often compared to a "black hole" [31]. The air-to-tissue ratio of lung parenchyma is high, which is unfortunate as air does not provide any MR signal and the number of water protons present per voxel imaged in lung parenchyma is low. This is not the case for central airways or vascular structures, which can be visualized quite easily [32].

A compromise between spatial resolution, SNR and acquisition time must be found to obtain the desired image quality [3]. To obtain a specific SNR several MRI parameters must be taken into account. A simplified formula for SNR is

$$SNR \propto K \times (voxel\ size) \times \sqrt{\frac{number\ of\ excitations\ (NEX)}{receiver\ readout\ bandwidth\ (BW)}}$$

* $\propto$ proportionality operator

The constant K in the formula includes those factors that are beyond the routine operator's control, such as hardware dependent factors (i.e. coil sensitivity) and tissue dependent parameters (proton density, $T_1$, $T_2$, $T_2$*) [33]. The influence of some MRI pulse sequence parameters (repetition time, TR; echo time, TE; flip angle, $\alpha$; specific absorption ratio, SAR; spin echo, SE; or gradient recalled echo, GRE readouts), voxel size, NEX and BW on SNR will be described below.

## Voxel size

Voxel size determines spatial resolution, which is in turn determined by the matrix size, the field of view (FOV) and slice thickness (SL) [33]. The matrix size is the number of frequency encoding steps, in one direction; and the number of phase encoding steps, in the other direction of the image plane [33]. Assuming FOV and SL as constant; increasing the number of frequency encodings or the number of phase steps results in improved resolution, at the expenses of scan time.

When comparing acquisition scenarios in lung MRI, increasing the voxel size proportionally augments the SNR [33], due to the greater number of protons per voxel. Therefore to ensure acceptable SNR, the voxel size chosen in lung MRI is significantly larger in comparison to CT [3]. Consequently, thicker slices are acquired (between 5 to10 mm) and spatial resolution is lowered to shorten acquisition time [34]. Depending on the MRI readout scheme used, SNR can selectively be augmented and smaller voxels acquired. In the case of 3D readout scans, this can be done by selecting more slices (partitions). In the case of 2D readouts, a multi-slice interleaved mode can be selected.

The FOV is the maximum diameter of the area of the scanned object that is represented in the reconstructed image [33]. Dividing the FOV by the matrix size provides the pixel size for a specific SL. When acquisition matrix is kept constant to retain the same acquisition time, increasing the FOV augments SNR, because it translates into larger voxel sizes [33] (Figure 4). Typically FOV is selected according to patient size and in lung MRI is usually large in order to get good SNR. For pediatric patients care must be taken not to select too small FOV and voxel size so as not to run out of SNR.

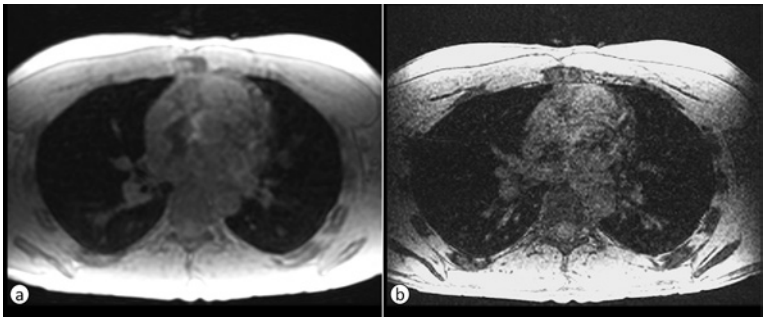


**Figure 4. Effect of voxel size on SNR.** SPGR with 3x3x3 $mm^3$ (a) and 1.5x1.5x1.5 $mm^3$ (b) isotropic voxels. Note that by halving each dimension by half there is a reduced signal-to-noise ratio (SNR) of a factor of 8 as shown by the increased image noise in (4b). Scan time for (4a) was 3 sec while for (4b) was 14 sec. In image 4b spatial resolution increases, with sharper contours of the lung structures; though at the expense of a slightly longer TR and TE.

## Number of excitations

A number of excitations (NEX) or number of signal averages (NSA) represents how many times a signal from a given slice is measured [33]. NEX is dependent on many factors, such as the number of

signal averages performed, matrix size selected, imaging speed selected (when selecting partial Fourier or parallel imaging readout schemes) and on whether two-dimensional (2D) or three-dimensional (3D) encoding is used. As described in the formula, the SNR improves proportional to the square root of the NEX, but unfortunately scan time also increases linearly with the NEX. Therefore, when MRI data are acquired during a breath-hold, acquisition time and SNR have to be balanced in such a way to allow data collection in a reasonable time.

## Bandwidth

The receiver readout bandwidth (BW) is the range of frequencies collected by an MR system during frequency encoding [33]. The MR data acquisition can take more or less time, depending on the receiver bandwidth. A broad BW corresponds to faster data acquisition and minimizes chemical shift artifacts, but also reduces SNR as more noise is included [33]. Halving BW improves SNR by $\sqrt{2}$. With a narrow BW, on the other hand, there will be more chemical shift and motion artifacts and the number of slices that can be acquired for a given TR will be limited (Figure 5). Narrow BW will create blurring and geometrical signal distortions around structures [32]. Therefore, a narrow BW setting may not be beneficial for lung imaging, especially for GRE pulse sequences, where narrow BW increases breath-hold times and enhances the sensitivity to motion and field inhomogeneity artifacts. This therefore results in SNR loss or decreasing spatial resolution [33].

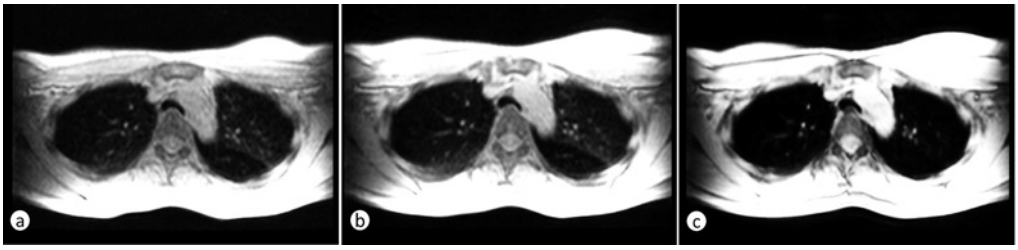


**Figure 5. Effect of Bandwidth to SNR.** 3D SPGR axial reformat with bandwidth (BW) of 142 (5a), 62.5 (b) and 31.25 (c) kHz. Note that longer BW influences appearance of lung parenchyma, which for small BW (longer acquisition) appears darker (c).

## Other factors affecting SNR

*Half-Fourier Imaging*

SNR loss is also factored if partial Fourier scanning or parallel imaging are used [35,6]. Partial Fourier imaging (partial NEX) is used in many instances to reduce scan time in lung imaging. Partial Fourier scanning takes advantage of the symmetry of k-space to reduce scan time, where just over half of the data (~60% k-space) is acquired and used to reconstruct the missing part [35]. When selecting a partial NEX of 0.5 cuts acquisition time by almost the same factor with a consequent loss of SNR of approximately $\sqrt{2}$ [35]. Scan time reduction achieved through parallel imaging techniques can suffer from SNR performance. Although SNR is reduced, in some sequences (i.e. gradient-echo) this can be

counterbalanced by a reduction in TE. Scans collected using parallel imaging can reduce breath holds substantially (5 to 10 seconds) with complete thoracic coverage with both 2D or 3D acquisitions and with higher spatial resolution [34].

*Parallel Imaging*

In parallel imaging, scan time reduction is achieved by scanning less phase encoding lines in k-space (2D or 3D acquisitions) and uses the different coil sensitivities of a phased array coil to reconstruct a full dataset [6]. All parallel imaging techniques reduce acquisition time according to the acceleration factor selected by the operator, and acquisition time is shortened by the same factor. For instance, when the acceleration factor is two, only half of the k-space is sampled and the acquisition time is halved. Although theoretically the acceleration factor can assume values up to the number of phased-array-coil, in practice most MRI vendors allow values ranging between 2 and 6 [36]. According to the numbers of coils and how the coils are distributed in the phased array receiver, the acceleration factor can range between 2 and 3 times for 2D and from 2 to 6 times for 3D acquisition techniques. Acceleration factors higher than 2 for 2D imaging are seldom used for lung parenchyma imaging [34]. The higher the parallel imaging factor or "acceleration" utilized, the higher the penalty in SNR (Figure 6). As the acceleration factor increases the greater the degree of noise induced magnification [36].

Different parallel imaging methods are available among the MRI vendors, such as Array coil Spatial Sensitivity Encoding (ASSET, SENSE, etc.) or Autocalibrating Reconstruction for Cartesian imaging (ARC, GRAPPA, etc.) [37]. While ASSET requires a separate calibration scan used to map the spatial sensitivity of the coil, in ARC the calibration acquisition is included in the parallel imaging acquisition. ASSET is usually preferred to achieve high temporal resolution, because it results in shorter acquisitions times than ARC. Moreover ASSET tends to provide better image quality than ARC for high acceleration factors. However ARC is the best choice for lung MRI, where accurate coil sensitivity maps are difficult to achieve [36]. ARC indeed reduces reconstruction artifacts when patient cannot execute breath-holding in a reproducible manner, which gives discrepancies between the calibration and the parallel imaging acquisitions [36]. Finally, ARC allows selecting FOV smaller than the imaged area without significant artifact, which might be important to achieve high spatial resolution (i.e. airways imaging).

In lung MRI, higher acceleration factors can be selected in case of diseased states, such as increased T2 from fluids or tumor, or larger and thicker airways (i.e. bronchiectasis) or when contrast agents are used to shorten the $T_1$ of lung parenchyma, blood or surrounding structures. When SNR is sufficient, the benefits of using partial Fourier and parallel imaging is to freeze motion and eliminate the detrimental effects of breathing by using breath-hold acquisitions, which can permit uncompromised imaging of lung parenchyma, vasculature and airway structures [4]. The acceleration obtained by these techniques can also make possible to freeze cardiac motion by collecting sub-second 2D or 3D scans or shortening cardiac gated acquisitions to a short breath-hold time. Finally, the high temporal resolution

obtained by combining these two techniques can be useful for applications in cine-mode, such as for the dynamic assessment of the central airways and the diaphragm.



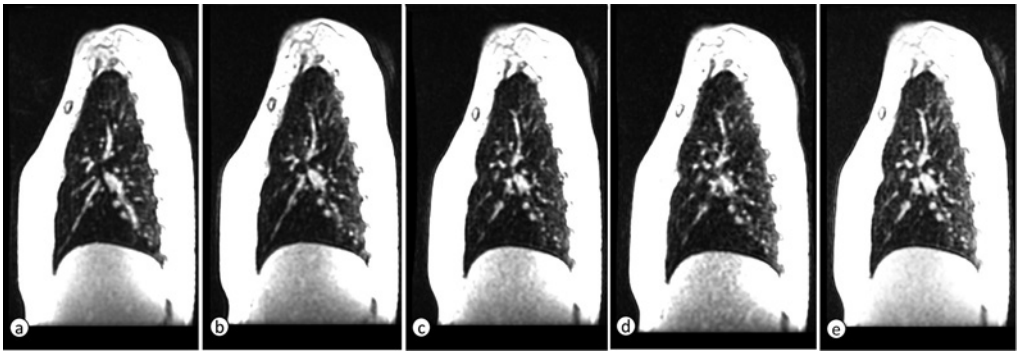


**Figure 6. Parallel imaging, SNR and Acquisition Time (TA).** SPGR acquired without and with parallel imaging using auto-calibrating reconstruction for cartesian sampling (ARC, GE, Milwaukee, USA) and increasing acceleration factor (AF): (a) no acceleration and TA 15 sec, (b) AF 1.25x1.25 and TA 10 sec, (c) AF 1.5x1.5 and TA 7 sec, (d) AF 2x2 and TA 5 sec, and (e) AF 2x3 and TA 4 sec. Note that by increasing AF the TA reduces from 15 sec to 4 sec, but at the same time SNR reduces, with the last image (e) appearing noisier than the first image (a).

## Coping with large magnetic susceptibility gradients

The choice of MR pulse sequences based on SE or GRE readouts can dramatically impact SNR and on how lung parenchyma and surrounding structures will appear. In lung MRI, an increase of TE can dramatically decrease SNR of lung parenchyma depending on $T_2$*. Imaging of the lung parenchyma is best performed with SE based techniques as these techniques can in most of the cases circumvent the need to acquire scans with short TEs [38]. Differently, irreversible dephasing of the MR signal due to short $T_2$* is critical with GRE techniques, whereas signal can be completely lost for most structures with slices thicker than 7 mm and TEs longer than 4 ms at mid and higher magnetic field strengths. This SNR loss appears as signal voids in the pulmonary vasculature and airways, especially in regions distally from the central large bronchial structures and the heart [39]. Nonetheless, GRE scans can be effectively used for imaging lung parenchyma, when the selected TE is below 1 ms (millisecond) for 3.0 Tesla scanners and 2 ms at 1.5 Tesla scanners. The most sophisticated MR GRE pulse sequences, which secure less signal loss and acquisition speed for lung parenchymal imaging, are based on projection reconstruction techniques with TEs on the order of microseconds (ultra-short TE, UTE), therefore mitigating signal dephasing due to the short $T_2$*s [40,41]. Similar sequence is also the zero TE (ZTE) gradient-echo, which combines high resolution images to a noiseless MRI acquisition and that might be especially suitable for pediatric lung imaging [42,43].

Independently of the choice made, scanning lungs in inspiration will result in more problems than scanning during expiration, when lung density is higher (Figure 7). However, for the correct

assessment of lung diseases, MRI should be performed in inspiration (Figure 8). On the other hand, MR acquisition at end expiration allows a better definition of trapped air (Figure 9).

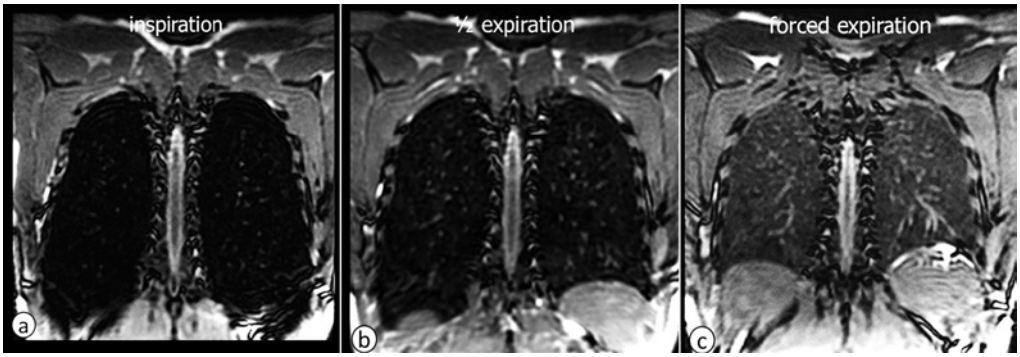


**Figure 7. Inspiratory level and SNR with 3D SSFP/TrueFISP.** 3D SSFP/TrueFISP coronal at end-inspiration (a), half-expiration (b) and forced expiration (c). Note the progressive increased SNR of the lung parenchyma from a to c.

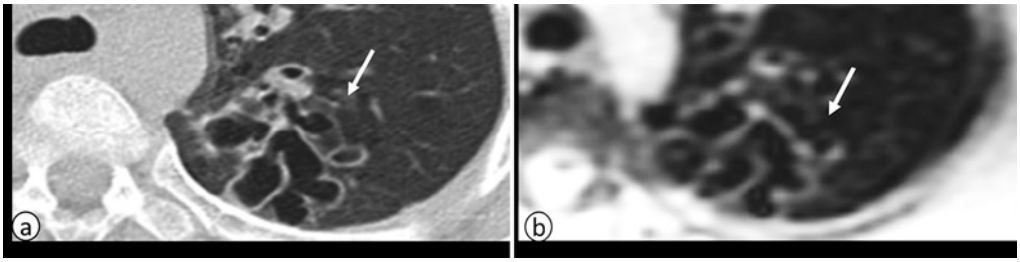


**Figure 8. Bronchiectasis.** CT (a) versus 2D SSFP MRI (b) in 14 year old cystic fibrosis boy with bronchiectasis (white arrows) in the left upper lobe.

*Respiratory and cardiac motion*

*A. Respiratory monitored acquisitions:* When patients cannot execute breath holds, respiratory monitored acquisitions during free breathing can be considered using navigator echoes or pneumobelts. Navigator echoes in the form of a pencil excitation are placed over the diaphragmatic dome and can be created in two different ways: 1) with an intersection of a SE generated signal from two overlapping slices excited with a 90°-180° RF excitation pair or 2), a beam or pencil like excitation generated using a 2D RF pulse with a GRE readout [44]. When using navigator echoes the diaphragm position is detected in real time, and can trigger the image acquisition prospectively based on a predetermined range of motion mostly selecting the diaphragm during expiration. The position in expiration is based on a short observation period at the beginning of the acquisition, during which a respiratory waveform is

reconstructed from a number of seconds of numerous breathing cycles during which pencil excitations are recorded [44] (Figure 10). To obtain better data acceptance during scanning, the data processed from the pencil excitation can be used to appropriately shift the slice or slab acquired in the region of interest. Navigator echo based techniques usually dramatically improves the image quality without the need for patient cooperation but at the expense of longer acquisition times (on average 5-9 minutes per acquisition). Acquisition time highly depends on the regularity of the breathing pattern, when using a prospective data acquisition scheme [44]. This technique has been used in children as young as 4 years old [45].


**Figure 9. Trapped air and MRI.** Trapped air assessment with MRI. (a) Free-breathing BLADE MRI, (b) CT at end expiration, performed the same day, (c) 3D SPGR MRI coronal reformat breath-hold at end-inspiration and (d) end-expiration. Note areas trapped air in the left lower lobe (thick arrow) and area of air trapping in the left upper lobe (thin arrow).

Respiratory gating can also be obtained using pneumobelts or with the use of other external respiratory devices to trigger the scan prospectively [46]. A pneumobelt consists of a flexible corrugated tube placed

around the rib cage or the abdomen, the positioning selected depends on the maximum distention of the tube possible during the respiratory cycle. A predefined threshold is automatically selected by the patient monitoring unit dependent on the maximum excursion of the signal recorded from the pneumobelt. Similar to the navigator echo system, image acquisition is mostly performed during expiration, because it is more reproducible compared to inspiration.

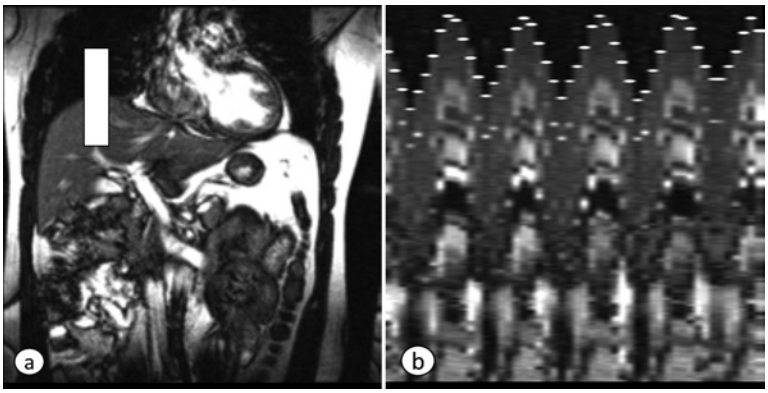


**Figure 10. Navigator technique.** (a) excitation pencil to determine diaphragmatic dome position at end expiration (white box), (b) respiratory waveform reconstructed.

*B. Non-monitored respiratory acquisitions:* Another established method to overcome breathing motion, is by averaging multiple acquisitions during free breathing. This method leads to image blurring, but reduces image ghosting [47]. In general this technique increases the acquisition time but mostly without increasing total MRI scanning time. Some special encoding techniques can even reduce scanning time, if the phase encoding lines collected are ordered depending on the signal acquired from the respiratory monitoring device [48]. Projection-like scanning techniques can also be used effectively without respiratory monitoring in order to better suppress the effect or motion and appearance of image artifacts. In many cases, when using this acquisition strategy, respiratory and cardiac waveforms may be extracted from the data collected and used to further reduce the detrimental effects from motion by correcting or eliminating data that may corrupt the acquisition (Figure 11).

*C. Cardiac monitored acquisitions:* To avoid blurring and ghosting artifacts from cardiac motion, ECG gating can be additionally incorporated [49]. ECG gating is not important for the upper portion of the lung, such as the apices, but it becomes more important for the diagnosis of pathologies involving the right middle lobe, lingula and the left lower lobe. The use of ECG and respiratory triggering together may increase scan time dramatically as imaging data is only accepted if both respiratory (at expiration) and cardiac triggering (at diastole) coincide [50]. Scans can be collected using retrospective or prospective schemes and may come in many different types as to reduce scanning time. MRI pulse sequences incorporating the projection reconstruction k-space encoding techniques can monitor both

types of motion and can reorder the data acquired as to produce datasets of the respiratory and cardiac cycles [7,8].



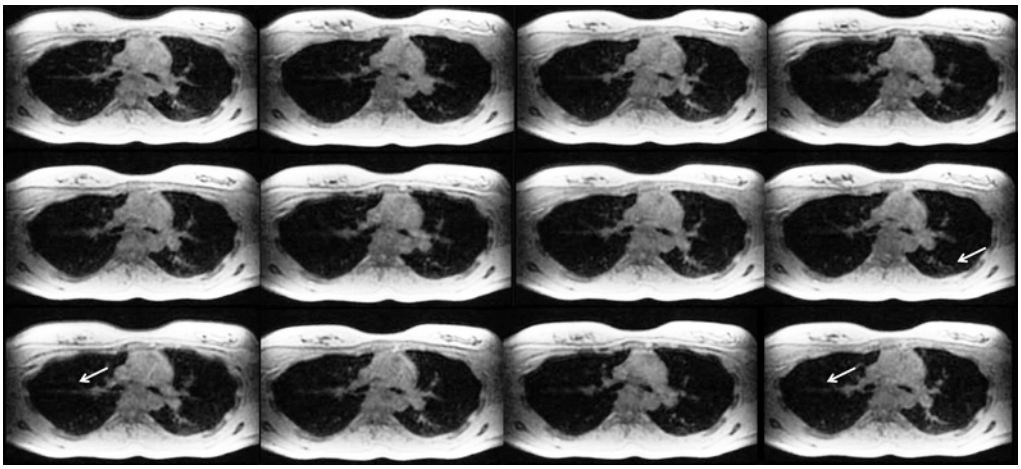

**Figure 11. Non-monitored respiratory acquisitions.** 3D SPGR free-breathing using parallel imaging (ARC 6) multiphase (20 phases in 1min, ~3sec/phase). Note that sequence is fast enough not being affected by lung motion. The only visible ghosting is due to cardiac and vessels pulsation (white arrows).

## MRI pulse sequences for lung MRI

Sequences for lung MRI must be selected based on the type of contrast required ($T_1$, $T_2$ or proton density), SNR, CNR, spatial and temporal resolution, and the sensitivity to motion and magnetic field inhomogeneity. Here, we summarize SE or GRE based MR pulse sequences for different vendors, which may collect 2D and 3D images during breath-hold conditions, because these are usually preferred for thoracic MRI and MRA [3] (Table 1).

### Turbo spin-echo sequence:

Turbo spin-echo (TSE) sequences are fast variants of conventional SE scans, which have the same low sensitivity to magnetic susceptibility artifacts and magnetic field inhomogeneities as SE and can be also used with sub-second acquisition times (i.e. single shot TSE scans) [38]. A typically robust sequence is the 2D T2-weighted single shot TSE scan, known under different acronyms as HASTE (Siemens) or SSFSE (GE) depending on the MRI scan manufacturer [51]. Single shot TSE techniques have high sensitivity and high SNR for fluid detection. TEs in the order of the $T_2$ of the lung parenchyma (~40 ms at 1.5 Tesla) are preferred for lung imaging with TSE [4].

One factor to consider with single shot TSE is the echo train length and the blurring introduced by the $T_2$ decay during acquisition. In fact when longer echo times are used, the $T_2$ decay in the phase encoding direction produces a filtering effect in the k-space, which manifests as blurring in the images [4]. This can be reduced in the lungs by using a rectangular FOV and orienting the phase-encode direction along the shortest axis e.g. anterior-posterior in an axial scan. Additionally parallel imaging and half-Fourier imaging option can help reduce this effect by reduction in the echo train length and the number of k-space line acquired [4]. Another problem of TSE readouts is that fat signal can be much brighter when compared to conventional SE scans due to J coupling refocusing of the coupled lipid spins [33]. Fat suppression schemes (FS) can be used to reduce this effect using chemically selective fat saturation techniques as fat resonates at a different frequency, or using short tau inversion recovery (STIR) preparations, because of the short $T_1$ of fat relative to many surrounding tissues in the thorax [52]. Although the FS is faster, it is less reliable than STIR, because of magnetic field inhomogeneities over such large FOVs, hence the effectiveness of the chemical fat suppression is compromised substantially when longer echo trains are used in a single-shot acquisitions. On the other hand, the inversion radiofrequency pulse used in STIR to cancel fat signal affects the signal in all the tissues contained in the slice acquired, leading to a generalized loss of SNR [52]. In general, the lung parenchyma and all tissues with longer $T_2$s, are best visualized when using these fat suppression techniques in combination with TSE readouts. Parallel imaging can dramatically reduce the effect of brighter fat, because fewer 180° refocusing pulses may be required when acquiring a particular slice per sequence TR at fixed resolution, so acquiring less phase encoding lines. Finally, Dixon-based fat separation techniques (i.e. DIXON, Siemens, or IDEAL, GE) can provide a more homogeneous removal of lipid signals than conventional frequency selective chemical saturation techniques [53] (Figure 12).

The clinical utility of single shot TSE scans for imaging the lung has been shown in different studies for the detection of lung pathologies, such as pneumonia in immune compromised patients [54,55]. In a study at low magnetic field strengths, TSE was the preferred sequence for the visualization of mediastinum and lung consolidations [56]. HASTE has been used to assess not only consolidations due to pneumonia, but also its complications, such as abscess, necrosis and empyema. These $T_2$-weighted sequences are also indicated in those cystic diseases with increased water-content, such congenital lung airway malformations (CPAMs), and CF [5]. In CF, HASTE sequence delineates easily bronchiectasis and mucus plugs, which have both high signal in $T_2$-weighted imaging [57] (Figure 13).

**Table 1.** MRI sequence acronyms according system vendors

| Sequence type | Siemens | GE | Philips | Hitachi | Toshiba |
|---|---|---|---|---|---|
| **GRE family** | | | | | |
| **Spoiled RF GRE** | FLASH | SPGR | T1-FFE | RF spoiled SARGE (RSSG) | Fast FE |
| **PD, T1, T2*weighted** | | | | | |
| **Fast GRE** | turboFLASH | FGRE | | | |
| **PD, T1, T2, T2* weighted** | | | | | |
| **Steady State Free precession T2/T1 weighted** | TrueFISP | FIESTA | Balanced FFE | Balanced SARGE (BASG) | True SSFP |
| **SE family** | | | | | |
| **Fast Spin Echo** | TurboSE | FSE(Fast SE) | TurboSE | FSE | FastSE |
| **PD, T1, T2 weighted** | | | | | |
| **Single-Shot Fast Spin Echo** | SSTSE/HASTE | SSFSE | SSH TSE | FSE-ADA | Super FASE |
| **T1, T2 weighted** | | | | | |
| **GRE/SE techniques and acquisition strategies** | | | | | |
| **Volume Interpolated 3D GRE** | VIBE | LAVA | THRIVE | TIGRE | QUICK 3D |
| **Accelerated 3D FSE** | SPACE | CUBE | ---- | ---- | ----- |
| **Motion Correction with Radial Blades** | BLADE | PROPELLER | Multi-Vane | RADAR | JET |
| **Motion correction** | PACE | RSPE | PEAR | ---- | PERRM |
| **Ramped RF profiles for enhanced MRA** | TONE | Ramped RF | TONE | ISCE | SSP |
| **Fluoro-monitored acquisition with contrast injections** | Care Bolus | SmartPrep | BolusTrak, MobiTrak | FLUTE | VisualPrep |
| **Time resolved 3D MRI/MRA** | TREAT,TWIST | TRICKS | 4D TRAK | Freeze Frame | TRAQ |
| **k-space scanning /contrast injection** | Elliptical scanning | Elliptic Centric | CENTRA | DRKS | PEAKS |
| **Parallel imaging techniques** | iPAT,mSENSE, GRAPPA | ASSET/ARC | SENSE | SPEEDER | RAPID |
| **Multi-channel receiver intensity correction normalization** | Prescan Normalize | SCIC/PURE | CLEAR | ----- | NATURAL |

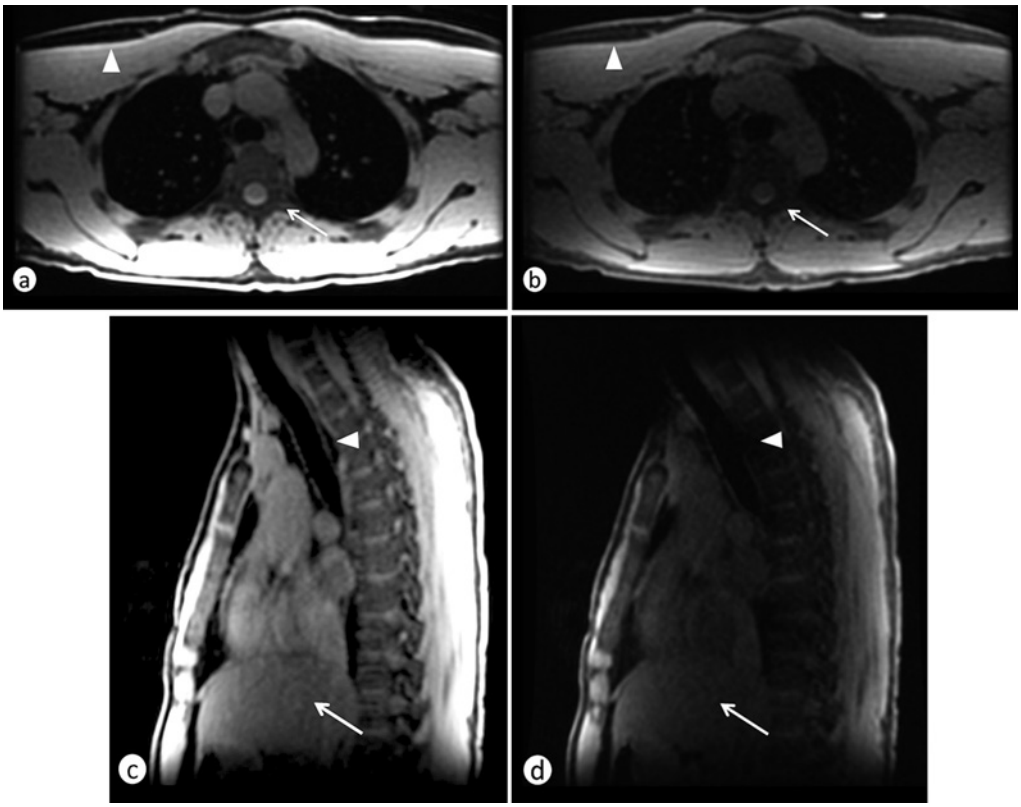


**Figure 12. Fat saturation.** Fat signal suppression techniques, DIXON (a and c) versus Fat Sat (b and d). Note more homogenous fat signal suppression in DIXON (arrow head) than Fat Sat technique. Note also the generalized loss of signal with Fat Sat technique (arrow). Image windowing and resolution are constant between the images.

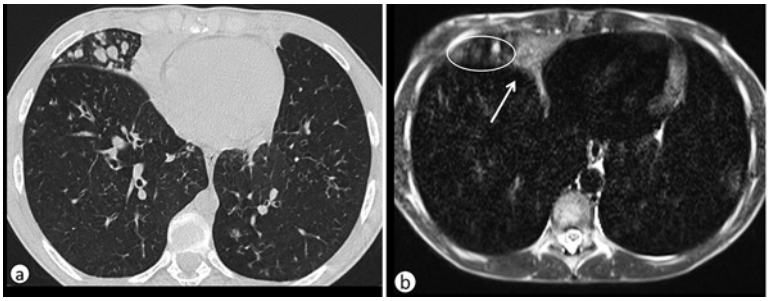


**Figure 13. a and b SSFSE/HASTE in CF.** CF patient, CT image (a) and SSFSE (b) at end-inspiration. Note the consolidation in the right middle lobe (white arrow) and the adjacent bronchi filled of mucus (white circle).

**Gradient recalled echo sequences**

All variations of 2D and 3D short and ultra-short TE (UTE) GRE readouts are typically considered as the most robust sequence for lung parenchyma and lung MR imaging [4]. Short and UTE GRE scans can overcome the short $T_2$* of lung parenchyma and minimize the signal loss created by the extensive air-tissue interfaces found around vascular and airway structures. GRE sequences are usually collected with very short TRs, when compared to single shot or slower gated TSE scans. A short TR is critical for patients, who are unable to accomplish long breath-holds (>10 seconds) [3]. Likewise, GRE scans have much lower specific absorption ratios values, when compared to TSE readouts, although this usually comes with a penalty on SNR. The specific absorption ratio is a direct indicator of the potential tissue heating that can happen due to the application of the RF during scanning [33].

In general, 3D GRE acquisitions are the preferred scanning methodology as they provide better SNR and are less sensitive to susceptibility artifacts than 2D scans. Nonetheless, 3D may not be as robust regarding to the detrimental effects of motion as compared to 2D scans, which can freeze cardiac and respiratory motion even in non- cooperative patients. Overall, 3D GRE acquisitions can acquire the entire thorax with adequate resolution with isotropic voxels (≥3 $mm^3$) and SNR in less than 15 seconds [10]. When isotropic voxels are collected, multi-planar reformats can be performed in any orientation which is crucial in the evaluation of vascular and airways structures [4] (Figure 14).

There are two types of GRE readouts: those MR pulse sequences that eliminate the transverse magnetization prior to the application of each RF pulse on each TR and those that do not. The first type includes the most typical scans performed and fall under the acronyms of FLASH (Siemens), SPGR (GE), etc. The second type is usually known under the steady state free precession (SSFP) family with acronyms such as TrueFISP (Siemens), FIESTA (GE), etc.

For a fixed repetition time TR, the first type (FLASH, SPGR) provides contrast ranging from proton-density weighting (low flip angle), mostly used to investigate lung parenchyma and airways without the use of contrast agents, to $T_1$ weighting (high flip angle), used to better characterize vascular structures and to map lung parenchymal perfusion after contrast administration. A limitation of GRE sequences is that they cannot readily provide T2 weighting, because the TE can never be chosen long enough and the T2* effects dominate signal behavior. Another limitation in GRE imaging is due to the strong tissue-air boundaries in the lung parenchyma that create substantial susceptibility artifacts. The net result is bright and dark areas with spatial distortion of surrounding anatomy.

The FLASH/SPGR sequences has been used in several clinical studies, for example volume interpolated 3D GRE (i.e. LAVA) was rated as the best sequence for lung nodule detection in vivo [56] (Figure 15). In another comparative study in porcine chest phantom, 3D GRE had similar diagnostic accuracy as CT in depicting lung nodules larger than 8 mm, and sensitivity between 80 and 90% for lesions larger than 4 mm [58]. Lesion smaller than 4 mm were difficult to detect with MRI [58]. 2D/3D SPGR is also the preferred sequence for contrast enhanced studies, where contrast enhancing lesions, vessels

and lymph nodes can better delineated after Gadolinium injection [3] and in MR angiography and dynamic contrast enhanced perfusion imaging of the lungs.

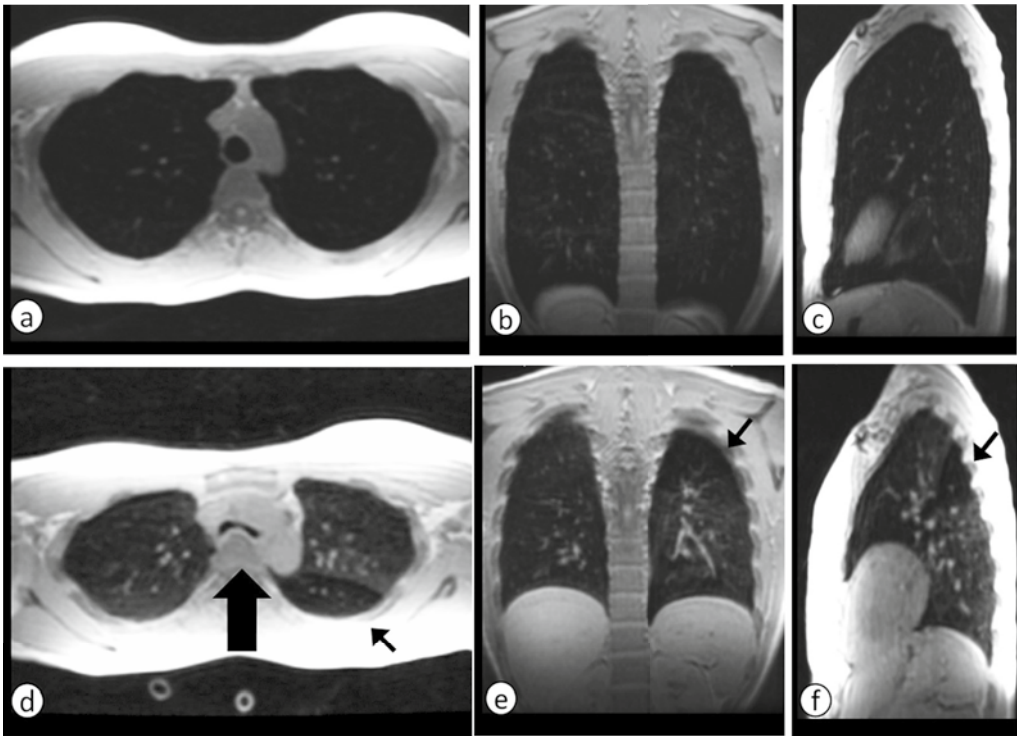


**Figure 14. SPGR (FLASH) 3 D.** 3D SPGR sagittal acquisition with axial and coronal reformats at end-inspiration (a-c) and end-expiration (d-f). Isotropic voxel 3 $mm^3$ with 6 seconds acquisition time. Note area of air trapping (thin arrow) in the left lower lobe with excessive collapse of trachea (thick arrow) in the expiratory image (lower row).

The second group of sequences (SSFP) generate a $T_2/T_1$ weighted contrast with medium to high flip angle settings (>30°) and very short TRs, so enhancing tissues in the lung with more water-like behavior, such as mucus plugs in the airways [33]. 2D SSFP scans are frequently used due to the inherent high SNR, which is mostly due to the use of higher flip angles than SPGR. 2D SSFP allows fast acquisition of the entire thorax in a single breath-hold with good SNR. At the same time, SSFP type can be quite sensitive to magnetic field inhomogeneities producing unwanted local variations in contrast behavior, which become quite problematic at higher magnetic field strengths, i.e. 3.0T. These inhomogeneities are usually described as off-resonance banding artifacts, which are seen with SSFP in regions of regional magnetic inhomogeneity, such as the area above the diaphragm [33]. This artifact tends to alter the lung signal intensity, so signal from nodules and vessels are subsequently cancelled [59]. This artifact can be reduced by substantially shortening TR [59]. Another limitation of SSFP imaging is that it has an intensive specific absorption ratio, especially when used with high flip

angles at higher field strengths. Repeated imaging with SSFP sequence can exceed the maximal specific absorption ratios level allowed in MRI.



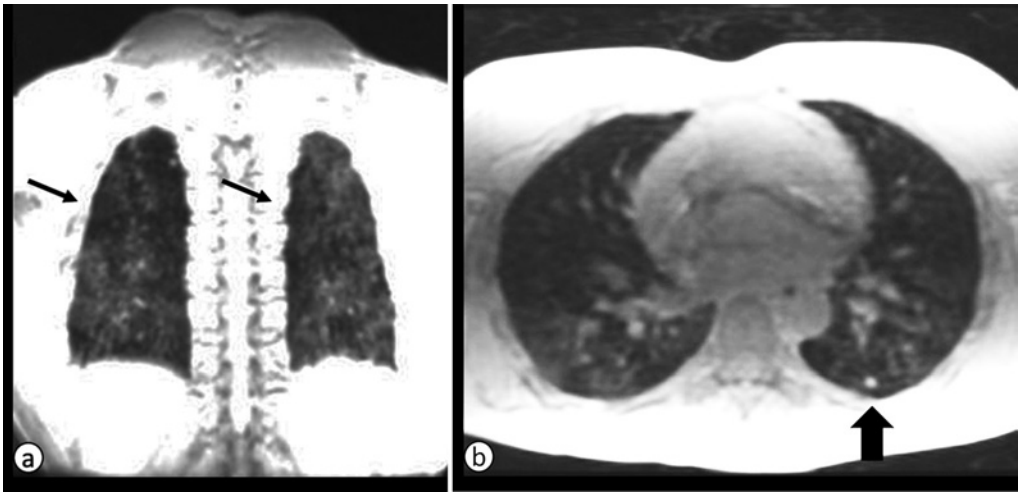


**Figure 15. SPGR.** 3D SPGR coronal (a) and axial (b) acquired with a 1.5 T system in a patient with flu symptoms. Note areas of air trapping (thin arrow) and left lower lobe subpleural nodule (thick arrow).

SSFP is commonly used in cardiac imaging, but it can also be used for lung MRI. In a comparative single center study between different MRI sequences, SSFP was the preferred sequence to visualize lung parenchyma in volunteers, and also the sequence that had the fewest motion artifacts [56]. In CF patients, SSFP showed to be sensitive in the detection of clinically relevant structural abnormalities, such as bronchiectasis, mucus plugging, and atelectasis [39] (Figure 16). In children with possible pneumonia SSFP was compared to chest radiograph [60], showing really good correlation between MRI and chest radiograph for all pathological findings [60]. More recently SSFP has been proposed as best sequence to assess lung fibrosis [59]. Finally, 3D SSFP provides an effective means of generating a lung MR angiogram without the need for contrast.

*Projection acquisition and reconstruction techniques*

PROPELLER is a particular TSE non-breath hold readout that has been used more extensively for lung MRI. PROPELLER collects imaging data using rotating k-space bands or blades, which is thought to be more robust to respiratory movements [61]. The collection of blades oversamples the center of k-space, so producing better SNR and reducing rotational and translational in-plane motion occurred between the images collected on each blade [62]. This sequence is more suitable for non-cooperative subjects, such as pediatric patients younger than 5 years old or adults unable to breath-holding. PROPELLER can also be combined with respiratory-gated techniques (i.e. navigators or pneumobelts), so further reducing the effects of motion. This combined approach allows full chest

coverage in 4-7 minutes, depending on the breathing pattern of the patient, with good in-plane spatial resolution (1-1.5 mm) [3]. However, studies have shown that PROPELLER frequently produces streak artifacts [5]. As result lines are projected in the lung parenchyma creating false signals resembling bronchial walls and bronchiectasis (Figure 17). To reduce this artifact, the blade width (k-space coverage acquired per blade), should be increased or a finer angular sampling used [62].

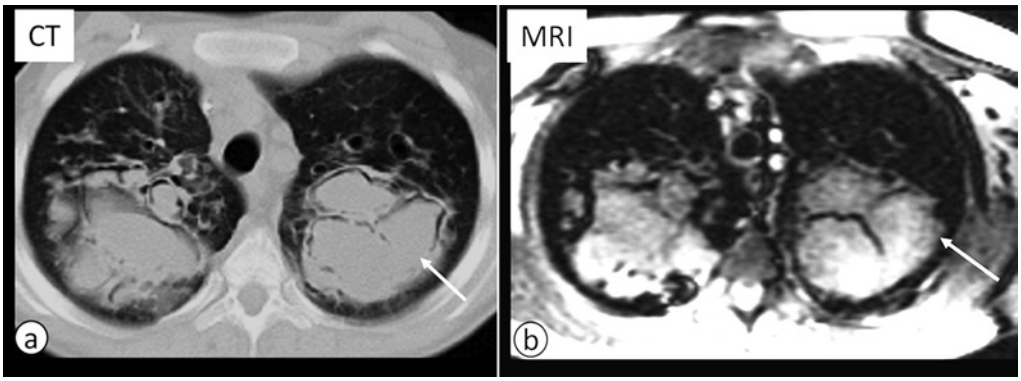


**Figure 16. Aspergillomas infection in CF.** CT (a) versus SSFP MRI (b) in 16 years old boy with end stage CF lung disease. Note widely dilated bronchi filled with thick mucus and aspergillomas (white arrow).

**Figure 17. PROPELLER/BLADE artifact.** 2D PROPELLER/BLADE free-breathing in CF patient. Note linear ghosting surrounding the heart and the external portion of the chest (white arrows) due to the helicoidal k-space reconstruction.

**Figure 18. PROPELLER/BLADE in CF.** 2D PROPELLER/BLADE coronal in CF patient. Note areas of mucus plug (arrows) and bronchiectasis (arrowhead).

In a multicenter study in CF patients comparing CT and MRI, PROPELLER showed good intra- and inter-observer agreement to assess CF-related lung abnormalities [63] (Figure 18). In another comparative study with chest radiography, PROPELLER was superior to detect lung abnormalities in patient with middle lobe syndrome [45]. In patients with common variable immunodeficiency, who are prone to suffer repeated lung infection, PROPELLER was proposed as alternative method to reduce cumulative dose due to repeated CT imaging [64].

## Functional Imaging

MRI offers different techniques to study different functional aspects of lung and airways. Gadolinium contrast has been used to assess the pulmonary vasculature, and lung perfusion [65,66]. The high temporal resolution of MRI has proven to be useful to assess lung- and central airways mechanics [10]. Hyperpolarized gases, such as helium ($^{3}$He) and Xenon ($^{129}$Xe) have been developed to produce high-contrast images of lung ventilation [5,17]. Finally Fourier Decomposition (FD), a recent developed MR technique, has been used to assess lung perfusion and lung ventilation without the use of contrast media [67]. These techniques will be briefly described starting with the clinical available to the most experimental technique.

## Lung Magnetic Resonance Angiography

Magnetic resonance angiography (MRA) of the lung can be obtained without and with the intravenous administration of contrast. In both cases, the low proton density of the lungs is ideal for generating high angiographic contrast with all sequence types (SPGR and SSFP).

### Non-contrast MRA acquisitions

The main advantage of these techniques is that they can be repeated without concerns related to the use of contrast, especially in patients with impaired renal function [5]. When using SPGR scans, MRAs can be obtained using a proton-density weighted contrast or employing the time-of-flight (TOF) enhancement phenomenon by choosing higher flip angles and the correct orientation for 2D slices or 3D volumes. TOF angiography is based on the phenomenon of flow-related enhancement of fully-magnetized blood spins entering into an imaged slice [33]. As a result of being unsaturated, these blood spins give more signal than surrounding saturated stationary spins, thus generating bright blood images. 3D angiograms can be generated using techniques, such as maximum intensity projection or volume rendering, making vessels appear similar to conventional X-ray angiography [33] (Figure 19). TOF always allows good depiction of vascular morphology whenever inflow effects are adequate (high flow velocities). Different acquisition strategies can be used to perform TOF 2D and 3D (Table 2).

Non-contrast MRA can also be obtained with 2D and 3D SSFP based sequences, which supply bright blood vessels images. Thin 3D slab SSFP scans (i.e. 3 mm) can be collected in a single breath-hold with reasonable resolution. Nevertheless, this sequence has been adapted for longer scanning scenarios, using respiratory navigators and higher resolution settings with larger slice coverage and smaller voxel sizes. With these improved settings, SSFP has been used for non-contrast MRA evaluation of the thoracic vasculature and pulmonary embolism [68,69] (Figure 20).

**Table 2.** Time of Flight (TOF) 2D and 3D

| **Breath-hold TOF 2D/3D SPGR scans** | |
|---|---|
| 2D slice/3D thin slab sequential acquisitions | Short TR (5-10ms), short TE (1-3ms), flip angle >45°. Tracking saturation bands for selective imaging of pulmonary arteries or veins (mostly for sagittal acquisitions) can be used. |
| 2D Interleaved | Long TR (100-280ms), short TE (1-3ms), intermediate flip angles (25°-45°). No tracking saturation bands. Inflow effects on the arterial side can provide higher signal than veins. |
| 2D Segmented k-space & cardiac triggering | Short TR (5-10 ms), short TE (1-3ms). Optimal inflow effect at peak systole allows higher SNR and distinction against veins. Can be performed in a cine loop. Usually one thick slice per breath-hold is acquired. |
| Thick slab 3D | Short TR (5-10ms), short TE (1-3ms).<br>Sagittal slab, one lung.<br>Low flip angles or spatially variable RF (TONE, VUSE). Arteries can be seen with higher intensity as compared to veins. |

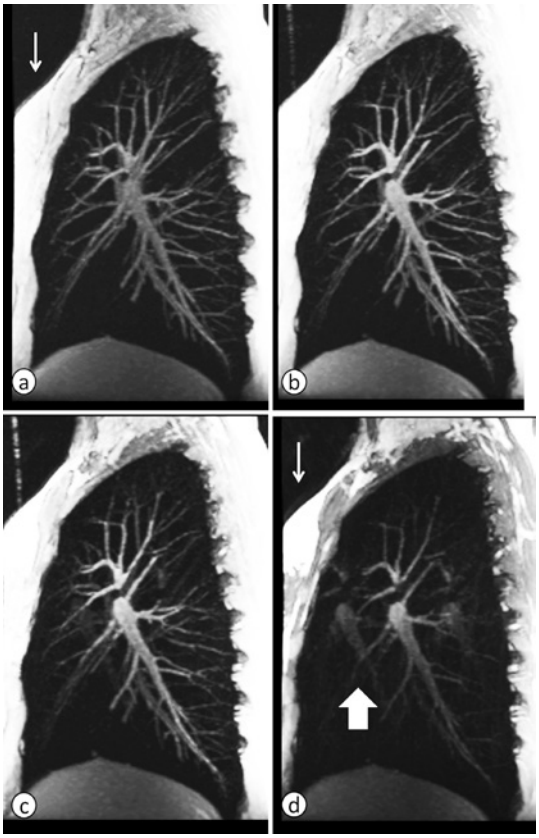


**Figure 19. Time of flight angiography.** 3D Time-of-Flight (TOF) SPGR with increasing flip angle (FA): (a) FA=2, (b) FA=6, (c) FA=8, and (d) FA=12. Note that by increasing the FA the weighting is shifting from PD to T1, as denoted by signal intensity of the fat in the anterior chest wall (white arrow). Echo-time is also increasing, thus SNR decay as denoted by vessel signal. Finally at the highest FA, (d) the signal from the vein disappears, but new ghosting artifact from artery pulsation is visible (thick arrow).

To detect pulmonary embolism, typically 2D or small slab 3D sequential SPGR TOF sequences have the best chance to show pulmonary embolism, because they maximize the TOF effect using higher angle imaging and thin slices/volumes. Other combinations of 2D and 3D scans are inadequate to demonstrate pulmonary embolism properly, especially in patients with compromised cardiac function because of poor inflow effects.

For pulmonary embolism detection, SSFP sequence showed a sensitivity ranging from 90 to 100% for central pulmonary embolism (main pulmonary arteries) and 68 to 80% for peripheral subsegmental pulmonary embolism [70,71]. It is important to underline how with SSFP, pulmonary embolism appearance depends on the age of the clot. In case the pulmonary embolism is chronic it appears as darker regions against brighter vessels. In case of acute pulmonary embolism, the signal can vary largely according the methaemoglobin content.

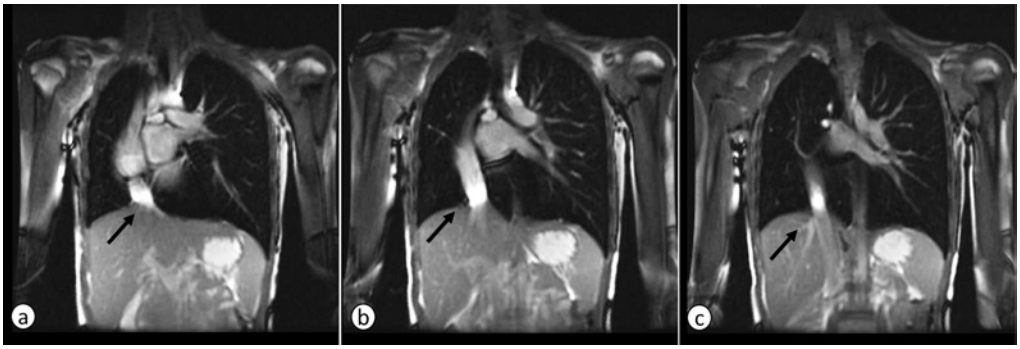

**Figure 20. Scimitar syndrome.** 2D SSFP/TrueFISP coronal in patient with anomalous partial pulmonary venous return (scimitar syndrome). Note the aberrant pulmonary vein connected to inferior vena cava (arrows).

## Dark blood angiography

ECG-gated black blood SSFSE with double inversion recovery has also been proposed as a non-contrast sequence that provides dark vessel images and provides better anatomical images of the diseased lung or thoracic abnormalities. Dark blood SSFSE acquisitions are frequently used to study the anatomy of the heart, great vessels and mediastinum [72]. Dark blood SSFSE has several advantages, including good SNR, minimal motion blurring, little artifact from field inhomogeneities and superb contrast characteristics. Pulmonary emboli can be well seen using this sequence at short TE [72] (Figure 21).

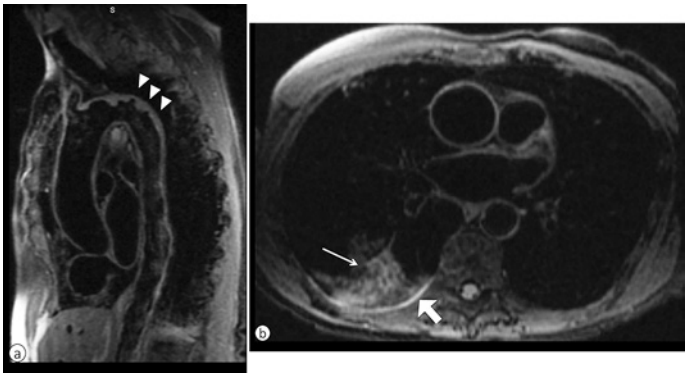

**Figure 21. a and b. Black blood SSFSE.** Sagittal (a) and axial (b) cardiac triggered fast spin echo with black blood preparation and fat suppression in patient with parietal thrombus in the aortic arch (arrowheads). Note clear depiction of right lower lobe infiltrate (thin arrow) and small pleural effusion (thick arrow).

## Arterial Spin labeling

Arterial Spin Labeling (ASL) is a technique based on "labeling" of blood protons in the supplying vessels outside the volume of interest (VOI) by using a selective radiofrequency pulse excitation [73]. The VOI is imaged after a period of time known as the post labeling delay (PLD), which is needed for the labeled blood to reach the targeted organ parenchyma. Images are obtained both in the labeled and control (i.e. unlabeled) state to perform subtraction imaging. ASL technique can be performed both with SSFP or SSFSE sequences, because both techniques allow short scan times and the use of various pre-pulses (fat-suppression, inversion and/or ASL pulses) [74]. While SSFSE is limited by flow characteristics (i.e. velocity and vessel orientation), SSFP is more flow independent and enables imaging of fast flow vessels [74]. For this reason SSFP is usually the preferred method for lung MRI [73].

The major advantage of ASL is the absence of contrast and the repeatability of the exam. These two characteristics make ASL suitable for patients with impaired renal function, where repeated contrast administration is limited or for young children where noninvasive techniques are preferred. However ASL is technically challenging to implement in clinical practice, because it is a single slice technique with limited voxel resolution that requires a regular cardiac cycle [73]. Moreover the SNR of ASL images is low, especially in the anterior portion of the lung, which in supine position is less perfused than the posterior portion. To increase sensitivity of ASL to perfusion defects, it is recommended positioning the patient so that the area of interest is down-gravity (i.e. prone position for upper lobes) [73]. Moreover, SNR can also be enhanced by performing ASL during end-expiratory breath-hold condition [75]. These technical challenges explain the limited number of works describing the clinical application of ASL [76,77].

## Contrast-enhanced MRA acquisitions

Despite non-contrast studies are feasible for lung MRA, contrast-enhanced MRA (CEMRA) studies using the intravenous injection of contrast media are the preferred method. CEMRA supplies high SNR and CNR using $T_1$-weighted scans, and hence supplying images with higher temporal and spatial resolution [5]. Likewise, CEMRA is reliable; the injection of contrast agents, mostly based on gadolinium chelates, renders angiographic images virtually acquired in any orientation (sagittal, coronal or axial) and is completely independent from inflow effects. CEMRA allows to identify even down to sixth order subsegmental pulmonary arteries of a normal lung [78]. Timing of contrast bolus is crucial to optimize image contrast, so k-space is acquired during contrast peak, and to limit venous contamination of MRA [79]. CEMRA usually collects data using a very short TR 2D/3D heavily $T_1$-weighted GRE acquisition. With scanning strategies using parallel imaging, volumetric CEMRA scans can be acquired even with sub-second time resolution using powerful imaging gradient systems. Typical breath-hold CEMRA settings consider very short TR (1.3-3 ms), short TE (0.5-1.3ms),

and flip angles ranging between 10-30º depending on contrast dosage, concentration and speed of administration. Resolution and coverage are usually adjusted to suit a comfortable breath-hold [3]. In adults CEMRA has used to study pulmonary emboli, especially when iodinated contrast agent and CT imaging is contraindicated [80]. In pediatric patients, CEMRA is frequently used to study congenital vascular anomalies, such as transposition of great vessel, tetralogy of Fallot, anomalous pulmonary venous return, pulmonary sequestration, thromboembolism, etc. [5,24,81] (Figure 22).

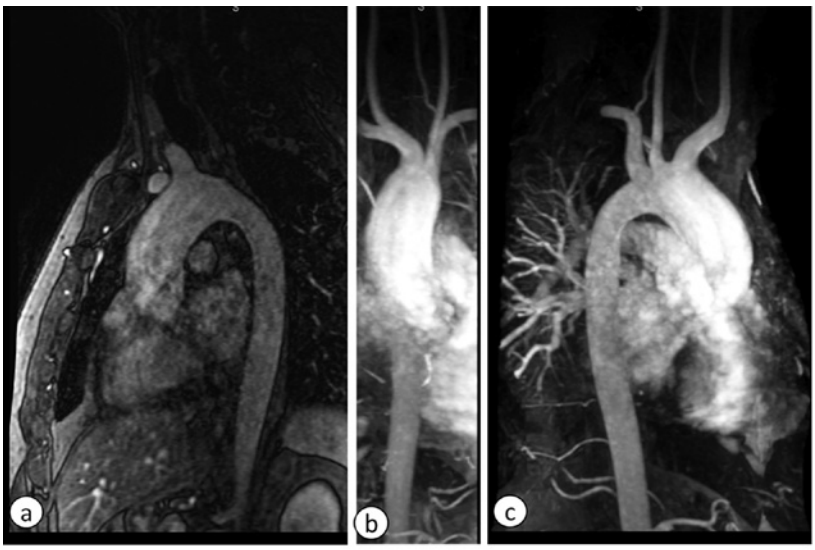


**Figure 22. MRA.** Contrast enhanced Magnetic Resonance Angiography (CEMRA) of aorta in patient with bicuspid aortic valve, moderate stenosis, complicated by mild insufficiency and ascending aorta dilatation. (a) 3D GRE after gadolinium injection (TR/TE/FA=3.2 ms/1.15 ms/17º) and (b-c) maximum intensity projection reconstructions (MIP).

## Magnetic Resonance Lung Perfusion

Different lung diseases alter lung perfusion through the physiologic mechanism of hypoxic lung vasoconstriction, also known as Euler-Liljestrand mechanism [82]. This mechanism determines constriction of the pulmonary arteries in poorly ventilated lung areas, redirecting blood flow to normally ventilated alveoli. These perfusion defects can be assessed by MRI sequences using gadolinium, such as dynamic contrast-enhanced (DCE) imaging, or without, such as Fourier Decomposition (FD), which is described in the following chapter. Despite DCE has a broader use in clinical practice than FD, both techniques are still used in experimental setting.

DCE is obtained by fast imaging of the first pass of contrast agent through the lungs after an intravenous bolus injection [5]. 3D gradient echo sequences are usually preferred over 2D techniques due to the

higher spatial resolution and anatomic coverage [73]. Different k-space acquisition strategies have been developed to improve temporal and spatial resolution of DCE, such as TREAT, TWIST (Siemens) and TRICKS (GE) [83,73] (Table 1). These techniques use key-hole and view sharing methods, which oversamples the center of the k-space (image contrast) compared to the periphery (image edge detail). This improves the temporal resolution, because only part of the k-space is collected, and provides the high CNR needed for perfusion MRI [84]. Key-hole and view sharing methods can also be combined with spiral or radial k-space readout trajectories (i.e. vastly undersampled isotropic projection, VIPR) that allow both central and peripheral k-space sampling, thus providing both high CNR and spatial resolution [84]. Further evolution of this technique is the highly constrained back-projection reconstruction (HYPR), which is a mask-based reconstruction technique capable of acceleration factors as large as 1000, with minimal tradeoff between spatial and temporal resolution [84]. Finally compress sensing (CS), a technique that allows to reconstruct images from fewer signal measurements, can be combined with the aforementioned k-space undersampling techniques [85]. CS is a promising technique for 3D lung perfusion imaging by enabling higher acceleration factors with reduced motion artifacts [86].

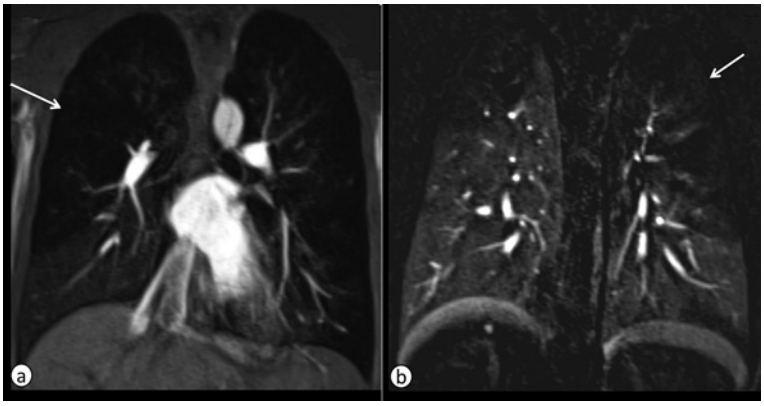


**Figure 23. Perfusion.** MR Perfusion study. Non-subtracted (a) and subtracted (b) coronal views of Time-resolved Angiography With Interleaved Stochastic Trajectories (TWIST@SIEMENS) after gadolinium injection in CF patients. Note multiple areas of mosaic perfusion likely representing areas of hypoperfusion (arrows).

DCE has mostly been tested in adults to assess pulmonary embolism, chronic thromboembolic pulmonary hypertension and chronic obstructive lung disease [87-89]. In these diseases, MRI showed similar sensitivity to nuclear medicine and CT studies to assess lung perfusion impairment, but with the advantage of higher spatial resolution and no radiation exposure [90,91]. DCE has also shown high reliability to quantify regional pulmonary microvascular perfusion [92]. Perfusion MRI showed higher potential than CT to distinguish controls from mild COPD patients and was more sensitive in identifying abnormalities amongst smokers with normal lung function [93]. In pediatric patients, DCE has also proved to be a very sensitive technique to assess early vascular functional impairment

and therapy control in CF [16,94] (Figure 23) and congenital diaphragmatic hernia [95]. In a study regarding childhood constrictive bronchiolitis obliterans, DCE showed to be more sensitive than $Tc^{99m}$ perfusion scintigraphy to detect perfusion defect and determine prognosis [96].

## Contrast agents for CEMRA

MRA and Perfusion MRI can be performed either with intravascular or extravascular Gadolinium based contrast agents (GBCA) [97]. Extravascular agents permit high-contrast first-passing imaging [79] but the rapid decline of contrast enhancement make the appropriate timing challenging. Different techniques exist to optimize contrast bolus timing with extravascular agent. The dual bolus technique relies in a small "test bolus" (1 to 2 ml) to compute the bolus arrival time in the main pulmonary artery. This small bolus is also used to compute the arterial input function (AIF), which is needed to obtain quantitative parameters (i.e. pulmonary blood flow) [79]. The single bolus technique uses a dose of 0.1-0.2 ml/kg GBCA followed by 20-30 ml saline solution at high flow injection (4-5 ml/sec). Single bolus technique is frequently combined with bolus tracking method, where contrast bolus is monitored in real time and injection is triggered when contrast reach pulmonary artery. Extravascular agents can be used both for MRA and Perfusion MRI [79]. In a recent comparison between extravascular agents and injections techniques, Gd-BOPTA (Multihance, Bracco, Italy) with single bolus showed the best SNR in the lung parenchyma [98].

Differently the intravascular (aka "blood pool") GBCA are used for steady state imaging (i.e. gadofosveset trisodium@Ablavar, Lantheus Medical Imaging, or @Vasovist, Bayern Schering Pharma). Blood pool GBCA have gained popularity in vascular imaging, especially in those patients where distinction between arteries and veins is not necessary [99]. Blood pool GBCA has a prolonged half-life, which allows high-resolution imaging at lower Gadolinium dose compared to extravascular agents [99]. In fact, the longer intravascular permanence of gadofosveset facilitates longer acquisition sessions of sub-millimetric isotropic voxels, frequently needed in pediatric patients [99]. Despite the good safety profile of this blood pool agents, its use in pediatric patients remains an off-label use [99,100].
Independently from the type of contrast and the administration technique used, GBCA administration should carefully considered according patient's renal function and after an appropriate risk-to-benefit assessment [97]. Guidelines for GBCA administration varies between United States and Europe [101-105]. In general, GBCA administration depends on patient's renal function, age, comorbidities, history of allergic reactions and specific gender-related conditions, such as pregnancy or lactation [97,106]. In these situations, the GBCA should be chosen according its safety profile, which varies according the chemical structure. In general, the macrocyclic nonionic GBCA (Gd-DOTA@Dotarem, Guerbet, Gd-HP-DO3A@Prohance, Bracco, Gd-BT-DO3A@GADOVIST, Bayer) have the safest administration profile, and are usually preferred in pediatric patients or those with impaired renal function [5,97,102].

## Fourier Decomposition

Fourier decomposition is a new technique of non-contrast-enhanced functional lung MRI that supplies perfusion and ventilation maps not dependent on intravenous or gaseous contrast agents [107]. This new technique is based on a 2D SSFP sequence with high temporal resolution of 3.33 images/s acquired in coronal and sagittal view without cardiac or respiratory gating. After data collection, first a non-rigid image registration algorithm is applied to compensate for respiratory motion. Then using the Fourier transformation, the signal intensity changes of the lung parenchyma related to the cardiac and respiratory cycle are decomposed to obtain the perfusion- and ventilation-weighted images [107]. Although this technique is currently only commercially available in Siemens scanner, preliminary results are promising (Figure 24). For example Fourier decomposition has shown high sensitivity and specificity to diagnose chronic pulmonary embolism [108]. Fourier decomposition has been recently applied in a group of pediatric CF patients [18], and it was able to provide equivalent diagnostic information to dynamic contrast enhanced MR imaging in CF patients.

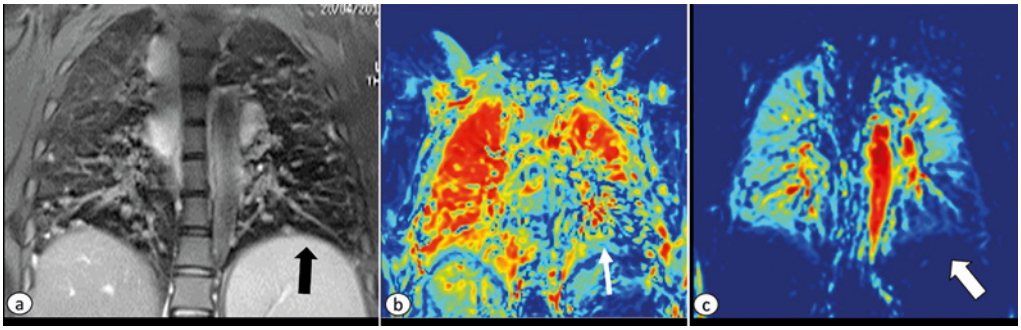


**Figure 24. Fourier Decomposition.** PROPELLER/ BLADE MRI (a) and FOURIER DECOMPOSITION MRI ventilation (b) and perfusion (c) maps, in patient with common variable immunodeficiency (CVID). Note in the morphological image darker area in the left lower lobe (black arrow), which consists of area of trapped air. In the correspondent ventilation map that area appears not ventilated (white thin arrow). The same area in the perfusion map shows reduced perfusion (thick white arrow), according the physiologic reflex of hypoxic vasoconstriction. Courtesy of Giovanni Morana, Ca'Foncello Treviso Hospital.

## Oxygen-enhanced MRI

Oxygen-enhanced MRI (OE-MRI) is a non-invasive method that supplies information on lung ventilation and tissue oxygenation. OE-MRI takes advantage on the concentration-dependent paramagnetic effect of oxygen on T1 relaxation time, which shortens at high $O_2$ concentration levels [109]. Gradient-echo readouts are used to perform T1-mapping at variable oxygen concentration and to compute the oxygen transfer function. Although inversion recovery single shot fast spin echo (IR-SSFSE) technique have been used in OE-MRI, the best results have been achieved with 3D radial UTE [109]. 3D radial UTE provides robust correction of cardiac motion and high CNR by

oversampling of the k-space center. Low cost and high accessibility of oxygen are the main advantages of OE-MRI technique, which is still hampered by different technical challenges. OE-MRI requires indeed long imaging acquisitions sessions (5-30 min), breath-hold imaging is not feasible and SNR is usually low when compared to other ventilation techniques, such as hyperpolarized gases MRI [109].

Despite these limitations OE-MRI has been used in different chronic lung diseases, such as COPD, asthma and CF. In patient with emphysema OE-MRI has been used to map the diffusing capacity of the lung [110] and to classify COPD patients accordingly to the pulmonary function loss [111]. In asthma patients, OE-MRI has been used to assess clinical stage and to evaluate response to treatment [112]. In CF, OE-MRI showed inhomogeneous ventilation compared to healthy volunteers (Figure 25), with patchy ventilation/perfusion defects [113].

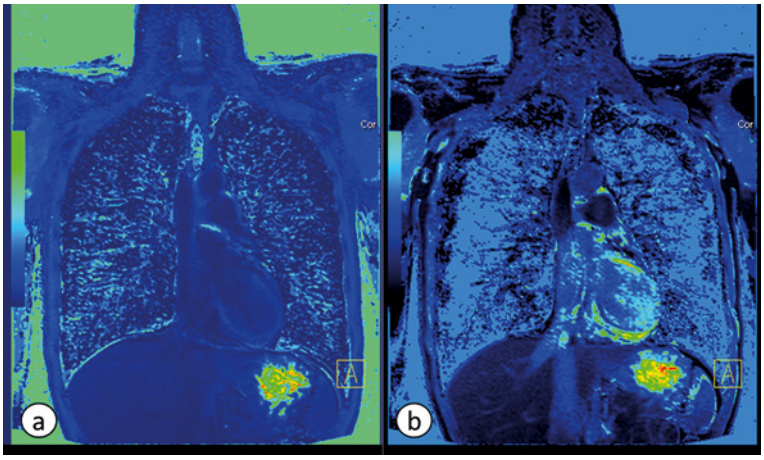


**Figure 25. Oxygen-enhanced MRI.** Coronal Oxygen-enhanced MRI in healthy volunteer at room air (a) and during oxygen administration (b). Note signal increase during oxygen administration for T1 shortening effect.

## Hyperpolarized Gases

Hyperpolarized gas MRI (HP MRI) allows regional measures of emphysema, gas trapping and airflow obstruction [109]. With 3D GRE and SSFP sequences high-resolution images of lung ventilation can be obtained which have the sensitivity to assess regional changes in lung intervention with therapy [114]. With rapid 2D imaging inspiratory gas flow can be monitored and multi-breath imaging gas washout time constants can be mapped [115,116]. Diffusion weighted imaging with HP MRI measures the restriction of gas diffusivity in lung microstructure, and supply an indirect measurement of airspaces dimension [109]. Despite the exquisite sensitivity of HP MRI to early signs of structure-function change in lung disease, the added complexity of the technology has so far limited its use in clinical practice to date. A well-known limit of HP MRI is the need of gas polarizer and multinuclear

technology that are not widely available [109]. Hyperpolarized gases MRI requires custom polarization systems for preparation of the gases and dedicated transmit/receive radiofrequency coils tuned to the $He^3$ or $Xe^{129}$ resonance frequency and as such is still primarily used for clinical research. Moreover the limited availability of $^3He$ has also meant that clinical uptake has been limited, but $^{129}Xe$ provides a cheaper alternative for clinical lung imaging in years to come and is now ready for evaluation pediatrics. Some concerns remain for the anesthetic effect of xenon, which remain to be studied in pediatric patients [109].

HP MRI has demonstrated the ability to detect changes in ventilation, and lung microstructure in different lung diseases, including COPD [117,118], asthma [119], CF [120], congenital diaphragmatic hernia and bronchopulmonary dysplasia [121] (Figure 26).

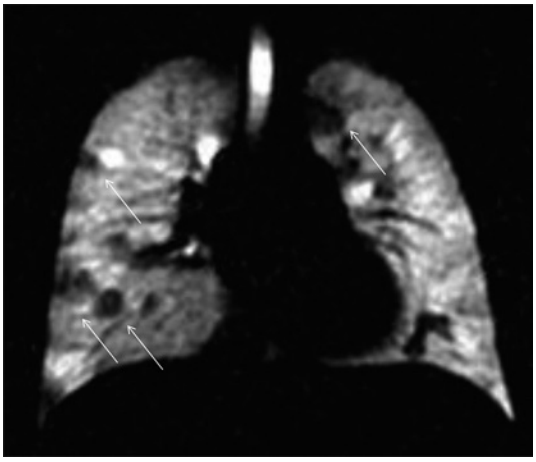

**Figure 26. He3 MRI.** Hyperpolarized helium ($He^3$) ventilation image from a cystic fibrosis (CF) child with normal spirometry and normal looking computed tomography (CT). Note areas of inhomogeneous ventilation (white arrows). Courtesy of Jim Wild, University of Sheffield.

## Fluorinated gases MRI

Fluorine-19 lung MRI ($^{19}F$ MRI) using inert fluorinated gases is the most recent technique for ventilation MRI [122]. This technique has been developed as cheaper alternative to HP MRI, but it can supply similar information. 19F MRI uses safe inert fluorinated gases which are abundant and do not need the hyperpolarization technology [122]. The two most used fluorinated gases are sulfur hexafluoride ($SF_6$) and hexafluoroethane ($C_2F_6$) gases [109]. Full 3D ventilation imaging with reasonable breath-holding time (~ 15 sec) can be achieved with 3D radial UTE sequences [123]. The short T1 relaxation time of these fluorinated gases also allows repeated imaging over short temporal windows, so it is suited for dynamic imaging of ventilation [109]. 19F MRI has shown ventilation maps

comparable to HP MRI in subjects with COPD and emphysema [124]. Although these preliminary results showed that 19F MRI is a promising and well-tolerated technique that can be used for several lung diseases, a true validation with a direct comparison to HP MRI is still lacking [122]. Future works might eventually prove 19F MRI as a cheaper alternative to HP MRI.

## Cine Studies

The high temporal resolution and the lack of radiation have made MRI suitable for studying lung mechanics in cine mode (cine-MRI). Fast 2D GRE and SSFP sequences with parallel imaging options can achieve temporal resolution ranging between 3-10 images per seconds, which are used for single slab dynamic assessment [125]. With the introduction of non-cartesians k-space acquisitions strategies, 3D coverage of the entire chest in dynamic condition is now feasible [126]. In general temporal and spatial resolution of 3D cine-MRI is lower than 2D, but it has the advantage to account for chest changes in all spatial direction [126]. 3D cine-MRI allows recording the continuous lung volume variation during the breathing cycle, which influences chest and airways mechanics. In fact 3D cine MRI has recently been used as conjunct to pulmonary function test to assess airways and diaphragm mechanics [10,127]. Cine MRI can supply regional information not readily available with pulmonary function. Despite pulmonary function test is a fast and economic method routinely used in clinical practice, which gives functional information representing the overall respiratory system, it does not supply any structural or regional information [15]. MRI can supply this regional information that can be also correlated to pulmonary function tests data. In a comparative study, good agreement was found between lung volumes as measured by pulmonary function tests and MR [128]. In a different study, fast temporal resolution techniques, such as 3D GRE FLASH, have been used to delineate the diaphragmatic domes and chest wall during active breathing [129]. These techniques have been proven to be useful for surgical and radiotherapy planning in patients with lung cancer [130,131]. Cine-MRI represents a simple non-invasive method to differentiate mobility of tumors with different diameters and its influence on the surrounding tissue. Cine-MRI has also been proposed to assess and monitor pediatric patients after spinal surgery for scoliosis [132,133]. In these patients, MRI might be useful to understand the complex biomechanical relation between reduced vital capacity and scoliosis, visualizing the functional deficit of both diaphragm and rib cage expansion of the lungs during tidal breathing respiration and efforts [132]. In COPD and emphysema patients, cine-MRI was used to assess the altered chest mechanics due to hyperinflation [134,135].

Finally, cine-MRI has also been used to assess tracheobronchomalacia in a group of pediatric patients [10]. This study has shown that Cine-MRI is a feasible technique, which might be an alternative to bronchoscopy and cine-CT for tracheobronchomalacia [10] (Figure 27).

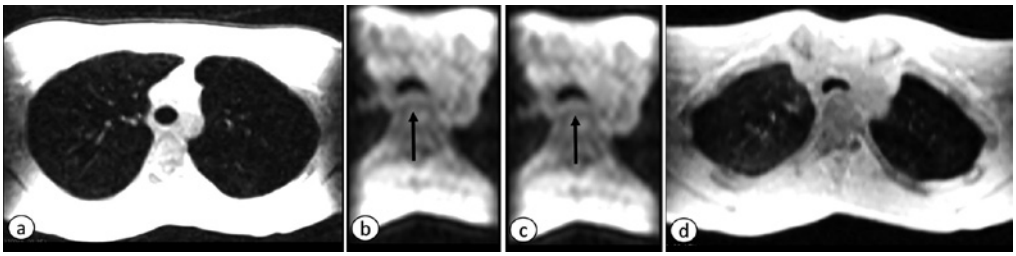


**Figure 27. Tracheomalacia assessment with cine-MRI.** 3D SPGR axial at end-inspiration (a), SPGR with Time Resolved Imaging of Contrast KineticS (TRICKS) dynamic during forced expiration (b), and coughing maneuver (c); 3 D SPGR axial at end expiration (d). Note increased collapse during breathing maneuvers compared to end expiration scan.

## Conclusion

MRI of the lung has reached a point that it can be used in routine clinical practice. Although MRI cannot yet be compared to CT in anatomical detail, new sequences allow acquisition of lung images with high diagnostic quality in less than 15 seconds, which makes MRI use in clinical practice feasible. MRI can be considered as an alternative imaging technique for CT to monitor lung diseases and response to the treatment. Moreover in some diseases, which require long-term follow-up, such as CF, MRI can play in important role to reduce lifelong radiation exposure related to repeated CT scans. More importantly, MRI has the ability to offer functional information, which can only be obtained by CT at the expense of high radiation exposure. Information about lung mechanics, perfusion and ventilation can give a new insight in different lung diseases. This functional information not only can improve our understanding about the pathophysiology of lung diseases, but also open new diagnostic and therapeutic options.

## Bibliography


1. Mayo JR (2000) MR imaging of pulmonary parenchyma. Magn Reson Imaging Clin N Am 8:105–23.
2. Bankier A a, O'Donnell CR, Mai VM, et al. (2004) Impact of lung volume on MR signal intensity changes of the lung parenchyma. J Magn Reson Imaging 20:961–6. doi: 10.1002/jmri.20198
3. Biederer J, Beer M, Hirsch W, et al. (2012) MRI of the lung (2/3). Why … when … how? Insights Imaging 3:355–71. doi: 10.1007/s13244-011-0146-8
4. Wild JM, Marshall H, Bock M, et al. (2012) MRI of the lung (1/3): methods. Insights Imaging 3:345–53. doi: 10.1007/s13244-012-0176-x
5. Liszewski MC, Hersman FW, Altes T a, et al. (2013) Magnetic resonance imaging of pediatric lung parenchyma, airways, vasculature, ventilation, and perfusion: state of the art. Radiol Clin North Am 51:555–82. doi: 10.1016/j.rcl.2013.04.004
6. Deshmane A, Gulani V, Griswold M a, Seiberlich N (2012) Parallel MR imaging. J Magn Reson Imaging 36:55–72. doi: 10.1002/jmri.23639
7. Hennig J (1999) K-space sampling strategies. Eur Radiol 9:1020–31.
8. Paschal CB, Morris HD (2004) K-space in the clinic. J Magn Reson Imaging 19:145–59. doi: 10.1002/jmri.10451
9. Eichinger M, Puderbach M, Smith H-J, et al. (2007) Magnetic resonance-compatible-spirometry: principle, technical evaluation and application. Eur Respir J 30:972–9. doi: 10.1183/09031936.00040607
10. Ciet P, Wielopolski P, Manniesing R, et al. (2014) Spirometer-controlled cine magnetic resonance imaging used to diagnose tracheobronchomalacia in paediatric patients. Eur Respir J 43:115–24. doi: 10.1183/09031936.00104512
11. Kuo W, Ciet P, Tiddens H a WM, et al. (2014) Monitoring cystic fibrosis lung disease by computed tomography. Radiation risk in perspective. Am J Respir Crit Care Med 189:1328–36. doi: 10.1164/rccm.201311-2099CI
12. Systems HC, Smith-bindman R, Miglioretti DL, et al. (2012) Use of Diagnostic Imaging Studies and Associated Radiation Exposure for Patients Enrolled in Large Integrated Health Care Systems, 1996-2010. Jama. doi: 10.1001/jama.2012.5960
13. Don S, Macdougall R, Strauss K, et al. (2013) Image gently campaign back to basics initiative: ten steps to help manage radiation dose in pediatric digital radiography. AJR Am J Roentgenol 200:W431–6. doi: 10.2214/AJR.12.9895
14. Brink J a, Amis ES (2010) Image Wisely: a campaign to increase awareness about adult radiation protection. Radiology 257:601–602. doi: 10.1148/radiol.10101335
15. Eichinger M, Heussel C-P, Kauczor H-U, et al. (2010) Computed tomography and magnetic resonance imaging in cystic fibrosis lung disease. J Magn Reson Imaging 32:1370–8. doi: 10.1002/jmri.22374
16. Eichinger M, Puderbach M, Fink C, et al. (2006) Contrast-enhanced 3D MRI of lung perfusion in children with cystic fibrosis--initial results. Eur Radiol 16:2147–52. doi: 10.1007/s00330-006-0257-7
17. Fain S, Schiebler ML, McCormack DG, Parraga G (2010) Imaging of lung function using hyperpolarized helium-3 magnetic resonance imaging: Review of current and emerging translational methods and applications. J Magn Reson Imaging 32:1398–408. doi: 10.1002/jmri.22375
18. Bauman G, Puderbach M, Heimann T, et al. (2013) Validation of Fourier decomposition MRI with dynamic contrast-enhanced MRI using visual and automated scoring of pulmonary perfusion in young cystic fibrosis patients. Eur J Radiol 82:2371–7. doi: 10.1016/j.ejrad.2013.08.018
19. Mullan CP, Madan R, Trotman-Dickenson B, et al. (2011) Radiology of chest wall masses. AJR Am J Roentgenol 197:W460–70. doi: 10.2214/AJR.10.7259
20. Tanaka O, Kiryu T, Hirose Y, et al. (2005) Neurogenic Tumors of the Mediastinum and Chest Wall. J Thorac Imaging 20:316–320. doi: 10.1097/01.rti.0000185140.02725.4e

21. Webb WR, Gamsu G, Stark DD, Moore EH (1984) Magnetic resonance imaging of the normal and abnormal pulmonary hila. Radiology 152:89–94. doi: 10.1148/radiology.152.1.6729141

22. Nason LK, Walker CM, McNeeley MF, et al. (2012) Imaging of the diaphragm: anatomy and function. Radiographics 32:E51–70. doi: 10.1148/rg.322115127

23. Kaminaga T, Takeshita T, Kimura I (2003) Role of magnetic resonance imaging for evaluation of tumors in the cardiac region. Eur Radiol 13 Suppl 6:L1–10. doi: 10.1007/s00330-002-1789-0

24. Baez JC, Seethamraju RT, Mulkern R, et al. (2015) Pediatric Chest MR Imaging: Sedation, Techniques, and Extracardiac Vessels. Magn Reson Imaging Clin N Am 23:321–35. doi: 10.1016/j.mric.2015.01.010

25. Schulte-Uentrop L, Goepfert MS (2010) Anaesthesia or sedation for MRI in children. Curr Opin Anaesthesiol 23:513–517. doi: 10.1097/ACO.0b013e32833bb524

26. Rappaport BA, Suresh S, Hertz S, et al. (2015) Anesthetic Neurotoxicity – Clinical Implications of Animal Models. N Engl J Med 372:796–797. doi: 10.1056/NEJMp1414786

27. Backeljauw B, Holland SK, Altaye M, Loepke AW (2015) Cognition and Brain Structure Following Early Childhood Surgery With Anesthesia. Pediatrics 136:e1–e12. doi: 10.1542/peds.2014-3526

28. Campbell K, Torres L, Stayer S (2014) Anesthesia and sedation outside the operating room. Anesthesiol Clin 32:25–43. doi: 10.1016/j.anclin.2013.10.010

29. Olsen JW, Barger RL, Doshi SK (2013) Moderate sedation: what radiologists need to know. AJR Am J Roentgenol 201:941–6. doi: 10.2214/AJR.12.9501

30. Chavhan GB, Babyn PS (2011) Whole-body MR imaging in children: principles, technique, current applications, and future directions. Radiographics 31:1757–72. doi: 10.1148/rg.316115523

31. Gurney JW (1991) Cross-sectional physiology of the lung. Radiology 178:1–10. doi: 10.1148/radiology.178.1.1984285

32. Bergin CJ, Glover GH, Pauly JM (1991) Lung parenchyma: magnetic susceptibility in MR imaging. Radiology 180:845–8. doi: 10.1148/radiology.180.3.1871305

33. Rinck PA (2013) Magnetic Resonance in Medicine. The basic Textbook of the European Magnetic Resonance Forum. 7th edition., Electronic.

34. Puderbach M, Hintze C, Ley S, et al. (2007) MR imaging of the chest: a practical approach at 1.5T. Eur J Radiol 64:345–55. doi: 10.1016/j.ejrad.2007.08.009

35. Xu Y, Haacke EM (2001) Partial Fourier imaging in multi-dimensions: a means to save a full factor of two in time. J Magn Reson Imaging 14:628–35.

36. Glockner JF, Hu HH, Stanley DW, et al. (2005) Parallel MR imaging: a user's guide. Radiographics 25:1279–97. doi: 10.1148/rg.255045202

37. MRI Acronyms. https://static.healthcare.siemens.com/siemens_hwem-hwem_ssxa_websites-context-root/wcm/idc/groups/public/@global/@imaging/@mri/documents/download/mdaw/mty1/~edisp/mri_acronyms-00033460.pdf

38. Mayo JR, MacKay A, Müller NL (1992) MR imaging of the lungs: value of short TE spin-echo pulse sequences. AJR Am J Roentgenol 159:951–6. doi: 10.2214/ajr.159.5.1414805

39. Failo R, Wielopolski PA, Tiddens HAWM, et al. (2009) Lung morphology assessment using MRI: a robust ultra-short TR/TE 2D steady state free precession sequence used in cystic fibrosis patients. Magn Reson Med 61:299–306. doi: 10.1002/mrm.21841

40. Bergin CJ, Pauly JM, Macovski A (1991) Lung parenchyma: projection reconstruction MR imaging. Radiology 179:777–81. doi: 10.1148/radiology.179.3.2027991

41. Johnson KM, Fain SB, Schiebler ML, Nagle S (2013) Optimized 3D ultrashort echo time pulmonary MRI. Magn Reson Med 70:1241–50. doi: 10.1002/mrm.24570

42. Dournes G, Grodzki D, Macey J, et al. (2015) Quiet Submillimeter MR Imaging of the Lung Is Feasible with a PETRA Sequence at 1.5 T. Radiology 276:258–65. doi: 10.1148/radiol.15141655

43. Gibiino F, Sacolick L, Menini A, et al. (2015) Free-breathing, zero-TE MR lung imaging. MAGMA 28:207–215. doi: 10.1007/s10334-014-0459-y

44. Firmin D, Keegan J (2001) Navigator echoes in cardiac magnetic resonance. J Cardiovasc Magn Reson 3:183–93.

45. Fraioli F, Serra G, Ciarlo G, et al. (2013) Chest MR imaging in the follow-up of pulmonary alterations in paediatric patients with middle lobe syndrome: comparison with chest X-ray. Radiol Med 118:444–55. doi: 10.1007/s11547-012-0889-3

46. Binks AP, Banzett RB, Duvivier C (2007) An inexpensive, MRI compatible device to measure tidal volume from chest-wall circumference. Physiol Meas 28:149–59. doi: 10.1088/0967-3334/28/2/004

47. Bailes DR, Gilderdale DJ, Bydder GM, et al. Respiratory ordered phase encoding (ROPE): a method for reducing respiratory motion artefacts in MR imaging. J Comput Assist Tomogr 9:835–8.

48. Jhooti P, Wiesmann F, Taylor AM, et al. Hybrid ordered phase encoding (HOPE): an improved approach for respiratory artifact reduction. J Magn Reson Imaging 8:968–80.

49. Scott AD, Keegan J, Firmin DN (2009) Motion in cardiovascular MR imaging. Radiology 250:331–51. doi: 10.1148/radiol.2502071998

50. Mark AS, Winkler ML, Peltzer M, et al. (1987) Gated acquisition of MR images of the thorax: advantages for the study of the hila and mediastinum. Magn Reson Imaging 5:57–63.

51. Hennig J, Nauerth a, Friedburg H (1986) RARE imaging: a fast imaging method for clinical MR. Magn Reson Med 3:823–33.

52. Rampton JW, Young PM, Fidler JL, et al. (2013) Putting the fat and water protons to work for you: a demonstration through clinical cases of how fat-water separation techniques can benefit your body MRI practice. AJR Am J Roentgenol 201:1303–8. doi: 10.2214/AJR.13.10606

53. Ragan DK, Bankson JA (2010) Two-point Dixon technique provides robust fat suppression for multi-mouse imaging. J Magn Reson Imaging 31:510–4. doi: 10.1002/jmri.22060

54. Biederer J, Mirsadraee S, Beer M, et al. (2012) MRI of the lung (3/3)-current applications and future perspectives. Insights Imaging 3:373–86. doi: 10.1007/s13244-011-0142-z

55. Leutner CC, Gieseke J, Lutterbey G, et al. (2000) MR imaging of pneumonia in immunocompromised patients: comparison with helical CT. AJR Am J Roentgenol 175:391–7. doi: 10.2214/ajr.175.2.1750391

56. Fink C, Puderbach M, Biederer J, et al. (2007) Lung MRI at 1.5 and 3 Tesla: observer preference study and lesion contrast using five different pulse sequences. Invest Radiol 42:377–83. doi: 10.1097/01.rli.0000261926.86278.96

57. Puderbach M, Eichinger M, Haeselbarth J, et al. (2007) Assessment of morphological MRI for pulmonary changes in cystic fibrosis (CF) patients: comparison to thin-section CT and chest x-ray. Invest Radiol 42:715–25. doi: 10.1097/RLI.0b013e318074fd81

58. Biederer J, Schoene A, Freitag S, et al. (2003) Simulated pulmonary nodules implanted in a dedicated porcine chest phantom: sensitivity of MR imaging for detection. Radiology 227:475–83. doi: 10.1148/radiol.2272020635

59. Rajaram S, Swift AJ, Capener D, et al. (2012) Lung morphology assessment with balanced steady-state free precession MR imaging compared with CT. Radiology 263:569–77. doi: 10.1148/radiol.12110990

60. Rupprecht T, Böwing B, Kuth R, et al. (2002) Steady-state free precession projection MRI as a potential alternative to the conventional chest X-ray in pediatric patients with suspected pneumonia. Eur Radiol 12:2752–6. doi: 10.1007/s00330-002-1404-4

61. Hirokawa Y, Isoda H, Maetani YS, et al. (2008) Evaluation of motion correction effect and image quality with the periodically rotated overlapping parallel lines with enhanced reconstruction (PROPELLER) (BLADE) and parallel imaging acquisition technique in the upper abdomen. J Magn Reson Imaging 28:957–62. doi: 10.1002/jmri.21538

62. Tamhane A A, Arfanakis K (2009) Motion correction in periodically-rotated overlapping parallel lines with enhanced reconstruction (PROPELLER) and turboprop MRI. Magn Reson Med 62:174–82. doi: 10.1002/mrm.22004

63. Ciet P, Serra G, Bertolo S, et al. (2015) Assessment of CF lung disease using motion corrected PROPELLER MRI: a comparison with CT. Eur Radiol. doi: 10.1007/s00330-015-3850-9

64. Serra G, Milito C, Mitrevski M, et al. (2011) Lung MRI as a possible alternative to CT scan for patients with primary immune deficiencies and increased radiosensitivity. Chest 140:1581–9. doi: 10.1378/chest.10-3147

65. Ohno Y, Hatabu H, Murase K, et al. (2004) Quantitative assessment of regional pulmonary perfusion in the entire lung using three-dimensional ultrafast dynamic contrast-enhanced magnetic resonance imaging: Preliminary experience in 40 subjects. J Magn Reson Imaging 20:353–65. doi: 10.1002/jmri.20137

66. Rajaram S, Swift AJ, Telfer A, et al. (2013) 3D contrast-enhanced lung perfusion MRI is an effective screening tool for chronic thromboembolic pulmonary hypertension: results from the ASPIRE Registry. Thorax 68:677–8. doi: 10.1136/thoraxjnl-2012-203020

67. Lederlin M, Bauman G, Eichinger M, et al. (2013) Functional MRI using Fourier decomposition of lung signal: reproducibility of ventilation- and perfusion-weighted imaging in healthy volunteers. Eur J Radiol 82:1015–22. doi: 10.1016/j.ejrad.2012.12.003

68. Kluge A, Müller C, Hansel J, et al. (2004) Real-time MR with TrueFISP for the detection of acute pulmonary embolism: initial clinical experience. Eur Radiol 14:709–18. doi: 10.1007/s00330-003-2164-5

69. Xu J, McGorty KA, Lim RP, et al. (2012) Single breathhold noncontrast thoracic MRA using highly accelerated parallel imaging with a 32-element coil array. J Magn Reson Imaging 35:963–8. doi: 10.1002/jmri.23535

70. Kluge A, Luboldt W, Bachmann G (2006) Acute pulmonary embolism to the subsegmental level: diagnostic accuracy of three MRI techniques compared with 16-MDCT. AJR Am J Roentgenol 187:W7–14. doi: 10.2214/AJR.04.1814

71. Mudge CS, Healey TT, Atalay MK, Pezzullo JA (2013) Feasibility of detecting pulmonary embolism using noncontrast MRI. ISRN Radiol 2013:729271. doi: 10.5402/2013/729271

72. Ridgway JP (2010) Cardiovascular magnetic resonance physics for clinicians: part I. J Cardiovasc Magn Reson 12:71. doi: 10.1186/1532-429X-12-71

73. Ley S, Ley-Zaporozhan J (2012) Pulmonary perfusion imaging using MRI: clinical application. Insights Imaging 3:61–71. doi: 10.1007/s13244-011-0140-1

74. Miyazaki M, Akahane M (2012) Non-contrast enhanced MR angiography: Established techniques. J Magn Reson Imaging 35:1–19. doi: 10.1002/jmri.22789

75. Mai VM, Chen Q, Bankier AA, et al. (2001) Effect of lung inflation on arterial spin labeling signal in MR perfusion imaging of human lung. J Magn Reson Imaging 13:954–9.

76. Schraml C, Schwenzer NF, Martirosian P, et al. (2012) Non-invasive pulmonary perfusion assessment in young patients with cystic fibrosis using an arterial spin labeling MR technique at 1.5 T. MAGMA 25:155–62. doi: 10.1007/s10334-011-0271-x

77. Lipson D A., Roberts D A., Hansen-Flaschen J, et al. (2002) Pulmonary ventilation and perfusion scanning using hyperpolarized helium-3 MRI and arterial spin tagging in healthy normal subjects and in pulmonary embolism and orthotopic lung transplant patients. Magn Reson Med 47:1073–1076. doi: 10.1002/mrm.10172

78. Greil GF, Powell AJ, Gildein HP, Geva T (2002) Gadolinium-enhanced three-dimensional magnetic resonance angiography of pulmonary and systemic venous anomalies. J Am Coll Cardiol 39:335–41.

79. Hecht EM, Rosenkrantz A (2009) Pulmonary MR Angiography Techniques and Applications. Magn Reson Imaging Clin N Am 17:101–131. doi: 10.1016/j.mric.2009.01.001

80. Ley S (2015) Imaging pulmonary arterial thromboembolism: challenges and opportunities. Magn Reson Imaging Clin N Am 23:261–71. doi: 10.1016/j.mric.2015.01.013

81. Thacker PG, Lee EY (2015) Pulmonary embolism in children. AJR Am J Roentgenol 204:1278–88. doi: 10.2214/AJR.14.13869

82. EULER US v., LILJESTRAND G (1946) Observations on the Pulmonary Arterial Blood Pressure in the Cat. Acta Physiol Scand 12:301–320. doi: 10.1111/j.1748-1716.1946.tb00389.x

83. Fink C, Ley S, Kroeker R, et al. (2005) Time-resolved contrast-enhanced three-dimensional magnetic resonance angiography of the chest: combination of parallel imaging with view sharing (TREAT). Invest Radiol 40:40–8.

84. Grist TM, Mistretta CA, Strother CM, Turski PA (2012) Time-resolved angiography: Past, present, and future. J Magn Reson Imaging 36:1273–1286. doi: 10.1002/jmri.23646

85. Tsao J, Kozerke S (2012) MRI temporal acceleration techniques. J Magn Reson Imaging 36:543–560. doi: 10.1002/jmri.23640

86. Bauman G, Johnson KM, Bell LC, et al. (2015) Three-dimensional pulmonary perfusion MRI with radial ultrashort echo time and spatial-temporal constrained reconstruction. Magn Reson Med 73:555–564. doi: 10.1002/mrm.25158

87. Wirth G, Brüggemann K, Bostel T, et al. (2014) Chronic Thromboembolic Pulmonary Hypertension (CTEPH) - Potential Role of Multidetector-Row CT (MD-CT) and MR Imaging in the Diagnosis and Differential Diagnosis of the Disease. Rofo 751–761. doi: 10.1055/s-0034-1366425

88. Kreitner K-F (2014) Noninvasive imaging of pulmonary hypertension. Semin Respir Crit Care Med 35:99–111. doi: 10.1055/s-0033-1363456

89. Ley-Zaporozhan J, Van Beek EJR (2010) Imaging phenotypes of chronic obstructive pulmonary disease. J Magn Reson Imaging 32:1340–1352. doi: 10.1002/jmri.22376

90. Serdengecti M, Sakarya ME, Ilerisoy ZY, Odev K (2013) Comparison of Ventilation-Perfusion Scintigraphy with MR Angiography in Patients with Swyer-James Syndrome. Clin Nucl Med 38:237–40. doi: 10.1097/RLU.0b013e3181d624dd

91. Rajaram S, Swift AJ, Capener D, et al. (2012) Diagnostic accuracy of contrast-enhanced MR angiography and unenhanced proton MR imaging compared with CT pulmonary angiography in chronic thromboembolic pulmonary hypertension. Eur Radiol 22:310–7. doi: 10.1007/s00330-011-2252-x

92. Hueper K, Parikh M a, Prince MR, et al. (2013) Quantitative and semiquantitative measures of regional pulmonary microvascular perfusion by magnetic resonance imaging and their relationships to global lung perfusion and lung diffusing capacity: the multiethnic study of atherosclerosis chronic obstructi. Invest Radiol 48:223–30. doi: 10.1097/RLI.0b013e318281057d

93. Fan L, Xia Y, Guan Y, et al. (2013) Capability of differentiating smokers with normal pulmonary function from COPD patients: a comparison of CT pulmonary volume analysis and MR perfusion imaging. Eur Radiol 23:1234–1241. doi: 10.1007/s00330-012-2729-2

94. Wielpütz MO, Puderbach M, Kopp-Schneider A, et al. (2014) Magnetic Resonance Imaging Detects Changes in Structure and Perfusion, and Response to Therapy in Early Cystic Fibrosis Lung Disease. Am J Respir Crit Care Med 1–49. doi: 10.1164/rccm.201309-1659OC

95. Zöllner FG, Zahn K, Schaible T, et al. (2012) Quantitative pulmonary perfusion imaging at 3.0 T of 2-year-old children after congenital diaphragmatic hernia repair: initial results. Eur Radiol 22:2743–9. doi: 10.1007/s00330-012-2528-9

96. Yilmaz O, Savaş R, Sogut A, et al. (2009) Effectiveness of magnetic resonance angiography in the evaluation of lung perfusion in constrictive bronchiolitis obliterans. Respirology 14:295–8. doi: 10.1111/j.1440-1843.2008.01456.x

97. Hao D, Ai T, Goerner F, et al. (2012) MRI contrast agents: basic chemistry and safety. J Magn Reson Imaging 36:1060–71. doi: 10.1002/jmri.23725

98. Bell LC, Wang K, Munoz Del Rio A, et al. (2015) Comparison of models and contrast agents for improved signal and signal linearity in dynamic contrast-enhanced pulmonary magnetic resonance imaging. Invest Radiol 50:174–178. doi: 10.1097/RLI.0000000000000122

99. Farmakis SG, Khanna G (2014) Extracardiac applications of MR blood pool contrast agent in children. Pediatr Radiol 44:1598–1609. doi: 10.1007/s00247-014-3167-x

100. Rigsby CK, Popescu AR, Nelson P, et al. (2015) Safety of Blood Pool Contrast Agent Administration in Children and Young Adults. Am J Roentgenol 205:1114–1120. doi: 10.2214/AJR.14.13991

101. Wang PI, Chong ST, Kielar AZ, et al. (2012) Imaging of pregnant and lactating patients: part 1, evidence-based review and recommendations. AJR Am J Roentgenol 198:778–84. doi: 10.2214/AJR.11.7405

102. Thomsen HS, Morcos SK, Almén T, et al. (2013) Nephrogenic systemic fibrosis and gadolinium-based contrast media: updated ESUR Contrast Medium Safety Committee guidelines. Eur Radiol 23:307–318. doi: 10.1007/s00330-012-2597-9

103. Sundgren PC, Leander P (2011) Is administration of gadolinium-based contrast media to pregnant women and small children justified? J Magn Reson Imaging 34:750–7. doi: 10.1002/jmri.22413

104. Bhargava R, Hahn G, Hirsch W, et al. (2013) Contrast-enhanced magnetic resonance imaging in pediatric patients: review and recommendations for current practice. Magn Reson Insights 6:95–111. doi: 10.4137/MRI.S12561

105. Nacif MS, Arai A a., Lima J a. C, Bluemke D a. (2012) Gadolinium-enhanced Cardiovascular Magnetic Resonance: Administered Dose in Relationship to United States Food and Drug Administration (FDA) Guidelines. J Cardiovasc Magn Reson 14:18. doi: 10.1186/PREACCEPT-4280658695831343

106. Ciet P, Litmanovich DE (2015) MR safety issues particular to women. Magn Reson Imaging Clin N Am 23:59–67. doi: 10.1016/j.mric.2014.09.002

107. Bauman G, Puderbach M, Deimling M, et al. (2009) Non-contrast-enhanced perfusion and ventilation assessment of the human lung by means of fourier decomposition in proton MRI. Magn Reson Med 62:656–64. doi: 10.1002/mrm.22031

108. Schönfeld C, Cebotari S, Voskrebenzev A, et al. (2015) Performance of perfusion-weighted Fourier decomposition MRI for detection of chronic pulmonary emboli. J Magn Reson Imaging 42:72–9. doi: 10.1002/jmri.24764

109. Kruger SJ, Nagle SK, Couch MJ, et al. (2015) Functional imaging of the lungs with gas agents. J Magn Reson Imaging n/a–n/a. doi: 10.1002/jmri.25002

110. Ohno Y, Hatabu H, Takenaka D, et al. (2002) Dynamic oxygen-enhanced MRI reflects diffusing capacity of the lung. Magn Reson Med 47:1139–1144. doi: 10.1002/mrm.10168

111. Ohno Y, Iwasawa T, Seo JB, et al. (2008) Oxygen-enhanced Magnetic Resonance Imaging versus Computed Tomography. Am J Respir Crit Care Med 177:1095–1102. doi: 10.1164/rccm.200709-1322OC

112. Ohno Y, Nishio M, Koyama H, et al. (2014) Asthma: Comparison of Dynamic Oxygen-enhanced MR Imaging and Quantitative Thin-Section CT for Evaluation of Clinical Treatment. Radiology 273:132660. doi: 10.1148/radiol.14132660

113. Jakob PM, Wang T, Schultz G, et al. (2004) Assessment of human pulmonary function using oxygen-enhanced T(1) imaging in patients with cystic fibrosis. Magn Reson Med 51:1009–16. doi: 10.1002/mrm.20051

114. Bannier E, Cieslar K, Mosbah K, et al. (2010) Hyperpolarized 3He MR for sensitive imaging of ventilation function and treatment efficiency in young cystic fibrosis patients with normal lung function. Radiology 255:225–32. doi: 10.1148/radiol.09090039

115. Koumellis P, van Beek EJR, Woodhouse N, et al. (2005) Quantitative analysis of regional airways obstruction using dynamic hyperpolarized 3He MRI-preliminary results in children with cystic fibrosis. J Magn Reson Imaging 22:420–6. doi: 10.1002/jmri.20402

116. Horn FC, Deppe MH, Marshall H, et al. (2014) Quantification of regional fractional ventilation in human subjects by measurement of hyperpolarized 3He washout with 2D and 3D MRI. J Appl Physiol 116:129–39. doi: 10.1152/japplphysiol.00378.2013

117. Kirby M, Mathew L, Wheatley A, et al. (2010) Chronic obstructive pulmonary disease: longitudinal hyperpolarized (3)He MR imaging. Radiology 256:280–9. doi: 10.1148/radiol.10091937

118. Kirby M, Mathew L, Heydarian M, et al. (2011) Chronic obstructive pulmonary disease: quantification of bronchodilator effects by using hyperpolarized $^{3}$He MR imaging. Radiology 261:283–92. doi: 10.1148/radiol.11110403

119. Fain SB, Korosec FR, Holmes JH, et al. (2007) Functional lung imaging using hyperpolarized gas MRI. J Magn Reson Imaging 25:910–23. doi: 10.1002/jmri.20876

120. van Beek EJR, Hill C, Woodhouse N, et al. (2007) Assessment of lung disease in children with cystic fibrosis using hyperpolarized 3-Helium MRI: comparison with Shwachman score, Chrispin-Norman score and spirometry. Eur Radiol 17:1018–24. doi: 10.1007/s00330-006-0392-1

121. Lilburn DML, Pavlovskaya GE, Meersmann T (2013) Perspectives of hyperpolarized noble gas MRI beyond 3He. J Magn Reson 229:173–86. doi: 10.1016/j.jmr.2012.11.014

122. Couch MJ, Ball IK, Li T, et al. (2014) Inert fluorinated gas MRI: a new pulmonary imaging modality. NMR Biomed 27:1525–34. doi: 10.1002/nbm.3165

123. Couch MJ, Ball IK, Li T, et al. (2013) Pulmonary ultrashort echo time 19F MR imaging with inhaled fluorinated gas mixtures in healthy volunteers: feasibility. Radiology 269:903–9. doi: 10.1148/radiol.13130609

124. Halaweish AF, Moon RE, Foster WM, et al. (2013) Perfluoropropane gas as a magnetic resonance lung imaging contrast agent in humans. Chest 144:1300–1310. doi: 10.1378/chest.12-2597

125. Fabel M, Wintersperger BJ, Dietrich O, et al. (2009) MRI of respiratory dynamics with 2D steady-state free-precession and 2D gradient echo sequences at 1.5 and 3 Tesla: an observer preference study. Eur Radiol 19:391–9. doi: 10.1007/s00330-008-1148-x

126. Biederer J, Hintze C, Fabel M, Dinkel J (2010) Magnetic resonance imaging and computed tomography of respiratory mechanics. J Magn Reson Imaging 32:1388–1397. doi: 10.1002/jmri.22386

127. Wens SC, Ciet P, Perez-Rovira A, et al. (2015) Lung MRI and impairment of diaphragmatic function in Pompe disease. BMC Pulm Med 15:54. doi: 10.1186/s12890-015-0058-3

128. Cluzel P, Similowski T, Chartrand-Lefebvre C, et al. (2000) Diaphragm and chest wall: assessment of the inspiratory pump with MR imaging-preliminary observations. Radiology 215:574–83. doi: 10.1148/radiology.215.2.r00ma28574

129. Tokuda J, Schmitt M, Sun Y, et al. (2009) Lung motion and volume measurement by dynamic 3D MRI using a 128-channel receiver coil. Acad Radiol 16:22–7. doi: 10.1016/j.acra.2008.07.021

130. Plathow C, Fink C, Ley S, et al. (2004) Measurement of tumor diameter-dependent mobility of lung tumors by dynamic MRI. Radiother Oncol 73:349–54. doi: 10.1016/j.radonc.2004.07.017

131. Plathow C, Fink C, Sandner A, et al. (2005) Comparison of relative forced expiratory volume of one second with dynamic magnetic resonance imaging parameters in healthy subjects and patients with lung cancer. J Magn Reson Imaging 21:212–8. doi: 10.1002/jmri.20255

132. Campbell RM (2013) VEPTR: past experience and the future of VEPTR principles. Eur Spine J 22 Suppl 2:S106–17. doi: 10.1007/s00586-013-2671-2

133. Chu WCW, Li AM, Ng BKW, et al. (2006) Dynamic magnetic resonance imaging in assessing lung volumes, chest wall, and diaphragm motions in adolescent idiopathic scoliosis versus normal controls. Spine (Phila Pa 1976) 31:2243–2249. doi: 10.1097/01.brs.0000232822.74349.32

134. Suga K, Tsukuda T, Awaya H, et al. (1999) Impaired respiratory mechanics in pulmonary emphysema: Evaluation with dynamic breathing MRI. J Magn Reson Imaging 10:510–520. doi: 10.1002/(SICI)1522-2586(199910)10:4<510::AID-JMRI3>3.0.CO;2-G

135. Unal O, Arslan H, Uzun K, et al. (2001) Evaluation of diaphragmatic movement with MR fluoroscopy in chronic obstructive pulmonary disease. Clin Imaging 24:347–50.

# Chapter 3

## Assessment of CF Lung Disease Using Motion Corrected PROPELLER MRI: a Comparison with CT

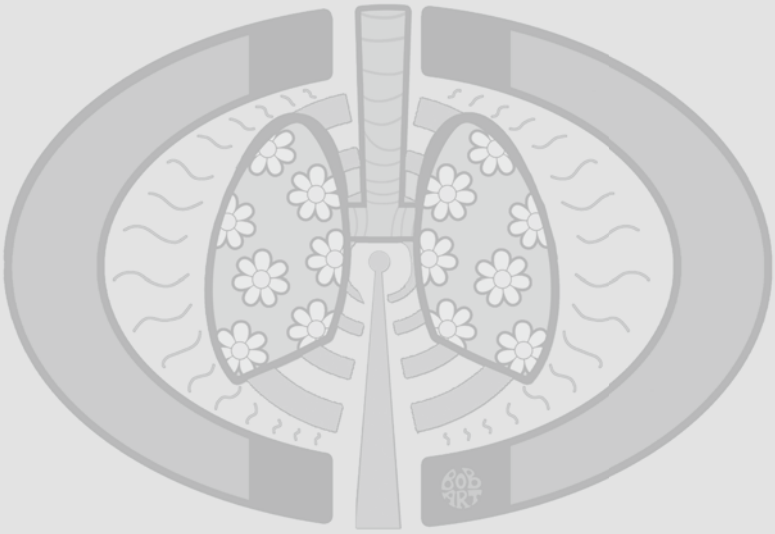

*Ciet P, Serra G, Bertolo S, Spronk S, Ros M, Fraioli F, Quattrucci S, Assael MB, Catalano C, Pomerri F, Tiddens HA, Morana G*

Eur Radiol. 2016 Mar;26(3):780-7.

## Abstract

**Objectives:** to date, PROPELLER MRI, a breathing-motion-insensitive technique, has not been assessed for cystic fibrosis (CF) lung disease. We compared this technique to CT for assessing CF lung disease in children and adults.

**Methods:** thirty-eight stable CF patients (median 21 years, range 6-51 years, 22 female) underwent MRI and CT on the same day. Study protocol included respiratory-triggered PROPELLER MRI and volumetric CT end-inspiratory and -expiratory acquisitions. Two observers scored the images using the CF-MRI and CF-CT systems. Scores were compared with intra-class correlation coefficient (ICC) and Bland-Altman plots. The sensitivity and specificity of MRI versus CT were calculated.

**Results:** MRI sensitivity for detecting severe CF bronchiectasis was 0.33 (CI 0.09-0.57), while specificity was 100% (CI 0.88-1). ICCs for bronchiectasis and trapped air were as follows: MRI-bronchiectasis (0.79); CT-bronchiectasis (0.85); MRI-trapped air (0.51); CT-trapped air (0.87). Bland-Altman plots showed an MRI tendency to overestimate the severity of bronchiectasis in mild CF disease and underestimate bronchiectasis in severe disease.

**Conclusions:** motion correction in PROPELLER MRI does not improve assessment of CF lung disease compared to CT. However, the good inter- and intra-observer agreement and the high specificity suggest that MRI might play a role in the short-term follow-up of CF lung disease (i.e. pulmonary exacerbations).


Key points:

- PROPELLER MRI does not match CT sensitivity to assess CF lung disease
- PROPELLER MRI has lower sensitivity than CT to detect severe bronchiectasis
- PROPELLER MRI has good to very good intra- and inter-observer variability
- PROPELLER MRI can be used for short-term follow-up studies in CF

## Introduction

Cystic fibrosis (CF) is the most common genetic disease, with a reduced life expectancy in Caucasians [1]. Life expectancy is reduced due to progressive lung disease, characterized by several structural lung changes, most importantly bronchiectasis and trapped air [2,3]. To guide therapy to prevent or reduce bronchiectasis and trapped air, it is crucial to monitor CF lung disease at regular intervals.

CF lung disease monitoring has changed in the last decade [4,5]. Nowadays, computed tomography (CT) is considered the most sensitive method to monitor CF lung disease in early and advanced stages [6] and is usually preferred over chest x-rays. The main disadvantage of CT is that it exposes patients to ionizing radiation. Therefore, CT protocols for CF are usually low or ultra-low dose [7,8]. Despite this relatively low radiation dose, it restricts the use of chest CT, especially in children, who are more sensitive to radiation exposure than adults [9]. Furthermore, ionizing radiation limits the frequency with which chest CT can be repeated for short and long-term monitoring of CF lung disease [10]. Magnetic resonance imaging (MRI), as radiation free technique, has been introduced as an alternative to CT [11,12]. To date, MRI has been directly compared to CT in only a few studies, using various MRI sequences [13-15], but none of those included motion correction free-breathing sequences, such as PROPELLER. The PROPELLER sequence has been designed to be relatively insensitive to respiratory movements, as it enables correction of in-plane motion, rotation and translation [16,17]. Moreover, PROPELLER is applied and increasingly proposed as a respiratory triggered sequence in non-compliant patients, such as patients not able to perform breath-hold maneuvers (i.e. CF children) [18]. Finally, to date PROPELLER has not been compared to CT for CF. Therefore, our study aims to assess if the breathing motion correction of PROPELLER-MRI improves diagnostic performance of MRI versus CT to assess CF lung disease in a group of stable CF patients, who had both examinations performed on the same day.

## Material and Methods

Stable CF patients were consecutively recruited in two CF centers by their treating clinicians. A CF patient was defined stable, when no signs or symptoms of acute or recent pulmonary exacerbations were present as defined in the exclusion criteria. Inclusion and exclusion criteria were as follows:
*Inclusion criteria:* CF proven by a positive sweat test, genotyping and clinical symptoms; willing and able to participate in the study; scheduled for biennial routine chest-CT scan requested by the attending physician; ability to comply with instructions during MRI and CT examinations; informed consent.
*Exclusion criteria:* minimum age of 6 years old; chronic oxygen therapy; present or recent (two weeks) pulmonary exacerbation defined as treatment with intravenous antibiotics (non-stable); history of lung transplantation; participation in other trials; contraindications for MRI; possible pregnancy.

On the same day, prior to MRI and CT, each patient underwent a clinical examination and spirometry (Masterscope, Jaeger-Care Fusion, Germany). Spirometry was performed according to "ATS/ERS guidelines" [19]. Approval for this multicenter prospective cohort study was obtained by the institutional review boards of both participating centers.

## MRI and CT Protocol

The MRI protocol was performed in 1.5 T scanners (Avanto, Siemens, Enlargen Germany) as follows: 16 channels torso superficial coil; PROPELLER (BLADE@Siemens) sequence proton density (PD) weighted with respiratory triggering (Navigator@Siemens) at end-expiration; (TR/TE/alpha/TA: 2000/27 ms/150º/18s, Ø=5 mm) axial and coronal. Average time per acquisition was 7 to 10 minutes. The complete MRI protocol lasted on average 35 minutes (range 20-45 minutes).

The CT protocol was performed in 16-row or 64-row scanners (Sensation, Siemens, Enlargen, Germany) as follows: volumetric end-inspiratory and end-expiratory optimized-dose scans, 100 kV for children <35kg and 120kV for children ≥35 kg, mAs 15-40, scan range lung apices to bases, slice collimation 1 mm, slice thickness (Ø) 1 mm, reconstruction increment 0.8 mm, pitch 1. For comparison with MRI, multiplanar reconstructions (axial, coronal) with slice thickness of 5mm, kernels B31f, B60f and B70f were obtained. Both MRI and CT protocols did not include the administration of contrast agent.

## Image analysis – CT and MRI

All MRI and CT images were anonymized and scored in random order by two independent radiologists (G.S. and P.C.), who were experienced in scoring and with 2 and 4 years of experience in thoracic CT and MR imaging respectively. Both radiologists were blinded to any clinical information.

To score CTs, we used the CF-CT scoring system (CF-CT) [20]. The total CF-CT score is the sum of the following sub-scores: bronchiectasis; mucous plugging; peribronchial thickening; parenchymal score; and trapped air. Each of the 5 sub-scores is rated according to presence and severity, in each of the six lobes, with the lingula as a separate lobe. All score and sub-scores are expressed as a percentage of the maximum possible score, ranging from 0 (no pathological findings) to 100 (maximum severity).

To score MRI images, we used a CF-MRI scoring system, equivalent of the CF-CT scoring system and used in previous studies [13,14]. To train both observers, MRI images of 16 patients excluded from final analysis due to an incomplete CT dataset (absence of end-expiratory scan) were used. Consensus meetings were held during and at the end of scoring all MRIs of the training set. To determine intra-observer agreement, observer 1 (P. C.) scored all CT and MRI images twice, separated by two months to avoid recall bias.

## Statistical Analysis

*Inter and intra-observer agreement*

Intraclass correlation coefficients (ICC) were used to evaluate inter- and intra-observer agreement for both MRI and CT scores. ICC values between 0.4 and 0.6, 0.6 and 0.8 or ≥0.8 are considered to indicate moderate, good and very good agreement, respectively [21].

To assess pairwise inter- and intra-observer agreement between MRI and CT scores Bland-Altman plots and identity plots were created for: 1) $MRI_{obs1}$ vs. $MRI_{obs2}$; 2) $CT_{obs1}$ vs. $CT_{obs2}$ and 3) $MRI_{obs1}$ vs. $MRI_{obs1}$ and $CT_{obs1}$ vs. $CT_{obs1}$. To compare MRI scores with CT scores, we evaluated $MRI_{mean\ obs\ 1+2}$ vs. $CT_{mean\ obs\ 1+2}$. All statistical analyses were performed using SPSS 16.0 (SPSS, Chicago, IL), and STATA 12.0 (STATA, College Station, TX).

*Sensitivity, specificity, PPV and NPV of MRI versus CT*

CF-CT bronchiectasis sub-score was used as main indicator of CF lung disease severity in order to determine sensitivity, specificity, positive predictive values (PPV) and negative predictive values (NPV) of MRI versus CT. Bronchiectasis has been recognized as a well-validated and clinically relevant outcome measure in CF [2]. Using chest-CT as the reference test, a cut-off value of 26% or higher, representing severe bronchiectasis, was defined as true-positive finding for MRI-bronchiectasis sub-score. 26% represents the percentage of maximum possible score for bronchiectasis which is according to CF-CT 12 per each lobe and 72 in totals. This cut-off of 26% was based on the median value of bronchiectasis severity observed in 2 cohort studies, either with mild or severe CF lung disease [3,22], using receiver operating characteristic analysis to determine different cut-off values. Sensitivity, specificity, PPV and NPV, were calculated for each observer ($obs_1$ and $obs_2$), in addition to the mean of the bronchiectasis scores of both observers (mean $obs_{1+2}$).

Descriptive statistics were used to characterize the patients at the time of their MRI and CT scans. All scoring data are numerical with results expressed as median (range) and scores expressed as percentage of the maximum possible score.

## Results

In this study, we enrolled 54 patients. 16 patients were excluded for the analysis because of missing the end-expiratory CT scans. MRIs of these 16 patients were used for training of the observers. Hence, 38 patients with stable CF (median 21 years, range 6-51 years, 22 female), were eligible for the comparison of CTs and MRIs. Baseline characteristics are shown in Table 1. Prevalence of bronchiectasis, trapped air, total CF scores with MRI and CT represented as first and third quartiles is shown in Table 2.

**Table 1.** Baseline patients' characteristics.

| **Demographic data** | **Value** |
|---|---|
| No. patients | 38 |
| Female sex | 22 (56 %) |
| Age, years | 21 (6-51) |
| **Morphofunctional data** | **Value** |
| FEV1 % predicted | 75 (51.1-109.9) |
| Total CF-CT | 25.9 (1.4-49.1) |
| Total CF-MRI | 20.5 (0-39.6) |
| CT-bronchiectasis | 22.7 (1.4-45.9) |
| MRI-bronchiectasis | 18 (0-35) |
| CT-trapped air | 46.3 (0-67) |
| MRI-trapped air | 37 (0-66) |

$FEV_1$%=Forced expiratory volume in one second % predicted. CF-CT=Cystic Fibrosis Computed Tomography total score, CF-MRI=Cystic Fibrosis Magnetic Resonance Imaging total score, CT-bronchiectasis=Computed tomography bronchiectasis sub-score, MRI-bronchiectasis=Magnetic Resonance Imaging bronchiectasis sub-score, CT-trapped air=Computed tomography trapped air sub-score, MRI-trapped air=Magnetic Resonance Imaging trapped air sub-score. The maximum absolute score for CF-CT/CF-MRI, bronchiectasis and trapped air sub-scores is 243, 72 and 27 respectively. Data are presented as median percentage of the maximum score and range.

**Table 2.** Prevalence of total MRI, total CT, bronchiectasis MRI, bronchiectasis CT, trapped air MRI and trapped air CT scores expressed in quartiles.

| **Quartiles** | **CF-CT** | **CT bronchiectasis** | **CT trapped air** | **CF-MRI** | **MRI bronchiectasis** | **MRI trapped air** |
|---|---|---|---|---|---|---|
| First (25%) | 17 | 15 | 25.9 | 15.8 | 13 | 27.8 |
| Third (75%) | 36 | 28.9 | 60 | 29 | 22.7 | 44 |

CF-CT=Cystic Fibrosis Computed Tomography total score, CF-MRI=Cystic Fibrosis Magnetic Resonance Imaging total score, CT-bronchiectasis=Computed tomography bronchiectasis sub-score, MRI-bronchiectasis=Magnetic Resonance Imaging bronchiectasis sub-score, CT-trapped air=Computed tomography trapped air sub-score, MRI-trapped air=Magnetic Resonance Imaging trapped air sub-score. Data are presented as percentage of the maximum score No. (%). For instance a CF-CT of 17 for the first quartile means that 25 % of the patients had a total CF-CT score to 17% of the maximum bronchiectasis score.

## Inter- and intra-observer agreement MRI versus CT

Inter- and intra-observer agreement, expressed as ICCs, for $MRI_{obs1}$ vs. $MRI_{obs2}$, $CT_{obs1}$ vs. $CT_{obs2}$, $MRI_{mean\ obs\ 1+2}$ vs. $CT_{mean\ obs\ 1+2}$, $CT_{obs1}$ vs. $CT_{obs1}$, and $MRI_{obs1}$ vs. $MRI_{obs1}$ are summarized in Table 3. In summary, the inter- and intra-observer agreement for MRI was good or very good, although lower than for CT. The ICCs for CF-CT sub-scores were higher compared to CF-MRI sub-scores, especially for peribronchial thickening and trapped air. Trapped air measurement by MRI did not match with CT as showed by the ICCs values: CT-trapped air (0.87); MRI-trapped air (0.51) and MRI/CT-trapped air (0.46).

Finally, the intra-observer agreement for the observer 1, who repeated the score twice, was overall very good, but lower for MRI than for CT.

Bland-Altman and identity plots showed that PROPELLER MRI, for almost all sub-scores, tends to overestimate mild CF cases and underestimate severe CF cases (Figures 1, 2).



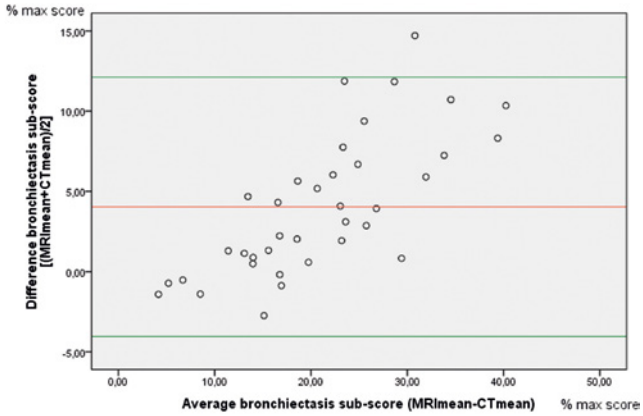


**Figure 1. Bland-Altman plot of MRImean obs 1+2 vs. CTmean obs 1+2.** All scoring data are numerical and scores are expressed as percentage of the maximal possible score. Horizontal axis: Average bronchiectasis sub-score [(MRImean + CTmean)/2]; Vertical axis=Difference bronchiectasis sub-score (MRImean – CTmean). Red and green lines represent mean and ±2 Standard deviations (SD) respectively

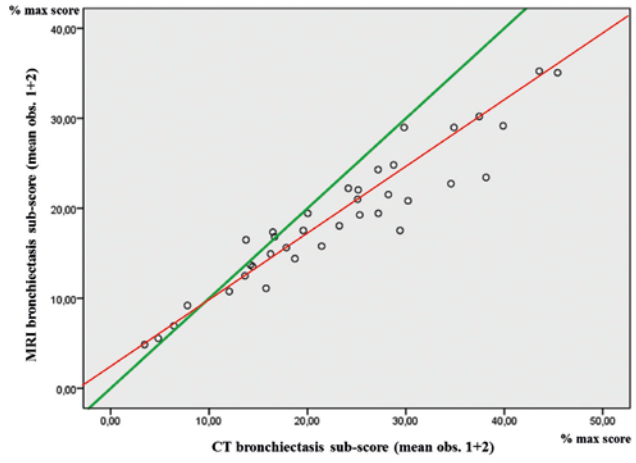


**Figure 2.** Identity plot MRI-bronchiectasis versus CT-bronchiectasis sub-scores (mean score observer 1+ observer 2). Green line identity line Y=1 * X+0. Note that MRI tends to overestimate mild CF cases and underestimate severe CF cases (red line).

**Table 3.** ICCs values of inter- and intra-observer agreement between observers for all sub-scores, CF-MRI total score and CF-CT total score.

| CF lung alterations | $MRI_{obs1}$ vs. $MRI_{obs2}$ | $CT_{obs1}$ vs. $CT_{obs2}$ | $MRI_{mean\ obs\ 1+2}$ vs. $CT_{mean\ obs\ 1+2}$ | $MRI_{obs1}$ vs. $MRI_{obs1}$ | $CT_{obs1}$ vs. $CT_{obs1}$ |
|---|---|---|---|---|---|
| Bronchiectasis | 0.79 | 0.85 | 0.78 | 0.83 | 0.92 |
| Air Wall Thickening | 0.60 | 0.74 | 0.79 | 0.81 | 0.95 |
| Mucus | 0.79 | 0.91 | 0.76 | 0.90 | 0.94 |
| Parenchyma | 0.85 | 0.91 | 0.84 | 0.92 | 0.88 |
| Trapped Air | 0.51 | 0.87 | 0.46 | 0.81 | 0.91 |
| **Total Score** | **0.80** | **0.93** | **0.82** | **0.91** | **0.96** |

Note that Trapped Air assessment shows the lowest ICC values, indicating poor agreement of MRI with CT. Moreover Bronchiectasis score agreement tends to decrease between observers from CT vs. CT to MRI vs. MRI and MRI vs. CT comparison.

## Sensitivity, Specificity, PPV and NPV

Sensitivity of MRI to detect severe bronchiectasis was low. Using the cut-off value of 26%, MRI identified six (16%) and CT fourteen (38%) patients with severe bronchiectasis. This was true for both observers ($obs_1$=25%; $obs_2$=50%) and also when the mean of both observers was used for analysis (mean $obs_{1+2}$ = 33%). Specificity for MRI to detect severe bronchiectasis was very high: $obs_1$=95%; $obs_2$=100% and average of $obs_{1+2}$ = 100%. Similarly PPV of MRI was high, while NPV was low, using either observer scores or the average. Sensitivity, specificity, PPV and NPV values for each observer and as an average of both observers are shown in Table 4.

**Table 4.** Differentiation of mild versus severe CF lung disease using chest-MRI.

| Parameter | Value | C.I (95%) |
|---|---|---|
| $Sensitivity_{obs1}$ | 0.25 (4/15) | 0.11-0.49 |
| $Sensitivity_{obs2}$ | 0.50 (9/18) | 0.24-0.76 |
| $Sensitivity_{obs1+2}$ | 0.33 (5/15) | 0.09-0.57 |
| $Specificity_{obs1}$ | 0.95 (19/20) | 0.86-1 |
| $Specificity_{obs2}$ | 1 (20/20) | 0.90-1 |
| $Specificity_{obs1+2}$ | 1 (23/23) | 0.88-1 |
| $PPV_{obs1}$ | 0.8 (3/4) | 0.24-1 |
| $PPV_{obs2}$ | 1 (8/8) | 0.8-1 |
| $PPV_{obs1+2}$ | 1 (6/6) | 0.55-1 |
| $NPV_{obs1}$ | 0.64 (21/34) | 0.46-0.81 |
| $NPV_{obs2}$ | 0.69 (20/30) | 0.51-0.87 |
| $NPV_{obs1+2}$ | 0.63 (20/32) | 0.45-0.80 |

PPV=Positive Predictive Value; NPV=Negative Predictive Value. Data are presented as ratio, with absolute values in brackets.

## Discussion

In this prospective two centers study, we compared a motion insensitive MRI sequence, PROPELLER, to CT to assess lung disease in a group of stable CF patients. This study showed that PROPELLER MRI is not as good as CT to assess CF lung disease. Moreover, our study confirmed low sensitivity of MRI compared to CT to detect trapped air.



Firstly, we showed that despite MRI had good or very good inter and intra-observer agreement, this was lower than for CT. Moreover, the inter-observer agreement for MRI was lower than for CT, indicating that it was more difficult for the observers to score MRIs compared to scoring CTs. In previous studies the inter-observer agreement between MRI and CT scores ranged from moderate to very good, while intra-observer agreement was not assessed [13,14]. In our study, the intra-observer agreement was very good, thus suggesting that the technique is robust, although less sensitive than CT.

Secondly, we confirmed that trapped air could not be reliably visualized with MRI, as previously demonstrated by Failo et al and more recently by Rajaram *et al* [14,15]. Trapped air is an early change associated with small airways disease [3,23]. Unfortunately our MRI protocol was not sensitive enough to differentiate trapped air from surrounding normal lung parenchyma. However, we believe that innovative sequences can be added to the MR examination that might be more sensitive to detect trapped air, such as the recently developed Fourier decomposition [24].

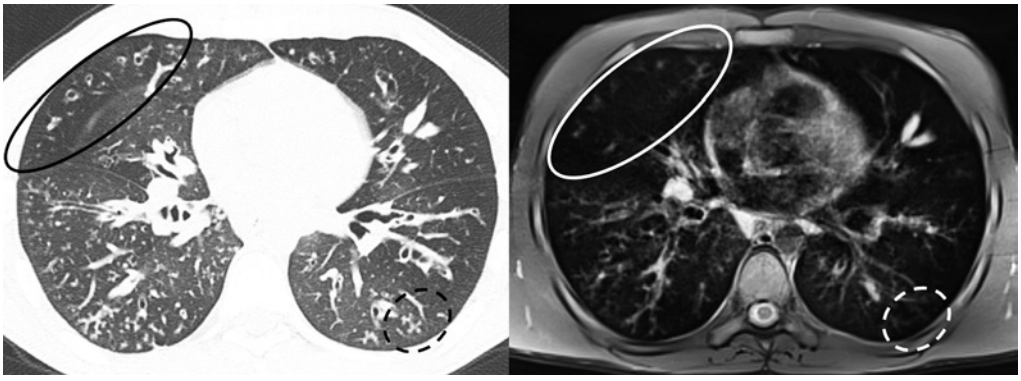

**Figure 3. Example of underestimation by chest MRI relative to chest CT.** On the left the CT image during inspiration and on the right the correspondent PROPELLER MRI image. Note the peripheral bronchiectasis depicted by CT in right upper lobe tend to disappear in the correspondent MRI image (white dotted ovals). Similarly the small areas of tree-in bud in the left lower lobe are blurred and therefore less visible in the correspondent MRI image.

Thirdly, in our study with PROPELLER, MRI tended to overestimate mild CF lung disease and underestimate severe CF lung disease compared to CT. CT appears to have superior sensitivity especially for changes in the periphery of the lung, where small abnormalities, such as bronchiolectasis and mucus plugs can be easily missed by MRI (Figure 3). To overcome this problem, it is important to further increase the spatial resolution of our routine MRI protocol. This is likely possible with new techniques, such as 3D T1 GRE sequences with radial acquisition in free breathing or in breath-hold condition and highly accelerated parallel imaging [25].

Finally, we found a low sensitivity and NPV for MRI to detect severe bronchiectasis compared to CT. This finding partially matches the study of Puderbach et al, where the lowest level of concordance between MRI and CT was for the severity of bronchiectasis [13]. Similarly, Failo et al demonstrated the lower spatial resolution of MRI relative to CT, especially at the periphery of the lung [14]. Conversely, we found a high specificity and PPV for MRI, which indicates that in case a structural abnormality is observed on MRI it is also visible on CT. Thus, such an abnormality on MRI can be further followed by MRI avoiding CT. The high specificity with the very good intra and inter-observer agreement of PROPELLER might result highly advantageous for short-term follow-up of CF patient with pulmonary exacerbation. The use of PROPELLER could allow assessing efficacy of antibiotic therapy without exposing patient to ionizing radiation. Moreover, PROPELLER might be even suitable for really young patient, who are not capable of breath-hold acquisition, or in those sick CF patients with reduced compliance.

There are some limitations might have reduced agreement between MRI and CT in our study.

The main limitation is that we evaluated a single sequence, which may have influenced the sensitivity of MRI to detect CF lung disease. We used a single sequence study design as in prior publications [13,14], because we want to assess if the motion correction technique of PROPELLER would have resulted in improved image quality in chest MRI by reducing the impact of respiratory movements [26]. However, a potential limitation of the use of PROPELLER is that this sequence can produce streak artifacts related to the K-space reconstruction [16,17]. To reduce this artifact we increased the blade width and the k-space coverage [27]. However, despite this adaptation, streak artifacts were still observed in about 20% of patients (Figure 4). Hence the occurrence of streak artifacts might have reduced the sensitivity of MRI in our study.

The second limitation, which might have affected our MRI-CT comparison, is that the image quality of the MRI images were partially impaired by motion artifacts related to pulsation of the heart and great vessels (Figure 5). We did not attempt to reduce these artifacts by using cardiac-gating since this would have added 5-10 minutes scan time to an already lengthy MRI protocol of 35 minutes (average 20-45 minutes). Purposely, PROPELLER sequence was applied with NAVIGATOR technique, which reduced problems related to patient cooperation, especially in younger patients, since the acquisition was automatically triggered at the end of the expiration, independently by the respiratory pattern. A

disadvantage of the NAVIGATOR technique was that in children with irregular breathing it prolonged acquisition time.

**Figure 4. Streak artifacts of propeller sequence.** On the left the CT image during inspiration and on the right the corresponding MRI image acquired using the PROPELLER sequence. Note that streaks artifacts are visible not only inside the parenchyma (arrow heads), but also outside (white arrows).

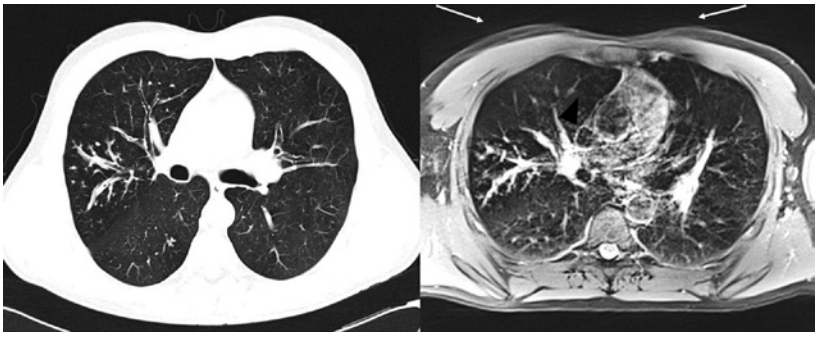

**Figure 5. Motion Artifacts of MRI PROPELLER (BLADE@Siemens)**. Note the motion artifacts around the heart (white arrows)

The third limitation of our study is that images were acquired using different breathing conditions for the CT and MRI protocols. As discussed, MRI images were acquired near functional residual volume level (FRC) using free breathing acquisition, while for CT bronchiectasis were assessed after a deep inspiration at a lung volume close to total lung capacity while trapped air was assessed at a lung volume close to residual volume during a breath hold maneuver at end-expiration. However, it has been shown that CT scans acquired near FRC overestimate trapped air relative to scans acquired near residual volume [28]. Therefore, our MRI protocol should have shown larger amount of trapped air compared to CT, but this was not the case.

Finally, the reduced sensitivity of chest MRI relative to CT might be related to the use of our CF-MRI semi-quantitative scoring system. We decided to use a similar scoring strategy for MRI as for CT, to allow a fair comparison between sub-scores. The CF-MRI scoring system was used by our group with success in previous studies [13,14]. As shown by the good intra and inter observer variability both the CF-CT and CF-MRI scoring system can be trained reliable. It is possible that the development of more sophisticated scoring methods for MRI might improve the sensitivity of MRI.

## Conclusions

In conclusion, this comparison showed that motion corrected MR images acquisition with PROPELLER does not show a good sensitivity to assess CF lung disease, and is still not able to assess severity of CF lung disease with the same precision of CT. However, the good or very good inter- and intra-observer agreement and the high specificity suggest that MRI can be applied in the follow-up of CF lung disease. MRI may be used for short term follow-up of major lung abnormalities, such as evaluating the efficacy of intravenous treatment for a pulmonary exacerbation, and, avoiding ionizing radiation which is an inherent limitation of CT. Likely in future, further protocol optimization and alternative more sensitive image analysis techniques will allow chest MRI to playing a more important role in the follow-up of CF lung disease.

## Acknowledgments

P.C. acknowledges support from the Italian cystic fibrosis league (Lega Italiana Fibrosi Cistica, LIFC). The researchers also wish to express their deepest gratitude to all CF patients, who participated in the study

## Bibliography


1. Cohen-Cymberknoh M, Shoseyov D, Kerem E (2011) Managing cystic fibrosis: strategies that increase life expectancy and improve quality of life. Am J Respir Crit Care Med 183:1463–71. doi: 10.1164/rccm.201009-1478CI
2. Tiddens HAWM, Rosenow T (2014) What did we learn from two decades of chest computed tomography in cystic fibrosis ? Pediatr Radiol 44:1490–1495. doi: 10.1007/s00247-014-2964-6.
3. Tepper LA, Utens EMWJ, Caudri D, et al. (2013) Impact of bronchiectasis and trapped air on quality of life and exacerbations in cystic fibrosis. Eur Respir J 42:371–9. doi: 10.1183/09031936.00137612
4. Tiddens HAWM, Donaldson SH, Rosenfeld M, Paré PD (2010) Cystic fibrosis lung disease starts in the small airways: can we treat it more effectively? Pediatr Pulmonol 45:107–17. doi: 10.1002/ppul.21154
5. Eichinger M, Heussel C-P, Kauczor H-U, et al. (2010) Computed tomography and magnetic resonance imaging in cystic fibrosis lung disease. J Magn Reson Imaging 32:1370–8. doi: 10.1002/jmri.22374
6. De Jong PA, Lindblad A, Rubin L, et al. (2006) Progression of lung disease on computed tomography and pulmonary function tests in children and adults with cystic fibrosis. Thorax 61:80–5. doi: 10.1136/thx.2005.045146
7. Loeve M, Lequin MH, de Bruijne M, et al. (2009) Cystic fibrosis: are volumetric ultra-low-dose expiratory CT scans sufficient for monitoring related lung disease? Radiology 253:223–9. doi: 10.1148/radiol.2532090306
8. O'Connor OJ, Vandeleur M, McGarrigle AM, et al. (2010) Development of low-dose protocols for thin-section CT assessment of cystic fibrosis in pediatric patients. Radiology 257:820–9. doi: 10.1148/radiol.10100278
9. Miglioretti DL, Johnson E, Williams A, et al. (2013) The use of computed tomography in pediatrics and the associated radiation exposure and estimated cancer risk. JAMA Pediatr 167:700–7. doi: 10.1001/jamapediatrics.2013.311
10. Macdougall RD, Strauss KJ, Lee EY (2013) Managing radiation dose from thoracic multidetector computed tomography in pediatric patients: background, current issues, and recommendations. Radiol Clin North Am 51:743–60. doi: 10.1016/j.rcl.2013.04.007
11. Puderbach M, Eichinger M, Gahr J, et al. (2007) Proton MRI appearance of cystic fibrosis: comparison to CT. Eur Radiol 17:716–24. doi: 10.1007/s00330-006-0373-4
12. Puderbach M, Kauczor H-U (2008) Can lung MR replace lung CT? Pediatr Radiol 38 Suppl 3:S439–51. doi: 10.1007/s00247-008-0844-7
13. Puderbach M, Eichinger M, Haeselbarth J, et al. (2007) Assessment of morphological MRI for pulmonary changes in cystic fibrosis (CF) patients: comparison to thin-section CT and chest x-ray. Invest Radiol 42:715–25. doi: 10.1097/RLI.0b013e318074fd81
14. Failo R, Wielopolski PA, Tiddens HAWM, et al. (2009) Lung morphology assessment using MRI: a robust ultra-short TR/TE 2D steady state free precession sequence used in cystic fibrosis patients. Magn Reson Med 61:299–306. doi: 10.1002/mrm.21841
15. Rajaram S, Swift AJ, Capener D, et al. (2012) Lung morphology assessment with balanced steady-state free precession MR imaging compared with CT. Radiology 263:569–77. doi: 10.1148/radiol.12110990
16. Hirokawa Y, Isoda H, Maetani YS, et al. (2008) Evaluation of motion correction effect and image quality with the periodically rotated overlapping parallel lines with enhanced reconstruction (PROPELLER) (BLADE) and parallel imaging acquisition technique in the upper abdomen. J Magn Reson Imaging 28:957–62. doi: 10.1002/jmri.21538
17. Tamhane AA, Arfanakis K (2009) Motion correction in periodically-rotated overlapping parallel lines with enhanced reconstruction (PROPELLER) and turboprop MRI. Magn Reson Med 62:174–82. doi: 10.1002/mrm.22004
18. Biederer J, Beer M, Hirsch W, et al. (2012) MRI of the lung (2/3). Why … when … how? Insights Imaging 3:355–71. doi: 10.1007/s13244-011-0146-8

19. Laszlo G (2006) Standardisation of lung function testing: helpful guidance from the ATS/ERS Task Force. Thorax 61:744–6. doi: 10.1136/thx.2006.061648

20. Wainwright CE, Armstrong DS, Byrnes CA, et al. (2011) Effect of Bronchoalveolar Lavage – Directed Therapy on Pseudomonas aeruginosa Infection and Structural Lung Injury in Children With Cystic Fibrosis. 306:

21. Portney LG WM (2000) Foundations of clinical research: applications to practice. Prentice Hall 560–567.

22. Loeve M, van Hal PTW, Robinson P, et al. (2009) The spectrum of structural abnormalities on CT scans from patients with CF with severe advanced lung disease. Thorax 64:876–82. doi: 10.1136/thx.2008.110908

23. Contoli M, Kraft M, Hamid Q, et al. (2012) Do small airway abnormalities characterize asthma phenotypes? In search of proof. Clin Exp Allergy 42:1150–60. doi: 10.1111/j.1365-2222.2012.03963.x

24. Lederlin M, Bauman G, Eichinger M, et al. (2013) Functional MRI using Fourier decomposition of lung signal: reproducibility of ventilation- and perfusion-weighted imaging in healthy volunteers. Eur J Radiol 82:1015–22. doi: 10.1016/j.ejrad.2012.12.003

25. Brodsky EK, Bultman EM, Johnson KM, et al. (2013) High-spatial and high-temporal resolution dynamic contrast-enhanced perfusion imaging of the liver with time-resolved three-dimensional radial MRI. Magn Reson Med. doi: 10.1002/mrm.24727

26. Serra G, Milito C, Mitrevski M, et al. (2011) Lung MRI as a possible alternative to CT scan for patients with primary immune deficiencies and increased radiosensitivity. Chest 140:1581–9. doi: 10.1378/chest.10-3147

27. Pandit P, Qi Y, King KF, Johnson GA (2011) Reduction of artifacts in T2 -weighted PROPELLER in high-field preclinical imaging. Magn Reson Med 65:538–43. doi: 10.1002/mrm.22624

28. Bonnel A-S, Song SM-H, Kesavarju K, et al. (2004) Quantitative air-trapping analysis in children with mild cystic fibrosis lung disease. Pediatr Pulmonol 38:396–405. doi: 10.1002/ppul.20091

# Chapter 4

## Diffusion-weighted MRI (DW-MRI) as New Technique to Assess Inflammation in CF Lung Disease

### Diffusion Weighted Imaging in Cystic Fibrosis Disease: Beyond Morphological Imaging

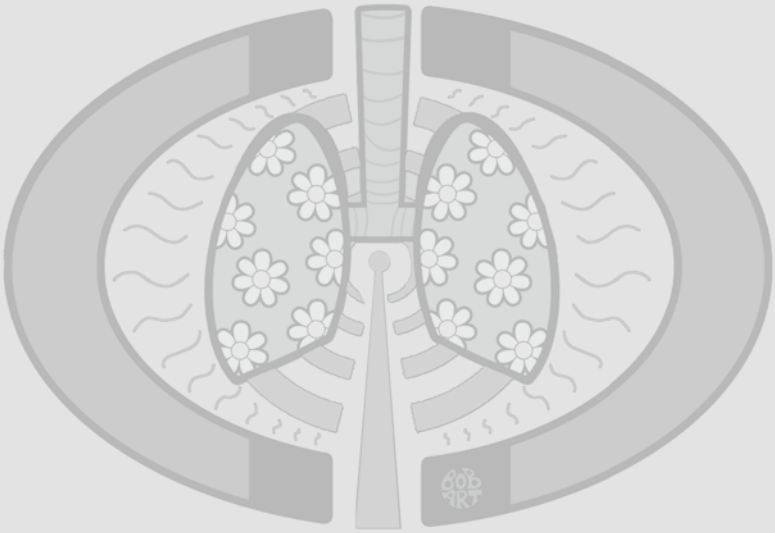

*Ciet P, Serra G, Andrinopoulou ER, Bertolo S, Ros M, Catalano C, Colagrande S, Tiddens HAWM, Morana G*

European Radiology. 2016 Feb 12

## Abstract

**Objectives:** To explore the feasibility of diffusion weighted imaging (DWI) to assess inflammatory lung changes in patients with Cystic Fibrosis (CF)

**Methods:** CF patients referred for their annual check-up had spirometry, chest-CT and MRI on the same day. MRI was performed in a 1.5T scanner with BLADE and EPI-DWI sequences (b=0-600 s/mm$^2$). End-inspiratory and end-expiratory scans were acquired in multi-row scanners. DWI was scored with an established semi-quantitative scoring system. DWI score was correlated to CT sub-scores for bronchiectasis (CF-CT$_{BE}$), mucus (CF-CT$_{mucus}$), total score (CF-CT$_{total\text{-}score}$), FEV$_1$, and BMI. T-test was used to assess differences between patients with and without DWI-hotspots.

**Results:** 33 CF patients were enrolled (mean 21 years, range 6-51, 19 female). 4% (SD 2.6, range 1.5-12.9) of total CF-CT alterations presented DWI-hotspots. DWI-hotspots coincided with mucus plugging (60%), consolidation (30%) and bronchiectasis (10%). DWI$_{total\text{-}score}$ correlated (all $p<0.0001$) positively to CF-CT$_{BE}$ ($r=0.757$), CF-CT$_{mucus}$ ($r=0.759$) and CF-CT$_{total\text{-}score}$ ($r=0.790$); and negatively to FEV$_1$ ($r=0.688$). FEV$_1$ was significantly higher ($p<0.0001$) in patients without DWI-hotspots.

**Conclusions:** DWI-hotspots strongly correlated with radiological and clinical parameters of lung disease severity. Future validation studies are needed to establish the exact nature of DWI-hotspots in CF patients.


**Key points**

- DWI hotspots only partly overlapped structural abnormalities on morphological imaging
- DWI strongly correlated with radiological and clinical indicators of CF-disease severity
- Patients with more DWI hotspots had lower lung function values
- Mucus score best predicted the presence of DWI-hotspots with restricted diffusion.

## Introduction

Cystic Fibrosis (CF) lung disease is characterized by chronic airways infection, inflammation and progressive lung damage starting in early childhood [1]. Exacerbations, acute episodes of infection and inflammation, eventually lead to end-stage lung disease, the main cause of death in patients with CF [2]. Regular monitoring that include a physical examination, spirometry, quality-of-life questionnaires and imaging [3], is used to detect lung changes, that require timely treatment [4].

To date, imaging techniques such chest x-ray (CXR) and chest-CT (CT) have been the preferred methods for CF monitoring, however both techniques have limitations [5]. CXR only allows detection of gross lung changes, such as consolidation, atelectasis and pleural effusion [5]. CT is far more sensitive to localize and quantify structural changes [6], however short-term follow-up with CT, for example during an exacerbation, is restricted by radiation exposure [7]. The latter limitation was the driving force to introduce MRI in CF lung monitoring [8]. Unfortunately, MRI has inferior sensitivity compared to CT to detect structural changes in the CF lung [9,10] due to a lower spatial resolution. However more recently the resolution has improved by using newly developed sequences, such as ultrashort [11] or zero echo time [12]. Furthermore, the interest to use MRI in CF has expanded towards functional imaging [13]. Multi-parametric MRI, such as Fourier Decomposition [14], hyperpolarized-gases MRI and oxygen-enhanced MRI [15,16], provide information not readily available with CT [17]. Diffusion-weighted imaging (DWI) is another MRI technique that might have great potential in CF lung monitoring [18]. To date, DWI has been primarily used to assess malignancies in thoracic imaging [19]. Interestingly, DWI has proved to be accurate in the identification of inflammation in various organs, such as brain, spine, muscle and intestines [20-23]. Based on these studies, we investigated whether DWI has potential to detect inflammatory changes in CF lung disease.

The main aims of our study were: (1) to explore the feasibility of DWI to detect lung inflammatory changes in CF patients, and (2) to correlate DWI with radiological and clinical indicators of CF lung disease severity.

## Material and Methods

In this multicenter prospective cross-sectional study, patients with CF scheduled for their routine annual evaluation were consecutively recruited in two Italian CF centers (Treviso and Rome) by their treating physicians. At the clinical evaluation, each patient was informed about the study and asked to participate. When willing to participate, the subject was planned for the study protocol within two weeks from the visit. The study was approved by the institutional review board in all participating centers (n. 292/AULSS9 and n. 419/09). All patients underwent a physical examination, spirometry, chest-CT and chest-MRI on the same day. Inclusion and exclusion criteria are described in Table 1.

**Table 1.** Inclusion / Exclusion criteria for patient selection.

| Inclusion criteria | Exclusion Criteria |
|---|---|
| – Proven CF as evidenced by positive sweat test or two CF gene mutations<br>– Scheduled for biennial routine chest-CT scan requested by the attending physician<br>– Ability to perform reproducible maneuvers for spirometry<br>– Ability to comply with instructions during CT and MRI examinations | – Age below 6-years<br>– Chronic oxygen therapy<br>– Present or recent (two weeks) pulmonary exacerbation<br>– History of lung transplantation<br>– Participation in other trial<br>– Contraindications for MRI<br>– Proved or possible pregnancy<br>– Not able or not willing to give informed consent |

## Physical examination and spirometry

Informed consent was obtained, and each patient underwent a clinical examination, pulse oximetry, and spirometry, prior to imaging. As part of the clinical exam, heart and respiratory rate, weight and height were recorded. Spirometry was performed according to the ATS/ERS guidelines [24].

## CT and MRI Protocol

The routine biennial CT protocol consisted of volumetric end-inspiratory and end-expiratory low-dose scans in a 16- or 64-row scanner (SOMATOM Sensation, Siemens, Erlangen, Germany) using the following parameters: 120kV for patients ≥35 kg,100 kV for patients <35kg, mAs 15-40, no contrast agent, 1 mm collimation, slice thickness 1 mm, reconstruction increment 0.8 mm, pitch 1. Five mm axial and coronal reformats with kernels B31f, B60f and B70f were obtained to match the slice thickness of MR images.

In addition to the routine CT protocol a chest MRI was performed on the same day. The MRI protocol consisted of respiratory-triggered scans using a 16 channel torso coil in a clinical 1.5 T scanner, with the following parameters: axial and coronal BLADE sequence proton-density (PD)-weighted with navigator (TR/TE/alpha/: ∞/28 ms/90º, in plane resolution 1.2x1.2 mm and slice thickness 5 mm) and T2-weighted axial BLADE sequence (TR/TE/alpha=2000ms/27ms/150°, in plane resolution 3.2x2.5 mm and slice thickness 5 mm). DWI was acquired using a single-shot echo-planar imaging sequence (EPI) in the axial plane, with gradients equal in all directions (readout, phase and slice-section orientations). DWI was obtained with b values of 0 and 600 s/mm$^2$ (TR/TE/alpha=5632ms/83ms/90°, slice thickness 5 mm, gap 0 mm, 2 average). All sequences were acquired at end-expiration during free-breathing using navigator echoes respiratory triggering. The MRI protocol was identical in both CF centers, which had the same MRI scanner (MAGNETOM Avanto, Siemens Healthcare, Erlangen, Germany).

## Image analysis

All CT and MRI images were anonymized and evaluated in random order by two radiologists (P.C. and G.S.), with 4 years and 1 year of experience in thoracic CT and MRI scoring, respectively. Both radiologists were blinded to any clinical information and to each other's CT and MRI assessment. Prior to this study, both radiologists were trained in the CF center of Erasmus MC (Rotterdam, the Netherlands) to the CF-CT and CF-MRI scoring systems [25], which were used to score the CT and BLADE MR images [26].The total score is the sum of the individual sub-scores per lobe of the following parameters: bronchiectasis ($CF\text{-}CT_{BE}$); mucus plugging ($CF\text{-}CT_{mucus}$); air wall thickening ($CF\text{-}CT_{AWT}$); trapped air ($CF\text{-}CT_{TA}$) and parenchyma ($CF\text{-}CT_{PAR}$) [26]. Sub-scores and total scores are expressed as % of the maximal possible score.



DWI images were scored in random order using a semi-quantitative scoring approach which has been used in previous studies [27-29]. This qualitatively analyzes the signal intensity of lung lesions with altered signal intensity (hotspots). Each hotspot was visually graded on a three-point score scale by signal intensity: score 0, no signal; score 1, weak signal and score 2, strong signal. Signal intensity was judged using the highest b-value (b=600 s/mm$^2$) images, compared to the signal of the spinal cord. Spinal cord was used as the reference structure as it has constant high signal intensity on high b values as a result of the anatomical organization of the sagittal nerve fascicles, and it is alongside the entire chest. When the DWI signal of lung parenchymal hotspots was lower than that of the cord, it was graded as "weak" ($DWI_{weak\ score}$, score=1), whereas if the signal was greater than or equal to that of the cord it was graded as "strong" ($DWI_{strong\ score}$, score=2). The total DWI score ($DWI_{total\ score}$) is the sum of all weak and strong hotspots for each of the 6 lung lobes, with lingula considered a separate lobe. A quantitative analysis was not performed based on the poor reliability of the apparent diffusion coefficient (ADC) maps due to residual motion and susceptibility-induced distortions. Following DWI scoring, using fusion technique (Image Fusion, Siemens Healthcare, Erlangen, Germany) between DWI and correlated morphological image (axial BLADE), the anatomical substrate and the distribution of the DWI hotspots was identified. In uncertain cases, the CT was used as reference image. The percentage of structural CT changes presenting hotspots in DWI images was computed as a ratio between the $DWI_{total\ score}$ and the $CF\text{-}CT_{total\ score}$. Anatomical substrates with DWI signal were categorized in a similar fashion to the CF-CT and CF-MRI scoring system (Online supplement digital content 1).

## Statistical analysis

For each patient, the mean DWI score of the two observers was used to assess frequency and distribution of the anatomical substrates with DWI signal. Inter-observer agreement for the CF-CT, CF-MRI and DWI scoring methods was assessed using the intraclass correlation coefficient (ICC) and Bland-Altman plots. ICC values between 0.40-0.60; 0.60-0.80; and ≥0.80 are considered to represent moderate, good and very good agreement, respectively.

Pearson's correlation was used to measure the strength of the association between DWI score and clinical and radiological parameters reflecting disease severity. These parameters included: forced expiratory volume in one second ($FEV_1$ % predicted); Body Mass Index (BMI); $CF\text{-}CT_{BE}$; $CF\text{-}CT_{mucus}$; and $CF\text{-}CT_{total\ score}$. According to Cohen's criteria correlations with r between 0.10 and 0.29 are considered weak, between 0.30 and 0.49 moderate and above 0.50 strong [30]. Multiple comparisons were adjusted using the Bonferroni correction. Differences in continuous variables between patients with and without DWI hotspots were examined using a Student t-test.

Finally, data were analyzed using mixed-effects models to investigate whether there was an association between specific covariates and the outcomes of interest, while accounting for the correlation within the same patients [31]. The covariates tested in the model were BMI, $FEV_1$, sex, $CF\text{-}CT_{BE,}$ $CF\text{-}CT_{mucus}$ and score of each observer (score observer 1 versus observer 2). The outcome tested for these covariates were: $DWI_{weak\ score}$, $DWI_{strong\ score}$ and $DWI_{total\ score}$. The Akaike information criterion (AIC) was used to investigate which model performs better [32]. The lowest AIC coefficient defines the best model for the given data, and differences in AIC coefficient greater than 5 points are considered significant [32]. Differences were statistically significant if $p<0.05$. Statistical analysis was performed with SPSS (version 20.0, SPSS, Chicago, IL, USA) and R (version 3.1.3, the R foundation for statistical computing, Vienna, Austria).

## Results

After 12 months of recruitment (April 2011-March 2012) period, thirty-eight consecutively selected patients with CF (mean age 24 years, range 6-51 years, 22 females) were enrolled in the study. Five subjects were excluded for incomplete study protocol, so eventually thirty-three patients with CF were used for data analysis. (mean age 21 years, range 6-51 years, 19 females). Patients' characteristics, CT and DWI scores are summarized in Table 2.

### Distribution and anatomical substrates of DWI signal

A mean number of 6 (SD 5.2, range 0-17.5) weak and 6.9 (SD 8.4, range 0-32) strong DWI hotspots were identified. DWI hotspots were distributed in decreasing order in the right upper lobe (mean 25.4%, SD 8.4, range 0-37.9%), right lower lobe (mean 24.7%, SD 6.8, range 16.3-50%), left lower lobe (mean 21.5%, SD 6.9, range 10-36.7%), left upper lobe (mean 13.5%, SD 3.6, range 6.7-20.6%), right middle lobe (mean 8.2%, SD 5.4, range 0-18.2%) and lingula (mean 6.7%, SD 3.1, 1.5-13.3%). The most frequent structural lung alterations as examined on axial BLADE with either weak or strong DWI signal were mucus plugging (mean 61%, SD 35, range 0-100%), followed by consolidation (mean 26.5%, SD 16.8, range 0-54%), and bronchiectasis (mean 12.5%, SD 9.3, range 0-37.5%). The DWI hotspots pattern only partially overlapped the structural lung changes on morphological MRI or CT, and only 4% (SD 2.6, range 1.5-12.9%) of total CF-CT structural lung changes presented DWI hotspots.

**Table 2.** Patients' characteristics.

| | Mean | Standard deviation | Range |
|---|---|---|---|
| **Clinical parameters** | | | |
| BMI (kg/m$^2$) | 19.1 | 3.4 | 12.9-29.9 |
| $FEV_1$ % predicted | 71.8 | 25.2 | 24-113.4 |
| **CT scores** | | | |
| CT-BE (%) | 22.4 | 10.6 | 3.5-43.8 |
| CT-Mucus (%) | 21.7 | 13.7 | 0-44.4 |
| CF-CT (%) | 25.1 | 11.6 | 2.7-45.1 |
| **DWI scores** | | | |
| Weak DWI score | 6.0 | 5.2 | 0-17.5 |
| Strong DWI score | 6.9 | 8.4 | 0-32 |
| Total DWI score | 20.4 | 14.0 | 1-54 |

BMI=Body Mass Index, CT-BE=Computed tomography bronchiectasis sub-score, CF-CT=Cystic Fibrosis Computed Tomography score, CT-Mucus=Computed tomography mucus plugs sub-score, DWI=Diffusion Weighted Imaging, $FEV_1$%=Forced expiratory volume in one second % predicted. All CT score and sub-scores are expressed as a percentage of the maximum possible score, ranging from 0 (no pathological findings) to 100 (maximum severity). The maximum possible scores for CF-CT, CT-BE and CT-mucus sub-scores are 243, 72 and 36 respectively. DWI scores are expressed as mean score of the two observers for each patient.



## Reliability of DWI score

Overall, inter-observer agreement for CF-CT and CF-MRI sub-scores was good or very good, except for the trapped-air sub-score. ICCs for CF-CT and CF-MRI are presented as table in the online supplement digital content 2$^{BLINDED}$. Inter-observer agreements for $DWI_{weak\ score}$, $DWI_{strong\ score}$ and $DWI_{total\ score}$ were good: ICC 0.76 (C.I. 95%, 0.55-0.87), 0.74 (C.I. 95%, 0.43-0.87) and 0.7 (C.I. 95%, 0.04-0.89), respectively. Bland-Altman and identity plots showed that observer 2 had systematically higher $DWI_{total\ score}$ scores than observer 1 (Figure 1). Bland-Altman and identity plots for total DWI hotspots identified by each observer are presented as online supplement digital content 3.

## Correlations of DWI signal with clinical and radiological parameters

Total DWI score had strong positive correlation with $CF\text{-}CT_{BE}$ (r=0.757 observer 1, r=0.510 observer 2), $CT_{mucus}$ (r=0.759 observer 1, r=0.584 observer 2) sub-scores, and $CF\text{-}CT_{total\ score}$ (r=0.790 observer 1, r=0.618 observer 2) (Figure 3). $DWI_{total\ score}$ had strong negative correlation with $FEV_1$ (r=-0.688 observer 1, r=-0.611 observer 2) (Figure 2): $FEV_1$ in patients without DWI hotspots (n=11) was significantly higher (p<0.0001) than those of patients with DWI hotspots. BMI did not correlate with $DWI_{total\ score}$ and no significant differences in BMI were found between the groups with or without hotspots.

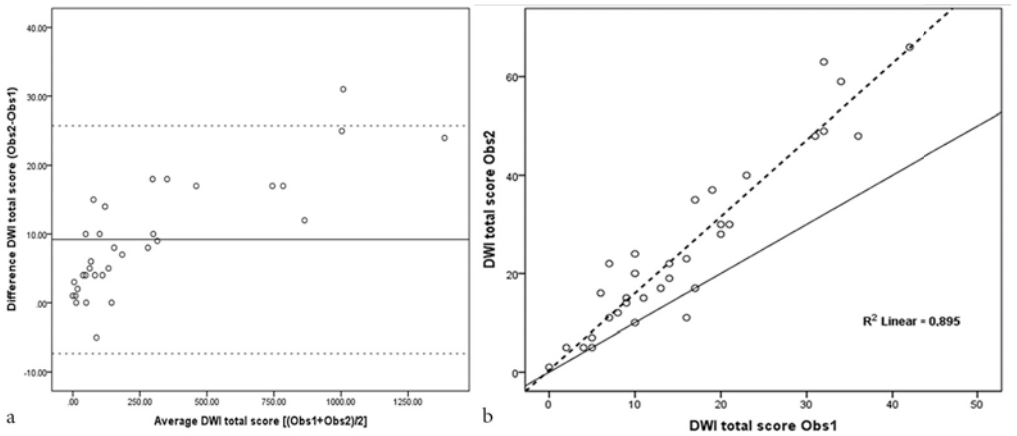


**Figure 1. (a) Bland-Altman for Total DWI score observer 1 (Obs1) versus observer 2 (Obs2). Thick line is the mean, dashed lines are ±2 standard deviations (SD).** (b) Identity Plot Total DWI score observer 1 versus observer 2. The continuous line is the identity line (y=1*x+0), dashed line is the correlations line. Note that observer 2 had higher scores than observer 1 (mean difference ~9).

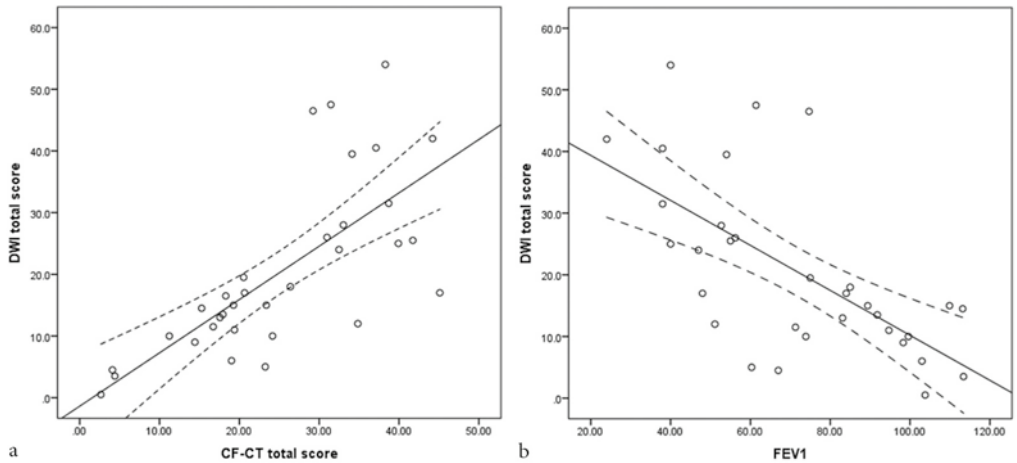


**Figure 2. (a) Correlation of total diffusion weighted imaging (DWI) score with total cystic fibrosis computed tomography score (CF-CT score).** (b) Correlation of total DWI score with forced expiratory volume in 1 second ($FEV_1$). Continuous lines are correlation lines, dashed lines are 95% confidence intervals. Note strong positive correlation of total DWI score with total CF-CT score (Pearson r=0.717, p<0.0001), and strong negative correlation with $FEV_1$ (Pearson r=-0.649, p<0.0001). Mean score of the two observers were used to build the plots.

## Relationship of covariates in DWI scores: mixed-model analysis

For the $DWI_{strong}$ outcome, the model with the covariate $CF\text{-}CT_{mucus}$ (AIC=398.6) was better than the model with $FEV_1$ (AIC=406.2). However, there were no significant differences in AIC coefficient between the model with $FEV_1$ or $CF\text{-}CT_{mucus}$ covariates when tested for the $DWI_{weak}$ and $DWI_{total\ score}$ outcomes ($DWI_{weak}$: $AIC\text{-}FEV_1$=367.4, $AIC\text{-}CF\text{-}CT_{mucus}$=368; $DWI_{total\ score}$:$AIC\text{-}FEV_1$=447, $AIC\text{-}CF\text{-}CT_{mucus}$=446.9). Therefore, we considered the best predictive model for all three DWI outcomes (weak, strong and total DWI) that including $CF\text{-}CT_{mucus}$ but not $FEV_1$. The final model included the covariates: BMI, sex, observer score, $CF\text{-}CT_{BE}$, $CF\text{-}CT_{mucus}$. In this model the $CF\text{-}CT_{mucus}$ and observer score covariates were significant for the $DWI_{strong}$, and for $DWI_{total\ score}$. For the $DWI_{weak\ score}$ outcome, the $CF\text{-}CT_{BE}$ covariate was significant, while $CF\text{-}CT_{mucus}$ tended to be significant (p=0.052). Mixed-model analysis results are summarized in Table 3. Figure 3 shows effect plots for each DWI score outcome ($DWI_{weak\ score}$, $DWI_{strong\ score}$ and $DWI_{total\ score}$) based on the mixed-effects model analysis.



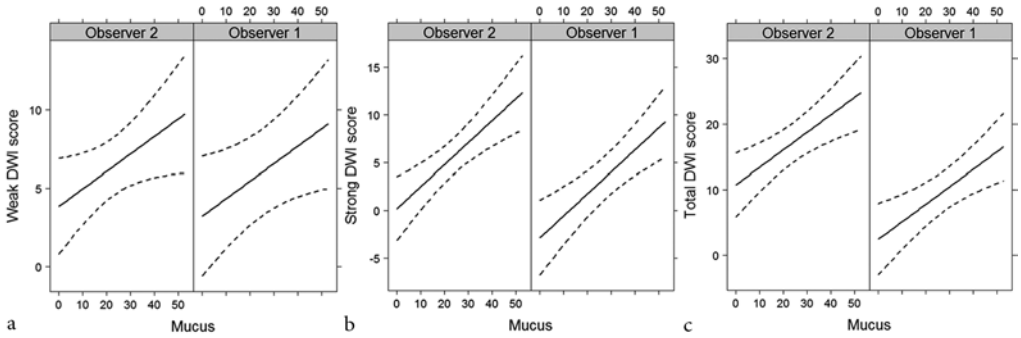


**Figure 3. Effects plots for diffusion-weighted imaging (DWI) scores outcomes (a) weak, (b) strong, and (c) total DWI score; and $CF\text{-}CT_{mucus}$ covariate.** Each plot has two curves, one for each observer. Y-axis represents DWI scores while x-axis the $CF\text{-}CT_{mucus}$ sub-score expressed as % of maximum score, which is 36 for mucus. Each plot simulates changes in $CF\text{-}CT_{mucus}$ sub-score according DWI scores for patients with mean BMI, mean $CF\text{-}CT_{BE}$ sub-score and male gender. For instance, an increase of about 10% in $CF\text{-}CT_{mucus}$ sub-score (c) produces an increase of $DWI_{total\ score}$ of almost 3 points. Note that, although observer 2 has overall higher total DWI scores (c); the slope of the relation between $DWI_{total\ score}$ and $CF\text{-}CT_{mucus}$ sub-score is the same as for observer 1.

**Table 3.** Effect table for DWI scores outcomes based on the mixed-effects models analysis.

| | $DWI_{weak\ score}$ | | | $DWI_{strong\ score}$ | | | $DWI_{total\ score}$ | | |
|---|---|---|---|---|---|---|---|---|---|
| | **Value** | **SE** | **p-value** | **Value** | **SE** | **p-value** | **Value** | **SE.** | **p-value** |
| **Intercept** | -1.5241 | 4.0634 | 0.7102 | 8.6896 | 4.3673 | 0.0558 | 16.3902 | 6.5247 | 0.0176* |
| **Observer score** | -0.6208 | 0.7530 | 0.4162 | -3.0626 | 1.1507 | 0.0124* | -8.2908 | 1.6539 | <0.0001* |
| **BMI** | 0.0389 | 0.2011 | 0.8480 | -0.3395 | 0.1976 | 0.0960 | -0.1354 | 0.2905 | 0.6445 |
| **Gender** | 1.3513 | 1.3371 | 0.3203 | -0.3958 | 1.3170 | 0.7658 | 0.6968 | 1.9399 | 0.7220 |
| **$CF\text{-}CT_{BE}$** | 0.1736 | 0.0705 | 0.0197* | 0.0645 | 0.1029 | 0.5355 | 0.2021 | 0.1485 | 0.1836 |
| **$CF\text{-}CT_{mucus}$** | 0.1113 | 0.0551 | 0.0524 | 0.2304 | 0.0597 | 0.0006* | 0.2660 | 0.0831 | 0.0032* |

BMI=Body Mass Index, $CF\text{-}CT_{BE}$=Computed tomography bronchiectasis score, $CF\text{-}CT_{mucus}$=Computed tomography mucus score, $FEV_1$=Forced expiratory Volume in 1 second % of predicted, SE=Standard Error. Note significant differences in observer score (scores observer 1 vs. observer 2) and $CF\text{-}CT_{mucus}$ covariates for $DWI_{strong\ score}$ and $DWI_{total\ score}$ outcomes (*). For the $DWI_{weak\ score}$ outcome, the $CF\text{-}CT_{BE}$ is significant (*), while $CF\text{-}CT_{mucus}$ tends to be significant.

## Discussion

To our knowledge, this is the first study that has used DWI to assess CF lung disease, and several observations can be made from these results.

The most important observation is that DWI hotspots only partially overlapped the structural lung changes as seen on morphological CT or MRI (Figure 4). Moreover, the DWI signal for the same parenchymal abnormality on MRI in a single patient was very different. For instance, mucous plug as observed on MRI in a lobe could show different signal intensities, from no signal to a very intense signal (Figure 5). Similar variability was also observed for other structural lung changes, such as consolidation and bronchiectasis, which were the most frequent structural lung changes presenting a DWI signal. We speculate that the observed differences in DWI signal intensity might be related to the severity of local inflammation, based on differences in the cellularity of the structure examined and consequently in differences in the restriction of proton movement.



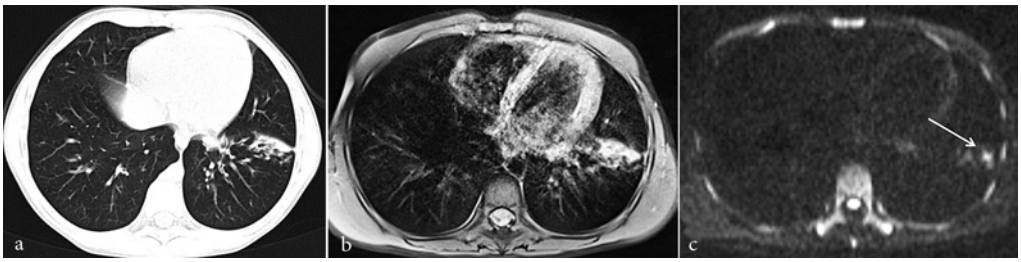


**Figure 4. (a) End-inspiratory axial CT, (b) Free-breathing PD-weighted axial BLADE image, and (c) diffusion-weighted imaging (DWI) free breathing (b=600 s/mm$^2$).** Note that DWI signal (hotspot) only partially overlaps the left lower lobe consolidation, with the most peripheral portion presenting the highest signal (arrow). This indicates that the lesion has non-homogenous DWI characteristics, with the most peripheral portion having more restricted diffusion.

Alternative explanations are that increased DWI signal intensity depend on an increased capillary perfusion in relation to inflammation, which can be detected by DWI as D* (pseudo-diffusion coefficient) associated with blood flow [33]. However, pseudo-diffusion was not assessed in our MRI protocol, as intravoxel incoherent motion imaging was not applied [34]. Furthermore, differences in DWI signal intensity (weak vs. strong) among the structural lung changes could be related to differences in water concentrations caused by T2-shine-through artifact [35]. To overcome this, we assessed and scored the DWI images in the highest b-value (b=600 s/mm$^2$), with reduced T2-shine-through effect (Figure 5).

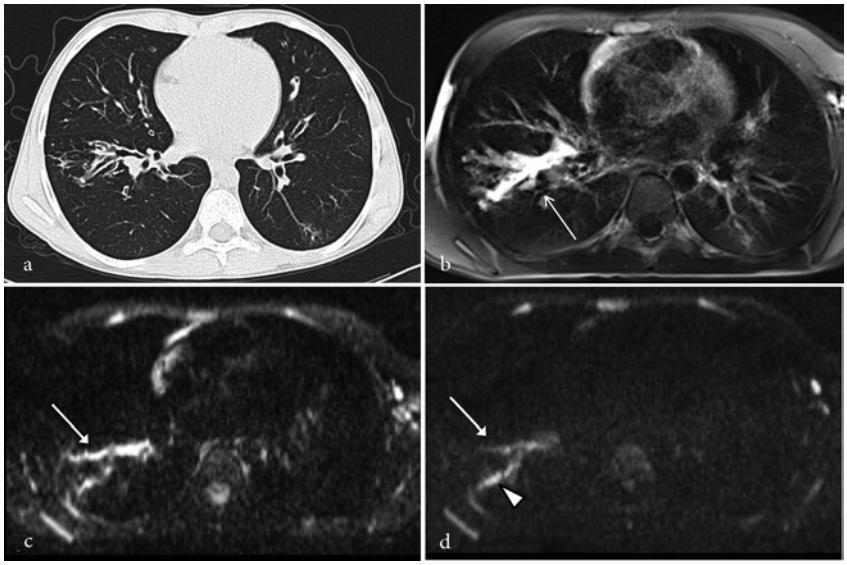


**Figure 5. (a) End-inspiratory axial CT, (b) free-breathing PD-weighted axial BLADE image, (c) Diffusion Weighted Imaging (DWI) free breathing (b=0 s/mm²) and D) DWI (b=600 s/mm²).** A large bronchiectasis filled with mucus can be appreciated in the right lower lobe (arrow in b) Note heterogeneous DWI signal decay in highest b-value of the mucus-filled bronchiectasis (arrow in c and d), although it persists in the dorsal branch due to persistent restricted diffusion (arrowhead in d).

The second important finding is that DWI scores correlated well with radiological and clinical indicators of CF lung disease severity. DWI scores had a strong positive correlation with CF-CT score and a moderate negative correlation with $FEV_1$. In particular, the higher the DWI score, the higher the CF-CT score, or the lower the DWI score, the lower the $FEV_1$. These correlations suggest that patients with more severe CF lung disease have a larger number of DWI hotspots. This observation is also supported by the findings that there were significant differences in $FEV_1$ between patients with and without DWI hotspots.

The third important observation is from the mixed-model analysis, which shows that for the $DWI_{strong}$ outcome, the best model (lowest AIC coefficient) was the model that included the $CF\text{-}CT_{mucus}$ sub-score instead of the $FEV_1$ covariate. $DWI_{strong}$ score represents those hotspots with high DWI signal, which suggests a restricted diffusion. Paired with the finding that mucus was also the most frequent alteration associated with DWI signal, it suggests that mucus significantly contributes to the "inflammatory" DWI hotspots in CF lung disease. This is not unlikely as reduced mucus clearance is considered to be the primary cause of chronic airway infection and inflammation in CF [1].

We acknowledge some limitations to this study. First, we used a semi-quantitative scoring system to assess DWI signal and did not compute ADC maps. The main reason was that the ADC maps were not reliable due to residual motion and susceptibility-induced distortions. Part of these distortion artifacts was counterbalanced by doubling the number of averages during image acquisition. More than two averages combined with respiratory-triggered acquisition were not feasible, as it would have led to unacceptably long acquisition times of the DWI sequence (>10 minutes). For these reasons, we used a semi-quantitative approach that has proved to be reliable in previous studies, with high sensitivity and specificity [29]. Moreover, this method showed good agreement between the observers.

Second, there were significantly different scores between the observers as shown by the Bland-Altman plots and by the mixed model analysis (observer score covariate). However, correlations using the individual scores of each observer instead of taking the mean scores of both observers obtained the same significant and concordant results (Table 3). Hence, it is unlikely that the differences in scores between the observers had any impact on our most important findings. The development of a fully quantitative approach will overcome this inter-observer limitation, by providing objective ADC maps that are independent of observer variability. For now, we are improving the image quality of our DWI protocol, to facilitate the use of ADC maps for future studies.



Finally, we did not objectively assess the exact nature of these DWI hotspots. However, our study had the main aim to investigate the information obtainable with DWI in CF lung disease. Clearly, further studies are needed to validate this technique in CF patients suffering from a pulmonary tract exacerbation.

## Conclusions

In summary, this study is the initial exploratory phase towards the development of DWI as technique to quantify lung inflammation in CF lung disease. We observed that the DWI hotspots pattern only partly overlapped structural abnormalities on morphological CT or MRI. In addition, DWI scores had a strong correlation with radiological and clinical indicators of CF lung disease severity. Significant differences in pulmonary function ($FEV_1$) were found between patients without and with DWI hotspots. Finally, we found that the amount of mucus in patients with CF was the best predictor of strong DWI hotspots (restricted diffusion).

These compelling results have established the foundations for future validation studies in CF patients with pulmonary exacerbation, to establish the exact nature of these DWI hotspots.

## Acknowledgments

P.C. acknowledges support from the Italian cystic fibrosis league (Lega Italiana Fibrosi Cistica, LIFC). The authors thank Elizabeth Salamon, department of Respiratory Medicine, Royal Perth Hospital, for offering invaluable detailed advices on grammar and organization of the manuscript. The authors also thank Thorsten Feiweier, Siemens Healthcare Erlangen, Germany, for technical advice in critically reviewing the manuscript. The researchers also wish to express their deepest gratitude to all CF patients, who participated in the study.

## Bibliography


1. Tiddens H A WM, Donaldson SH, Rosenfeld M, Paré PD (2010) Cystic fibrosis lung disease starts in the small airways: can we treat it more effectively? Pediatr Pulmonol 45:107–17. doi: 10.1002/ppul.21154
2. Loeve M, Gerbrands K, Hop WC, et al. (2011) Bronchiectasis and pulmonary exacerbations in children and young adults with cystic fibrosis. Chest 140:178–85. doi: 10.1378/chest.10-1152
3. Conway S, Balfour-Lynn IM, De Rijcke K, et al. (2014) European Cystic Fibrosis Society Standards of Care: Framework for the Cystic Fibrosis Centre. J Cyst Fibros 13:S3–S22. doi: 10.1016/j.jcf.2014.03.009
4. Grasemann H, Ratjen F (2013) Early lung disease in cystic fibrosis. Lancet Respir Med 1:148–157. doi: 10.1016/S2213-2600(13)70026-2
5. Eichinger M, Heussel C-P, Kauczor H-U, et al. (2010) Computed tomography and magnetic resonance imaging in cystic fibrosis lung disease. J Magn Reson Imaging 32:1370–8. doi: 10.1002/jmri.22374
6. Loeve M, Hop WCJ, De Bruijne M, et al. (2012) Chest computed tomography scores are predictive of survival in patients with cystic fibrosis awaiting lung transplantation. Am J Respir Crit Care Med 185:1096–1103. doi: 10.1164/rccm.201111-2065OC
7. Kuo W, Ciet P, Tiddens H A WM, et al. (2014) Monitoring cystic fibrosis lung disease by computed tomography. Radiation risk in perspective. Am J Respir Crit Care Med 189:1328–36. doi: 10.1164/rccm.201311-2099CI
8. Wielpütz MO, Eichinger M, Puderbach M (2013) Magnetic Resonance Imaging of Cystic Fibrosis Lung Disease. J Thorac Imaging 28:151–159. doi: 10.1097/RTI.0b013e31828d40d4
9. Failo R, Wielopolski PA, Tiddens HAWM, et al. (2009) Lung morphology assessment using MRI: a robust ultra-short TR/TE 2D steady state free precession sequence used in cystic fibrosis patients. Magn Reson Med 61:299–306. doi: 10.1002/mrm.21841
10. Ciet P, Serra G, Bertolo S, et al. (2015) Assessment of CF lung disease using motion corrected PROPELLER MRI: a comparison with CT. Eur Radiol. doi: 10.1007/s00330-015-3850-9
11. Ma W, Sheikh K, Svenningsen S, et al. (2015) Ultra-short echo-time pulmonary MRI: Evaluation and reproducibility in COPD subjects with and without bronchiectasis. J Magn Reson Imaging 41:1465–1474. doi: 10.1002/jmri.24680
12. Dournes G, Grodzki D, Macey J, et al. (2015) Quiet Submillimeter MR Imaging of the Lung Is Feasible with a PETRA Sequence at 1.5 T. Radiology 276:258–265. doi: 10.1148/radiol.15141655
13. Tiddens HAWM, Stick SM, Wild JM, et al. (2015) Respiratory tract exacerbations revisited: Ventilation, inflammation, perfusion, and structure (VIPS) monitoring to redefine treatment. Pediatr Pulmonol 50:S57–S65. doi: 10.1002/ppul.23266
14. Bauman G, Puderbach M, Heimann T, et al. (2013) Validation of Fourier decomposition MRI with dynamic contrast-enhanced MRI using visual and automated scoring of pulmonary perfusion in young cystic fibrosis patients. Eur J Radiol 82:2371–7. doi: 10.1016/j.ejrad.2013.08.018
15. van Beek EJR, Hill C, Woodhouse N, et al. (2007) Assessment of lung disease in children with cystic fibrosis using hyperpolarized 3-Helium MRI: comparison with Shwachman score, Chrispin-Norman score and spirometry. Eur Radiol 17:1018–24. doi: 10.1007/s00330-006-0392-1
16. Stadler A, Stiebellehner L, Jakob PM, et al. (2007) Quantitative and o(2) enhanced MRI of the pathologic lung: findings in emphysema, fibrosis, and cystic fibrosis. Int J Biomed Imaging 2007:23624. doi: 10.1155/2007/23624
17. Ciet P, Tiddens HAWM, Wielopolski PA, et al. (2015) Magnetic resonance imaging in children: common problems and possible solutions for lung and airways imaging. Pediatr Radiol. doi: 10.1007/s00247-015-3420-y
18. Attariwala R, Picker W (2013) Whole body MRI: Improved lesion detection and characterization with diffusion weighted techniques. J Magn Reson Imaging 38:253–268. doi: 10.1002/jmri.24285

19. Luna A, Sánchez-Gonzalez J, Caro P (2011) Diffusion-weighted imaging of the chest. Magn Reson Imaging Clin N Am 19:69–94. doi: 10.1016/j.mric.2010.09.006

20. Gaviani P, Schwartz RB, Hedley-Whyte ET, et al. (2005) Diffusion-weighted imaging of fungal cerebral infection. Am J Neuroradiol 26:1115–1121.

21. Moritani T, Kim J, Capizzano AA, et al. (2014) Pyogenic and non-pyogenic spinal infections: emphasis on diffusion-weighted imaging for the detection of abscesses and pus collections. Br J Radiol 87:20140011. doi: 10.1259/bjr.20140011

22. Qi J, Olsen NJ, Price RR, et al. (2008) Diffusion-weighted imaging of inflammatory myopathies: Polymyositis and dermatomyositis. J Magn Reson Imaging 27:212–217. doi: 10.1002/jmri.21209

23. Ream JM, Dillman JR, Adler J, et al. (2013) MRI diffusion-weighted imaging (DWI) in pediatric small bowel Crohn disease: Correlation with MRI findings of active bowel wall inflammation. Pediatr Radiol 43:1077–1085. doi: 10.1007/s00247-013-2712-3

24. Miller MR, Hankinson J, Brusasco V, et al. (2005) Standardisation of spirometry. Eur Respir J 26:319–338. doi: 10.1183/09031936.05.00034805

25. Tepper L A., Ciet P, Caudri D, et al. (2015) Validating chest MRI to detect and monitor cystic fibrosis lung disease in a pediatric cohort. Pediatr Pulmonol n/a–n/a. doi: 10.1002/ppul.23328

26. Tepper L A, Utens EMWJ, Caudri D, et al. (2013) Impact of bronchiectasis and trapped air on quality of life and exacerbations in cystic fibrosis. Eur Respir J 42:371–9. doi: 10.1183/09031936.00137612

27. Liu H, Liu Y, Yu T, Ye N (2010) Usefulness of diffusion-weighted MR imaging in the evaluation of pulmonary lesions. Eur Radiol 20:807–815. doi: 10.1007/s00330-009-1629-6

28. Tanaka R, Horikoshi H, Nakazato Y, et al. (2009) Magnetic resonance imaging in peripheral lung adenocarcinoma: correlation with histopathologic features. J Thorac Imaging 24:4–9. doi: 10.1097/RTI.0b013e31818703b7

29. Uto T, Takehara Y, Nakamura Y, et al. (2009) Higher sensitivity and specificity for diffusion-weighted imaging of malignant lung lesions without apparent diffusion coefficient quantification. Radiology 252:247–254. doi: 10.1148/radiol.2521081195

30. Cohen J (1988) Statistical Power Analysis for the Behavioral Sciences. Routledge; 2 edition

31. Verbeke, Geert; Molenberghs G (2000) Linear Mixed Models for Longitudinal Data, 1st ed. doi: 10.1007/978-1-4419-0300-

32. Burnham KP (2004) Multimodel Inference: Understanding AIC and BIC in Model Selection. Sociol Methods Res 33:261–304. doi: 10.1177/0049124104268644

33. Deng Y, Li X, Lei Y, et al. (2015) Use of diffusion-weighted magnetic resonance imaging to distinguish between lung cancer and focal inflammatory lesions: a comparison of intravoxel incoherent motion derived parameters and apparent diffusion coefficient. Acta radiol 0:1–8. doi: 10.1177/0284185115586091

34. Le Bihan D (2008) Intravoxel incoherent motion perfusion MR imaging: a wake-up call. Radiology 249:748–752. doi: 10.1148/radiol.2493081301

35. Chavhan GB, Alsabban Z, Babyn PS (2014) Diffusion-weighted Imaging in Pediatric Body MR Imaging: Principles, Technique, and Emerging Applications. Radiographics 34:E73–88. doi: 10.1148/rg.343135047

## On-line supplement digital content figures

**Online supplement digital content 1**

| SIGNAL B600 | RUL | RML | RLL | LUL | Lin | LLL | TOTAL |
|---|---|---|---|---|---|---|---|
| **WEAK DWI SI (score 1)** | | | | | | | |
| **STRONG DWI SI (score 2)** | | | | | | | |
| **MUCUS PLUGGING** | | | | | | | |
| **CONSOLIDATION** | | | | | | | |
| **CYSTS&BULLAE** | | | | | | | |
| **OTHER** | | | | | | | |



DWI scoring sheet. DWI signal is assessed in highest b-value images (b = 600 s/mm$^2$). Signal intensity (SI) of DWI hotspots is compared to SI of the spine and scored 1 when SI hotspots is lower than SI spine, or scored 2 when SI hotspot is equal or greater of SI spine. The number of hotspots is counted per lobe, with the lingula considered a separate lobe. Moreover, each hotspot is identified in the same categories defined in the CF-CT and CF-MRI scoring system. RUL=Right upper lobe, RML=Right middle lobe, RLL=Right lower lobe, LUL=Left upper lobe, Lin=Lingula, LLL=Left lower lobe

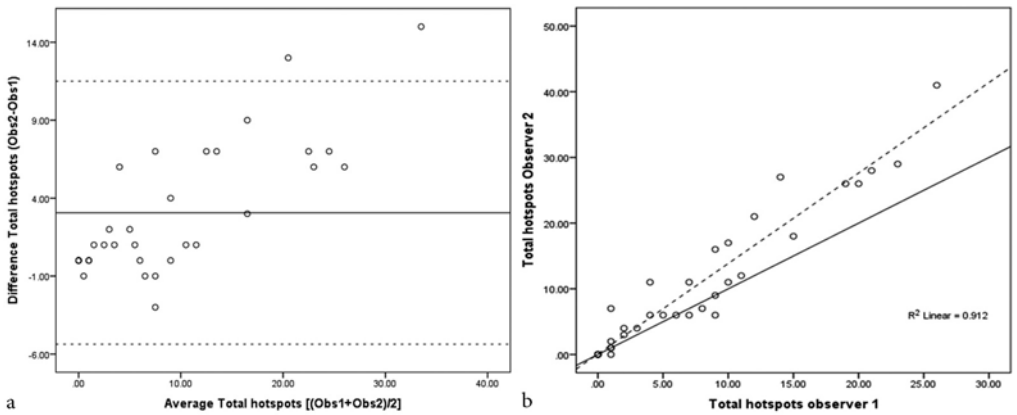


**Online supplement digital content 3. (a) Bland-Altman for total number of DWI hotspots identified by observer 1 (Obs1) and observer 2 (Obs2).** Thick line is the mean, dashed lines are ±2 standard deviations (SD). (b) Identity Plot total DWI hotspots Obs1 versus Obs2. The continuous line is the identity line (y=1*x+0), dashed line is the correlations line. Note that that Obs2 detected more hotspots than Obs1 (mean difference ~3).

# Chapter 5

## Quantification of Lung Inflammation in Cystic Fibrosis during Respiratory Tract Exacerbation using Diffusion-Weighted Magnetic Resonance Imaging

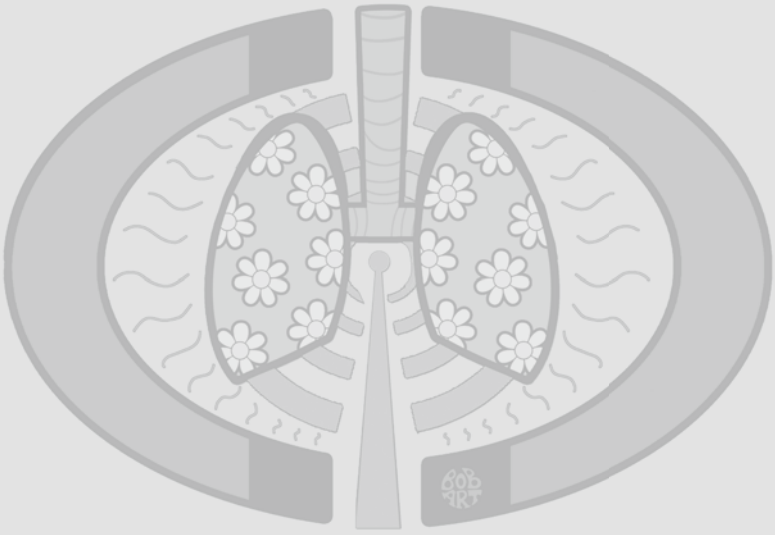

*Ciet P, Bertolo S, Ros M, Andrinopoulou ER, Tavano V, Lucca F, Feiweier T, Krestin GP, Tiddens HAWM, Morana G*

Submitted

## Evidence before the study

Despite there is no clear understanding of respiratory tract exacerbation (RTE) in Cystic Fibrosis (CF) lung disease, it is universally accepted that acute infection and inflammation are two important components of RTE. Several blood-based inflammatory biomarkers have been proposed to monitor RTE, but their clinical usefulness is limited. Other methods to assess inflammation, such as bronchoalveolar lavage (BAL) or positron emission tomography (PET) are not feasible as a routine clinical tool, mainly because BAL is an invasive procedure and PET exposes patients to relatively high doses of radiation. Hence, there are no established, sensitive and safe techniques available to monitor lung inflammation over the short time course of a RTE. Recently, diffusion weighted MRI (DW-MRI) has been developed as a non-invasive method to assess tissue inflammation, and has been used to quantify inflammation in several organs, such as brain, liver, muscle, and intestine.

## Added value of this study

This study demonstrates for the first time that DW-MRI is a sensitive and safe method to monitor lung inflammation during RTE. We have shown that DW-MRI is a reliable and accurate biomarker to distinguish an RTE from the baseline variability that is part of clinical stability in CF lung disease. More importantly, we also showed that DW-MRI is a good test to localize and objectively quantify the severity of inflammation during RTE.

## Implications of all the available evidence

The most important implication is that DW-MRI may serve to monitor the therapeutic effectiveness of antibiotic and anti-inflammatory medications during CF RTE. In children age 6 years and older, spirometry remains the preferred method to assess recovery of lung function values to pre-RTE levels. However, spirometry only gives an overall assessment of the lung and a wide regional variability can be expected, with persistent foci of inflammation despite RTE treatment. Our method represents a non-invasive and safe alternative to visualize these foci to guide BAL when needed, and to use as an outcome measure for tailored therapies. Furthermore, DW-MRI can improve our understanding of the patho-physiology of RTE and explain why one quarter to half of the patients with CF do not achieve pre-RTE lung function levels following treatment. This study will be of considerable interest to a broad audience, because DW-MRI has potential to be applied in other lung diseases where inflammation is a major component. Finally, our method could have important implications for testing effectiveness of new anti-inflammatory drugs for early phase clinical trials.

## Abstract

**Background:** Currently there are no established, sensitive and safe techniques available to monitor lung inflammation during cystic fibrosis (CF) respiratory tract exacerbations (RTE). We investigated whether diffusion-weighted magnetic resonance imaging (DW-MRI) detects inflammatory and lung function changes over the course of RTE treatment in patients with CF.

**Methods:** 29 patients with CF and RTE underwent DW-MRI pre and post antibiotic treatment. A control group of 27 stable patients with CF, matched for age and sex, underwent DW-MRI with the same time gap as those undergoing RTE treatment. Clinical status and lung function were also assessed at each DW-MRI time point. The CF-MRI scoring system was used to assess structural lung changes in both CF groups.

**Findings:** Significant reduction in the DW-MRI score over the course of antibiotic treatment ($p<0{\cdot}0001$) was observed in patients with RTE, but not in the control group. DWI score had a strong inverse correlation with clinical status ($r=-0{\cdot}504$, $p<0{\cdot}0001$) and lung function ($r=-0{\cdot}635$, $p<0{\cdot}0001$) in patients with RTE. Interestingly, there were persistent significant differences in the CF-MRI score between the RTE and control group at both baseline and follow-up ($p<0{\cdot}001$), while the differences in DWI score were only observed at baseline ($p<0{\cdot}001$). The intra and inter-observer agreement for DWI score was excellent (ICC-inter=0·877-0·904; ICC-intra=0·9-0·939).

**Interpretation:** DW-MRI is a promising imaging biomarker for noninvasive quantification of pulmonary inflammation during RTE, and may be used to assess treatment efficacy or to test new anti-inflammatory drugs.


**Funding:** Italian Cystic Fibrosis Foundation (FFC).

## Introduction

Cystic Fibrosis (CF) lung disease is characterized by chronic airways infection and inflammation, respiratory tract exacerbation (RTE), and progressive lung damage, starting in early childhood [1]. RTE is defined by acute infections with more severe symptoms, reduced pulmonary function test (PFT) parameters, and radiographic changes [2]. During RTE, it is important to localize and monitor inflammatory changes to assess the efficacy of treatment [3]. To date, such information cannot be obtained accurately by physical exam, laboratory tests or PFT, due to their limited sensitivity to regional abnormalities [4].

Structural changes related to RTE are assessed mostly by chest x-ray (CXR) or by chest CT (CT), depending on the center [5]. CXR is the first imaging method used for RTE because of its low-cost, low radiation dose and availability. CXR is not useful however, in determining whether a patient with CF is having a RTE [6]. In contrast, chest CT localizes and quantifies early regional structural and inflammatory lung changes [7]. However, short-term monitoring with CT for RTE is limited by radiation exposure, particularly in children [8]. To date, few techniques have been used to monitor inflammatory changes in CF [9]. PET-CT has been proposed, but its' use is also restricted by high radiation exposure and cost [10]. Besides PET-CT, Lung Clearance Index (LCI) and Fraction of Exhaled Nitric Oxide (FeNO) have been used to quantify lung inflammation, but like with spirometry, they do not provide regional information [11,12]. Consequently, a reliable and radiation-free technique to localize and quantify lung inflammatory changes during RTE is still needed.

Magnetic resonance imaging (MRI) [13] can fulfill the requirements of a reliable and safe monitoring tool for RTE. MRI does not require ionizing radiation and enables safe short-term monitoring needed for RTE [13]. Among the available MRI techniques, diffusion-weighted MRI (DW-MRI) is accurate in the identification of inflammation in various organs [14] and can provide functional information regarding inflammation [14]. To date, DW-MRI has been mostly used to characterize malignant thoracic lesions [15]. Only recently, DW-MRI has been used to discriminate between lung cancer and post-obstructive pneumonia [16], and to detect lung alterations in patients with primary antibody deficiencies [17].

For these reasons, we conducted a cross-sectional study in a group of stable patients with CF, where DW-MRI showed foci of high signal ("hotspots"), which only in part overlapped the structural lung changes on morphological CT or MRI [18]. We also observed that DW-MRI scores had a strong correlation with radiological and clinical parameters indicators of CF lung disease severity [18]. In addition, there were significant differences in PFT parameters between patients with and without DW-MRI hotspots [18].

Driven by these compelling results, we sought to investigate whether DW-MRI: 1) is able to differentiate between stable patients with CF and those with RTE; 2) is able to track changes over the

course of RTE treatment; 3) correlates with established clinical parameters of CF lung disease severity and 4) shows a relationship with structural lung changes established by CF MRI score during RTE.

## Material and Methods

For full details of the methods see the online appendix.

### Study design and patient enrolment

This single-center prospective study was approved by the local ethical committee (protocol n. 314/AULSS9). Following informed consent, patients with CF admitted for RTE treatment underwent a study protocol that included clinical examination, spirometry, and MRI on the same day. For each RTE patient enrolled, the next suitable CF subject without RTE in the previous 6 months was selected for the control group. Controls were CF subjects recruited during the annual follow-up and matched with RTE subjects for age, sex, mean $FEV_1$ in the previous 6 months before the visit. General inclusion and exclusion criteria for cases and controls are described in Table 1.



**Table 1.** General inclusion and exclusion criteria for both groups.

| Inclusion criteria | Exclusion criteria |
|---|---|
| – Proven CF as evidenced by positive sweat test or gene mutation | – Chronic oxygen therapy |
| – Ability to perform reproducible maneuvers with spirometry | – Isolation of Burkholderia cepacia |
| – Ability to comply with MRI procedures | – Lung transplantation |
| – $FEV_1$ (% predicted) ≥40 | – Participation in another trial |
| – Age ≥8 years old | – Any contraindications to MRI |
| | – Pregnancy |
| | – Not able or not willing to give consent |
| | – Allergic bronchopulmonary aspergillosis |

Patients with RTE repeated the study protocol following completion of a course of intravenous antibiotic treatment. Similarly, control subjects repeated the study protocol over the same median time gap as the RTE group.

### Clinical examination, laboratory and pulmonary function tests

Clinical examination included physical exam, heart and respiratory rate measurements, oxygen saturation, weight and height. Spirometry was performed according to "ATS/ERS guidelines" using a Masterscope (Jaeger-Carefusion, Hoechberg, Germany) spirometer [19]. The following parameters were recorded: forced vital capacity (FVC), Forced expired volume in one second ($FEV_1$) % predicted and forced expiratory flow at 25-75% ($FEF_{25-75}$).

RTE was defined and scored according to the Rosenfeld criteria for pulmonary exacerbation (PEX score) [20]. The criteria and the scoring system are listed in the online supplement (Table E1).

## MRI Protocol

Each subject in the RTE group underwent a chest MRI at admission (baseline) and at the end of antibiotic treatment (follow-up). The same median time gap (20 days) was used for subjects in the control group.

MRI was performed at 1.5 Tesla (MAGNETOM Avanto, Siemens Healthcare, Erlangen, Germany) using morphological and functional sequences. Morphological sequences included axial and coronal end-expiratory triggered PROPELLER (BLADE@SIEMENS) with proton density (PD) weighting [21], and breath-hold axial and coronal SSFP (TrueFISP@SIEMENS).

The functional data were acquired in the axial plane using diffusion-weighted DW-MRI. DW-MRI measures the random Brownian motion of the extra-cellular water molecules in the body. In biologic tissues, this motion is dependent and limited by interactions with cell membranes and macromolecules. In dense cellular tissues or in case of cellular swelling this water motion is reduced or "restricted", because of reduced extracellular space and by cell membranes. Tumors, edema and inflammation are all characterized by restricted diffusion.

DW-MRI provides two types of images: the native DW images, which are repeated at least twice, varying a parameter in the sequence called "b value", and the post-processed Apparent Diffusion Coefficient (ADC) map. The former allows a qualitative assessment of tissue diffusion, where tissue with restricted diffusion appears bright at high b values (b value varies from 0 to >1000 $mm/s^2$). As high water content (independently from restriction: e.g. cyst) can also provide high signal intensity on native DW images, ADC map are obtained allowing correct characterization. These post-processed images derived from the native DW acquisitions integrate the information obtained by different b values and allow quantitative measurements of tissue diffusion, where restricted diffusion appears dark while non-restricted diffusion appears white. Detailed description of the DW-MRI protocol is provided in the online supplement.

## Image analysis

MRI images were anonymized and evaluated in random order by two radiologists (V.T. and S.B.), with 4 and 8 years of experience in thoracic MRI scoring respectively. Both radiologists were blinded to any clinical information and to each other's MRI assessment. BLADE and TrueFISP MR images were scored with the CF MRI scoring system. DW images were scored in random order using a semi-quantitative scoring approach which has been used in previous studies [22,23]. A more detailed description of the CF MRI and DWI scoring systems is provided in the online supplement.

DW images were also assessed quantitatively with ADC maps [24]. A region of interest (ROI) was placed in the largest pulmonary area with restricted diffusion on ADC maps by using a freehand tracing tool. Adjacent vessels and areas with susceptibility artifact caused by air-tissue interface were excluded from image analysis. ROI of the same size and location was placed on ADC maps from MRI at baseline and follow-up in both groups.

**Statistical analysis**

Descriptive statistics, Q-Q plots and the Shapiro-Wilk tests were used to test data normality. To assess baseline difference between the groups, we used the unrelated t-test and the Mann-U-Whitney test. To assess difference between baseline and follow-up MRI, we performed the related t-test and Wilcoxon test.

Inter- and intra-observer agreement for the CF-MRI and DWI scoring methods was assessed using the intraclass correlation coefficient (ICC) and Bland-Altman plots.



Pearson's correlation was used to measure the strength of the association between DWI score and clinical, spirometry and radiological parameters reflecting disease severity. These parameters included: PEX score, $FEV_1$ % predicted, FVC, $FEF_{25-75}$, and total CF MRI score ($CFMRI_{TOT}$). Multiple comparisons were adjusted using the Bonferroni correction. According to Cohen's criteria, correlations with r between 0·10 and 0·29 are considered weak, between 0·30 and 0·49 moderate, and above 0·50 strong [25].

Receiver operating characteristic (ROC) curve were used to determine accuracy of DW-MRI to detect patient with CF and RTE. Accuracy was expressed as area under the curve (AUC). AUC values between 0·90-1, 0·80-0·90, 0·70-0·80, 0·60-0·70 correspond to an excellent, good, fair and poor accuracy respectively [26].

Finally, using mixed-effects models the outcome total DWI score was tested for the following covariates: time (baseline versus follow-up) + group (RTE vs control) + time*group, observer (scores observer 1 versus scores observer 2) and observer*time. The covariates "time*group" and "observer*time" specify the factorial interaction between time points within the group and observers. Differences were considered statistically significant if p-value was <0.05. Statistical analysis was performed with SPSS (version 20.0, SPSS, Chicago, IL, USA) and R (version 3.1.3, the R foundation for statistical computing, Vienna, Austria).

# Results

## Patients' Characteristics

Fifty-six patients with CF were enrolled in the study (mean age 24 years, range 12-58 years, 35 female). Twenty-nine subjects were included in the RTE group (mean age 24 years, range 13-48 years, 20 female) and twenty-seven subjects in the control group (mean age 23 years, range 12-58, 15 female). Subjects were correctly matched for age and sex between the groups. PEX score (p<0·001), DWI score (p=0·002) and ADC (p<0·001) were significantly different between the RTE and control group at baseline, but not at follow-up. CF-MRI scores between the groups were significantly different at both time points. Patients' characteristics, spirometry, CF-MRI, DWI scores and ADC are summarized in Table 2.

**Table 2.** Patients' characteristic, PFT, CF-MRI,DWI scores and ADC.

| Parameters | Controls | RTE | p-value |
|---|---|---|---|
| **Age (years)** | 18.50 (15-31) | 21 (17-36) | 0.3 |
| **Sex (M/F)** | 12/15 | 9/20 | 0.2 |
| **$FEV_1$_6M** | 85.9 (25.4) | 69.7 (21.7) | 0.011* |
| **FVC_6M** | 97.3 (14.2) | 85.7 (14.9) | 0.004* |
| **$FEV_1$–$t_0$** | 88.2 (17.6) | 70.7 (19.5) | 0.001* |
| **FVC_$t_0$** | 98.6 (13.3) | 81.9 (21.8) | 0.01* |
| **$FEF_{25-75}$–$t_0$** | 68.8 (31.8) | 44.2 (23.8) | 0.002* |
| **$FEV_1$–$t_1$** | 88.3 (18.9) | 77.3 (19.5) | 0.036* |
| **FVC_$t_1$** | 96.7 (14.2) | 86.9 (15.6) | 0.016* |
| **$FEF_{25-75}$–$t_1$** | 68.6 (33.4) | 52.6 (27.9) | 0.053 |
| **PEX_$t_0$** | 0 | 4.5 (4.1-5.9) | <0.001* |
| **PEX_$t_1$** | 0 | 1.2 (0-1.2) | 0.1 |
| **CF-MRI_$t_0$** | 16.2 (11-36) | 42 (25-61) | <0.001* |
| **CF-MRI_$t_1$** | 16 (1-34.5) | 39 (18-56) | 0.002* |
| **DWI_$t_0$** | 7 (0-16.7) | 22 (9-26) | 0.002* |
| **DWI_$t_1$** | 9 (0-17.7) | 13 (5-19) | 0.179 |
| **ADC_$t_0$** | 1.55 (1.49-1.64) | 1.26 (1.21-1.46) | <0.001* |
| **ADC_$t_1$** | 1.56 (1.48-1.61) | 1.57 (1.35-1.63) | 0.9 |

Parameters are presented as median (25-75 percentiles) or mean (standard deviation) according variable's distribution. $FEV_1$_6M=forced expiratory volume in 1 second % predicted six months before baseline MRI; FVC_6M=functional vital capacity six months before baseline MRI; $FEV_1$–$t_0$ and $FEV_1$–$t_1$=$FEV_1$ at baseline MRI ($t_0$) and follow-up MRI ($t_1$); FVC_$t_0$ and FVC_t1=functional vital capacity at $t_0$ and at $t_1$; $FEF_{25-75}$–$t_0$ and $FEF_{25-75}$–$t_1$=forced expiratory flow 25-75% at $t_0$ and $t_1$; PEX_$t_0$ and PEX_$t_1$=pulmonary exacerbation score at $t_0$ and $t_1$; CF-MRI_$t_0$ and CF-MRI_$t_1$=cystic fibrosis magnetic resonance imaging score at $t_0$ and $t_1$; DWI_$t_0$ and DWI_$t_1$=Diffusion-weighted imaging total score at $t_0$ and $t_1$; ADC_$t_0$ and ADC_$t_1$= Apparent Diffusion Coefficient at $t_0$ and $t_1$. Significant differences between the groups are indicated by asterisk (*).

## Differences between baseline and follow-up MRI

The RTE group showed significant differences between baseline and follow-up MRI for spirometry, PEX score, CF-MRI score, DWI score and ADC (all p<0·0001). Conversely, no significant differences were found in the control group between baseline and follow-up for all parameters. Table 3 summarizes differences between baseline and follow-up MRI within the groups. Figure 1 shows changes of PEX score, $FEV_1$ and DWI score between the groups in time.

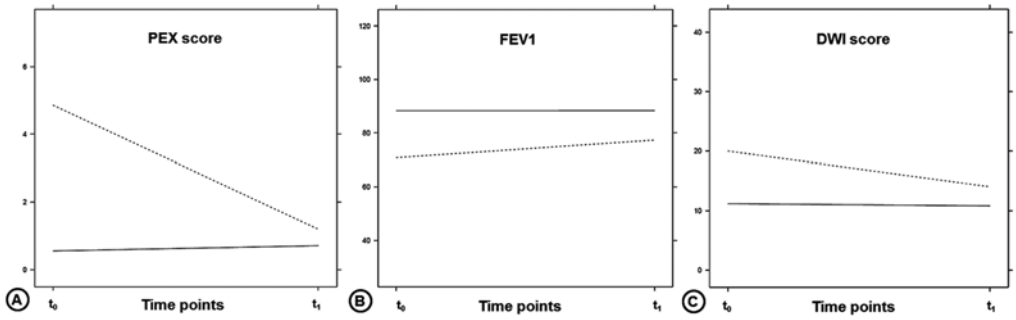


**Figure 1. Changes in (a) pulmonary exacerbation score (PEX), (b) forced expiratory volume in 1 second ($FEV_1$) and (c) total diffusion-weighted imaging score (DWI) between case (dotted lines) and control (continuous lines) groups.** X-axis represents baseline ($t_0$) and follow-up ($t_1$) time points, while the y-axis of each plot represents unit of measure for each variable. Note that RTE group (dotted lines) has significant changes in PEX score, $FEV_1$ and DWI score, while the control group (continuous line) remains stable.

## Correlations

The DWI score had a strong inverse correlation with $FEV_1$ and $FEF_{25-75}$ at baseline ($FEV_1$ r=-0·635; $FEF_{25-75}$ r=-0·611; all p<0.0001) and follow-up ($FEV_1$ r=-0·633; $FEF_{25-75}$ r=-0·626; all p<0.0001). DWI score had a strong positive correlation with PEX score at baseline (r=0·504, p<0.0001), but not at follow-up (r=0·364, p=0.005; not significant after Bonferroni). ADC had a strong negative correlation with PEX score at baseline (r=-0·634, p<0·0001), but not at follow-up (r=-0·43, p=0·766). DWI score had a strong positive correlation with $CFMRI_{TOT}$ at baseline (r=0·809, p<0·0001) and follow-up (r=0·767, p<0·0001).

## ROC curves

Figure 2 shows ROC curves for DWI score and ADC. DWI score had a fair diagnostic accuracy (AUC=0·73, C.I. 0·59-0·86, p=0·003). For the DWI score a cut-off of 14 had a sensitivity of 73% and a specificity of 68%. ADC maps had a good diagnostic accuracy (AUC=0·818, C.I. 0·69-0.94, p<0·0001). For the ADC maps, a cut-off value of $1.45*10^{-3}$ $mm^2/s$ had a sensitivity of 72% and a specificity of 84%.

**Table 3.** Differences in spirometry, clinical and MRI parameters between baseline ($t_0$) and follow-up ($t_1$) MRI.

| Parameters | Controls | | | RTE | | |
|---|---|---|---|---|---|---|
| | Baseline | Follow-up | p-value | Baseline | Follow-up | p-value |
| **$FEV_1$** | 88.2 (17.6) | 88.3 (18.9) | 0.976 | 70.7 (19.5) | 77.3 (19.5) | <0.0001* |
| **FVC** | 98.6 (13.3) | 96.7 (14.2) | 0.33 | 81.9(21.8) | 86.9 (15.6) | <0.0001* |
| **$FEF_{25-75}$** | 68.8 (31.8) | 68.6 (33.4) | 0.948 | 44.2 (23.8) | 52.6 (27.9) | <0.0001* |
| **PEX** | 0 | 0 | 0.805 | 4.5 (4.1-5.9) | 1.2 (0-1.2) | <0.0001* |
| **CMFRI** | 16.2 (11-36) | 16 (1-34.5) | 0.824 | 42 (25-61) | 39 (18-56) | <0.0001* |
| **DWI** | 7 (0-16.7) | 9 (0-17.7) | 0.652 | 22 (9-26) | 13 (5-19) | <0.0001* |
| **ADC** | 1.55 (1.49-1.64) | 1.56 (1.48-1.61) | 0.178 | 1.26 (1.21-1.46) | 1.57 (1.35-1.63) | <0.0001* |

Parameters are presented as median (25-75 percentiles) or mean (standard deviation) according variable's distribution. $FEV_1$=forced expiratory volume in 1 second % predicted; FVC=functional vital capacity; FEF=forced expiratory flow at 25-75%; PEX=pulmonary exacerbation score; CF-MRI=cystic fibrosis magnetic resonance imaging score; DWI=Diffusion-weighted imaging total score; ADC=Apparent Diffusion Coefficient. Significant differences are indicated by asterisk.

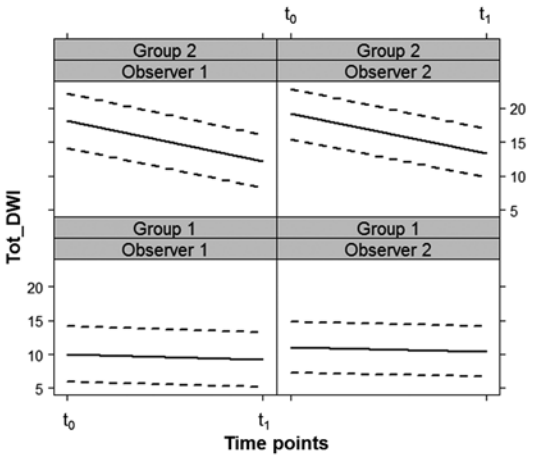


**Figure 2. Receiver operating characteristic (ROC) curve for DWI score (a) and ADC (b).** Note higher diagnostic accuracy of ADC measurements than DWI score to differentiate patient with CF and respiratory tract exacerbation.

## Mixed-model analysis

Mixed-model analysis showed that total DWI score outcome was significantly different between the groups (group: value=13·3, Std. Error (SE)=3·1, p=0·0003) and that it significantly reduced between baseline and follow-up MRI for the RTE group (group*time: value=-5.2, SE=1.4, p=0.0003). There were no significant differences in DWI total score between the observers (observer: value=0·7, SE=1·3, p=0·58). Moreover the trend of DWI total score between baseline and follow-up was the same for both observers (observer*time: value=0·26, SE=0·8, p=0·74). Figure 3 shows effect plots for total DWI score outcome based on the mixed-effects model analysis.

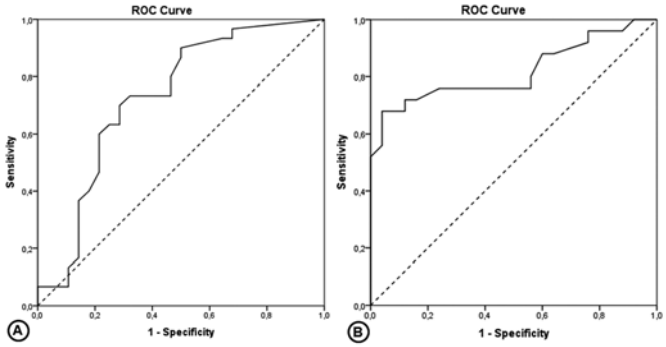


**Figure 3. Effects plots for total diffusion-weighted imaging (DWI) score outcome (Tot_DWI) and "time" covariate.** Each column represents a different observer (observer 1 versus observer (2), while each row represents control (group (1) and RTE (group 2) groups. Y-axis represents total DWI score while x-axis the baseline ($t_0$) and follow-up ($t_1$) time points. Each plot simulates changes in total DWI score between the time points and the groups. Dotted lines are confidence interval lines.



### Reliability of DWI score

Inter-observer agreement at baseline and follow-up MRI was excellent for all sub and total DWI scores: sub-score A (ICC baseline=0·918; ICC follow-up=0·904), sub-score B (ICC baseline=0·895; ICC follow-up=0·873), and total DWI score (ICC baseline =0·904; ICC follow-up=0·877). Also intra-observer agreement was excellent: sub-score A (ICC baseline =0·947; ICC follow-up=0·920), sub-score B (ICC baseline=0·936; ICC follow-up=0·894), and total DWI score (ICC baseline=0·939; ICC follow-up=0·9). Larger variability for both observers was noted at follow-up MRI as shown by lower ICC values compared to baseline. Bland-Altman plots did not show systematic differences between the observers. Bland-Altman plots for inter- and intra-observer agreements are presented as online supplement materials (Figures E3 and E4).

## Discussion

We showed that DWI score and ADC detected the clinical changes related to RTE as determined by the PEX score and spirometry parameters. DWI provides a noninvasive method to quantify pulmonary inflammation in CF patients with RTE, supporting its potential as radiation-free imaging biomarker for lung inflammation to assess therapy efficacy during RTE.

The most interesting observation is that in patients with RTE, following antibiotic treatment, native DWI signal at high b values showed a significant reduction overall (Figure 4). Conversely, in the control group without RTE, no significant differences in DWI signal between baseline and follow-up were observed. This was confirmed both by the DWI score and by the ADC. More importantly these

findings were also confirmed by mixed-model analysis after adjustment of confounders (i.e. observer's score), which showed a different trend of DWI score between baseline and follow-up between groups.

These observations strongly support the concept that DWI can track inflammatory changes over the course of RTE treatment.

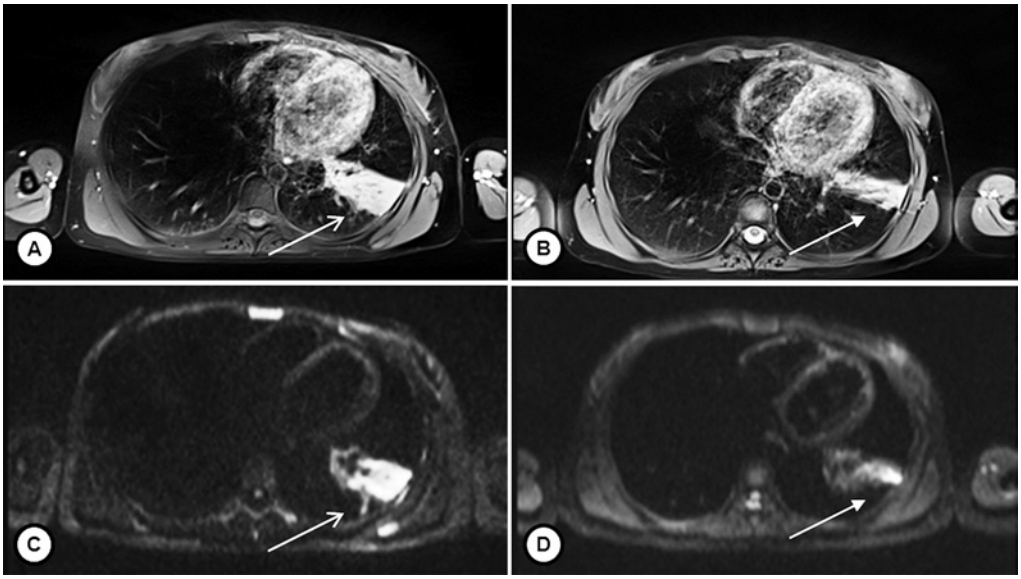


**Figure 4. DWI changes pre (a-c) and post (b-d) RTE treatment in CF patient with respiratory tract exacerbation.** Left column is imaging at baseline and right column is at follow-up. Upper row displays morphological free-breathing BLADE (Siemens) images, while lower row DW images at b=800 mm/s$^2$. Note that left lower consolidation (open arrow in a) with high DWI signal (open arrow in c) became smaller after RTE treatment (close arrow in b) and DWI signal also reduced (close arrow in d).

The second interesting finding is the relationship between CF-MRI and DWI scores. In the RTE group, CF-MRI score was significantly different between baseline and follow-up at the end of treatment. The CF-MRI scores between the RTE and control groups were significantly different at baseline and follow-up. This confirms the findings of prior studies that CF patients with more severe lung disease are at greater risk of developing an RTE [27,28]. Interestingly, DWI score and ADC were significantly different at baseline, but not at follow-up. This difference in DWI can be important to assess the acute changes of RTE. Prior studies have shown limited correlation between inflammatory biomarkers and reversible structural components assessed by chest x-ray and CT [6,29]. For example, a consolidation or mucus plug could remain following antibiotic treatment, while the severity of local inflammation was reduced, or vice versa (Figure 5). The ability of DWI to track acute changes related to RTE could be of value to assess treatment efficacy of RTE and to develop new treatment strategies

for RTE. The sensitivity of the DWI technique may allow such studies to proceed using relatively small number of patients.

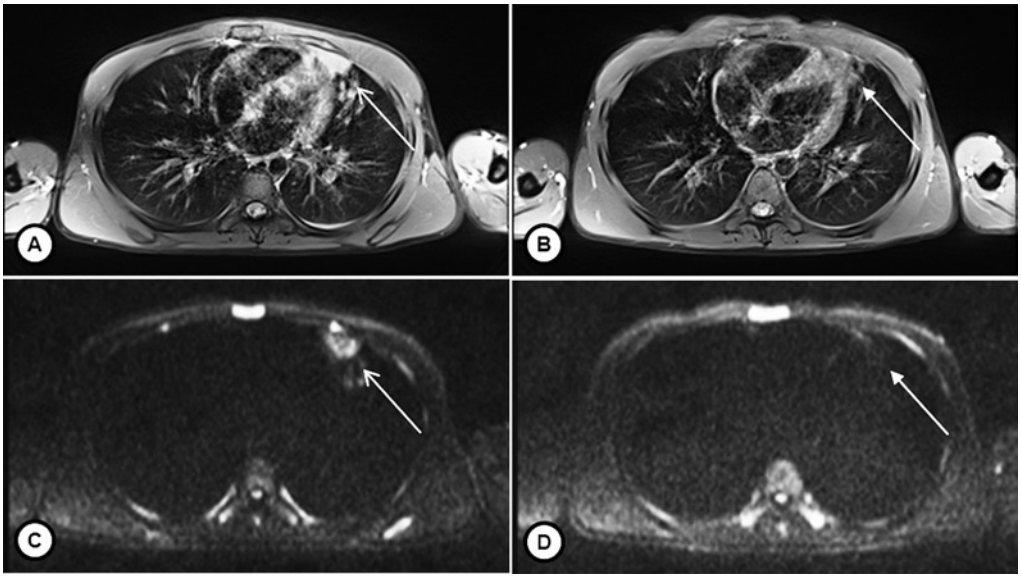


**Figure 5. Relation between morphological and functional lung changes during respiratory tract exacerbations in CF patient.** Left column is imaging at baseline and right column is at follow-up. Upper row contains morphological free-breathing BLADE (Siemens) images (a-b), while lower row are DW images at b=800 mm/s$^2$ (c-d). Note small consolidation in the lingula (open arrow in a) with high DWI signal (open arrow in c). After RTE treatment this consolidation is still present (close arrow in b), but the DWI signal has disappeared (close arrow in d), showing a discordant pattern between morphological and functional images.

The third important finding is the strong positive correlation of DWI and ADC with PEX score and strong negative correlation with $FEV_1$ and $FEF_{25-75}$. Moreover, DWI score and ADC did not correlate with PEX and CF-MRI score at the follow-up scan at the end of treatment. Additionally, CF-MRI score had a stronger correlation with $FEV_1$ than with DWI score. These correlations confirm the discrepancy between structural and functional MR lung changes during RTE, where CF-MRI better reflects the severity of structural lung disease, while DWI reflects more the acute inflammatory changes related to RTE.

The fourth important finding was the fair to good accuracy of DWI score and ADC to differentiate patients with CF treated for a RTE. The better diagnostic performance of ADC than DWI score confirms the superiority of the quantitative assessment provided by ADC map, compared to the semi-quantitative DWI score.

The last noteworthy finding is that both DWI score and ADC are robust parameters with low intra- and inter-observer variability. The strength of our DWI score was also confirmed after adjustment of confounders with mixed-model analysis. This supports the usefulness of our scoring method in clinical trials focused on RTE treatment.

We acknowledge some limitations to this study. Firstly, we did not obtain direct samples of the DWI hotspots which we deemed to be inflammatory. This would have required bronchoscopy, an invasive procedure not routinely performed during RTE in our institution and not standard clinical of care in CF centers. However, the differences between observations in the RTE and control group showed that the DWI signal is often dissociated from the structural changes as quantified by the CF-MRI score. We indeed proved that only the RTE group had significant difference in DWI score and ADC between the baseline and follow-up. Based on our promising results, we aim to perform further validation studies that include BAL to investigate difference between lung areas with and without hotspots and/or pre and post RTE therapy. Another option would be to perform a comparison of the DWI technique with PET-MR. The radiation burden of PET-MR is about 70% lower than PET-CT and will allow a simultaneous comparison between DWI and PET hotspots [30].

Lastly, we acknowledge that this is a single-center study, therefore for further clinical translation, our method needs to be tested in a larger cohort multi-center study. Despite these limitations, this study represents the next important phase towards validating DWI as tool to quantify pulmonary inflammation.

## Conclusions

Our study demonstrated that DWI score and ADC detected the clinical changes of patients with CF treated for a RTE with fair to good accuracy. Moreover, DWI score and ADC were strongly correlated with symptom score and spirometry measures in these patients.

DW-MRI is a noninvasive promising imaging biomarker for a radiation-free quantification of pulmonary inflammation during RTE in the CF population. DWI has potential to assess treatment efficacy during RTE in CF patients and to develop new therapies for RTE treatment.

## Acknowledgements

The authors thank Elizabeth Salamon, department of Respiratory Medicine, Royal Perth Hospital, for offering invaluable detailed advice on grammar and organization of the manuscript. The researchers also wish to express their deepest gratitude to all CF patients who participated in the study.

## Bibliography


1. Tiddens H A WM, Donaldson SH, Rosenfeld M, Paré PD. Cystic fibrosis lung disease starts in the small airways: can we treat it more effectively? Pediatr Pulmonol 2010; 45: 107–17.
2. Tiddens HAWM, Stick SM, Wild JM, et al. Respiratory tract exacerbations revisited: Ventilation, inflammation, perfusion, and structure (VIPS) monitoring to redefine treatment. Pediatr Pulmonol 2015; 50: S57–65.
3. Bhatt JM. Treatment of pulmonary exacerbations in cystic fibrosis. Eur. Respir. Rev. 2013; 22: 205–16.
4. de Jong P A, Lindblad A, Rubin L, et al. Progression of lung disease on computed tomography and pulmonary function tests in children and adults with cystic fibrosis. Thorax 2006; 61: 80–5.
5. Eichinger M, Heussel C-P, Kauczor H-U, Tiddens H, Puderbach M. Computed tomography and magnetic resonance imaging in cystic fibrosis lung disease. J Magn Reson Imaging 2010; 32: 1370–8.
6. Greene KE, Takasugi JE, Godwin JD, Richardson ML, Burke W, Aitken ML. Radiographic changes in acute exacerbations of cystic fibrosis in adults: a pilot study. AJR Am J Roentgenol 1994; 163: 557–62.
7. Tiddens H A WM, Stick SM, Davis S. Multi-modality monitoring of cystic fibrosis lung disease: The role of chest computed tomography. Paediatr Respir Rev 2013; : 1–6.
8. Kuo W, Ciet P, Tiddens H A WM, Zhang W, Guillerman RP, van Straten M. Monitoring cystic fibrosis lung disease by computed tomography. Radiation risk in perspective. Am J Respir Crit Care Med 2014; 189: 1328–36.
9. Cohen-Cymberknoh M, Kerem E, Ferkol T, Elizur A. Airway inflammation in cystic fibrosis: molecular mechanisms and clinical implications. Thorax 2013; 68: 1157–62.
10. Amin R, Charron M, Grinblat L, et al. Cystic Fibrosis: Detecting Changes in Airway Inflammation with FDG PET/CT. Radiology. 2012; 264: 868–75.
11. Belessis Y, Dixon B, Hawkins G, et al. Early cystic fibrosis lung disease detected by bronchoalveolar lavage and lung clearance index. Am J Respir Crit Care Med 2012; 185: 862–73.
12. Keen C, Gustafsson P, Lindblad a, Wennergren G, Olin a-C. Low levels of exhaled nitric oxide are associated with impaired lung function in cystic fibrosis. Pediatr Pulmonol 2010; 45: 241–8.
13. Wielpütz MO, Puderbach M, Kopp-Schneider A, et al. Magnetic Resonance Imaging Detects Changes in Structure and Perfusion, and Response to Therapy in Early Cystic Fibrosis Lung Disease. Am J Respir Crit Care Med 2014; : 1–49.
14. Attariwala R, Picker W. Whole body MRI: Improved lesion detection and characterization with diffusion weighted techniques. J Magn Reson Imaging 2013; 38: 253–68.
15. Luna A, Sánchez-Gonzalez J, Caro P. Diffusion-weighted imaging of the chest. Magn Reson Imaging Clin N Am 2011; 19: 69–94.
16. Deng Y, Li X, Lei Y, Liang C, Liu Z. Use of diffusion-weighted magnetic resonance imaging to distinguish between lung cancer and focal inflammatory lesions: a comparison of intravoxel incoherent motion derived parameters and apparent diffusion coefficient. Acta radiol 2015; 0: 1–8.
17. Milito C, Pulvirenti F, Serra G, et al. Lung magnetic resonance imaging with diffusion weighted imaging provides regional structural as well as functional information without radiation exposure in primary antibody deficiencies. J Clin Immunol 2015; 35: 491–500.
18. Ciet P., Serra G., Andrinopoulou E.A. et al. Diffusion weighted imaging in cystic fibrosis disease: beyond morphological imaging. Eur Radiol. February 2016
19. Laszlo G. Standardisation of lung function testing: helpful guidance from the ATS/ERS Task Force. Thorax 2006; 61: 744–6.
20. Rosenfeld M, Emerson J, Williams-Warren J, et al. Defining a pulmonary exacerbation in cystic fibrosis. J Pediatr 2001; 139: 359–65.
21. Ciet P, Serra G, Bertolo S, et al. Assessment of CF lung disease using motion corrected PROPELLER MRI: a comparison with CT. Eur Radiol 2015; 26: 780–7.

22. Liu H, Liu Y, Yu T, Ye N. Usefulness of diffusion-weighted MR imaging in the evaluation of pulmonary lesions. Eur Radiol 2010; 20: 807–15.

23. Uto T, Takehara Y, Nakamura Y, et al. Higher sensitivity and specificity for diffusion-weighted imaging of malignant lung lesions without apparent diffusion coefficient quantification. Radiology 2009; 252: 247–54.

24. Hagmann P, Jonasson L, Maeder P, Thiran J, Wedeen VJ, Meuli R. Central Nervous System: State of the art Understanding Diffusion MR Imaging Techniques : From Scalar Imaging to Diffusion. Radio Graph 2006; 26: 205–24.

25. Cohen J. Statistical Power Analysis for the Behavioral Sciences. Routledge; 2 edition, 1988.

26. Pines, Jesse M.; Carpenter, Christopher R.; Raja, Ali S. ; Schuur JDS. Evidence-Based Emergency Care: Diagnostic Testing and Clinical Decision Rules, 2nd Edition Wiley.

27. Loeve M, Gerbrands K, Hop WC, Rosenfeld M, Hartmann IC, Tiddens H A W M. Bronchiectasis and pulmonary exacerbations in children and young adults with cystic fibrosis. Chest 2011; 140: 178–85.

28. Sanders DB, Li Z, Brody AS. Chest computed tomography predicts the frequency of pulmonary exacerbations in children with cystic fibrosis. Ann Am Thorac Soc 2015; 12: 64–9.

29. Dakin CJ, Pereira JK, Henry RL, Wang H, Morton JR. Relationship between sputum inflammatory markers, lung function, and lung pathology on high-resolution computed tomography in children with cystic fibrosis. Pediatr Pulmonol 2002; 33: 475–82.

30. Kanal E, Barkovich A J, Bell C, et al. ACR guidance document on MR safe practices: 2013. J Magn Reson Imaging 2013; 37: 501–30.

# Supplementary Material

## Methods

This was a cross-sectional observational study of patients with cystic fibrosis (CF) with and without respiratory tract exacerbation (RTE). All subjects with RTE attended on a two occasions, whilst admitted for RTE (baseline) and after antibiotic therapy (follow-up), and underwent a series of clinical, lung function and radiological examinations during the same visit. Similarly, control subjects repeated the study protocol over the same median time gap as the RTE group. Visits took place between September 2011-September 2013. Parents/guardians signed informed consent and paediatric subjects provided assent.



## Patient selection

### Respiratory tract exacerbation group

No universally accepted definition of a respiratory tract exacerbation (RTE) exists. A general definition, described as "clinical need for additional treatment as indicated by acute changes in clinical parameters", has been recently adopted by the Eurocare CF Working Group [1]. These acute changes during RTE include: change in sputum; increased cough; increased malaise; fatigue or lethargy; anorexia or weight loss; decrease in spirometry outcomes by 10% or more or radiographic changes; and increased dyspnea. These changes are also used by the Rosenfeld criteria to score the clinically likelihood of RTE in patient with CF (Table E1) [2]. All subjects enrolled in the study were scored with the Rosenfeld criteria for RTE both at baseline at follow-up in.

**Table E1.** Rosenfeld criteria for respiratory tract exacerbations.

| Rosenfeld Criteria | PEX scoring system |
|---|---|
| – Reduced exercise tolerance | – Each criterion is assigned a coefficient |
| – Increased cough | – PEX score is the sum of the coefficient per each criterion when present |
| – Increased sputum/cough congestion | – Threshold value to define RTE is 2.6 |
| – School or work absenteeism | |
| – Increased adventitial sounds on lung examination | |
| – Reduced appetite | |
| – Reduced $FEV_1$ (≥10% predicted) | |

PEX=pulmonary exacerbation scoring system, RTE=respiratory tract exacerbation, $FEV_1$=Forced expiratory volume in 1 sec.

### Clinically stable CF patients – Control group

Clinically stable patients with CF were asked to participate to the study at the annual follow-up visit. Clinically stability was defined when patient had no signs or symptoms of RTE in the previous 6 month to the visit. Each control subject was selected after inclusion of an RTE group subject and matched for age, sex, and mean of $FEV_1$ in the previous 6 months before the visit.

### Study protocol

The study protocol consisted of clinical examination, spirometry and magnetic resonance imaging (MRI). Each RTE subject performed the study protocol at admission (baseline) and after antibiotic treatment (follow-up). Each control subject performed the study protocol twice with the similar median time gap (~20 days) of RTE subjects.

### Clinical examination

Clinical examination started with collection of recent patient history, in particular variation on coughing, amount and color of sputum, dyspnea, exercise tolerance, and work or school absenteeism. Physical exam consisted of heart and respiratory rate measurements, $O_2$ saturation, weight and height recording for body mass index measurement, oral and ear inspection, cardiac and lung auscultation. During the clinical examination, was also performed the PEX score to define whether the subject with CF had or not RTE.

### Spirometry

Repeated spirometry efforts were performed until 3 acceptable maximal maneuvers were obtained according to "ATS/ERS guidelines" using a Masterscope (Jaeger-Carefusion, Hochberg, Germany) spirometer [3]. When spirometry traces showed evidence of incomplete expiration, cough, and air leak were repeated. Acceptable repeatability was obtained when the difference between the largest and next largest maneuvers was ≤100 ml or 5% depending on which was the larger value. The recorded result for Forced expiratory volume in 1 second ($FEV_1$) and forced vital capacity (FVC) was the highest achieved across all technically correct efforts, with the ratio calculated from this $FEV_1$/FVC and reduction in forced expiratory flow at 25-75% of the FVC ($FEF_{25-75}$) were expressed as % of predicted value.

### MRI

MRI was performed at 1.5 Tesla (MAGNETOM Avanto, Siemens Healthcare, Erlangen, Germany) using morphological and functional sequences.

Morphological sequences included axial and coronal end-expiratory triggered Periodically Rotated Overlapping ParallEL Lines with Enhanced Reconstruction (PROPELLER; SIEMENS brand name, BLADE) with proton density (PD) weighting (TR/TE/alpha/TA: 710/26 ms/150°/4' 25", voxel size 1 x 1 x 6 $mm^3$; bandwidth 601 Hz/pixel, slice gap 0 mm, average n=4) [4], and breath-hold spirometry gated axial and coronal steady state free precession (SSFP; SIEMENS brand name, TrueFISP) with

$T_2/T_1$ weighting (TR/TE/alpha/TA: 229/0.99 ms/66°/14", voxel size 2.3x2.3x6 $mm^3$; bandwidth 1291 Hz/pixel, slice gap 0 mm, average n=1).

The functional data were acquired in the axial plane using a diffusion-weighted (DW) single shot echo-planar imaging (EPI) sequence prototype (TR/TE=4800 ms/54ms, voxel size 2.5x2.5x6 $mm^3$; bandwidth 1644 Hz/pixel, slice gap 1.8 mm, average n=3) with end-expiratory triggering. Eleven b-values at different time intervals (0, 10, 20, 30, 50, 70, 100, 150, 200, 400, 800 s/$mm^2$) were acquired in three orthogonal directions. The entire MRI scan required approximately 25-30 min.

### Image analysis

Image analysis was conducted using the picture archiving and communication system (PACS) SYNAPSE (Fujifilm Healthcare Europe, Dusseldorf, Germany). MRI images were anonymized and evaluated in random order by two radiologists (V.T. and S.B.), with 4 and 8 years of experience in thoracic MRI scoring respectively. Both radiologists were blinded to any clinical information and to each other's MRI assessment.



### Morphological scoring system: CF-MRI scoring system

Morphological images BLADE and TrueFISP were scored with the Cystic Fibrosis MRI scoring system (CF-MRI), a scoring system derived from the Brody scoring system and adapted to MRI [4,5]. This scoring system evaluates the five lung lobes and lingula as the sixth lobe. The CF-MRI scores assess the following components: bronchiectasis, mucus plug, parenchymal changes (atelectasis, consolidation, ground-glass), trapped air. Differently from CT, air wall thickening is combined with bronchiectasis in the CF-MRI, because of the lower spatial resolution of MRI [4]. For the same reason, the pattern of trapped air is not scored in CF-MRI, as this has previously been shown to be unreliable [4]. A composite score for each component is calculated and expressed as a percentage of a maximum score, on a 0-100 scale. The higher the score the more severe the disease.

## Diffusion Weighted Imaging (DWI) Analysis

### DW images and Apparent Diffusion Coefficient (ADC) maps: qualitative and quantitative analysis

The sensitivity of the DWI technique to water motion depends on scanner's parameters, which are summarized by the b-value, expressed as sec/mm [6,7]. Water molecules with a large degree of motion (i.e. fluid) will have a fast DWI signal decay with high b-values. Conversely, slow-moving water molecules show a lower DWI signal decay with large b-values. DWI is typically performed using at least two b values to enable meaningful interpretation [8]. The interpretation of the relative attenuation of DWI signal intensity on images obtained at different b values, allows the analysis of different tissue components. For instance, in a tumor with cystic and solid components, the cystic portion will show greater signal decay on high b-value images because water diffusion is less restricted.

By contrast, the more cellular solid portion will show relatively high signal intensity at high b-value [8]. Therefore, in case of tumors and inflammation high DWI signal (bright) can be visually assessed at high b-values. However, this qualitative visual assessment is limited by the T2 shine-through artefact, where tissues with long T2-relaxation time have high DWI signal at high b-value, despite normal water diffusion [7]. This potential source of error can be eliminated by using an apparent diffusion coefficient ADC map, which is an average image obtained by DWI signal at different b-values. Areas of restricted diffusion in highly cellular tissue have low ADC values compared with less cellular areas that return higher ADC values. It is important to notice that areas of restricted diffusion will appear as low-signal intensity areas (dark) on ADC map, and as high-signal intensity areas (bright,) on DW images (opposite to ADC maps). Hence, ADC maps are complementary to DW images for a correct interpretation of DWI signal.

**Table E2.** DW imaging analysis.

| Parameter | Score |
|---|---|
| **Presence of hotspot** | – Score 1: presence of hotspots greater than 5% of lobe volume |
| | – Score 0: no hotspot |
| **Extension** | – Score 1: hotspots occupying a volume smaller than 33% of the lobe |
| | – Score 2: hotspots occupying a volume between 33% and 67% of the lobe |
| | – Score 3: hotspots occupying a volume greater than 67% of the lobe |
| **Signal Intensity (SI) dominant hotspot** | – Score 1: SI hotspots greater than SI cord spine |
| | – Score 0: SI hotspots smaller than SI cord spine |
| **Mean signal intensity ($SI_{mean}$)** | – Score 1: mean SI hotspots within a lobe is greater than SI of cord spine |
| | – Score 0: mean SI hotspots within a lobe is smaller than SI of cord spine |
| **Sub-score A** | – A=(E + SI) |
| **Sub-score B** | – B=(E + $SI_{mean}$) |
| **Total DWI score (DWI)** | – DWI=P+A+B |

DW images were scored using a semi-quantitative scoring system which assesses each lobe using the following parameters: presence of hotspot (P), extension of hotspot (E), signal intensity of the dominant hotspot (SI) and average signal intensity of the hotspots within a lobe ($SI_{mean}$). For each lobe, we obtained two sub-scores: A=(E + SI) and B=(E + $SI_{mean}$). The total DWI score is the sum of P + A + B, and the maximum possible score is 54. The DW images with the highest b-value (b= 800mm/$sec^2$) were scored.

In this study, we combined a semi-quantitative scoring system to score DW images and quantitative measurement performed on ADC maps. The DWI scoring system presented in table E2 describes how the lesions with high-signal intensity on DW images with high b value, defined as hotspots, were quantified. This method proved to be reliable in previous studies, with high sensitivity and specificity [9-12].

ADC map were used to objectively quantify diffusion in those dominant pulmonary lesions, which showed restricted diffusion at high b-values [13]. A region-of-interest (ROI) of the same size and location was positioned in these dominant lesions with restricted diffusion on ADC maps, on both baseline and follow-up MRI. Adjacent vessels and areas with susceptibility artifact caused by air-tissue interface were excluded from image analysis.

## Results

### Score reliability

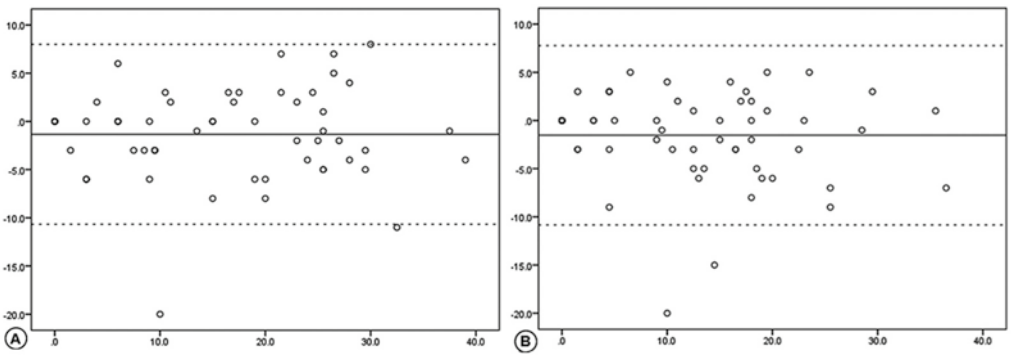


**Figure E3. Inter-observer agreement for total DWI score.** Bland-Altman plot of inter-observer agreement (observer 1 versus observer (2) at (a) baseline and (b) follow-up MRI. Note that mean differences are close to zero and that all observations are around the mean.

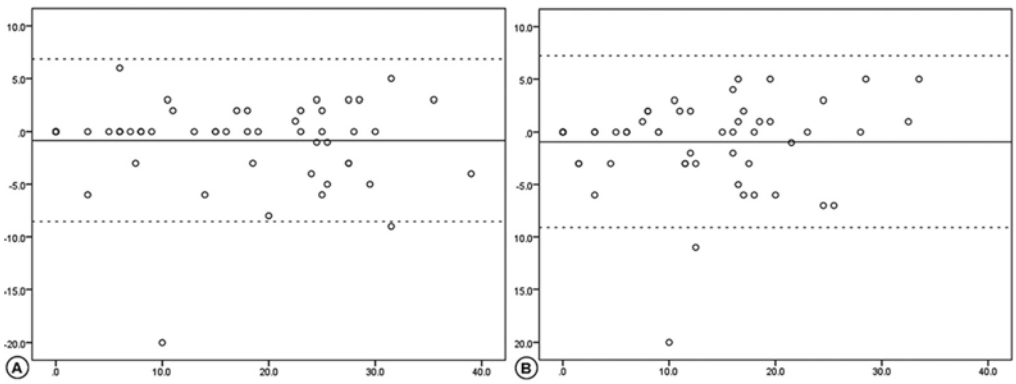


**Figure E4. Intra-observer agreement for total DWI score.** Bland-Altman plot of intra-observer agreement (observer 1, one month time gap between scores) at (a) baseline and (b) follow-up MRI. Note that mean differences are close to zero and that all observations are around the mean.

## Bibliography


1. Bilton D, Canny G, Conway S, et al. Pulmonary exacerbation: Towards a definition for use in clinical trials. Report from the EuroCareCF Working Group on outcome parameters in clinical trials. J Cyst Fibros 2011; 10: S79–81.
2. Rosenfeld M, Emerson J, Williams-Warren J, et al. Defining a pulmonary exacerbation in cystic fibrosis. J Pediatr 2001; 139: 359–65.
3. Laszlo G. Standardisation of lung function testing: helpful guidance from the ATS/ERS Task Force. Thorax 2006; 61: 744–6.
4. Ciet P, Serra G, Bertolo S, et al. Assessment of CF lung disease using motion corrected PROPELLER MRI: a comparison with CT. Eur Radiol 2015; 26: 780–7.
5. Tepper L A., Ciet P, Caudri D, Quittner AL, Utens EMWJ, Tiddens H A. WM. Validating chest MRI to detect and monitor cystic fibrosis lung disease in a pediatric cohort. Pediatr Pulmonol 2015; : n/a – n/a.
6. Qayyum A. Diffusion-weighted Imaging in the Abdomen and Pelvis: Concepts and Applications1. RadioGraphics 2009; 29: 1797–810.
7. Chavhan GB, Alsabban Z, Babyn PS. Diffusion-weighted Imaging in Pediatric Body MR Imaging: Principles, Technique, and Emerging Applications. Radiographics 2014; 34: E73–88.
8. Koh D, Collins DJ. Diffusion-Weighted MRI in the Body: Applications and Challenges in Oncology. Am J Roentgenol 2007; 188: 1622–35.
9. Uto T, Takehara Y, Nakamura Y, et al. Higher sensitivity and specificity for diffusion-weighted imaging of malignant lung lesions without apparent diffusion coefficient quantification. Radiology 2009; 252: 247–54.
10. Ciet P, Serra G, Andrinopoulou ER, et al. Diffusion weighted imaging in cystic fibrosis disease: beyond morphological imaging. Eur Radiol 2016; published online Feb 12. DOI:10.1007/s00330-016-4248-z.
11. Liu H, Liu Y, Yu T, Ye N. Usefulness of diffusion-weighted MR imaging in the evaluation of pulmonary lesions. Eur Radiol 2010; 20: 807–15.
12. Tanaka R, Horikoshi H, Nakazato Y, et al. Magnetic resonance imaging in peripheral lung adenocarcinoma: correlation with histopathologic features. J Thorac Imaging 2009; 24: 4–9.
13. Attariwala R, Picker W. Whole body MRI: Improved lesion detection and characterization with diffusion weighted techniques. J Magn Reson Imaging 2013; 38: 253–68.

# Chapter 6

## Mosaic Pattern in Cystic Fibrosis Lung Disease: Trapped Air or Hypoperfusion?

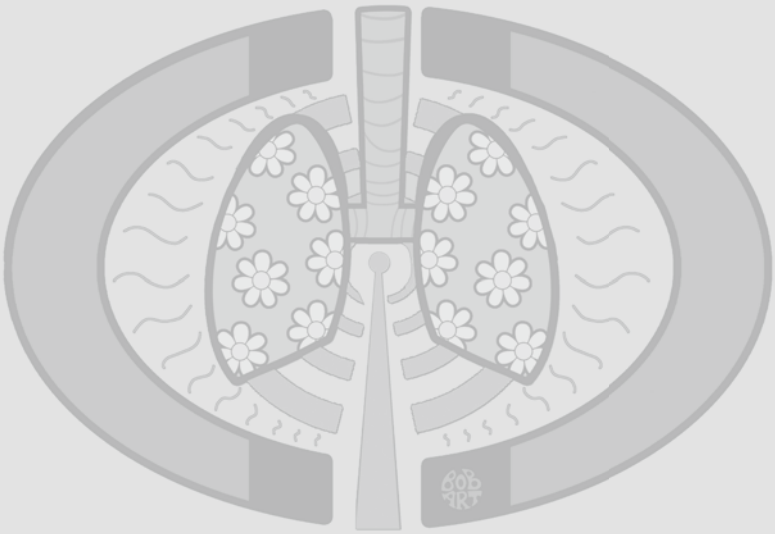

*Ciet P, Wielopolski P, Li S, Andrinopolou EA, van Der Wiel E, Morana G, Tiddens HAWM*

Submitted

## Abstract

**Objectives**: To compare trapped air (TA) on MRI ($MRI_{TA}$) to TA on chest CT in the year before ($CT_{TA\text{-}pre}$) and after ($CT_{TA\text{-}post}$) the MRI, and to regions of hypoperfusion (HP) on contrast-enhanced chest MRI ($CEMRI_{HP}$) and to pulmonary function tests (PFT).

**Methods**: During their annual examination patients with CF underwent MRI, CEMRI spirometry and plethysmography. CEMRI was scored for TA and HP and CT for TA using CF-MRI and CF-CT scoring systems. Descriptive statistics were used to compute the extent of TA and HP and Pearson test to assess association between TA, HP and PFT parameters.

**Results**: Twenty-six patients were enrolled (mean 14 years, range 8-18, 11 female). TA and HP were observed in 12/24 (50%) and 17/24 (71%) patients respectively. $MRI_{TA}$ correlated with $CT_{TA\text{-}pre}$, ($r=0.54$, $p=0.008$), $CEMRI_{HP}$ ($r=0.66$, $p<0.0001$), and $FEF_{75}$ ($r=-0.54$, $p=0.006$). $MRI_{TA}$ was smaller compared to $CT_{TA\text{-}pre}$, and $CT_{TA\text{-}post}$ ($z=-3.52$; $p<0.0001$). $MRI_{TA}$ was not significant different from TA as established by plethysmography ($z=-1.154$; $p=0.24$). $CEMRI_{HP}$ was significantly larger than $MRI_{TA}$ ($p=0.008$).

**Conclusions**: TA as observed on CT and MRI is a mix of TA and HP. For CT the term TA can be better replaced by low-attenuation region (LAR) and for MRI by low-intensity region (LIR).


**Keywords**: magnetic resonance imaging, perfusion magnetic resonance imaging, pulmonary function tests, trapped air, hypoperfusion, mosaic pattern.

**Key points**

1. Hypoperfusion is more frequent and significantly larger than trapped air
2. For CT and MRI the term trapped air is a misnomer
3. 'Trapped air' on CT can better be named low-Attenuation Region (LAR)
4. 'Trapped air' on MRI can better be named Low-Intensity Regions (LIR)
5. LAR on expiratory CT is larger than LIR on expiratory MRI
6. The role of HP and potential therapies should be further investigated

## Introduction

Regions of low attenuation as detected on chest computed tomography (CT) scans are a common finding of cystic fibrosis (CF) lung disease [1]. These regions are present in early stage CF lung disease and often match areas of structural changes [2]. Radiologists described these regions with the term mosaic pattern, which can represent either trapped air (TA) or hypoperfusion (HP) due to hypoxic vasoconstriction [3]. It is also recognized that low attenuation regions can be a mix of HP with or without TA [4].

Traditionally, TA has been quantified using pulmonary function tests (PFT) using body plethysmography and helium dilution tests. Unfortunately, these techniques have not been well validated [5,6]. Clearly, PFT are not able to detect HP. Using chest CT in combination with a contrast agent, we can measure the contribution of TA and HP to the observed regions of low attenuation. However, contrast agent is not routinely administered by those CF centers, which have included chest CT as a routine examination in the annual CF follow-up [7]. The main reason for this is the 1.5 times higher radiation exposure needed for a perfusion CT study compared to a standard chest-CT [8] as well as the risk to adverse reaction to contrast agents [9]. Over the last decades, chest MRI has been developed as alternative technique to assess CF lung disease [10]. By administration of gadolinium-based contrast agents, perfusion can be assessed with contrast-enhanced magnetic resonance imaging (CEMRI) techniques [11]. In addition, MRI can also be used to detect TA, by using expiratory scans with short or ultra-short echo-time (TE) sequences [12,13]. Therefore, MRI allows to visualize both TA and HP in a single session without the use of ionizing radiation [14]. A disadvantage of using gadolinium-based contrast agents for routine chest MRI protocol in CF, is that it introduces a small risk related to the use of the contrast agent [15]. The importance of acquiring both ventilation and perfusion information in CF lung disease has recently been highlighted as a novel biomarker to assess therapy efficacy of respiratory tract exacerbations [16]. Before CEMRI can be recommended, the diagnostic advantage over PFT and CT should be further investigated. To date, no study has directly correlated PFT estimates of TA to CT and MRI estimates of TA and to HP as assessed by CEMRI [4,16-18].

The main aims of this study were: 1) to compare TA on expiratory MRI ($MRI_{TA}$) to TA on chest CT performed in the year before ($CT_{TA\text{-}pre}$) and after ($CT_{TA\text{-}post}$) the MRI, and 2) to establish the contribution of HP using CEMRI ($CEMRI_{HP}$) to regions of $MRI_{TA}$ and 3) to compare $MRI_{TA}$ and $CEMRI_{HP}$ regions to PFT parameters of TA and small airways disease.

## Materials and Methods

This cross-sectional prospective single centre study was approved by the ethical committee of the Erasmus MC (MEC 2007-289). Patients with CF in the Erasmus MC Sophia Children's Hospital

have a biennial chest CT starting at the age of 1 year and a biennial chest MRI starting at the age of 8 years. Those patients, who were scheduled for their annual examination that included a routine biennial MRI, were informed about the study at least three weeks before the annual examination, and informed consent was obtained the day of the visit. For this study, CEMRI was added to the routine MRI protocol. Inclusion and exclusion criteria are presented as online supplement material in Table 1E.

### Physical examination, blood sample, and PFT

On the day of the annual visit, each patient underwent physical examination, weight and height measurements, PFT, microbiology, and blood withdrawal for blood chemistry and hematology. For the purpose of the study the blood withdrawal was executed using an indwelling peripheral intravenous catheter that was left in place after the withdrawal for later contrast agent infusion.

Before the MRI, each study patient performed spirometry test according to "ATS/ERS guidelines [19] during sitting and supine positions using a spirometer (Masterscope, CareFusion, Houten, The Netherlands). Each patient was instructed on how to perform the breathing manoeuvres needed during the scans. The following forced expiratory flows and volumes were recorded: forced vital capacity (FVC), forced expiratory volume in 1 second % predicted ($FEV_1$), forced expiratory flow at 75% ($FEF_{75}$). Additionally, Total Lung Capacity (TLC) was measured using whole body plethysmography ($TLC_{bb}$,) and helium dilution ($TLC_{He}$) [20]. Using these techniques we computed $TA_{BB\text{-}He}$ using the formula $TLC_{BB}$-$TLC_{He}$/$TLC_{BB}$. The PFT protocol took approximately 30 minutes.

### MRI, CEMRI and CT protocols

MR images were acquired in a 1.5 T Signa Hdxt MRI (General Electric Healthcare, Milwaukee, WI, USA) using the whole body coil for radiofrequency excitation and an eight-channel torso coil for signal reception. The protocol consisted of unenhanced and Gd-enhanced images with administration of gadopentetate dimeglumine (Magnevist, Bayer Schering Pharma, Berlin, Germany), 0.2 mL/kg at 2 ml/sec followed by 20 ml saline flush. Non-contrast images included 2D steady-state free precession (SSFP) sequences at end-inspiration and end-expiration in the axial, coronal and sagittal planes. Scan parameters have been previously reported [21].

CEMRI consisted of end-expiratory 3D spoiled gradient echo (SPGR) sequence with time resolved imaging of contrast kinetics (TRICKS) platform and the following scan parameters: TR/TR/$\alpha$=2.1ms/1ms/12°, bandwidth=63.84 MHz, averages=0.5, in plane resolution=1.4x2.3 mm, slice thickness=5 mm, and average temporal resolution of 1.5 sec per phase (40 phases in 60 sec). The MRI protocol lasted about 35 minutes.

CT volumetric inspiratory and expiratory images were acquired using a 6-slice multi-detector CT scanner (Somaton Emotion, Siemens Medical Solutions, Erlangen, Germany). CT scan parameters

are described in Table 2E of the online supplement. CT scans were performed with spirometry control [22].

## Imaging Analysis

All MR and CT images were anonymized and scored in random order in the Advantage Windows Server (General Electric Healthcare, Milwaukee, WI, USA) imaging platform. For the purpose of this study we used two scoring systems. The first observer, with 7 years of experience in chest scoring, scored separately MRI and CEMRI scans using the CF-MRI scoring system, which is an adapted version of the CF-CT scoring system that was used in previous studies [23,24]. The use of the CF-MRI scoring system allows comparing CF related findings between the CT and MRI images.

To compare the extent of TA and HP between MRI and CT, the first observer scored TA on CT images obtained in the year prior ($CT_{TA\text{-}pre}$) and after ($CT_{TA\text{-}post}$) the MRI using the CF-CT scoring system [25,26]. It is well recognized that the total volume of TA on chest CT does not change significantly over a two-year interval [27]. However, the pattern of TA can change of this time interval. For the purpose of this study, we scored only the extent of TA on expiratory CTs ($CT_{TA}$) to match the CF-MRI TA sub-score ($MRI_{TA}$) [27]. $CT_{TA}$ was scored in 8 mm axial reformats, to match slice thickness of MR images, using sharp kernel (B70s) and standard window setting: window width=1500 Hounsfield Unit (HU) and window length=-450 HU. All score and sub-scores were expressed as a percentage of the maximum possible score, ranging from 0 (no pathological findings) to 100 % (maximum severity).

A second observer, with 3 years of experience in chest scoring, scored simultaneously MRI and CEMRI scans using the newly developed PatteRn OverlaPping Rotterdam (PROPeR) scoring system to determine if HP as depicted by CEMRI was larger, equal or smaller than TA as depicted by MRI. In short, the PROPeR scoring system overlaps the end-expiratory MRI with CEMRI by using imaging registration techniques, which allow scoring per lobe of the differences between TA and HP ($TA/HP_{lobe}$). For instance, when the extent of HP is 0-25 % larger than the extent of TA a score of 1 is assigned; vice versa a score of -1 is assigned when TA is 0-25% larger than HP. When HP overlaps TA, a score of zero is assigned.

The first and second scorers were blinded for each other's scores. A more detailed description of both MRI scoring systems is available in the online supplement (Table 3E-4E and Figure 1E-3E).

## Statistics

Descriptive statistics were used for patient characteristics and to describe the extent of $MRI_{TA}$, $CT_{TA}$ and $CEMRI_{HP}$. Intra-observer variability of the $MRI_{TA}$ and $CEMRI_{HP}$ were evaluated with Intraclass Correlation Coefficient (ICC) and Bland-Altman plots. ICC values of <0.20, 0.21-0.40, 0.41-0.60, 0.61-0.80 and 0.81-1 are generally considered to represent poor, fair, moderate, good and very good observer variability, respectively [28]. The $MRI_{TA}$ was compared to $CEMRI_{HP}$ using Wilcoxon test for paired samples. In addition, the observer evaluated independently using the PROPeR scoring system,

pairs of CT and MRI scans without patient identifiers to evaluate whether $CT_{TA}$ was more, the same or less relative to $MRI_{TA}$ and $CEMRI_{HP}$.

Finally, Spearman test was used to correlate $MRI_{TA}$, $CT_{TA}$, $CEMRI_{HP}$, and PFT parameters. According to Cohen's criteria correlations with an r between 0.10 and 0.29 are considered weak, between 0.30 and 0.49 moderate and above 0.50 as strong [29]. Statistical analyses were performed using SPSS version 20.0 for windows. Continuous variables are displayed as mean (±Standard Deviations) or median (interquartile range) depending on data distribution. P-values less than 0.05 (two tailed) were considered statistically significant. Multiple correlations were adjusted using Bonferroni correction.

## Results

Fifty-nine patients with CF were asked to participate in the study. Thirty-three declined to participate in the study primarily because of the required contrast injection. Twenty-six consecutive patients were enrolled in the study (mean 14 years, range 8-18 years, 11 female). Two patients were excluded for incomplete MRI data (no contrast administration), and 3 patients for incomplete CT data (no expiratory CT), so eventually twenty-one patients with CF were included for data analysis (median age 14 years, range 8-17 years, 9 females). Patients' PFT, MRI, CEMRI and CT scores are summarized in Table 1.

**Table 1.** Patients' characteristics and MRI, CEMRI and CT sub-scores.

| Parameters | Value |
|---|---|
| **FVC** | 92.35% (81.7-108.7) |
| **$FEV_1$** | 89.65% (74.4-101.5) |
| **$FEF_{25-75}$** | 51.4% (35.5-70.1) |
| **$TLC_{bb}$-$TLC_{he}$** | 0.14±0.7 |
| **$TLC_{bb}$-$TLC_{he}$/$TLC_{bb}$** | 3.81±15.88 % |
| **$MRI_{TA}$** | 2.78 (0-23.6) % |
| **$CEMRI_{HP}$** | 6.9 (0-33.3) % |
| **$CT_{TA\text{-}pre}$** | 22.2 (16.6-55.5) % |
| **$CT_{TA\text{-}post}$** | 33.3 (16.6-50) % |

All data are presented as mean±2SD or median (interquartile range) according data distribution. FVC=Forced vital capacity percentage of predicted; $FEV_1$=Forced Expiratory Volume in 1 sec percentage of predicted; $FEF_{75}$=Forced expiratory Flow at 75 % percentage of predicted; $TLC_{bb}$=Total lung capacity measured with body-box technique; $TLC_{he}$=TLC measured with helium-dilution technique; $MRI_{TA}$=Magnetic Resonance Imaging trapped air score, $CEMRI_{HP}$= Contrast Enhanced MRI hypoperfusion score; $CT_{TA\text{-}pre}$=Computed Tomography TA score of CT performed 1 year before MRI, $CT_{TA\text{-}post}$=CT-TA score of CT performed 1 after MRI. MRI and CT scores are all presented as percentage of the maximum score, ranging from 0 (no TA or HP) to 100 (TA or HP).

### Extent of Trapped Air and Hypoperfusion on MRI, CT and PFT

$MRI_{TA}$ was detected in 12/24 (50%) patients, while $CEMRI_{HP}$ in 17/24 (71%). $CT_{TA\text{-}pre}$ was detected in 17/23 patients (74%), and $CT_{TA\text{-}post}$ in 20/23 (87%). The first observer showed that the median $CEMRI_{HP}$ score was two-times higher compared to $MRI_{TA}$, however this difference was not statistically significant (z=-0.44; p=0.6). Also the second observer showed that HP was larger than TA, with a median $TA/HP_{lobe}$ score of 1 (IQR -1; 2), which was statistically significant (p= 0.008). $MRI_{TA}$ scores were 16.7 % lower relative to $CT_{TA\text{-}pre}$ (z=-3.29; p<0.001) and 22.2 % lower relative to $CT_{TA\text{-}post}$ (z=-3.51; p<0.0001). The mean not significant (p=0.17) difference between $CT_{TA\text{-}pre}$ and $CT_{TA\text{-}post}$ was 5%. $MRI_{TA}$ was not significant different from $TA_{BB\text{-}He}$ (z=-1.15; p=0.25). $TA_{BB\text{-}He}$ was significant lower relative to $CT_{TA\text{-}pre}$ (z=-3.243; p=0.001) and $CT_{TA\text{-}post}$ (z=-3.527; p<0.0001).

### Correlation between trapped air, hypoperfusion and pulmonary function test

After Bonferroni correction, the p-value for multiple correlations was set to p=0.00625. A strong positive correlation was found between $MRI_{TA}$ and $CT_{TA\text{-}pre}$ (r=0.6; p=0.004), $CT_{TA\text{-}post}$ (r=0.59, p=0.005), and $CEMRI_{HP}$ (r=0.58, p=0.006). $MRI_{TA}$ had a negative correlation with FVC (r=-0.572, p=0.007; not significant after Bonferroni) $FEV_1$ (r=-0.6, p=0.004), and $FEF_{75}$ (r=-0.64, p=0.002). $CEMRI_{HP}$ has a strong negative correlation with $FEF_{75}$ (r=-0.65, p=0.001), but weak correlations with $CT\text{-}TA_{pre}$ (r=0. 57, p=0.007), and $CT_{TA\text{-}post}$ (r=0.55, p=0.009). $CT_{TA\text{-}pre}$ had negative correlation with, $FEV_1$ (r=-0.59, p=0.004), and $FEF_{75}$(r=-0.59, p=0.004), but not with FVC (r=-0.52, p=0.01). $TA_{BB\text{-}He}$ did not correlate significantly with any tested parameters.

### Score reliability

Intra-observer variability for $MRI_{TA}$ and $CEMRI_{HP}$ was very good (ICC= 0.85) and good (ICC=0.72) respectively. Bland-Altman plots showed no systematic errors both for $MRI_{TA}$ and $CEMRI_{HP}$ (Figure 4E, online supplement)

## Discussion

In this study we compared the ability to detect trapped air by MRI with that of CT and of PFT. In addition, we investigated how far the severity of trapped air as established by MRI overlapped regions of hypoperfusion.

The first important finding of our study is that we are able to detect TA with proton MRI. $MRI_{TA}$ had a strong positive correlation with $CT_{TA\text{-}pre}$ and $CT_{TA\text{-}post}$, and a strong negative correlation with PFT parameters of airway obstruction. These results were somewhat unexpected, because the SSFP sequence had shown previously poor performance for TA assessment [23,30]. However in our protocol, we standardized image acquisition by extensive training of the patient prior to the MRI to perform adequate breath-hold maneuvers. Patient's training allowed to acquire expiratory images at nearly residual lung volume, with a optimal characterization of TA due to higher contrast with the

surrounding normal and hyperperfused lung tissue [22]. Moreover, we noticed that patient's training improved image quality by reducing motion artefacts (Figure 1).

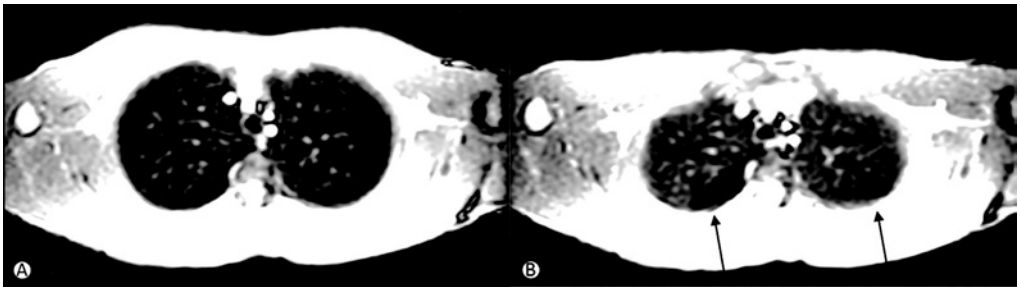


**Figure 1. 2D Steady State Free Precession (SSFP) scans at (A) end-inspiration (Total Lung Capacity) and (B) end-expiration (Residual Volume)**. Note sharp definition of low intensity region (LIR) in the end-expiratory image (arrows in B) and no evidence of motion artifacts.

The second important finding of our study is that there was dissociation between $MRI_{TA}$ and $CEMRI_{HP}$. Previous study have demonstrated that HP is an early and common feature of CF lung disease [4,16] 2 m; median age 16 years. In our cohort study, we not only confirmed that HP is a common feature of CF lung disease, but also significantly larger than TA (Figure 2). We also found that the $CEMRI_{HP}$ was strongly correlated to PFT parameters of airways obstruction. These findings suggest that HP is not only the result of hypoxic pulmonary vasoconstriction due to airway obstruction, where regions of TA overlap HP; but there are also regions of HP that do not match TA and that might result from other CF-related factors, such as chronic lung inflammation, in the absence of obstructive airway disease [31]. A second option is that the hypoxic pulmonary vasoconstriction is reducing perfusion to a larger area than the hypo ventilated lung region. A third possible explanation is that $CEMRI_{HP}$ also detects areas of "micro-hypoventilation", which are not detectable by proton MRI and PFT. This would make of HP a high sensitivity biomarker to detect ventilation impairment in CF lung disease.

A third finding of our study is that the extent of $MRI_{TA}$ was not significant different from $TA_{BB\text{-}He}$. Differently, the $CT_{TA}$ (pre and post) were both significantly higher compared to $TA_{BB\text{-}He}$ and $MRI_{TA}$ (Figure 3). These differences in TA assessment between MRI and CT might be attributed to the lower sensitivity of MRI for air [32]. However, our results suggest that the regions of low attenuation as observed on chest CT might reflect a mix of TA and HP (Figure 4), being $MRI_{TA}$ significantly smaller than $CEMRI_{HP}$. Low attenuation on CT can be caused by TA as well as by HP, while $MRI_{TA}$ reflects just low signal intensity caused by incomplete deflation of the lung. In a non-contrast CT, radiologist can only define HP indirectly, as in case of concordant low-density regions in inspiration and expiration. Conversely, CEMRI gives a direct evaluation of HP and when combined with $MRI_{TA}$ assessment on expiratory MRI allows differentiating between TA and HP. Hence, from our study it becomes clear that the term TA for regions of low attenuation on expiratory chest CT is not appropriate and should

be avoided as these regions are likely to be the result of a combination of TA and HP. We suggest that a more appropriate term for TA is low-attenuation region (LAR) for CT and low-intensity region (LIR) for MRI. For the clarity of this discussion section we will however continue to use the term TA in this paper.

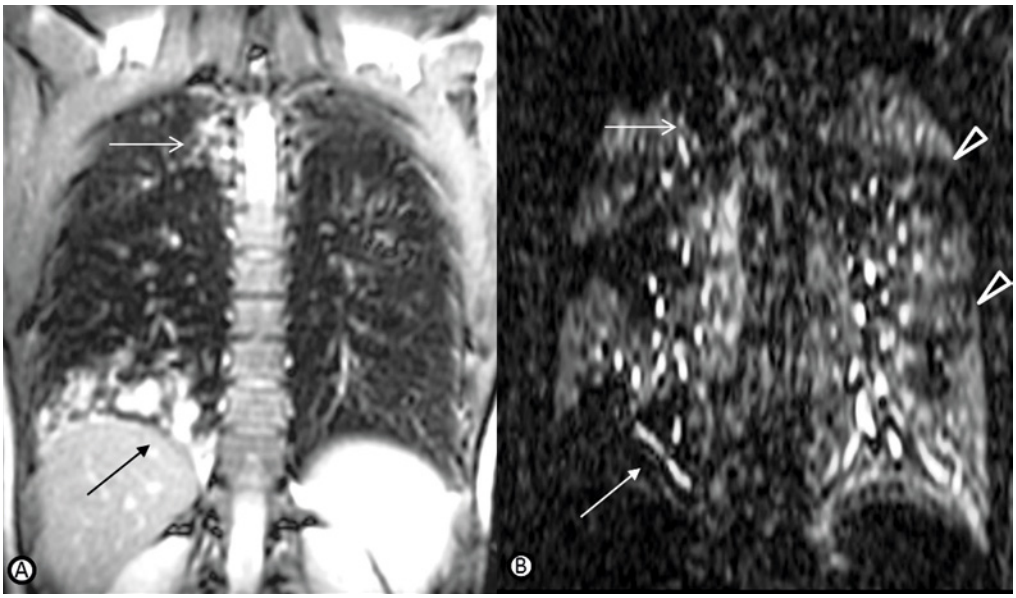


**Figure 2. Trapped Air (TA) and Hypoperfusion (HP)**. (A) end-expiratory coronal 2D Steady-State Free Precession (SSFP) proton-MRI and (B) coronal end-expiratory reformat 3D Spoiled Gradient Echo (SPGR) with TRICKS contrast-enhanced MRI. Note that HP areas often match areas of structural changes as in right upper (open arrows) and lower lobes (close arrows), but that there are also clearly HP on the CEMRI that are apparently free of disease on proton-MRI (arrowheads).

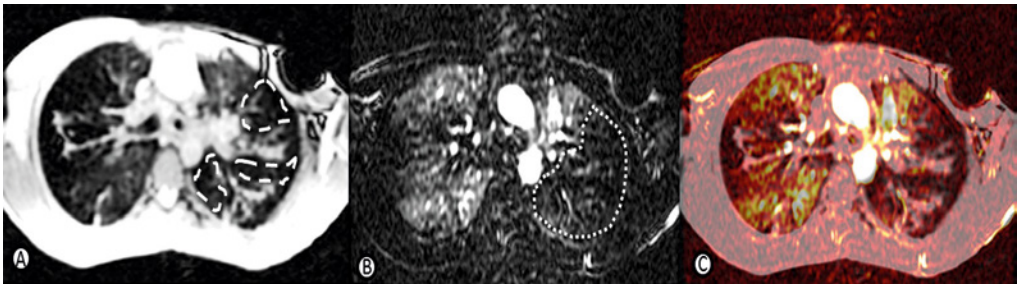


**Figure 3. Comparison between $MRI_{TA}$ and $CEMRI_{HP}$.** (A) End-expiratory axial 2D Steady-State Free Precession (SSFP) proton-MRI, (B) axial end-expiratory reformat 3D Spoiled Gradient Echo (SPGR) with TRICKS contrast-enhanced MRI (CEMRI), and (C) Fusion Image CEMRI overlaid on MRI. Note that the hypoperfusion area in the left upper lobe (dotted area, in image B) is larger than the trapped air areas (dashed lines in A).

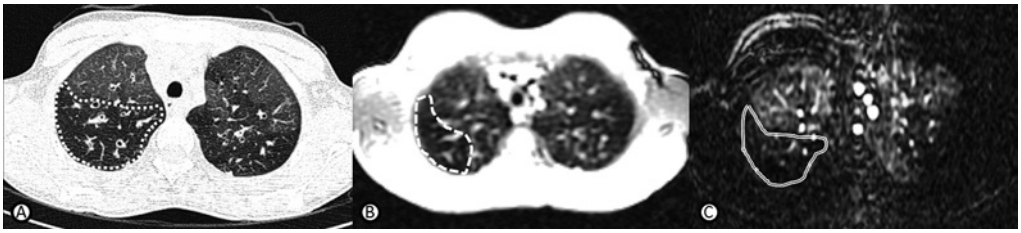

**Figure 4. Comparison between CT, MRI and CEMRI.** (A) End-expiratory axial CT, (B) end-expiratory axial 2D Steady-State Free Precession (SSFP) proton-MRI and (C) axial end-expiratory reformat 3D Spoiled Gradient Echo (SPGR) with TRICKS contrast-enhanced MRI. Note that the hypodense area in image A (dotted area) is larger than the hypointense area in B (dashed line), and similar to the hypointense area in C (double line).

Our findings support HP as a relevant independent biomarker of CF lung disease in addition to TA to monitor and target therapy [31]. When studying lung perfusion this justifies the use of contrast agent with chest MRI. However, there are MRI techniques in development to assess lung perfusion without the need for a contrast agent, such as Fourier Decomposition and arterial spin labelling [11,33]. This would avoid the possible risks related to the use of Gadolinium, such as deposition of Gd in the brain, as recently highlighted by the literature [15]. Hence, our study supports further development and validation of these non-contrast MRI techniques and to establish their sensitivity relative to CEMRI to detect HP.

Finally, we acknowledge some limitations to this study. Firstly, we assessed TA and HP using semi-quantitative scoring systems. We did so in order to reduce variability as it allowed us using for CT and MRI the same scoring strategy for TA and for MRI and CEMRI the same scoring strategy for TA and HP. Moreover, this scoring system was already successfully used by our group and similar to single morphologic-functional MRI scoring system proposed in the literature [34].

Secondly, for the comparison of the extent of TA with that of HP, we used two scoring systems, which were executed by two independent observers. The new PROPeR scoring system was especially developed to allow a sensitive comparison between the extent of HP with that of TA. Our approach confirmed the results of the first independent observer, who showed that the median $CEMRI_{HP}$ score was a factor two higher compared to $MRI_{TA}$, although not significant. Importantly, intra-observer variability with the CF-MRI scoring system was good with ICCs being 0.81 [35].

Finally, there was a 1-year time gap between $CT_{TA\text{-}pre}$ and $MRI_{TA}$ and between $MRI_{TA}$ and $CT_{TA\text{-}post}$. This comparison was justified as not much change in $CT_{TA}$ over a two-year period can be expected. Loeve *et al*, did not find a significant change in $CT_{TA}$ over a two year time period using a sensitive quantitative image analysis system [27]. Similarly, we did not find a significant difference between $CT_{TA\text{-}pre}$ than $CT_{TA\text{-}post}$. However, we showed a consistent higher median score of $CT_{TA\text{-}pre}$ and of $CT_{TA\text{-}post}$ relative to $MRI_{TA}$.

## Conclusions

By comparing MRI, CT and PFT, we showed that $CEMRI_{HP}$ is more frequent and its extent larger than of $MRI_{TA}$ and that $MRI_{TA}$ was similar to TA as quantified by PFT. Furthermore, we showed that $CT_{TA}$ is substantially larger than $MRI_{TA}$. Our findings show that HP contributes importantly to regions often described in radiology reports as ”trapped air” or as “mosaic pattern” on CT. Therefore, we propose that these terms can be better replaced by low-attenuation region (LAR) for CT and low-intensity region (LIR) for MRI respectively. Finally, the findings of our study highlight the importance of HP in CF lung disease as independent outcome measure in addition to TA to monitor and target therapy. Further studies using CEMRI or non-contrast perfusion MRI techniques are needed to investigate the role of HP and potential therapies.

## Bibliography


1. Loeve M, van Hal PTW, Robinson P, et al. (2009) The spectrum of structural abnormalities on CT scans from patients with CF with severe advanced lung disease. Thorax 64:876–82. doi: 10.1136/thx.2008.110908
2. Sly PD, Brennan S, Gangell C, et al. (2009) Lung disease at diagnosis in infants with cystic fibrosis detected by newborn screening. Am J Respir Crit Care Med 180:146–52. doi: 10.1164/rccm.200901-0069OC
3. Hansell DM, Bankier AA, MacMahon H, et al. (2008) Fleischner Society: glossary of terms for thoracic imaging. Radiology 246:697–722. doi: 10.1148/radiol.2462070712
4. Eichinger M, Puderbach M, Fink C, et al. (2006) Contrast-enhanced 3D MRI of lung perfusion in children with cystic fibrosis--initial results. Eur Radiol 16:2147–52. doi: 10.1007/s00330-006-0257-7
5. Castile RG, Iram D, McCoy KS (2004) Gas Trapping in Normal Infants and in Infants with Cystic Fibrosis. Pediatr Pulmonol 37:461–469. doi: 10.1002/ppul.10446
6. Miller MR, Hankinson J, Brusasco V, et al. (2005) Standardisation of spirometry. Eur Respir J 26:319–338. doi: 10.1183/09031936.05.00034805
7. Kuo W, Kemner-van de Corput M, Perez-Rovira A, et al. (2016) Multicenter chest CT standardization in children and adolescent with CF: The way forward. Eur. Respir. J.
8. Goh V, Dattani M, Farwell J, et al. (2011) Radiation dose from volumetric helical perfusion CT of the thorax, abdomen or pelvis. Eur Radiol 21:974–981. doi: 10.1007/s00330-010-1997-y
9. Dillman JR, Ellis JH, Cohan RH, et al. (2007) Frequency and severity of acute allergic-like reactions to gadolinium-containing IV contrast media in children and adults. Am J Roentgenol 189:1533–1538. doi: 10.2214/AJR.07.2554
10. Wielpütz MO, Mall MA (2015) Imaging modalities in cystic fibrosis. Curr Opin Pulm Med 21:609–616. doi: 10.1097/MCP.0000000000000213
11. Ley S, Ley-Zaporozhan J (2012) Pulmonary perfusion imaging using MRI: clinical application. Insights Imaging 3:61–71. doi: 10.1007/s13244-011-0140-1
12. Eichinger M, Puderbach M, Smith H-J, et al. (2007) Magnetic resonance-compatible-spirometry: principle, technical evaluation and application. Eur Respir J 30:972–9. doi: 10.1183/09031936.00040607
13. Dournes G, Menut F, Macey J, et al. (2016) Lung morphology assessment of cystic fibrosis using MRI with ultra-short echo time at submillimeter spatial resolution. Eur Radiol. doi: 10.1007/s00330-016-4218-5
14. Tiddens HAWM, Stick SM, Wild JM, et al. (2015) Respiratory tract exacerbations revisited: Ventilation, inflammation, perfusion, and structure (VIPS) monitoring to redefine treatment. Pediatr Pulmonol 50:S57–S65. doi: 10.1002/ppul.23266
15. Ramalho J, Semelka RC, Ramalho M, et al. (2016) Gadolinium-Based Contrast Agent Accumulation and Toxicity: An Update. Am J Neuroradiol 1–7. doi: 10.3174/ajnr.A4615
16. Wielpütz MO, Puderbach M, Kopp-Schneider A, et al. (2014) Magnetic Resonance Imaging Detects Changes in Structure and Perfusion, and Response to Therapy in Early Cystic Fibrosis Lung Disease. Am J Respir Crit Care Med 1–49. doi: 10.1164/rccm.201309-1659OC
17. Teufel M, Ketelsen D, Fleischer S, et al. (2013) Comparison between high-resolution CT and MRI using a very short echo time in patients with cystic fibrosis with extra focus on mosaic attenuation. Respiration 86:302–11. doi: 10.1159/000343085
18. Renz DM, Scholz O, Böttcher J, et al. (2015) Comparison Between Magnetic Resonance Imaging and Computed Tomography of the Lung in Patients With Cystic Fibrosis With Regard to Clinical, Laboratory, and Pulmonary Functional Parameters. Invest Radiol 50:21–24. doi: 10.1097/RLI.0000000000000178
19. Laszlo G (2006) Standardisation of lung function testing: helpful guidance from the ATS/ERS Task Force. Thorax 61:744–6. doi: 10.1136/thx.2006.061648
20. Wanger J, Clausen JL, Coates A, et al. (2005) Standardisation of the measurement of lung volumes. Eur Respir J 26:511–22. doi: 10.1183/09031936.05.00035005

21. Failo R, Wielopolski P a, Tiddens H a WM, et al. (2009) Lung morphology assessment using MRI: a robust ultra-short TR/TE 2D steady state free precession sequence used in cystic fibrosis patients. Magn Reson Med 61:299–306. doi: 10.1002/mrm.21841

22. Salamon ER, Lever S, Kuo W, et al. (2015) Spirometer guided chest imaging in children: It is worth the effort. Pediatr Pulmonol Submitted:1–9. doi: 10.1002/ppul.23490

23. Ciet P, Serra G, Bertolo S, et al. (2015) Assessment of CF lung disease using motion corrected PROPELLER MRI: a comparison with CT. Eur Radiol 26:780–787. doi: 10.1007/s00330-015-3850-9

24. Tepper L a., Ciet P, Caudri D, et al. (2015) Validating chest MRI to detect and monitor cystic fibrosis lung disease in a pediatric cohort. Pediatr Pulmonol n/a–n/a. doi: 10.1002/ppul.23328

25. Loeve M, Gerbrands K, Hop WC, et al. (2011) Bronchiectasis and pulmonary exacerbations in children and young adults with cystic fibrosis. Chest 140:178–85. doi: 10.1378/chest.10-1152

26. Brody AS, Kosorok MR, Li Z, et al. (2006) Reproducibility of a scoring system for computed tomography scanning in cystic fibrosis. J Thorac Imaging 21:14–21. doi: 10.1097/01.rti.0000203937.82276.ce

27. Loeve M, Rosenow T, Gorbunova V, et al. (2015) Reversibility of trapped air on chest computed tomography in cystic fibrosis patients. Eur J Radiol 84:1184–1190. doi: 10.1016/j.ejrad.2015.02.011

28. Portney LG WM (2000) Foundations of clinical research: applications to practice. New Jersey

29. Cohen J (1988) Statistical Power Analysis for the Behavioral Sciences. Routledge; 2 edition

30. Rajaram S, Swift AJ, Capener D, et al. (2012) Lung morphology assessment with balanced steady-state free precession MR imaging compared with CT. Radiology 263:569–77. doi: 10.1148/radiol.12110990

31. Nichols DP, Chmiel JF (2015) Inflammation and its genesis in cystic fibrosis. Pediatr Pulmonol 50 Suppl 4:S39–56. doi: 10.1002/ppul.23242

32. Ciet P, Tiddens HAWM, Wielopolski PA, et al. (2015) Magnetic resonance imaging in children: common problems and possible solutions for lung and airways imaging. Pediatr Radiol. doi: 10.1007/s00247-015-3420-y

33. Bauman G, Puderbach M, Heimann T, et al. (2013) Validation of Fourier decomposition MRI with dynamic contrast-enhanced MRI using visual and automated scoring of pulmonary perfusion in young cystic fibrosis patients. Eur J Radiol 82:2371–7. doi: 10.1016/j.ejrad.2013.08.018

34. Eichinger M, Optazaite D-E, Kopp-Schneider A, et al. (2012) Morphologic and functional scoring of cystic fibrosis lung disease using MRI. Eur J Radiol 81:1321–9. doi: 10.1016/j.ejrad.2011.02.045

35. Ley-Zaporozhan J, Molinari F, Risse F, et al. (2011) Repeatability and reproducibility of quantitative whole-lung perfusion magnetic resonance imaging. J Thorac Imaging 26:230–9. doi: 10.1097/RTI.0b013e3181e48c36

# Supplement

**Table 1E.** Inclusion and exclusion criteria.

| Inclusion criteria | Exclusion criteria |
|---|---|
| – Age between 6 and 18 years old (age range for MRI in our institution)<br>– Diagnosis of CF confirmed by sweat-test and/or DNA analysis and/or electro physiology testing<br>– Stable condition defined as: no requirement for i.v. antibiotics at the time of the annual check-up<br>– Ability to perform pulmonary function tests<br>– Ability to do breath-hold manoeuvres<br>– CT scan made in the year before and after the MRI<br>– Signed written informed consent<br>– Able to comply with protocol requirements. | – Inability to follow instructions of the investigator<br>– Current respiratory tract infection requiring i.v. antibiotics<br>– Pulmonary complications that might put the patient at risk to participate in the study<br>– Claustrophobia<br>– History of anaphylactic reaction on contrast agent<br>– Any clinical condition which, according to the treating physician, might put the patient at risk<br>– Severe asthma and/or severe allergies as determined by physician<br>– Ferro-magnetic implants |

**Table 2E**

| **Inspiratory** | | | | | | | |
|---|---|---|---|---|---|---|---|
| | *kV* | *mAs* | *Rotation time (sec)* | *Collimation (mm)* | *Pitch* | *Kernels* | *MPR* |
| | 110 (80[#]) | 20 CD4D | 0.6 | 6*2 | 1.50 | B60s, B30s | 1, 5, 8 mm axial |
| **Expiratory** | | | | | | | 3 mm coronal and sagittal |
| | 110 (80[#]) | 10 eff mAs | 0.6 | 6*2 | 1.50 | | Recon increment 1.2 mm |

CD4D=CareDose; MPR=multiplanar reformats. ([#]) kV voltages for children below 25 kg.

# Imaging Analysis

To set the best Contrast-to-Noise (CNR) between high and low density lung structure for MRI, we used an approach similar to chest CT using the standard lung window. Due to the lack of defined window setting for proton Magnetic Resonance Imaging (MRI) and Contrast Enhanced MRI (CEMRI), we set for each patient the window level above the background noise level and the window width approximately two-folds higher than the window level [17]. This method supplies the best CNR between high and low density lung structures, similar to Computed Tomography (CT) using the standard lung window. The level of ambient (background) lighting was kept constant during all viewing sessions to ensure consistent viewing conditions. The contrast enhanced phase of CEMRI

scan that was selected for HP scoring was that of the first pass of the contrast in the lung and that with the highest CNR. First, the end-expiratory MRI and CEMRI scans were anonymized and scored in random order by the first observer using the Cystic Fibrosis (CF) MRI scoring system (CF-MRI).

### CF-MRI scoring system

For the CF-MRI scoring system the following items are scored: bronchiectasis, air wall thickening, mucus plugging, parenchyma score (including bullae, cysts, atelectasis, consolidation and ground glass opacity) and trapped air (TA). Hypoperfusion (HP) is not routinely scored with CF-MRI [22,23]. To score HP, the same categories used to score TA are used in order to enable the comparison. The extent of TA and HP is defined per lobe according the categories shown in Table E3. The total score per patient for TA (or HP) is calculated by summing up the scores of the five lobes and lingula as sixth lobe, with higher scores indicating more TA (or HP). The maximum possible absolute score for TA as well as for HP is 18. For the purpose of this study only TA and HP were scored with the CF-MRI.

**Table 3E.** Cystic Fibrosis Magnetic Resonance Imaging (CF-MRI) scoring system for trapped air and hypoperfusion.

| Extent | Score |
|---|---|
| No TA (or HP) | 0 |
| TA (or HP) less than 33% lobe volume | 1 |
| TA (or HP) between 33% and 67% lobe volume | 2 |
| TA (or HP) more than 67% lobe volume | 3 |

TA=Trapped air, HP=hypoperfusion.



### PatteRn OverlaPping Rotterdam (PROPeR) scoring system

A second observer, blinded to the assessment of the first observer, who scored with the CF-MRI scoring system, scored MRI and CEMRI scans using the PatteRn OverlaPping Rotterdam (PROPeR) scoring system. This PROPeR score is performed for each lobe separately, with the lingula considered as sixth lobe. First, the observer compares simultaneously slice by slice the end-expiratory proton-MRI and the CEMRI scans of the same patient in order to determine if HP is greater, equal or smaller than TA. Next, end-expiratory MRI and CEMRI are merged using the imaging registration tools of Advantage Windows Server (General Electric Healthcare, Milwaukee, WI, USA) imaging platform. This tool overlaps the end-expiratory MRI with the CEMRI scans, and superimposed the signal of the CEMRI to the end-expiratory MRI. This allows scoring per lobe the different extent between TA and HP ($TA/HP_{lobe}$). Differences in extent between TA and HP are scored as shown in Table 4E.

**Table 4E.** Comparison of Contrast Enhanced Magnetic Resonance Imaging (CEMRI) and MRI scans.

| **PatteRn OverlaPping Rotterdam (PROPeR) score Scoring** | | | | | |
|---|---|---|---|---|---|
| *HP>TA* | | *HP=TA* | | *HP<TA* | |
| Extent | Score | Extent | Score | Extent | Score |
| HP greater than TA of 0-25% | 1 | HP equal to TA | 0 | HP smaller than TA of 0-25% | -1 |
| HP greater than TA of 26-50% | 2 | HP greater than TA of 51-75% | | HP greater than TA of 26-50% | -2 |
| HP greater than TA of 51-75% | 3 | HP greater than TA of 76-100% | | -3 | |
| HP greater than TA of 76-100% | 4 | | | -4 | |

HP=hypoperfusion; TA=Trapped Air.

For instance, when the extent of HP is 0-25 % larger than the extent of TA a score of 1 is assigned (Figure 1E), vice versa a score of -1 is assigned when TA is 0-25% larger than HP (Figure 2E). When HP overlaps TA or there is homogenous signal both in MRI and CEMRI a score of zero is assigned (Figure 3E).

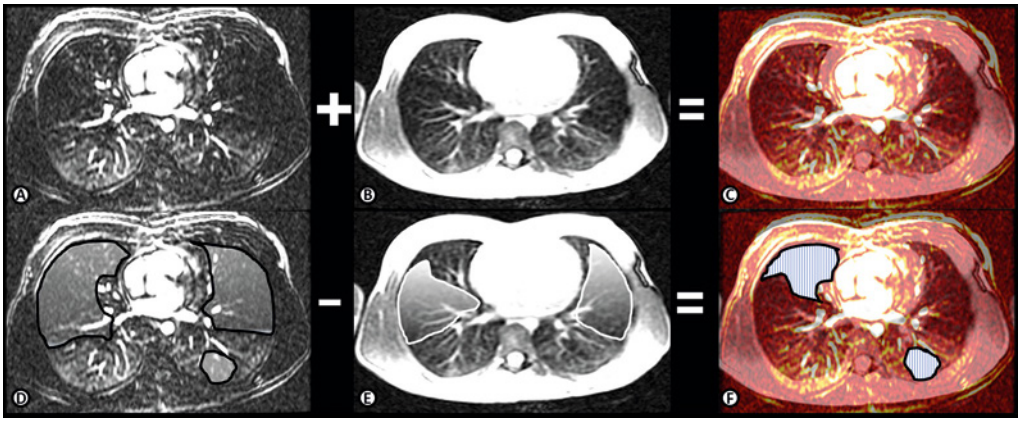

**Figure 1E. Comparison between $MRI_{TA}$ and $CEMRI_{HP}$ by the second observer using the PROPER scoring system.** (A and D) axial end-expiratory reformat 3D Spoiled Gradient Echo (SPGR) with TRICKS contrast-enhanced MRI (CEMRI); (B and E) end-expiratory axial 2D Steady-State Free Precession (SSFP) proton-MRI; and C and F) Fusion Image CEMRI overlaid on MRI. Note areas of hypoperfusion in both lungs in image D (black line areas) and areas of trapped air in image E (white line areas). When compared on fusion image F, hypoperfusion is larger than the trapped air areas (line pattern areas in F). Hence, for these lobes (right middle and left lower lobes) a score of 1 is given.

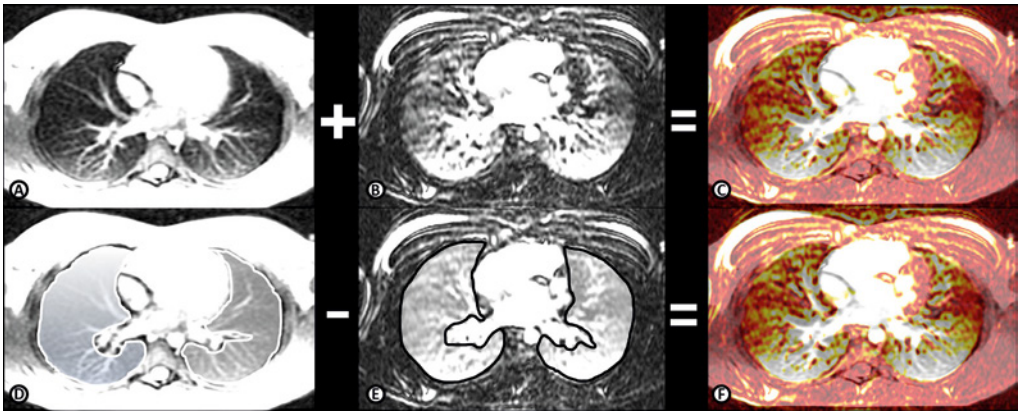

**Figure 2E. Comparison between $MRI_{TA}$ and $CEMRI_{HP}$ by the second observer using the PROPER scoring system.** (A and D) end-expiratory axial 2D Steady-State Free Precession (SSFP) proton-MRI; (B and E) axial end-expiratory reformat 3D Spoiled Gradient Echo (SPGR) with TRICKS contrast-enhanced MRI, and C and F) Fusion Image CEMRI overlaid on MRI. Note homogeneous signal both in end-expiratory MRI (white line areas in D) and CEMRI (black line areas in image E). When compared, no differences are seen in the fusion image (image F). Hence, in this case a score of 0 is given.



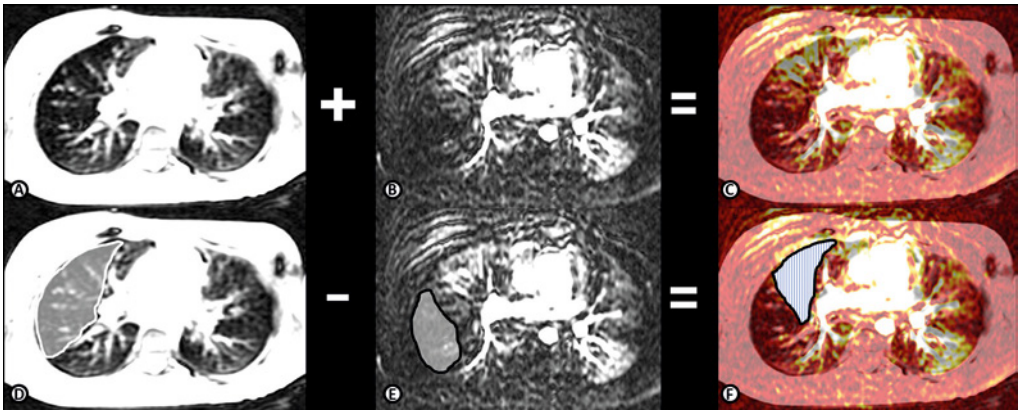

**Figure 3E. Comparison between $MRI_{TA}$ and $CEMRI_{HP}$ by an observer using the PROPER scoring system.** (A and D) end-expiratory axial 2D Steady-State Free Precession (SSFP) proton-MRI, (B and E) axial end-expiratory reformat 3D Spoiled Gradient Echo (SPGR) with TRICKS contrast-enhanced MRI (CEMRI), and C and F) Fusion Image CEMRI overlaid on MRI. Note that area trapped air in right upper lobe in image D (white line area) and area of hypoperfusion in image E (black line area). When compared on fusion image F, trapped air is larger than the hypoperfusion (line pattern area in F). Hence, for this lobe a score of -1 is given.

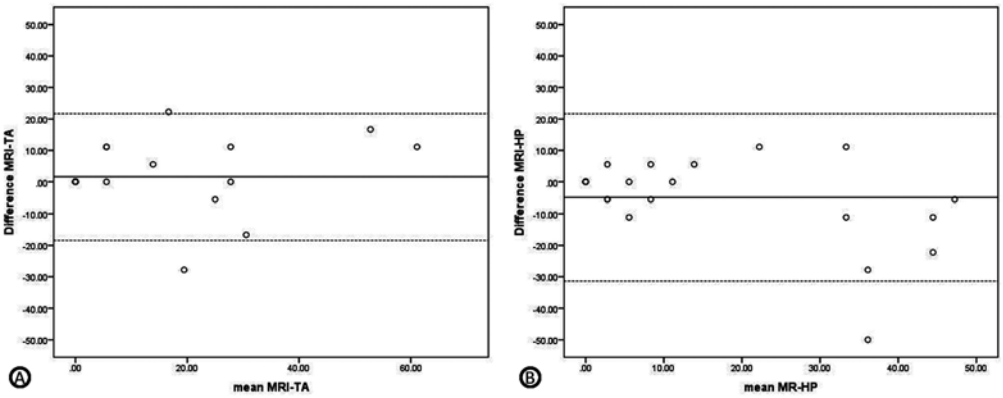


**Figure 4E. Intra-observer variability trapped air and hypoperfusion assessment.** Bland-Altman plot of intra-observer agreement (observer 1, one month time gap between scores) for (A) Magnetic Resonance Imaging Trapped Air ($MRI_{TA}$) score and (B) Contrast enhanced MRI Hypoperfusion ($CEMRI_{HP}$) score. Note that mean differences are close to zero and that all observations are around the mean.

# Chapter 7

## Three-dimensional Fourier Decomposition Ventilation Magnetic Resonance Lung Imaging

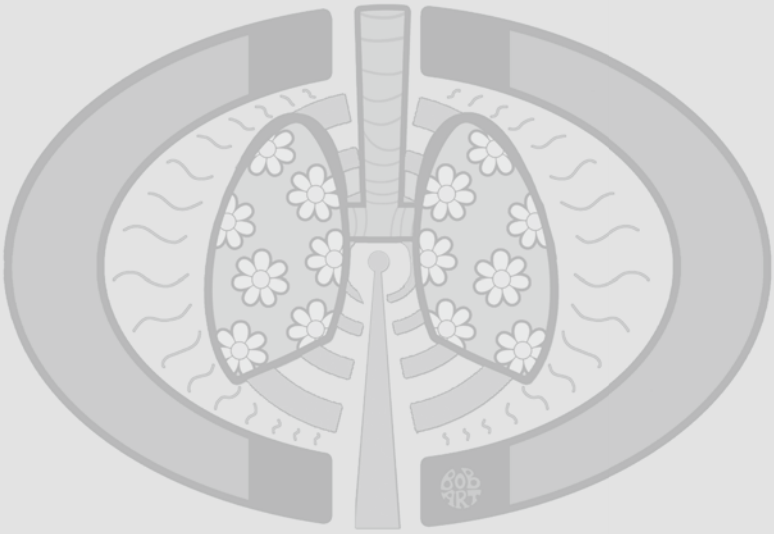

*Ciet P, Bos AC, Wielopolski P, Hernández-Tamames JA, de Bruijne M, Tiddens HAWM, Perez-Rovira A*

Submitted

## Abstract

**Purpose:** to evaluate feasibility of 3D-Fourier Decomposition (FD) lung ventilation MRI with highly time-resolved 4D MRI on a 3T system.

**Methods:** five volunteers and four patients with Cystic Fibrosis (CF) were enrolled in the study. MRI protocol consisted of breath-hold 3D-SPGR ($SPGR_{bh}$) and two free-breathing multiphase 3D-SPGR with different temporal resolutions: conventional 3D-SPGR (1sec/volume) and 3D DIfferential Subsampling with Cartesian Ordering (DISCO) (343 ms/volume). 3D-FD ventilation maps were obtained with in-house developed software. The 4D sequences were scored for image quality and signal-to-noise ratio (SNR). Trapped-air (TA) was assessed using the CF-MRI scoring system in end-expiratory $SPGR_{bh}$ ($TA_{bh}$) and in the 3D-FD ventilation maps ($TA_{FD}$). Statistics included t-test, Intraclass-Correlation Coefficient (ICC) and Pearson correlation coefficient (r).

**Results:** median age of volunteers and patients were 30 and 23 years respectively. Image quality ($p=0.2$) and SNR ($p=0.79$) were similar between both conventional SPGR and DISCO. Both sequences enabled 3D-FD ventilation maps. Good agreement ($ICC=0.875$) and high correlation ($r=0.877$, $p<0.001$) were found between $TA_{FD}$ and $TA_{bh}$. 3D-FD ventilation maps facilitated TA scoring ($p<0.0001$).

**Conclusion**

Both conventional SPGR and DISCO sequences enable 3D-FD ventilation maps. 3D-FD facilitates TA assessment compared to conventional $SPGR_{bh}$. 3D-FD techniques enable a faster and more comprehensive assessment of TA compared to 2D-FD techniques**.**

## Introduction

Several obstructive lung diseases cause ventilation impairment, frequently secondary to structural changes such as bronchial wall thickening, mucus plugs and bronchiectasis [1]. Computed tomography (CT) and Magnetic Resonance Imaging (MRI) allow for detection and quantification of ventilation impairment. Current quantitative assessment mostly consists of measuring trapped air (TA), hypoperfusion (HP) or a combination of both [2]. Quantification of TA and HP are relevant for several lung diseases, such as asthma and cystic fibrosis (CF) [3,4]. Recent evidence confirmed that TA and HP are important disease biomarkers to assess treatment efficiency [5,6]. For this reason, imaging has been increasingly used in clinical practice to monitor TA and HP [7]. To date CT has been the preferred method, being recognized as the most sensitive technique to monitor structural lung changes [8]. TA with CT can be assessed indirectly through visualization of low attenuation regions on end-expiratory CT scans, which adds extra radiation dose to the CT protocol. Similarly, HP assessment requires intra venous contrast administration and additional radiation exposure. Cumulative dose is thus the major disadvantage of CT, which restricts its use and disqualifies CT as the first choice for the detection and monitoring of functional information [9]. To reduce radiation exposure, MRI techniques have been introduced [10]. TA can be visualized on conventional short TE gradient-echo sequences (TE~0.4-0.7ms), but they have limited sensitivity to detect TA, because they suffer of fast signal decay due to T2* effects or SNR [11]. The reduced sensitivity to assess TA on end-expiratory MRI scans has promoted the development of new MRI techniques to improve TA quantification. One of those techniques is the extraction of ventilation maps using two-dimensional (2D) Fourier Decomposition (FD). 2D FD is a free-breathing gradient-echo technique that have been shown useful for the assessment of TA and HP without the need for intravenous or gaseous contrast agents [12]. Ventilation and perfusion maps obtained with 2D FD have been validated in healthy volunteers and in patients with CF, lung cancer and pulmonary embolism using mostly 2D steady state free precession (SSFP) [13-16]. However, despite the good temporal resolution (3-4 images/sec), this 2D FD has been limited by relatively lengthy scan time, poor spatial resolution and Specific Absorption Ratio (SAR) limitations at 3T [12]. The introduction of highly time resolved three-dimensional (3D) FD variants has not yet been reported using 3D Spoiled Gradient echo (SPGR) techniques. The challenge is to develop 3D sequences with sufficient temporal and spatial resolution in order to compute FD maps. Optimally In order to separate signals contributing from respiratory and cardiac cycles, a minimal temporal resolution of at least double the frequency of the highest frequency signal component (i.e. heart rate) is required according to the Nyquist criterion [12]. To achieve this with 3D, we included highly accelerated 3D SPGR sequences and special view shared variant called DIfferential Sub-sampling with Cartesian Ordering (DISCO) in order to achieve similar temporal resolution of 2D FD [17]. High parallel imaging acceleration is possible with 3D scanning, and the view sharing of the DISCO sequence enables even higher temporal resolution than conventional cartesian 3D SPGR acquisition scheme [17].

In this pilot study, we aimed to evaluate the feasibility of 3D FD lung MRI using conventional 3D SPGR ($SPGR_C$) and DISCO data acquisition schemes in a group of healthy volunteers and patients with CF. In particular we compared image quality and signal-to-noise ratio (SNR) of $SPGR_C$ and DISCO. Then we compared TA assessment using 3D SPGR breath-hold end-expiratory scans ($SPGR_{bh}$) and the 3D FD ventilation maps obtained with the aforementioned 3D multiphase sampling schemes.

## Methods

MRI experiments with healthy volunteers were conducted following institutional review board approval and informed consent (MEC-2014-096). Patients with CF were included from a clinical study which tested a new administration device for inhaled antibiotics (MEC-2014-260) and which MRI protocol included the required sequences. Exclusion and inclusion criteria for volunteers and patients are displayed in Table 1.

### Breathing maneuvers

Subjects were trained to perform breathing maneuvers by a lung function technician prior the MRI. Breathing maneuvers were repeated in supine position on a stretcher using a custom made MRI-compatible spirometer (Masterscope, CareFusion, Houten, The Netherlands). Aims of the training were to monitor and standardize breathing maneuvers during the MRI by using spirometer volume data during the MRI. For the static MRI acquisitions subjects were trained to obtain a maximal breath hold time of 15 seconds at ≥95% of the inspiratory vital capacity (IVC) and at ≥90% expiratory vital capacity (EVC). For the dynamic maneuvers subjects were instructed to have a regular breathing pace (5-7 seconds per respiratory cycle).

### MRI protocol

MRI scans were performed at 3.0T (Discovery MR750, GE Healthcare, Milwaukee, WI, USA) using a 32 channels phased-array receiver only torso-coil and with the whole body coil for transmission. The MRI protocol included spirometer controlled breath-hold end-inspiratory and end-expiratory accelerated 3D SPGR scans covering the entire lung volume: TR/TE/$\alpha$=1.1 ms/0.5ms/2°; voxel resolution 3 $mm^3$ isotropic. Eight to ten seconds breath-hold time were achieved using the Autocalibrating Reconstruction for Cartesian (ARC) parallel imaging with factors ranging between 1-2. Then two 4D SPGR scans were performed during tidal breathing for an acquisition time of around 1 minute with different data collection strategies at maximum ARC acceleration (ARC=6). The first 4D SPGR ($SPGR_C$) scan used a TR/TE/$\alpha$=1 ms/0.4ms/1°; actual voxel resolution of 7.5x7.5x4 $mm^3$ for a temporal resolution of 1.13 sec/volume. The DISCO scan used TR/TE/$\alpha$=1.1/0.4/1°, actual voxel resolution of 6x6x6 $mm^3$ with a predefined A region fraction of 0.5 with a number of B regions of 6, providing an effective temporal resolution of 343 ms/volume. A and B regions were predefined based on prior phantom and volunteer testing regarding ghosting artifacts in the anterior- posterior direction.

**Table 1.** Inclusion and Exclusion criteria volunteers and patients.

| **Volunteers** | |
|---|---|
| *Inclusion criteria* | *Exclusion criteria* |
| – Healthy subject defined as a volunteer who is not referred to the hospital with signs and symptoms of disease;<br>– Age ≥18 years old;<br>– Signed informed consent. | – Any contra-indication to an MRI (i.e. metal implants)<br>– Woman who are pregnant or lactating;<br>– Physical or mental status that interferes with the informed consent procedure;<br>– Participation in another clinical study. |
| **CF Patients** | |
| *Inclusion criteria* | *Exclusion criteria* |
| – Age ≥8 years;<br>– Clinical diagnosis of CF by a positive sweat test or two CF-related mutations;<br>– Chronic Pseudomonas Aeruginosa (Pa) colonization requiring maintenance therapy with inhaled tobramycin, defined according to the Leeds criteria (>50% Pa positive airway cultures over last 12 months);<br>– Small airways obstruction present on spirometry defined as follows: dissociation between FVC and $FEF_{75}$ values (i.e. $FEF_{75}$ at least 20% (absolute percent predicted) less than FVC);<br>– Ability to breathe through a mouthpiece and to use the inhaler;<br>– Ability to perform lung function tests;<br>– Written informed consent. | – Severe acute exacerbation of pulmonary infection (requiring intravenous treatment with antibiotics) within one month prior to start or during the study;<br>– Known impaired kidney function (estimated creatinine clearance <60 ml/min);<br>– Known aminoglycoside hypersensitivity;<br>– Start of nephrotoxic or ototoxic drugs, e.g. aminoglycosides, within 1 month prior to start or during the study;<br>– Therapy (e.g. furosemide) or disease which may complicate evaluation of the study protocol, as judged by the investigator;<br>– Participation in another drug-investigating clinical study at the start or within 1 month prior to the start;<br>– Inability to follow instructions of the investigator;<br>– Use of Tobramycin Inhalation Powder as part of the maintenance therapy. |

## Image analysis

All images were anonymized and analyzed in random order by a single observer (A.B.) on 3D Slicer (http://www.slicer.org). Ventilations maps were obtained using in-house developed software. Then, image analysis was conducted in three steps: image quality, SNR and TA assessment.

*Fourier Decomposition ventilation maps*

The computation of the FD ventilation map was performed in 5 steps. First, in order to facilitate the alignment of all acquired volumes in the dynamic sequence, this was processed to remove the characteristic bias field of MR images using N4ITK [18]. The shrink factor was four, and the B-spline fitting was set to two elements in each spatial dimension. Second, the Elastix image registration framework [19] was used to align the 3D time frames using a group wise deformable registration by minimizing the variance of intensity over time. Similarly to Mogalle *et al* [20], the 4D free-form B-spline that provides smoothness in the three spatial dimensions and in the time dimension had a resolution of 20 mm in space and 1 frame in time. Registration was achieved using a stochastic,

adaptive gradient descent optimizer and a multi-resolution scheme with four resolution levels. After successful registration, each voxel $v_{(x,y,z,t)}$ will correspond to the same anatomical position in the patient, independent of $t$. Third, the intensity profile (Figure 1, top) along time, $t$, of each voxel $v_{(x,y,z)}$ is analyzed using the Fourier transformation, which decomposes the signal into the frequencies that make it up (Figure 1, middle). The first and last five frames of each sequence were discarded for this step, to ensure that the analyzed portion of the sequence contained only the instructed breathing maneuver. Fourth, all Fourier decomposition vectors are averaged for the entire sequence and the mode in the frequency domain is automatically detected as the breathing frequency (Figure 1, bottom). For each voxel position, the response around the detected peak is integrated within a window of 8/60 Hz, to allow variations in the breathing frequency, resulting in a single value per voxel that corresponds to the amount of ventilation at that location. Finally, the ventilation maps are normalized by linear scaling, such that the 5$^{th}$ and 95$^{th}$ percentile of the entire 3D ventilation map are set to 0 and 1, respectively and values outside that range are clipped.

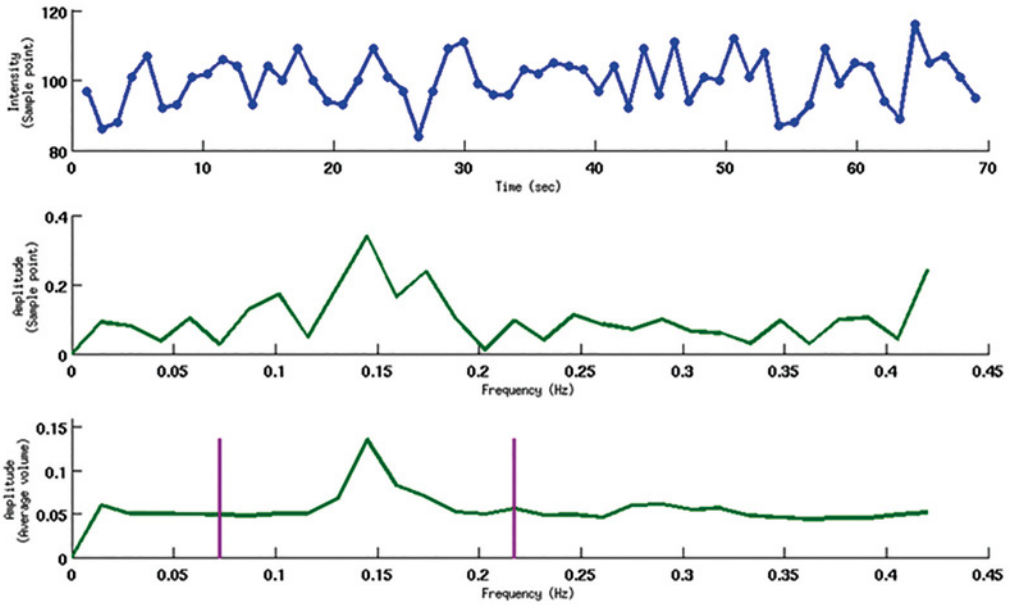


**Figure 1. Top:** Intensity value along time for a fixed point in the lung after registration and bias correction, where the breathing pattern can be seen (conventional SPGR multiphase, temporal resolution around 1 sec/ image). **Middle:** Fourier decomposition of the intensity profile. **Bottom:** Averaged results of the Fourier decomposition for all voxels. A clear peek at 0.14Hz can be seen, corresponding to a slow breathing frequency of around 7 seconds per cycle. Values between the purple lines are integrated to produce the ventilation maps.

*Image Quality analysis*

Image quality of $SPGR_C$ and DISCO sequences was scored regarding blurring and ghosting using a 5 points scale ranging from 1=severe to 5=imperceptible. Imperceptible was defined when the signal

in the lung parenchyma was less than 20% of the max signal of the anterior chest wall at a point a maximum chest wall displacement. Similarly, image quality was scored with a five point scale in $SPGR_{bh}$ scans and the 3D FD regarding ability to define region of TA, ranging from 1=non-diagnostic, TA region non identifiable to 5=no noise of motion artifact interfering with assessment of TA region.

*SNR measurement*

SNR was computed in $SPGR_C$ and DISCO images. SNR was computed according to the formula: [mean Signal Intensity (SI)/Standard Deviation (SD) of noise]. SI of the lung was recorded as mean pixel intensity value of a region of interest (ROI) manually positioned in the lung parenchyma without including major blood vessels. To take into account variation in SI between anterior and posterior lung parenchyma due to effect of gravity on blood distribution, ROIs were positioned at three levels: anterior, mid and posterior lung parenchyma (Figure 2). ROIs were positioned in the slices passing at the level of the carina bifurcation and in both right and left lung. The ROIs to measure SD of the noise were positioned in the background air outside of the chest in an area without ghosting artefacts. This procedure was repeated in three representative inspiratory and three expiratory phases for each dynamic scan in order to take SI variation related to breathing cycle into account. For each dynamic scan were therefore positioned 42 ROIs.



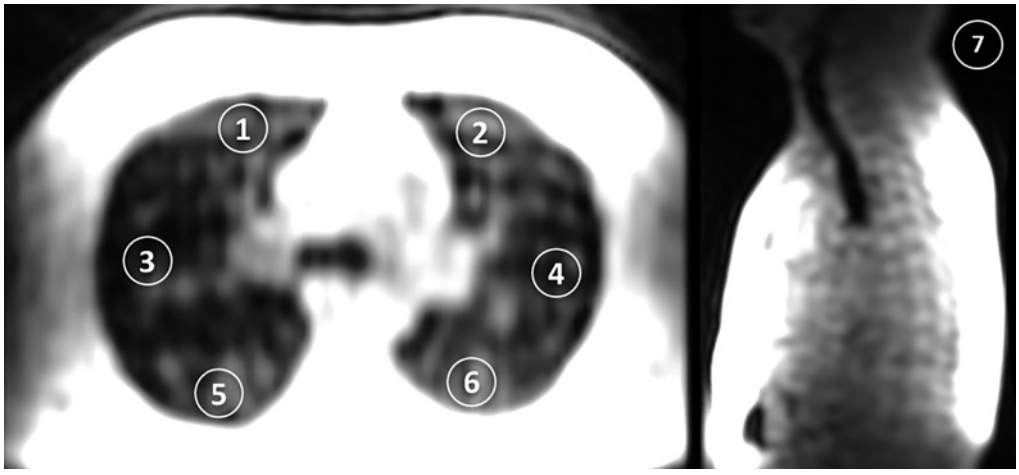


**Figure 2. Signal-to-noise ratio analysis.** Example slice of region of interest (ROI) positioning for signal-to-noise ratio (SNR) measurements. Six ROIs are positioned in the lung parenchyma: 1=right anterior, 2=left anterior, 3=mid-right, 4=mid-left, 5=right posterior and 6=left posterior. ROI number 7 is positioned in the air outside of the body to measure image noise.

*Trapped air quantification*

TA was quantified using the CF-MRI scoring system [21]. This scoring system evaluates the five lung lobes and lingula as the sixth lobe. CF-MRI quantifies the extent of TA in 4 categories per lobe:

0=absent, 1=TA<33% lobe volume; 2=TA between 33-67% lobe volume; 3=TA>67% of the lobe volume(21). TA was scored on breath-hold end-expiratory SPGR ($TA_{bh}$) and on the FD ventilation maps ($TA_{FD}$). On 3D FD maps, TA was detected when large color scale variations were present outside the major blood vessels. TA scores were expressed as a percentage of the maximum possible score, on a 0-100 scale. The observer was also asked to judge if ventilation maps were useful to detect TA relative to breath-hold scans according to a five point scale (Utility score): 1=disagree strongly; 2=disagree; 3=neither agree nor disagree; 4=agree; 5=strongly agree.

### Statistics

Descriptive statistics were used. T-test was used to assess differences for repeated measurement of SNR, image quality, and TA. Strength of association between TA score on breath-hold images ($TA_{bh}$) and on FD ventilation maps ($TA_{FD}$) was computed with the Pearson test. Finally, Intra-Class Correlation Coefficient test was used to assess agreement on TA score between $TA_{bh}$ and $TA_{FD}$. Statistical analyses were performed using SPSS version 20.0 for windows. Continuous variables are displayed as mean (±Standard Deviations) or median (interquartile range) depending on data distribution. P-values less than 0.05 (two tailed) were considered statistically significant.

## Results

Five healthy volunteers (median age 30 years, age range 27-35 years, 2 female) and four patients (mean age 23 years, age range 10-43 years, no female) were enrolled in the study. All subjects successfully completed the MRI protocol.

### Image quality

Image quality, SNR and TA data are summarized in table 1. There were no significant differences in image quality between $SPGR_C$ and DISCO regarding ghosting and motion artifacts (p=0.2). Similarly there were no significant differences on image quality for scoring TA between $SPGR_{bh}$ and FD ventilation maps (p=0.16).

### SNR

There were no significant differences in SNR between $SPGR_C$ and DISCO (p=0.79). Differences in SNR were found between ventral and mid lung portions (t=4.1, p<0.001; 95% C.I. 4.7-13.8), between ventral and dorsal lung portions (t=-4.62, p<0.001; 95% C.I. -23.2- -9.2), and between mid and dorsal lung portions (t=-8.2, p<0.001; 95% C.I. -31.7- -19.2) (Figure 3). SNR was significantly lower in inspiration than in expiration (t=3.53, p<0.01; 95% C.I. 3.6-12.7), while there were no significant differences in SNR between right and left lung (p=0.38).

## Trapped air assessment

There were no significant differences between $TA_{bh}$ and $TA_{FD}$ (p=0.44). Good agreement between $TA_{bh}$ and $TA_{FD}$ was also confirmed by ICC analysis (ICC=0.875). Bland-Altman and identity plots did not show systematic errors, although $TA_{FD}$ was slightly higher than $TA_{bh}$ (Figure 4). The observer agreed on judging FD ventilation maps useful to detect TA (p<0.0001). High correlation between $TA_{bh}$ and $TA_{FD}$ was found (r=0.877; p<0.001).

**Table 1.** Image quality, signal-to-noise ratio and trapped air.

| Parameter | Value |
|---|---|
| **Image quality $SPGR_{bh}$** | 4.55±1.04 |
| **Image quality $SPGR_{C}$** | 4.44±1.05 |
| **Image quality DISCO** | 4±1.15 |
| **$SNR_{SPGRC}$** | 32±33.87 |
| **$SNR_{DISCO}$** | 31.4±29.3 |
| **$TA_{bh}$** | 21.7±38.3 % |
| **$TA_{FD}$** | 24.2±43.1 % |
| **Utility score FD** | 4±1.5 |

$SPGR_{bh}$=3D Spoiled Gradient echo breath-hold; $SPGR_{C}$=conventional SPGR multi-phase; DISCO=DIfferential Sub-sampling with Cartesian Ordering; $SNR_{SPGRC}$=Signal-to-noise ratio $SPGR_{C}$; $TA_{bh}$=Trapped Air scored on breath-hold SPGR; $TA_{F}$=TA scored on Fourier Decomposition ventilation maps. Data are presented as mean ±2 Standard Deviations

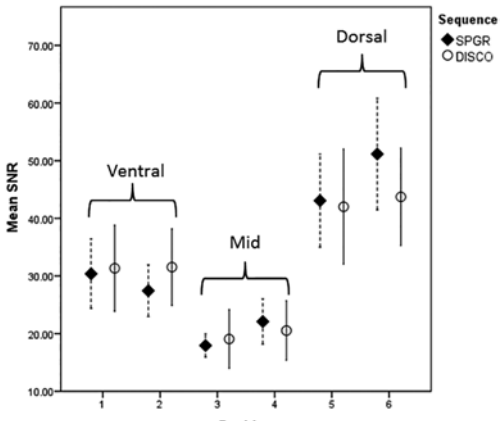


**Figure 3.**

Y-axis=Mean Signal-to-Noise Ratio (SNR). X-axis=positions of region of interest (ROI) on lung parenchyma: 1=right anterior, 2=left anterior, 3=mid-right, 4=mid-left, 5=right posterior and 6=left posterior. Note significant differences in SNR between anterior and mid, anterior and dorsal, and between mid and dorsal lung portions (all p<0.001).

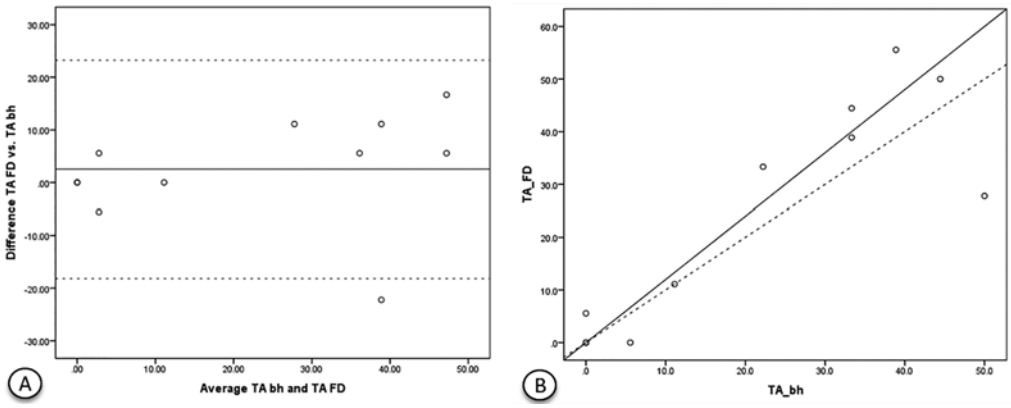


**Figure 4. Bland-Altman and identity plots.** (A) Bland-Altman plot of trapped air (TA) assessment between Fourier Decomposition (FD) ventilation maps ($TA_{FD}$) and Spoiled Gradient echo (SPGR) end-expiratory breath-hold scans ($TA_{bh}$). Solid line=mean difference $TA_{FD}$ vs $TA_{bh}$, dotted line=±2 SD. (B) Identity plots between $TA_{FD}$ and $TA_{bh}$; solid line =correlation line, dotted line= identity line (y=1*x+0). Note that $TA_{FD}$ is slightly higher than $TA_{bh}$.

## Discussion

In this study, we evaluated feasibility of 3D FD lung MRI using $SPGR_C$ and DISCO scans. We also compared image quality, SNR and TA assessment using $SPGR_{bh}$, against the 3D FD ventilation maps.

Firstly, we showed that both $SPGR_C$ and DISCO allowed obtaining 3D FD ventilation maps with similar quality despite different temporal resolution. For perfusion imaging, the temporal resolution of $SPGR_C$ was not able to detect changes in perfusion because was similar to the heart rate. While faster scan rate (>5 Hz) could lead to FD analysis with two spectral peaks, one for ventilation and one for perfusion, the acquisition speed of our DISCO implementation could not detect reliably the perfusion peak. This might be explained by the lack of in-flow effect in the 3D technique compared to the 2D scanning approaches. Scan rate might also be increased by enabling higher ARC parallel imaging accelerator factors up to 12 or higher [11] for perfusion peak detection. Compressing sensing (CS) could be also used to increase the scan rate more effectively and allow a better detection of the perfusion peak [22]. In our institution CS was not available at the time of the study, therefore we could not evaluate it.

Secondly, we observed that similar image quality and SNR were achieved with $SPGR_C$ and DISCO because similar imaging parameters were used. DISCO may introduce more ghosting and blurring artifact derived from the view sharing but in our study it was not critical for imaging registration and 3D FD imaging. SNR analysis also confirmed heterogeneity of SNR in lung parenchyma due to the known effect of gravity on blood distribution and due to the respiratory cycle [23].

Finally, we showed that TA assessed on breath-hold scan and FD ventilation maps was equivalent (Figure 5). Despite slightly higher values for $TA_{FD}$ compared to $TA_{bh}$, this was not significant and good agreement between the methods was seen. Interestingly, the observer considered the FD ventilation maps easier to score TA because the color scale facilitated the detection. In our protocol, the use of a MRI compatible spirometer also improved detection of TA on $SPGR_{bh}$ but with limited SNR and spatial resolution than a typical CT scan [23]. This problem may be overcome using ultra-short TE (UTE) sequences in the future. Nonetheless UTE scans are characterized by long free-breathing scans (e.g. 5-7 min) and may be prone to respiratory artifact hampering TA detection [24]. Our 3D FD method allows obtaining similar information about TA, but with shorter acquisition times that might be critical in severely ill or non-compliant patients.

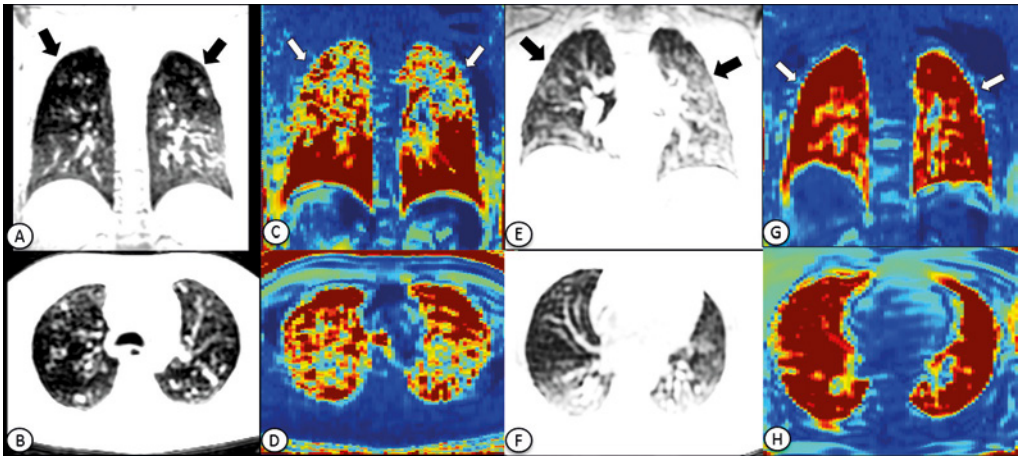


**Figure 5. Coronal and axial 3D SPGR breath-hold (a-b-e-f) and 3D Fourier Decomposition ventilation maps (c-d-g-h) in a patient with CF (a-d) and a healthy volunteer (e-h).** Note the signal void in the upper lobes in an area of severe trapped air (black arrows in a and white arrow in d) and homogeneous signal in the volunteer (black arrows in e and white arrows in h).

There are some limitations that might have reduced agreement between $TA_{bh}$ and $TA_{FD}$. The first limitation of our study is that TA was compared in images acquired using different breathing conditions. As discussed, FD ventilation maps were acquired near functional residual volume level (FRC) using free breathing acquisition, while $SPGR_{bh}$ was acquired after a deep expiration at residual volume (RV). It has been shown that CT scans acquired near FRC overestimate TA relative to scans acquired near RV [26]. This coincides with our findings that $TA_{FD}$ was slightly higher than $TA_{bh}$, although still not significantly different.

The second limitation of our study is that we did not compare SNR and image quality of 2D FD versus our 3D FD ventilation maps. We did not add 2D FD because of time constraint and ethical board approval. However, we aimed to demonstrate feasibility of 3D FD against breath-hold expiratory scans.

The third limitation of our study was that it was a single center study in a small number of subjects, which limits external validity of our findings. Further improvement of MRI protocol will allow us to apply this method in a larger cohort study and to compare TA assessment with 3D FD with other established techniques for measuring TA (i.e. plethysmography or hyperpolarized-noble gases MRI).

## Conclusions

We have shown that both 3D $SPGR_C$ and DISCO acquisition schemes enable 3D FD ventilation maps of similar quality despite different temporal resolutions. 3D FD ventilation maps were as good as end-expiratory breath-hold scan to quantify TA, but the observer judged 3D FD easier to interpret. 3D FD enables a more comprehensive assessment of TA compared to 2D FD techniques and it is more amenable for patient comfort. This method might be applied in critically ill or non-collaborative patients to perform ventilation imaging with MRI.

## Bibliography


1. Teel GS, Engeler CE, Tashijian JH, duCret RP. Imaging of small airways disease. Radiographics [Internet] 1996;16:27–41. doi: 10.1148/radiographics.16.1.27.
2. Coxson HO, Leipsic J, Parraga G, Sin DD. Using pulmonary imaging to move chronic obstructive pulmonary disease beyond FEV1. Am. J. Respir. Crit. Care Med. 2014;190:135–144. doi: 10.1164/rccm.201402-0256PP.
3. Sung A, Naidich D, Belinskaya I, Raoof S. The role of chest radiography and computed tomography in the diagnosis and management of asthma. Curr Opin Pulm Med [Internet] 2007;13:31–36. doi: 10.1097/MCP.0b013e328011bfbc.
4. Tiddens H A WM, Donaldson SH, Rosenfeld M, Paré PD. Cystic fibrosis lung disease starts in the small airways: can we treat it more effectively? Pediatr. Pulmonol. [Internet] 2010;45:107–17. doi: 10.1002/ppul.21154.
5. Wielpütz MO, Puderbach M, Kopp-Schneider A, et al. Magnetic Resonance Imaging Detects Changes in Structure and Perfusion, and Response to Therapy in Early Cystic Fibrosis Lung Disease. Am. J. Respir. Crit. Care Med. [Internet] 2014:1–49. doi: 10.1164/rccm.201309-1659OC.
6. Tepper L A, Utens EMWJ, Caudri D, Bos AC, Gonzalez-Graniel K, Duivenvoorden HJ, van der Wiel ECW, Quittner AL, Tiddens H a WM. Impact of bronchiectasis and trapped air on quality of life and exacerbations in cystic fibrosis. Eur. Respir. J. [Internet] 2013;42:371–9. doi: 10.1183/09031936.00137612.
7. Ley S. Lung imaging. Eur. Respir. Rev. [Internet] 2015;24:240–245. doi: 10.1183/16000617.00011214.
8. Tiddens HAWM, Rosenow T. What did we learn from two decades of chest computed tomography in cystic fibrosis ? Pediatr. Radiol. 2014;44:1490–1495. doi: 10.1007/s00247-014-2964-6.
9. Kuo W, Ciet P, Tiddens H a WM, Zhang W, Guillerman RP, van Straten M. Monitoring cystic fibrosis lung disease by computed tomography. Radiation risk in perspective. Am. J. Respir. Crit. Care Med. [Internet] 2014;189:1328–36. doi: 10.1164/rccm.201311-2099CI.
10. Wielpütz MO, Mall MA. Imaging modalities in cystic fibrosis. Curr. Opin. Pulm. Med. [Internet] 2015;21:609–616. doi: 10.1097/MCP.0000000000000213.
11. Ciet P, Tiddens HAWM, Wielopolski PA, Wild JM, Lee EY, Morana G, Lequin MH. Magnetic resonance imaging in children: common problems and possible solutions for lung and airways imaging. Pediatr. Radiol. [Internet] 2015. doi: 10.1007/s00247-015-3420-y.
12. Bauman G, Puderbach M, Deimling M, Jellus V, Chefd'hotel C, Dinkel J, Hintze C, Kauczor H-U, Schad LR. Non-contrast-enhanced perfusion and ventilation assessment of the human lung by means of fourier decomposition in proton MRI. Magn. Reson. Med. [Internet] 2009;62:656–64. doi: 10.1002/mrm.22031.
13. Bauman G, Scholz A, Rivoire J, Terekhov M, Friedrich J, De Oliveira A, Semmler W, Schreiber LM, Puderbach M. Lung ventilation- and perfusion-weighted Fourier decomposition magnetic resonance imaging: In vivo validation with hyperpolarized 3He and dynamic contrast-enhanced MRI. Magn. Reson. Med. 2013;69:229–237. doi: 10.1002/mrm.24236.
14. Bauman G, Puderbach M, Heimann T, Kopp-Schneider A, Fritzsching E, Mall M a, Eichinger M. Validation of Fourier decomposition MRI with dynamic contrast-enhanced MRI using visual and automated scoring of pulmonary perfusion in young cystic fibrosis patients. Eur. J. Radiol. [Internet] 2013;82:2371–7. doi: 10.1016/j.ejrad.2013.08.018.
15. Sommer G, Bauman G, Koenigkam-Santos M, Draenkow C, Heussel CP, Kauczor H-U, Schlemmer H-P, Puderbach M. Non-contrast-enhanced preoperative assessment of lung perfusion in patients with non-small-cell lung cancer using Fourier decomposition magnetic resonance imaging. Eur. J. Radiol. [Internet] 2013;82:e879–e887. doi: 10.1016/j.ejrad.2013.06.030.
16. Schönfeld C, Cebotari S, Voskrebenzev A, et al. Performance of perfusion-weighted Fourier decomposition MRI for detection of chronic pulmonary emboli. J. Magn. Reson. Imaging [Internet] 2015;42:72–9. doi: 10.1002/jmri.24764.

17. Saranathan M, Rettmann DW, Hargreaves BA, Clarke SE, Vasanawala SS. DIfferential subsampling with cartesian ordering (DISCO): A high spatio-temporal resolution dixon imaging sequence for multiphasic contrast enhanced abdominal imaging. J. Magn. Reson. Imaging 2012;35:1484–1492. doi: 10.1002/jmri.23602.

18. Tustison NJ, Cook PA, Gee JC. NIH Public Access. 2011;29:1310–1320. doi: 10.1109/TMI.2010.2046908. N4ITK.

19. Klein S, Staring M, Murphy K, Viergever MA, Pluim JPW. elastix: a toolbox for intensity-based medical image registration. IEEE Trans. Med. Imaging [Internet] 2010;29:196–205. doi: 10.1109/TMI.2009.2035616.

20. Mogalle K, Perez-rovira A, Ciet P, Doorn PA Van, Tiddens HAWM, Ploeg AT Van Der, Bruijne M De, Mc E. Quantification of Diaphragm Mechanics in Pompe Disease using Dynamic 3D MRI. PLoS One 2016;(In Press):1–23. doi: 10.1371/journal.pone.0158912.

21. Tepper L A., Ciet P, Caudri D, Quittner AL, Utens EMWJ, Tiddens H a. WM. Validating chest MRI to detect and monitor cystic fibrosis lung disease in a pediatric cohort. Pediatr. Pulmonol. [Internet] 2015:n/a–n/a. doi: 10.1002/ppul.23328.

22. Tsao J, Kozerke S. MRI temporal acceleration techniques. J. Magn. Reson. Imaging [Internet] 2012;36:543–560. doi: 10.1002/jmri.23640.

23. Bankier A a, O'Donnell CR, Mai VM, Storey P, De Maertelaer V, Edelman RR, Chen Q. Impact of lung volume on MR signal intensity changes of the lung parenchyma. J. Magn. Reson. Imaging [Internet] 2004;20:961–6. doi: 10.1002/jmri.20198.

24. Dournes G, Grodzki D, Macey J, Girodet P-O, Fayon M, Chateil J-F, Montaudon M, Berger P, Laurent F. Quiet Submillimeter MR Imaging of the Lung Is Feasible with a PETRA Sequence at 1.5 T. Radiology [Internet] 2015;276:258–65. doi: 10.1148/radiol.15141655.

25. Salamon ER, Lever S, Kuo W, Ciet P, Tiddens HAWM. Spirometer guided chest imaging in children: It is worth the effort. Pediatr. Pulmonol. 2015;Submitted:1–9. doi: 10.1002/ppul.23490.

26. Bonnel A-S, Song SM-H, Kesavarju K, Newaskar M, Paxton CJ, Bloch D a, Moss RB, Robinson TE. Quantitative air-trapping analysis in children with mild cystic fibrosis lung disease. Pediatr. Pulmonol. [Internet] 2004;38:396–405. doi: 10.1002/ppul.20091.

# Part 2

## Airways imaging using MRI

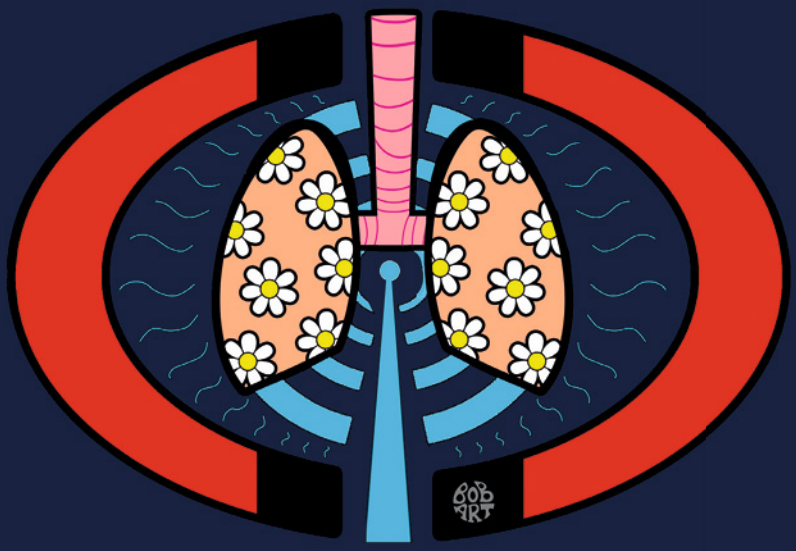

# Chapter 8

## Spirometer-controlled Cine Magnetic Resonance Imaging Used to Diagnose Tracheobronchomalacia in Paediatric Patients

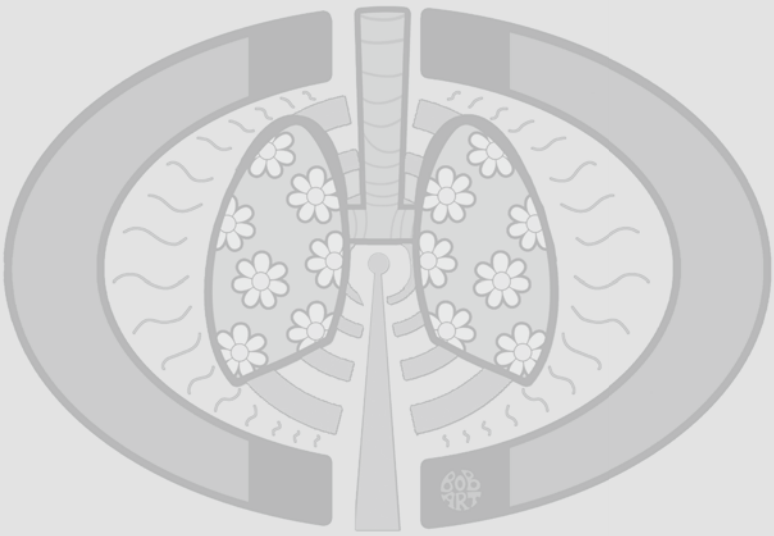

*Ciet P, Wielopolski P, Manniesing R, Lever S, de Bruijne M, Morana G, Muzzio PC, Lequin MH, Tiddens HAWM*

Eur Respir J. 2014 Jan;43(1):115-24

## Abstract

Tracheobronchomalacia (TBM) is defined as an excessive collapse of the intrathoracic trachea. Bronchoscopy is the gold standard for diagnosing TBM; however it has major disadvantages, such as general anaesthesia. Cine computed tomography (CT) is a noninvasive alternative used to diagnose TBM, but its use in children is restricted by ionising radiation. Our aim was to evaluate the feasibility of spirometer-controlled cine magnetic resonance imaging (MRI) as an alternative to cine-CT in a retrospective study.

12 children with a mean age (range) of 12 years (7-17 years), suspected of having TBM, underwent cine-MRI. Static scans were acquired at end-inspiration and expiration covering the thorax using a three-dimensional spoiled gradient echo sequence. Three-dimensional dynamic scans were performed covering only the central airways. TBM was defined as a decrease of the trachea or bronchi diameter >50% at end-expiration in the static and dynamic scans.

The success rate of the cine-MRI protocol was 92%. Cine-MRI was compared with bronchoscopy or chest CT in seven subjects. TBM was diagnosed by cine-MRI in seven (58%) out of 12 children and was confirmed by bronchoscopy or CT. In four patients, cine-MRI demonstrated tracheal narrowing that was not present in the static scans.

Spirometer controlled cine-MRI is a promising technique to assess TBM in children and has the potential to replace bronchoscopy.

## Introduction

Tracheobronchomalacia (TBM) is defined as an excessive collapse of the intrathoracic part of the trachea and/or main bronchi during expiration [1]. When TBM is suspected, a diagnostic bronchoscopy, which is the current gold standard, is used to confirm the diagnosis [1,2]. In paediatric populations, bronchoscopy has the disadvantage that it is invasive and requires general anaesthesia, while the child maintains spontaneous breathing [1]. In addition, relevant daily life breathing manoeuvres, such as forced expiration and coughing, cannot be routinely performed during the procedure [3-4]. Bronchoscopy using conscious sedation, which preserves spontaneous ventilation for the evaluation of TBM, is used in adults [4]. However, this technique in children is, in general, not feasible due to a lack of cooperation [4]. Finally, bronchoscopy does not provide exact measurements of airway dimensions comparable to that provided by imaging techniques [3-5].

For these reasons an alternative to bronchoscopy, cine computed tomography (CT), has been used to assess TBM [6]. An advantage of this technique is that the collapsibility of trachea and mainstem bronchi can be evaluated during static and dynamic conditions [7-9]. However cine-CT to detect TBM exposes the patient to ionising radiation [1], which is a more significant problem for children than adults because they are more susceptible to the harmful effects of ionising radiation [10-14]. Cine-magnetic resonance imaging (MRI) might be an attractive, radiation-free alternative to cine-CT to diagnose TBM [15-19]. Recent improvements in MR technology (ultrafast imaging) allow dynamic evaluations of the central airway dimensions (cine-MRI) [15]. Ideally, breathing manoeuvres during cine-MRI should be standardised using cine-MRI spirometry. A MRI compatible spirometer was recently developed and tested [20]. To our knowledge, spirometer controlled cine-MRI has not been applied before in TBM assessment [16,18].



We have previously demonstrated feasibility of the spirometer-controlled cine-MRI protocol in healthy adult volunteers [21]. The aim of this study was to retrospectively evaluate the diagnostic feasibility of this protocol in a group of children, who needed a chest MRI for various indications and in whom the treating clinician requested assessment of TBM to be included in the evaluation. In this paper we describe our methodology and the results of a retrospective image analysis of static and dynamic changes in central airway dimensions in 12 patients.

## Materials and Methods

### MRI

The cine-MRI protocol for the diagnosis of TBM was developed in 10 healthy adult volunteers mean age (range) 31 years (30-33 years) for which approval was obtained from our institutional ethics committee [21]. Scanning was performed using a 1.5T Signa Hdxt MRI (General Electric Healthcare, Milwaukee, WI, USA) and using the whole body coil for radiofrequency excitation and an eight-

channel torso coil for signal reception. The protocol consisted of static and dynamic acquisitions. Three-dimensional (3D) "static" images at total lung capacity and residual volume were acquired by two 13-s breath-holds covering the complete thoracic region at end-inspiration and end-expiration using a 3D radiofrequency-spoiled gradient echo sequence (SPGR) with repetition time /echo time=1.4/0.6 ms, flip angle 2°, sagittal volume acquisition with a true isotropic 3.0×3.0×3.0 $mm^3$ voxels. 3D cine-MRI acquisitions were acquired with the same imaging parameters and voxel resolution, but only covering the trachea and mainstem bronchi (12 cm sagitally). This was used to measure their dimensions and to monitor, in pseudo-real time, the airway dimensions to detect dynamic TBM during forced expiration and cough. The temporal resolution of 400 ms per volume was achieved using the temporally resolved imaging of contrast kinetics scan platform with accelerated imaging options [22]. 48 volumes were collected in 19 s. Overall the acquisition time per patient, including localisers, adjustments, breathing instructions and executing all scans, was ~15 min (range 9-20 min). The videos of the dynamic acquisitions are provided in the online supplementary material.

### Bronchoscopy

Bronchoscopies in six out of the 11 patients were carried out by a paediatric pulmonologist as part of diagnostic workup in routine patient care, using a flexible bronchoscope, external diameter 3.5 mm or 5.5 mm (Olympus; Tokyo, Japan), during general anaesthesia while maintaining spontaneous breathing. Airway malacia was diagnosed by visual inspection of the airway shape and dynamics during spontaneous breathing without positive end-expiratory pressure, and during spontaneous coughing in case this occurred. Malacia was defined as collapse of at ≥50% of the airway lumen, during the expiration phase while spontaneous breathing or while the patient was coughing [2].

### Breathing instructions

Paediatric patients, who needed a chest MRI for various clinical indications and in whom the treating clinician requested assessment of TBM, based on their clinical presentation, were scheduled for a spirometer controlled cine-MRI. Half an hour before the MRI all children did a routine upright spirometry, coached by a lung function technician. Next, the required breathing manoeuvres were repeated in the supine position on a stretcher using an MRI-compatible spirometer (custom made Masterscope MRI; CareFusion, Houten, The Netherlands). The purpose of the training was: 1) to monitor and standardise breathing manoeuvres by using spirometer volume data during the MRI; 2) to reduce anxiety related to MRI investigations; and 3) to increase the number of successful MRI investigations. For the static MRI acquisitions, children were trained to obtain a maximal breath-hold time of 15 s at ≥95% of the inspired vital capacity (VC) and at ≥90% of the expired VC. For the dynamic cine-MRI sequences, patients were asked to perform two expiration manoeuvres, both starting at ≥95% of the inspired VC. The first dynamic manoeuvre was a full forced expiration, which was done as follows. From tidal breathing, patients were asked: 1) to take a deep breath and reach ≥95% of inspired VC; 2) to hold their breath for a few seconds; 3) to perform a forced expiration and reach ≥90% of the expired VC; 4) to hold their breath for a few seconds; and 5) to breathe quietly i.e.

tidal volume breathing. The second dynamic manoeuvre was a full expiration manoeuvre while the patient produced a series of repeated coughs starting at ≥95% of inspired VC ≥90% of the expired VC. After the training session, the patient was transferred to the MRI scanner. Breathing instructions during the MRI were given by the same lung function technician that performed the training, using the MRI compatible built-in patient audio system. During the MRI investigation, the lung technician sitting next to the MRI technician monitored the inspired and expired volumes and dynamic flows on the computer screen of the MRI-compatible spirometer set-up (Figure 1). Based on the spirometer data, the lung function technician instructed the MRI technician on when to start or stop the scans in case of patient error.

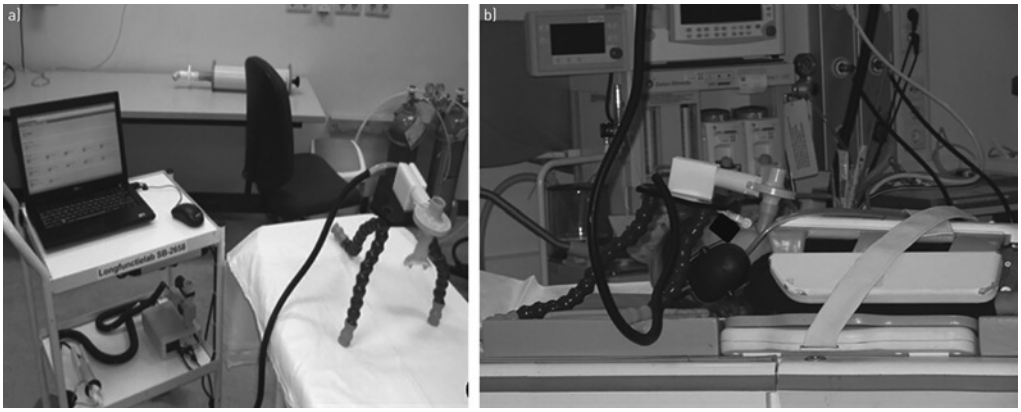


**Figure 1. Magnetic resonance imaging (MRI) spirometer set-up.** (a) Metal-free plastic tripod, mouthpiece and the MRI compatible spirometer in the lung function room where the breathing manoeuvres were trained. (b) In the MRI suite, the spirometer is connected to the computer by long plastic tubing, which is introduced into the Faraday cage, to measure differential pressure for computation of flow.



## Image analysis

The first post-processing step for the lung and central airway images was performed on the scanner console and consisted of equalising the inhomogeneity/signal attenuation of the receiver array coil by using a surface coil correction intensity algorithm and adaptive filtering to enhance the signal-to-noise ratio. Image quality criteria were defined for both static and dynamic scans. Static scans were repeated if blurring of structures and ghosting were observed. Dynamic scans were repeated when excessive blurring and ghosting of the chest wall was observed. The latter was indicative of a lack of temporal resolution or due to a suboptimal breath-hold, as shown on the spirometer screen.

The image data were then transferred to an Advantage windows workstation, or onto the Advantage Windows Server (General Electric Healthcare) to perform cine multi-planar reformats (MPR) from the 3D cine-MRI data collected. The MRIs were jointly evaluated by two radiologists (P. Ciet and M.H.

Lequin) and a standard report was written. For the retrospective analysis, all images were assessed by a radiologist (P. Ciet) blinded to all clinical data using manual tracing as described below.

The manual assessment started by analysing both the end-inspiration and end-expiration static volumes in the four-dimensional (4D) MPR platform. Reformats were performed to measure the diameters of the trachea and main stem bronchi using a window and magnification setting (zoom factor 3.0). Windowing was performed by setting the window level at one half of the maximum signal recorded around the trachea with a window width of 0. First, the narrowest section of the trachea in expiration was determined using a two-dimensional (2D) calliper to measure the anteroposterior diameter in a view perpendicular to the trachea midline (Figure 2). To compare the degree of narrowing, a similar section, angled according to the main tracheal axis, was reformatted using the surrounding anatomical structures as spatial reference and the distance to the carina. Next, the dynamic acquisitions (both forced expiration and coughing) were evaluated in cine-mode on the 4D reconstruction platform both in longitudinal and perpendicular views of the trachea to determine which one of the 48 volumes showed the greatest tracheal collapse (Figure 3). Having selected the "most collapsed" volume, the same distance measurements were performed as described for the breath-hold acquisitions.

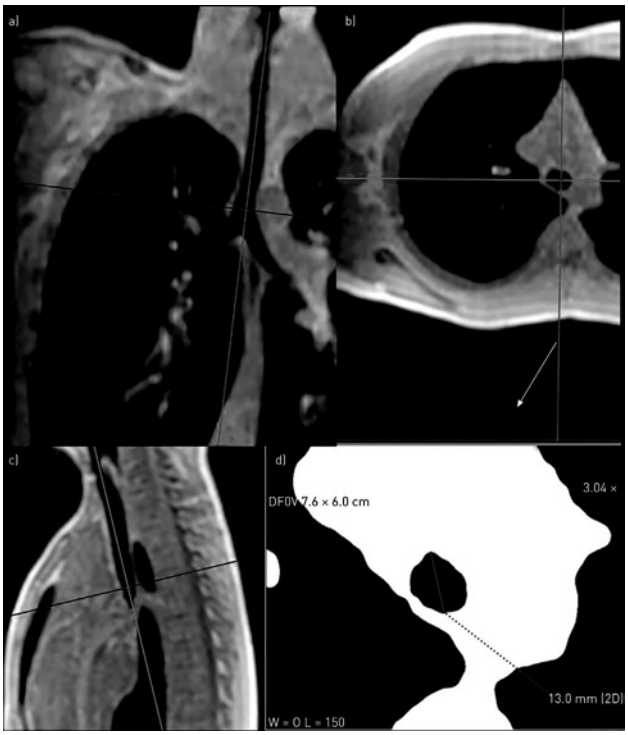


**Figure 2. Image analysis of dimensions for the trachea in patient B.** (a-c) Reformats of three-dimensional radiofrequency-spoiled gradient echo sequence breath-hold during inspiration. In part a) blue line and in part (c) the orange line indicates the correct orientation along the midline of the trachea. (d) Shows the anteroposterior diameter in reformatted axial view (double oblique) and with the window set at full-width half-maximum image.

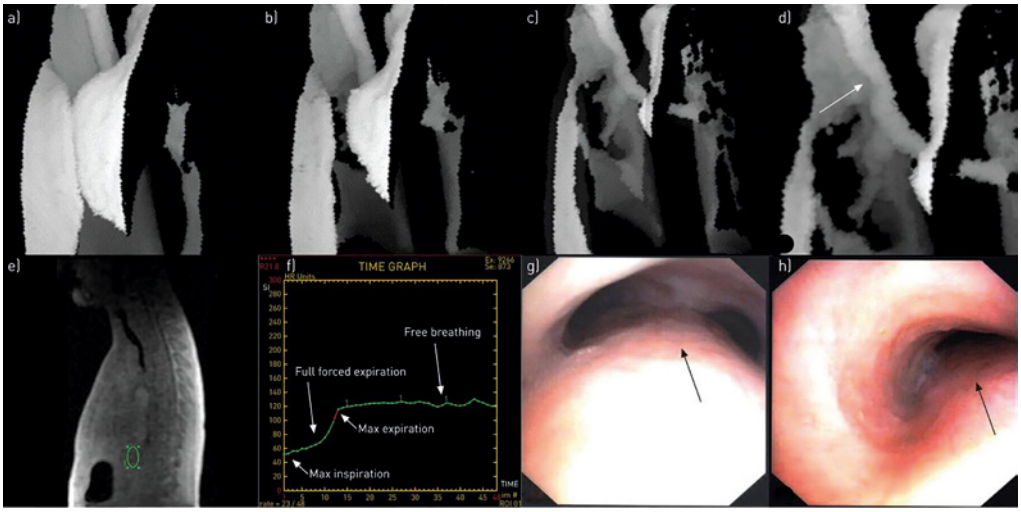


Figure 3. **Dynamic magnetic resonance imaging (a-e), respiratory waveform (f) and bronchoscopy images (g, h) in patient C.** (a-d) Three-dimensional volume rendering at different time points during the forced expiration manoeuvre. Note the trachea impression above the carina (d) indicated by a white arrow. (e) Sagittal view with green region of interest to assess signal intensity changes according to the breathing cycle. (f) Correspondent signal intensity changes (approximate respiratory waveform) over time, where y-axis represents signal intensity and x-axis the time. Note the inverted relationship between volume of air in the lungs and signal intensity. The patient started the forced expiratory manoeuvre from maximum inspiration, which showed the lowest signal intensity, until maximum expiration, which had the greatest signal intensity. (g,h) Screen shots of the bronchoscopy evaluation in the same patient show bulging of the pars membranacea (black arrows) in addition to the anterior impression (h) just above the carina caused by the innominate artery, which corresponds to the tracheal impression as shown on image (d).



TBM was defined as a reduction in airway anteroposterior diameter of the trachea of >50% between static end-inspiration and end-expiration scans or between end-inspiration and dynamic scans as routinely used in the bronchoscopy assessment of TBM [17]. This definition was used to compare the diagnosis of TBM using cine-MRI with the subjective diagnosis made by the physician for those patients in whom a bronchoscopy was performed.

## Comparison between MRI and bronchoscopy or CT

In six subjects bronchoscopy reports were available, which were compared to 3D cine-MRI. Since, using bronchoscopy, TBM is diagnosed by visual assessment and not by exact measurements of airway dimensions, bronchoscopy reports were used to verify the 3D cine-MRI findings. In one subject, only a spirometer controlled CT was available for confirmation of the diagnosis of TBM. For this patient, chest CT images were compared to cine-MRI findings.

**Table 1**

| Patient | Age | Sex | Clinical diagnosis | Cine-MRI | Broncho-scopy | CT | Ins (mm) | Exp (mm) | %Δ | Ins (mm) | Exp (mm) | %Δ | Notes on the point of maximal collapse |
|---|---|---|---|---|---|---|---|---|---|---|---|---|---|
| | | | | | | | Static | | | Dynamic | | | |
| **A** | 11 | M | Upper recurrent airway infections | No TBM | NA | NA | 11.3 | 9.7 | 14.15 | 18 | 12.1 | 32.77 | -------- |
| **B** | 15 | F | Cystic fibrosis | TBM | NA | TBM | 13.7 | 5.9 | 56.93 | 12.6 | 4.5 | 64.28 | Static, TM and LBM (ØΔ=52.88% (10.4 vs. 4.9 mm) |
| **C** | 7 | M | Tracheo-oesophageal fistula | TBM | TBM | NA | 11.5 | 6.2 | 46.08 | 11.3 | 4.2 | 62.83 | TM, :dynamic and complete collapse above carina |
| **D** | 13 | M | Atrial Sept Defect Type II | TBM | BM | NA | 12.1 | 10.5 | 13.22 | 10.5 | 8.1 | 22.85 | LBM, dynamic and complete collapse of left Bronchus |
| **E** | 14 | F | Chronic cough | No TBM | NA | NA | 12.5 | 9.5 | 24 | 12.5 | 8.4 | 32.8 | -------- |
| **F** | 17 | M | Lower respiratory tract infections, Laryngomalacia | TBM | TBM | NA | 13.3 | 8.4 | 36.84 | 11.3 | 4.2 | 62.83 | TM above carina |
| **G** | 11 | F | Chronic cough | NA | NA | NA | 15.3 | 13.4 | 12.41 | 15.4 | 10.1 | 34.41 | -------- |
| **H** | 9 | M | CCAML | No TBM | Mild laryngo-malacia | NA | 12.2 | 7.8 | 36.06 | 11.9 | 7.1 | 40.33 | -------- |
| **I** | 15 | M | Asthma | No TBM | Normal anatomy | NA | 12.9 | 8.3 | 35.65 | 12.9 | 7.5 | 41.86 | -------- |
| **L** | 16 | M | Premature, asthma | TBM | NA | NA | 17.2 | 11.8 | 31.39 | 17 | 5.6 | 67.05 | -------- |
| **M** | 13 | M | Atypical Asthma | TBM | NA | NA | 13.5 | 8.8 | 34.81 | 13.3 | 6 | 54.88 | -------- |
| **N** | 11 | F | Frequent upper and lower airway infections, asthma | TBM | TBM | NA | 11.8 | 9 | 23.72 | 11.8 | 5.1 | 56.77 | Dynamic, (T and LMB) |

MRI=magnetic resonance imaging; CT=computed tomography; Ins=inspiration; Exp=expiration; %Δ=calibre reduction expressed as a percentage of inspiratory cross-sectional area; TBM=tracheobronchomalacia; NA=not available; TM=tracheomalacia; LBM=left bronchomalacia; ØΔ=change in diameter; BM=bronchomalacia; CCAML=congenital cystic adenomatoid malformation of the lung; T=trachea; LMB=left main bronchus.

## Results

Our retrospective analysis included 12 paediatric patients (Table 1), who all had a cine-MRI made for various clinical diagnostic reasons. Informed consent was obtained from the parents of the patient for anonymous analysis of the data and registered in the electronic patient record. Approval for this retrospective study was obtained from the institutional review board.

The success rate of the MRI protocol was 92%, only one participant was not able to successfully complete all required breathing manoeuvres, because of fear induced by the noise in the MRI scanner. Images were of diagnostic quality for analysis in all subjects, except for the patient mentioned above. Airway dimensions measured by the manual assessment are displayed in Table 1. TBM was diagnosed in seven children (58%): patient B, C, D, F, L, M and N (Table 1). In patients B and C, TBM was visible on the static and dynamic MRI images, whereas in patients D, F, L, M and N, TBM was visible only in the dynamic MRI acquisitions. Patient B and N had severe TBM, which involved the trachea at the level of the carina and the left main bronchus.

In patient B, who declined bronchoscopy, a follow-up chest CT scan confirmed the diagnosis of TBM. Patient C had TBM 1 cm above the carina, confirmed by bronchoscopy (Figure 3). Patient D had complete collapse of the left, main bronchus during forced expiration, which was defined as "isolated distal narrowing" by bronchoscopy. Patient F had a severe TBM, just above the carina, clearly visible during forced expiration, which was confirmed by bronchoscopy evaluation (Figures 4 and 5).

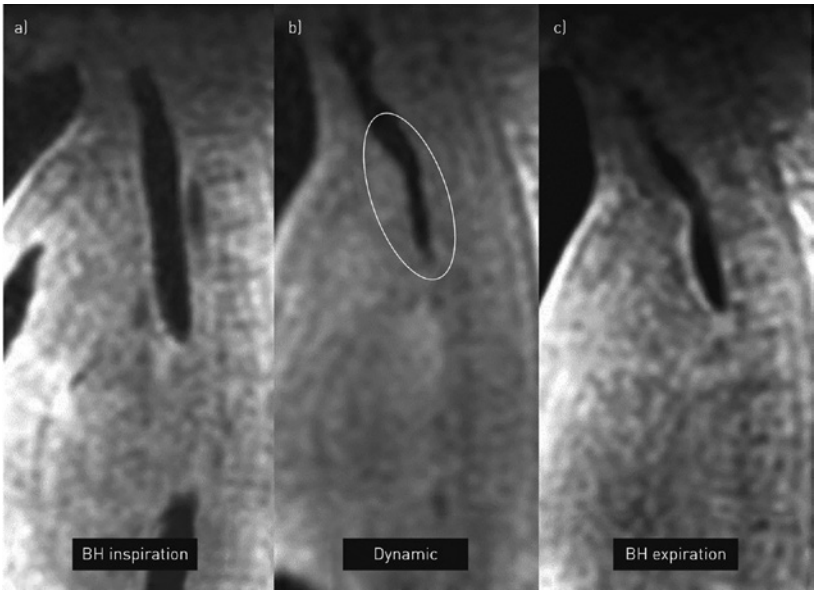


**Figure 4. Tracheobronchomalacia in patient F.** Breath-hold (BH) inspiration (a), dynamic forced expiration manoeuvre (b) and BH expiration (c). Note the trachea lumen in the dynamic acquisition is smaller than the breath-hold expiration acquisition (white oval).

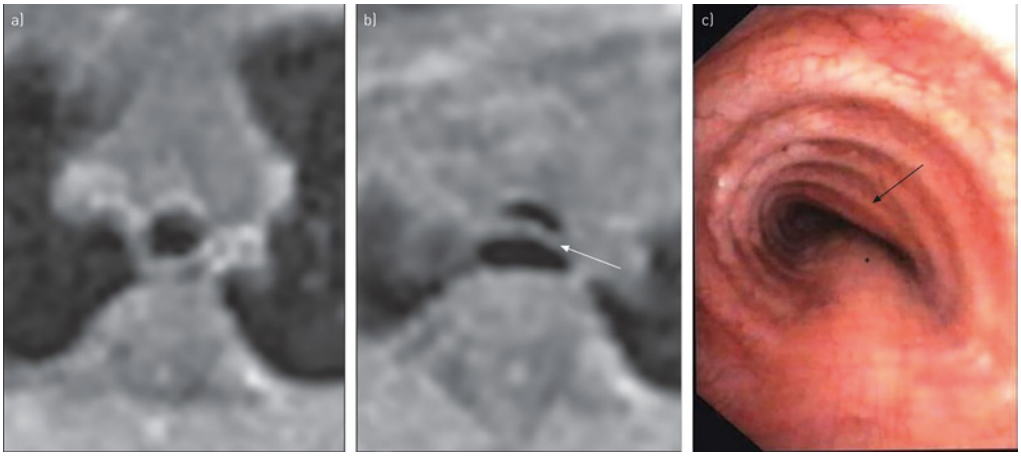


**Figure 5. Axial reformatted images of patient F.** (a) Breath-hold magnetic resonance image at end inspiration showing a normal round configuration of the trachea. (b) Breath-hold at end expiration at the same level, note that the pars membranacea is bulging into the lumen (white arrow). (c) Shows the same location as a) and b) during bronchoscopy evaluation during tidal volume breathing, which confirms tracheomalacia caused by an abnormal configuration of cartilage rings (black arrow) combined with bulging of the pars membranacea (*).

Patients L and M had TBM ~1.5 cm above the carina bifurcation. Patients H and I had negative results for TBM both on MRI and bronchoscopy assessments. Patients A, E, and G were negative for TBM to cine-MRI assessment and no further diagnostic procedures were felt necessary by the treating physician. Patients L and M had positive results for TBM by cine-MRI assessment, and further assessment by bronchoscopy was proposed by the treating physician but declined by the parents. Hence, for all seven patients with available bronchoscopy and/or CT, cine-MRI was in concordance with bronchoscopy and/or CT for the presence or absence of TBM. For four patients this could not be evaluated.

## Discussion

Our retrospective study shows that spirometer controlled 3D cine-MRI is a promising technique in children for the static and dynamic evaluation of central airway dimensions and could potentially replace bronchoscopy for the evaluation of TBM.

### Cine-MRI *versus* bronchoscopy

The most important advantage of 3D cine-MRI was that airway dimensions could be studied during standardised static and dynamic breathing manoeuvres, such as forced expiration and cough. The use of a MRI compatible spirometer allowed us to monitor inspiratory and expiratory flows and volume during the MRI acquisitions [20]. By acquiring simultaneous functional and morphological data, the severity of the TBM can be established in a standardised fashion.

To evaluate airway dimensions using bronchoscopy in a child, general anaesthesia is frequently needed. The challenge for the anaesthesiologist is to control the level of anaesthetic in such a way that the child continues to breathe spontaneously. In instances where the anaesthesia is not deep enough, the patient begins to move and often coughs, a situation that the anaesthesiologist tries to avoid. In cases where the anaesthesia is too deep or when a muscle relaxant is used, spontaneous breathing stops and positive-pressure ventilation is needed, which can obscure TBM due to the positive trans-pulmonary pressure. Conscious sedation enables controlled breathing manoeuvres during flexible bronchoscopy to be attempted. However, in children, this technique is not used routinely since it is highly dependent on cooperation, which is considered challenging for most children [4]. Hence, cine-MRI in children aged ≥8 years is an attractive alternative for bronchoscopy to study airway dimensions using standardised breathing manoeuvres.

The second advantage of cine-MRI is that it allowed us to obtain objective airway dimensions using post-processing image analysis tools. This is complicated to do with bronchoscopy and, therefore, not routinely performed [5]. Despite developments in bronchoscopy optics, the image remains essentially 2D and distorted [5]. Hence, the diagnosis of malacia using bronchoscopy is mostly subjective and not very reproducible [5]. Importantly MRI has multiplanar imaging capabilities, so 3D data sets can be reconstructed providing measurements in every possible plane and cross-section [16,18].

The third advantage of 3D cine-MRI is that the procedure is less invasive, relative to bronchoscopy, since it does not require general anaesthesia and anaesthesia related risks can be avoided. Bronchoscopy under general anaesthesia introduces a small risk of complications, such as respiratory depression, oxygen desaturation, apnoea, bradycardia, epistaxis, airway bleeding, excessive cough, transient laryngospasm, procedure induced atelectasis, pneumothorax and in rare cases, even fatalities [3-4].



### Cine-MRI *versus* cine-CT

The most important advantage of cine-MRI compared with cine-CT was that it did not expose the children to ionising, which is a greater risk for children than adults [10-14]. Since cine-MRI does not require ionising radiation, all required breathing manoeuvres can be tested without concerns for radiation exposure. In addition, the procedure can be repeated when not executed correctly. In our group of patients, we had to repeat at least one acquisition per examination in 50% of tested children. Hence, this could be done without adding risks for the child.

### Feasibility of spirometer controlled cine-MRI

Cine-MRI also has a number of limitations, the most important of which is the need for optimal cooperation by the patient. This is a clear challenge, especially in young children. Most children are able to do spirometry from the age of ≥6 years, however, having a child enter the bore of the MRI covered by a body-coil, with a spirometer in their mouth (Figure 1c), followed by the requested breathing manoeuvres, requires careful preparation and coaching. In general we consider our spirometer

controlled cine-MRI feasible for children aged ≥8 years. In our small series we only had one child, aged 11 years, who could not complete the intended manoeuvres.

The second limitation of our cine-MRI protocol was the low spatial resolution. Clearly, the resolution of the MRI images is inferior to that of CT [9]. In our MRI protocol we obtained an isotropic voxel of 3.0 $mm^3$, which is inferior to the submillimetric voxels that can be achieved with CT [9]. However, this resolution was sufficient to detect the reduction of the airway lumen of the large airways, with diameters ranging from 1 to 2 cm in children 6-18 years [23]. For smaller airways and dynamic images a higher spatial resolution will be needed. We expect that by using parallel imaging, a dedicated torso coil and a higher field strength, the spatial and temporal resolution can be further improved in the near future.

### Further validation

A major limitation of our retrospective study is that we evaluated a small selected group of patients. However, the main aim of our study was to test the feasibility of the method for later use on a larger scale with a more heterogeneous group of patients [24]. Therefore, further validation of cine-MRI as a diagnostic method for TBM is required using a prospective study. We aim to do this comparing the diagnostic performance of bronchoscopy to spirometer controlled 3D cine-MRI.

## Conclusions

This retrospective study showed that spirometer controlled 3D cine-MRI is a promising method to assess static and dynamic changes of central airway dimensions when TBM is suspected. Cine-MRI may be a more sensitive, faster and safer alternative for the diagnosis of static and dynamic TBM in cooperative children than bronchoscopy or cine-CT. Further prospective validation studies are required comparing the sensitivity and specificity of cine-MRI *versus* bronchoscopy and/or CT to diagnose TBM.

## Bibliography


1. Carden KA, Boiselle PM, Waltz DA, et al. Tracheomalacia and tracheobronchomalacia in children and adults: an in-depth review. Chest 2005; 127: 984–1005.
2. Boogaard R, Huijsmans SH, Pijnenburg MWH, et al. Tracheomalacia and bronchomalacia in children: incidence and patient characteristics. Chest 2005; 128: 3391–3397.
3. de Blic J, Marchac V, Scheinmann P. Complications of flexible bronchoscopy in children: prospective study of 1,328 procedures. Eur Respir J 2002; 20: 1271–1276.
4. Midulla F, de Blic J, Barbato A, et al. Flexible endoscopy of paediatric airways. Eur Respir J 2003; 22: 698–708.
5. Williamson JP, James AL, Phillips MJ, et al. Quantifying tracheobronchial tree dimensions: methods, limitations and emerging techniques. Eur Respir J 2009; 34: 42–55.
6. Gilkeson RC, Ciancibello LM, Hejal RB, et al. Tracheobronchomalacia: dynamic airway evaluation with multidetector CT. AJR Am J Roentgenol 2001; 176: 205–210.
7. Baroni RH, Feller-Kopman D, Nishino M, et al. Tracheobronchomalacia: comparison between end-expiratory and dynamic expiratory CT for evaluation of central airway collapse. Radiology 2005; 235: 635–641.
8. Heyer CM, Nuesslein TG, Jung D, et al. Tracheobronchial anomalies and stenoses: detection with low-dose multidetector CT with virtual tracheobronchoscopy–comparison with flexible tracheobronchoscopy. Radiology 2007; 242: 542–549.
9. Lee EY, Boiselle PM. Tracheobronchomalacia in infants and children: multidetector CT evaluation. Radiology 2009; 252: 7–22.
10. de Jong PA, Mayo JR, Golmohammadi K, et al. Estimation of cancer mortality associated with repetitive computed tomography scanning. Am J Respir Crit Care Med 2006; 173: 199–203.
11. Kubo T, Lin PJ, Stiller W, et al. Radiation dose reduction in chest CT: a review. AJR Am J Roentgenol 2008; 190: 335–343.
12. Sadetzki S, Mandelzweig L. Childhood exposure to external ionising radiation and solid cancer risk. Br J Cancer 2009; 100: 1021–1025.CrossRefMedlineWeb of ScienceGoogle Scholar
13. Strauss KJ, Goske MJ, Kaste SC, et al. Image gently: ten steps you can take to optimize image quality and lower CT dose for pediatric patients. AJR Am J Roentgenol 2010; 194: 868–873.
14. Brink JA, Amis ES. Image wisely: a campaign to increase awareness about adult radiation protection. Radiology 2010; 257: 601–602.
15. Eichinger M, Tetzlaff R, Puderbach M, et al. Proton magnetic resonance imaging for assessment of lung function and respiratory dynamics. Eur J Radiol 2007; 64: 329–334.
16. Yedururi S, Guillerman RP, Chung T, et al. Multimodality imaging of tracheobronchial disorders in children. Radiographics 2008; 28: e29.
17. Suto Y, Tanabe Y. Evaluation of tracheal collapsibility in patients with tracheomalacia using dynamic MR imaging during coughing. AJR Am J Roentgenol 1998; 171: 393–394.
18. Faust RA, Remley KB, Rimell FL. Real-time, cine magnetic resonance imaging for evaluation of the pediatric airway. Laryngoscope 2001; 111: 2187–2190.
19. Heussel CP, Ley S, Biedermann A, et al. Respiratory lumenal change of the pharynx and trachea in normal subjects and COPD patients: assessment by cine-MRI. Eur Radiol 2004; 14: 2188–2197.
20. Eichinger M, Puderbach M, Smith HJ, et al. Magnetic resonance-compatible-spirometry: principle, technical evaluation and application. Eur Respir J 2007; 30: 972–979.
21. Wielopolski PA, Ciet P, Krestin GP, et al. Automated airway lumen segmentation and characterization for use in patients with traqueomalacia: a feasibility Study. 2010. Proceedings of the ISMRM-ESMRMB Joint Annual Meeting, 2010. Abstract 4610. Available from: http://cds.ismrm.org/protected/10MProceedings/files/1_program.htm

22. Turski PA, Korosec FR, Carroll TJ, et al. Contrast-enhanced magnetic resonance angiography of the carotid bifurcation using the time-resolved imaging of contrast kinetics (TRICKS) technique. Top Magn Reson Imaging 2001; 12: 175–181.

23. Griscom NT, Wohl ME. Dimensions of the growing trachea related to age and gender. AJR Am J Roentgenol 1986; 146: 233–237.

24. Thabane L, Ma J, Chu R, et al. A tutorial on pilot studies: the what, why and how. BMC Med Res Methodol 2010; 10: 1.

# Chapter 9

## Technical Innovation: Cine-MRI of Tracheal Dynamics in Healthy Volunteers and Patients with Tracheomalacia

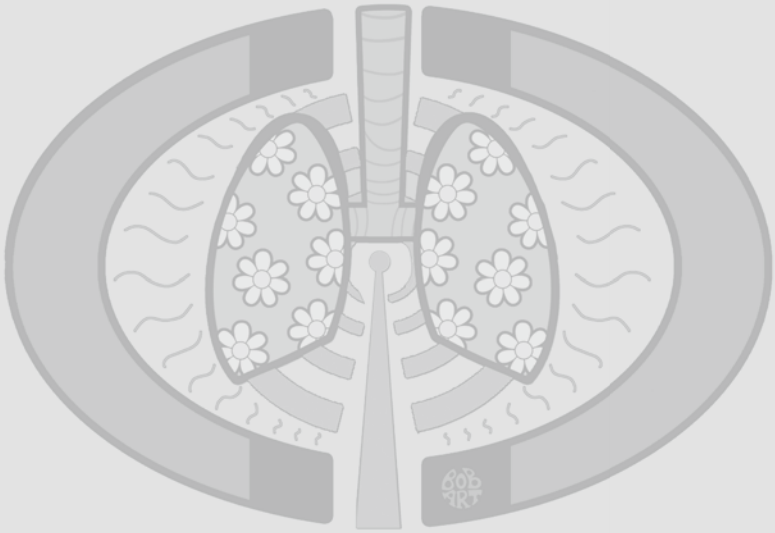

*Ciet P, Boiselle PA, Heidinger B, O'Donnel C, Andrinopolou EA, Alsop D, Litmanovich DE*

*Submitted*

## Abstract

Bronchoscopy and multi-Detector Computed Tomography (MDCT) are routinely used to assess tracheobronchomalacia (TBM). Recently, dynamic Magnetic Resonance Imaging (cine-MRI) has been proposed as a radiation-free alternative to MDCT. To date, cine-MRI has not been directly compared to MDCT to assess TBM. In this study, we tested cine-MRI assessment of airway dynamics during various breathing conditions and compared cine-MRI and MDCT measurements in healthy volunteers and patients with suspected TBM.

## Introduction

Multi-Detector Computed Tomography (MDCT) is routinely used to assess tracheobronchomalacia (TBM) [1]. MDCT has comparable sensitivity to bronchoscopy for diagnosing TBM [2], but is limited by radiation exposure. Recently, dynamic Magnetic Resonance Imaging (cine-MRI) has been proposed as radiation-free alternative to MDCT [3]. Cine-MRI enables repeated imaging during a variety of breathing conditions [3]. To date, cine-MRI has not been directly compared to MDCT to assess TBM, nor has its feasibility been determined for assessing airway dynamics during a wide range of breathing maneuvers. The aims of this study are two-fold: 1) to develop and test a protocol for cine-MRI assessment of central airway dynamics during different breathing conditions; and 2) to compare cine-MRI measurements with MDCT in a group of healthy volunteers and COPD patients.

## Material and Methods

Detailed description of the technique is provided in the online supplement.

Following informed consent (IRB Protocol number: 2013P000286), healthy volunteers and COPD patients with suspected TBM underwent cine-MRI and MDCT on the same day. Inclusion and exclusion criteria are displayed in the online supplement (OLS) (Table 1E).

### MRI

We used a cine-MRI protocol developed for pediatric patients to assess central airway dynamics while employing an expanded series of breathing maneuvers in both healthy volunteers and several patients with COPD [3]. Scanning was performed using a 1.5T Signa Hdxt MRI (General Electric Healthcare, Milwaukee, WI, USA) scanner and an eight-channel torso coil for signal reception. The protocol consisted of static end-inspiratory and expiratory scans, and three dynamic maneuvers: forced vital capacity (FVC), tidal breathing (TB) and hyperventilation (HV). All maneuvers were performed through active respiratory coaching by a respiratory physiologist. The protocol lasted 25-30 minutes. Videos of each dynamic scan are provided in the OLS.

### CT

All CT examinations were performed using a 64-detector row scanner in the craniocaudal direction for both end-inspiratory and 1 dynamic mid expiratory scan. For healthy volunteers, a validated low-dose protocol was employed [4]. For COPD patients, MDCT consisted of a validated protocol [5], as described in the OLS.

### Imaging analysis

MRI and CT images were analyzed by an experienced thoracic radiologist. Patients' identifications were coded, scans were reviewed in randomized order, CT and MRI scans were reviewed on different

dates. Images were analyzed using Myriam (Intrasense, Montpellier, France). Cross-sectional area (CSA), anterior-posterior (AP) and left-right (LR) diameters were recorded at 7 levels: 1 cm (T1), 2 cm (T2), 3 cm (T3), 4 cm (T4), 5 cm (T5) above the carina in the trachea and 1 cm below the carina in the right (RMB) and left (LMB) main bronchus. CSA and AP/LR diameters were measured with a hand-tracing tool on axial reformat perpendicular to the trachea centerline. %Collapse was calculated: $\%CSA=100x[1 - CSA_{FVC}/CSA_i]$ where $CSA_i$ and $CSA_{FVC}$ are the CSA of the airway lumen at end-inspiration and during FVC, respectively. The % variation for AP (%AP) and LR (%LR) diameters between inspiration and expiration were calculated with the same formula. The observer repeated 50% of the MRI and CT measurements one month apart to determine intra-observer variability.

### Statistics

Descriptive statistics were used to summarize central airways measurements between volunteers and patients. Intra-Class Correlation coefficient (ICC) and Bland-Altman plots were used to assess inter-modality (MRI versus CT) and intra-observer agreements (MRI versus MRI and CT versus CT).

Finally, using mixed-effects models analysis, we assessed the contribution of %AP and %LR to %CSA. Moreover, we assessed %CSA between the breathing maneuvers and the central airways positions (T1-T5 and RMB-LMB). Differences were statistically significant if $p<0.05$.

## Results

The MRI and CT data of twelve participants (median 64.5 years, range 45-77 years, 7 female) including nine volunteers and three COPD patients, were compared. All MRI and MDCT examinations were technically successful.

### Inter-modality and intra-observer agreement

Table 1 shows ICC for inter-modality and inter-observer agreements. Bland-Altman plots are presented in OLS (Figure 2E-8E). Inter-modality agreement was very good (ICC>0.81) for end-inspiratory images, and good (ICC>0.61) for dynamic expiratory images. Intra-observer agreement for MRI measurements was good to very good (ICC 0.77-0.99) for all breathing maneuvers and very good (ICC. 0.98) for CT measurements.

### Central airways dynamics in different breathing conditions

Central airways %collapse for the static and dynamic scans for volunteers and patients are summarized in Table 2. Cine-MRI showed an increasing tracheal %collapse according to the respiratory effort required by the breathing maneuvers. In volunteers, the greatest tracheal %collapse was for the FVC maneuver, followed by BH, HV and TB. In COPD patients, tracheal %collapse was higher during HV than BH. Main bronchi %collapse followed the same decreasing order of the tracheal %collapse in volunteers, but not in patients that showed increased airways changes during TB.

## Central airways dynamics for volunteers and patients

All three COPD patients had "saber-sheath" tracheas as diagnosed by CT, with excessive collapse of the LR diameter. COPD patients showed higher tracheal changes during dynamic breathing maneuvers compared to healthy volunteers (Table 2). Tracheal %collapse was 1.5 times higher in COPD patients than healthy volunteers for all three dynamic maneuvers, except BH maneuvers. Tracheal %AP was greater in COPD patients during FVC and HV maneuvers. Tracheal %LR was 1.4 (FVC maneuver) and 7 (TB maneuver) times greater in COPD patients than volunteers. Main stem bronchi also showed larger dynamic changes in patients than in volunteers.

Central airways %collapse per position between volunteers and patients is presented in OLS (Tables 2E-5E). %CSA per position was homogenous in the group of volunteers, while larger variability was seen in 3 COPD patients.

## Mixed-model analysis

Mixed model analysis showed that %AP and %LR equally contributed to %CSA (Table 3). There were significant differences in CSA changes between BH (used as reference) and TB, but not between FVC and HV. Changes of CSA were significantly different between T2 (used as reference), and T4 and T5, but not for T1, T3, RMB and LMB (Table 4).

**Table 1.** Inter-modality (MRI versus CT) and intra-observer agreement for MRI and CT measurements.

| **Inter-modality agreement (MRI vs. CT)** | | | | |
|---|---|---|---|---|
| | *End-Inspiratory* | | | *Dynamic expiratory* |
| **CSA** | 0.928 | | | 0.81 |
| **AP** | 0.884 | | | 0.616 |
| **LR** | 0.815 | | | 0.670 |
| **Intra-observer agreement MRI** | | | | |
| | *BH* | *FVC* | *TB* | *HV* |
| **CSA** | 0.987 | 0.992 | 0.985 | 0.897 |
| **AP** | 0.944 | 0.939 | 0.946 | 0.774 |
| **LR** | 0.928 | 0.958 | 0.948 | 0.825 |
| **Intra-observer agreement CT** | | | | |
| **CSA** | 0.996 | | | |
| **AP** | 0.991 | | | |
| **LR** | 0.981 | | | |

BH=breath-hold maneuver; FVC=forced vital capacity maneuver; TB=tidal breathing maneuver; HV=hyperventilation maneuver; CSA=cross-sectional area; AP=anterior-posterior diameter; LR=left-right diameter. ICC values between 0.40-0.60; 0.60-0.80; and ≥0.80 are considered to represent moderate, good, and very good agreement, respectively.

**Table 2.** Percentage of collapse (%Collpase) for trachea and main bronchi between volunteers and patients.

| | **Volunteers** | | | | **Patients** | | | |
|---|---|---|---|---|---|---|---|---|
| **TRACHEA** | | | | | | | | |
| | *BH* | *FVC* | *TB* | *HV* | *BH* | *FVC* | *TB* | *HV* |
| **CSA** | 26.4 (19.2-27.4)% | 52 (29.5-64.2)% | 9.9 (5.7-11.8)% | 14.2 (13.3-17.1)% | 14 (11.4-17.7)% | 77 (71.7-77.7)% | 14.9 (14.4-27.3)% | 21.5 (11.1-25.3)% |
| **AP** | 16 (13.3-19.8)% | 35.1 (25.5-49.4)% | 7.2 (0.6-8.7)% | 9.2 (6.9-10.5)% | 17.2 (12.4-17.5)% | 41.7 (39.7-54.4)% | 10 (8.4-13.1)% | 13.9 (9.2-15)% |
| **LR** | 9.7 (8.3-13.8)% | 29 (9.7-33.2)% | 2 (-0.3-6.8)% | 5.9 (3.3-7.2)% | 7.7 (2.7-7.8)% | 42.1 (39-49.7)% | 14.2 (6.5-21.4)% | 9.8 (6-10.8)% |
| **MAIN STEM BRONCHI** | | | | | | | | |
| | *BH* | *FVC* | *TB* | *HV* | *BH* | *FVC* | *TB* | *HV* |
| **CSA** | 24.3 (10.8-33.4)% | 54.4 (40.4-58.7)% | 8.4 (1.6-9.9)% | 21.9 (17.6-24.6)% | 21.5 (8.7-22.8)% | 62.8 (58.6-71.8)% | 20.7 (18-23.3)% | 20.6 (11.4-24.9)% |
| **AP** | 13.6 (2.2-20.3)% | 46.8 (21.1-59)% | 4.4 (0.4-6.3)% | 9 (8.8-18.9)% | 20.8 (15.1-21.9)% | 61.1 (48-61.9)% | 12.3 (10.4-16.7)% | 18.7 (7.5-25.5)% |
| **LR** | 0.5 (0.1-16.6)% | 16.2 (11.2-30.8)% | 2.3 (1.8-4.2)% | 8.6 (5.7-16.4)% | 10.8 (9.2-13.2)% | 37.8 (36.5-44.4)% | 7.4 (5.8-8.7)% | 9.8 (6.3-15.4)% |

BH=breath-hold, FVC=forced vital capacity; TB=tidal breathing; HV=hyperventilation; CSA=cross-sectional area, AP=anterior-posterior diameter; LR=left-right diameter. Data are expressed as median ($1^{st}$-$3^{rd}$ quartiles) for volunteers and as median (min - max) for patients.

**Table 3.** Effect table for %CSA outcomes based on the mixed-effects models analysis.

| **Outcome: CSA (%)** | | | |
|---|---|---|---|
| | **Estimate effect** | **SE** | **p-value** |
| **Intercept** | 9.5019 | 1.5993 | p<0.0001* |
| **AP (%)** | 0.6141 | 0.0419 | p<0.0001* |
| **LR (%)** | 0.5938 | 0.0522 | p<0.0001* |
| **TB** | -3.1546 | 1.4439 | 0.0289* |
| **FVC** | 2.5527 | 2.0474 | 0.2125 |
| **HV** | -2.7399 | 1.4367 | 0.0565 |
| **T1** | -0.1041 | 1.3715 | 0.9395 |
| **T3** | -1.9429 | 1.3365 | 0.1460 |
| **T4** | -3.8882 | 1.4036 | 0.0056* |
| **T5** | -2.6775 | 1.2745 | 0.0357* |
| **RMB** | -1.3526 | 1.9216 | 0.4815 |
| **LMB** | 1.1488 | 1.8268 | 0.5294 |

AP=Anterior-posterior diameter; LR=left-right diameter; %CSA=cross-sectional area changes in %;%AP=anterior-posterior dimeter changes in %, LR%=left-right diameter changes in %, TB=tidal breathing maneuver; FVC=Forced Vital Capacity maneuver; HV=hyperventilation maneuver; T1, T3, T4, T5=tracheal points at 1 cm, 3 cm, 4 cm and 5 cm from carina respectively; RMB=1 cm below the carina in the right main bronchus, LMB=1 cm below the carina in the left main bronchus; SE=Standard Error. To compare airways changes during dynamic maneuvers, BH maneuver was used as reference because representing the most standardized procedure. To compare airways changes between the central airways positions, T2 was used as reference instead of T1 to exclude the area next to the carina, which usually shows the largest changes. Note that %AP and %LR have similar estimate effect on %CSA. For example, when comparing two patients with equal %LR, a change of 1% of %AP determined a change of 0.61 % of CSA. Similarly in two patients with equal %AP, a change of 1% of %LR determined a change of 0.59 % of CSA. Significant differences are indicated by star (*).

## Discussion



Our study is the first to compare cine-MRI to MDCT in the assessment of central airway dynamics. We found that cine-MRI offered potential advantages to MDCT, most notably in terms of its enhanced capability to capture the maximal degree of expiratory collapse.

The higher %collapse for cine-MRI compared to MDCT resulted in lower inter-modality ICCs for the dynamic expiratory measurements than the end-inspiratory. This was because cine-MRI enabled to acquire multiple images during dynamic expiration and to select the time point where the trachea showed the greatest collapse (Figure 1). Conversely, MDCT only provided a single "snapshot" of the expiratory phase. Therefore, cine-MRI has the potential to avoid underestimation of TBM.

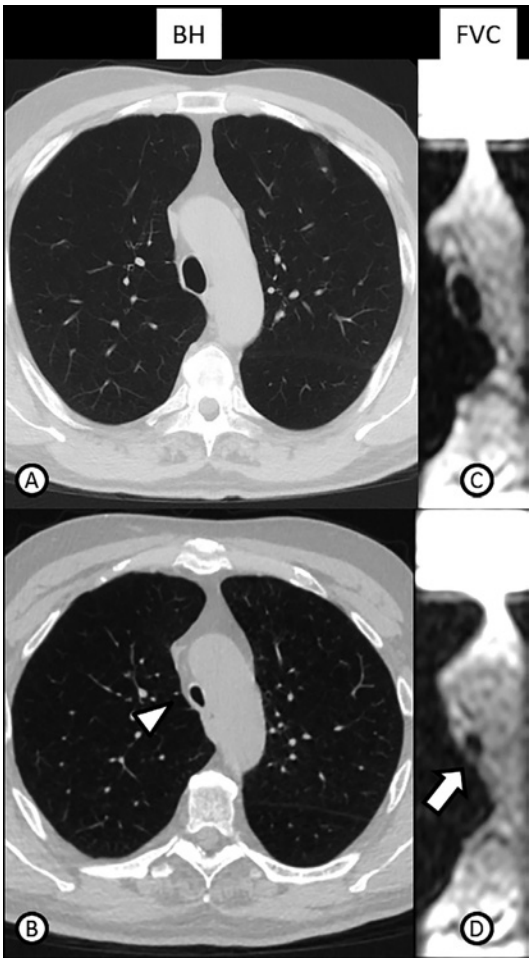


**Figure 1. Static and dynamic MRI and CT scans in a patient with saber-sheath tracheobronchomalacia (TBM).** Breath-hold end-inspiratory (A) and dynamic-expiratory (B) axial CT reformats. Forced vital capacity (FVC) inspiratory (C) and maximum dynamic expiratory (D) axial MRI reformats. Note severe lateral tracheal collapse during FVC maneuver both with CT (arrowhead) and with cine-MRI (arrow).

Secondly, we showed that cine-MRI allows comparing airways dynamics in different breathing conditions between volunteers and COPD patients. All COPD patients with TBM had greater %collapse than volunteers in the dynamic maneuvers but not during the breath hold maneuvers (Figure 2), confirming the importance of the dynamic scans to assess TBM [6].

Thirdly, for COPD patients, we found that AP and LR diameters equally contribute to CSA changes. Previous studies had shown that AP diameter contributes more than LR diameter to CSA changes [4]. This discrepancy might derive from the wider range of airways dynamics tested in our study (BH, FVC, TB and HV) compared to the BH and FVC maneuvers previously investigated. This

technique may improve our understanding of the relative contributions of AP and LR movement to tracheal collapse. This can facilitate selection of those patients who are most likely to benefit from tracheobronchoplasty to reinforce the posterior tracheal wall from those who may benefit from more conservative measures such as Continuous Positive Airway Pressure [7].

We acknowledge that the small number of participants enrolled in this pilot study is a major limitation. Although sufficient to demonstrate the feasibility and promise of these methods, a future larger study of COPD patients is needed to validate our findings and to determine their clinical utility in predicting treatment options.

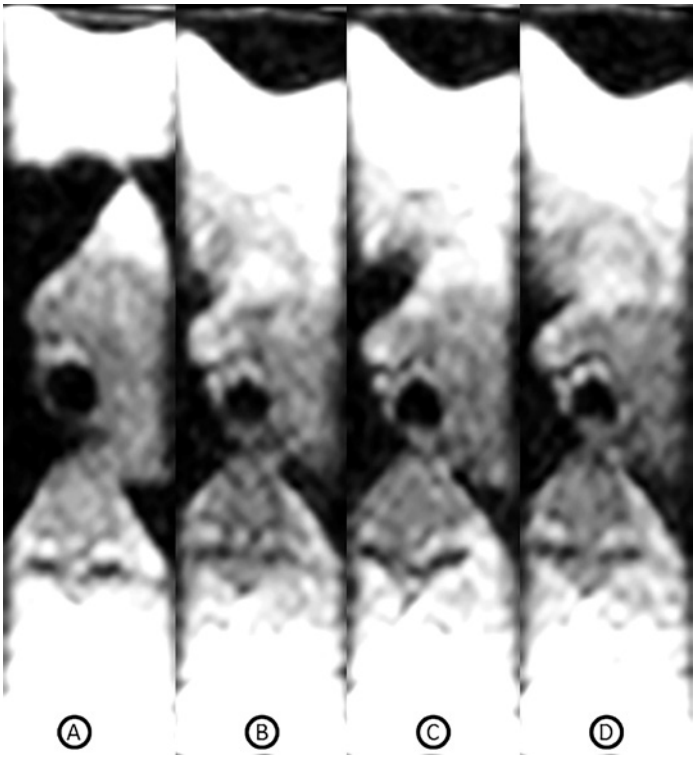


**Figure 2. Forced vital capacity (FVC) maneuver, 48 phases (3D volumes) are acquired in 19 seconds. Axial reformats of phase 1 (A), phase 13 (B), phase 21 (C) and phase 29 (D)**. Note that phase 13 (image B) shows the smallest tracheal lumen ("most collapsed").

## Conclusions

Cine-MRI is a technically feasible alternative to MDCT for assessing central airways dynamics while avoiding potentially unnecessary radiation exposure. Future studies are needed to determine its role in predicting the optimal therapeutic intervention for COPD patients with TBM.

## Bibliography


1. Carden KA, Boiselle PM, Waltz DA, Ernst A. Tracheomalacia and tracheobronchomalacia in children and adults - An in-depth review. Chest [Internet]. 2005;127(3):984–1005. Available from: <Go to ISI>://WOS:000227777500048
2. Lee EY, Litmanovich D, Boiselle PM. Multidetector CT evaluation of tracheobronchomalacia. Radiol Clin North Am [Internet]. 2009 Mar [cited 2014 May 29];47(2):261–9. Available from: http://www.ncbi.nlm.nih.gov/pubmed/19249455
3. Ciet P, Wielopolski P, Manniesing R, Lever S, de Bruijne M, Morana G, et al. Spirometer-controlled cine magnetic resonance imaging used to diagnose tracheobronchomalacia in paediatric patients. Eur Respir J [Internet]. 2014 Jan [cited 2014 Jan 29];43(1):115–24. Available from: http://www.ncbi.nlm.nih.gov/pubmed/23598953
4. Boiselle PM, O'Donnell CR, Bankier AA, Ernst A, Millet ME, Potemkin A, et al. Tracheal Collapsibility in Healthy Volunteers during Forced Expiration: Assessment with Multidetector CT. Radiology [Internet]. 2009;252(1):255–62. Available from: <Go to ISI>://WOS:000268362900031
5. O'Donnell CR, Bankier AA, O'Donnell DH, Loring SH, Boiselle PM. Static end-expiratory and dynamic forced expiratory tracheal collapse in COPD. Clin Radiol. 2014;4(164):357–62.
6. Baroni RH, Feller-kopman D, Nishino M, Hatabu H, Loring SH, Ernst A, et al. Radiology Tracheobronchomalacia : Comparison between End-expiratory and Dynamic Expiratory CT for Evaluation of Central Airway Collapse 1. 2005;(7):635–41.
7. Carden K A, Boiselle PM, Waltz D A, Ernst A. Tracheomalacia and tracheobronchomalacia in children and adults: an in-depth review. Chest [Internet]. 2005 Mar [cited 2014 May 29];127(3):984–1005. Available from: http://www.ncbi.nlm.nih.gov/pubmed/15764786

# Supplement

## Material and Methods

### Participants' selection

From September 2013 to April 2015, fifteen participants were recruited in the study according the inclusion and exclusion criteria shown in table 1E. Two subjects were consented but not scanned, the first one for a contraindication to MRI namely ferromagnetic osteosynthesis material) and the second subject for sickness on the day of the MRI. MR images of one participant could not be accessed on Myriam platform and therefore excluded. The MRI and CT data of nine healthy volunteers (median age 60 years, range 45-72 years, 6 female) and three COPD patients (median age 72 years, range 70-77 years, 1 female) were compared.

**Table 1E.** Inclusion and exclusion criteria for volunteers and patients with TBM.

| **Volunteers** | |
|---|---|
| *Inclusion criteria* | *Exclusion criteria* |
| – Between the ages of 45-75 years.<br>– Non-smoker.<br>– No known history of respiratory disease.<br>– No recent hospitalizations that required intubation.<br>– Ability to give written informed consent and willing to comply with the protocol requirements.<br>– Willing to undergo a research MRI and a research CT on the same day. | – Pregnant or lactating females.<br>– Moderate-to-severe renal impairment defined as glomerual filtration rate (GFR)/eGFR ≤ 45 mL/min.<br>– History of respiratory illness or taking any medications for respiratory issues.<br>– Unable to hold their breath for longer than 15 seconds or are unable to follow breathing instructions.<br>– Movement disorder.<br>– Known allergy to one or more of the ingredients in the investigational products, or have a history of hypersensitivity to any metals.<br>– Have any contraindications to MRI such as a pace-maker, magnetic material (i.e., surgical clips) or any other conditions that would preclude proximity to a strong magnetic field.<br>– Severe claustrophobia.<br>– Diabetic. |

| **Patients** | |
|---|---|
| *Inclusion criteria* | *Exclusion criteria* |
| – Between the ages of 45-75 years.<br>– Able to give written informed consent and are willing to comply with the protocol requirements.<br>– Meet the GOLD Stage II-IV criteria for COPD.<br>– Referred at BIDMC for MDCT assessment of the trachea for known or suspected tracheobronchomalacia.<br>– Willing to undergo an MRI in addition to their clinically scheduled MDCT. | – Pregnant or lactating females.<br>– Moderate-to-severe renal impairment, defined as a glomerular filtration rate (GFR)/eGFR ≤ 45 mL/min.<br>– History of acute respiratory illness requiring antibiotics, hospitalization, or an emergency room visit in the past 2 months.<br>– Unstable cardiac disease or myocardial infarction in the past 6 months.<br>– History of tracheal surgery, including tracheostomy.<br>– History of prior therapeutic radiation to chest or neck.<br>– History of prolonged intubation beyond 7 days.<br>– Unable to hold their breath for longer than 15 seconds or are unable to follow breathing instructions.<br>– Movement disorder.<br>– Known allergy to one or more of the ingredients in the investigational products, or have a history of hypersensitivity to any metals.<br>– Any contraindications to MRI such as a pace-maker, magnetic material (i.e., surgical clips) or any other conditions that would preclude proximity to a strong magnetic field.<br>– Severe claustrophobia.<br>– Unwilling to undergo both the MDCT and an MRI on the same day. |

## Breathing maneuvers

Subjects were asked to perform three dynamic maneuvers: forced vital capacity (FVC), tidal breathing (TB) and hyperventilation (HV). In the FVC maneuver, subjects were asked while tidal breathing,: 1) to take a deep breath and reach Total Lung capacity (TLC); 2) to hold their breath for a few seconds; 3) to perform a forced expiration and reach residual volume (RV); 4) to hold their breath for a few seconds; and 5) to breathe quietly [1]. In the TB maneuver, subjects were asked to breath-quietly, while in the HV maneuver patients increased their respiratory frequency with a respiratory cycle every 2 seconds. All static and dynamic maneuvers were performed through active spirometric monitoring by a respiratory physiologist, who ensured that maneuver was correctly performed, using a dry-seal volume displacement spirometer (Eagle II Survey spirometer; Collins Sensormedics, Yorba Linda, CA, USA).

## MRI

The cine-MRI protocol consisted of three-dimensional (3D) "static" images at TLC and RV were acquired by two 12-s breath-holds covering the complete thoracic region at end-inspiration and end-expiration. 3D cine-MRI acquisitions were acquired with the same imaging parameters and voxel

resolution of the static scans, but only covering the trachea and main stem bronchi (12 cm sagitally). In the cine-MRI scan, 48 volumes were collected in 19 seconds achieving a temporal resolution of 400 ms per volume (2)such as general anaesthesia. Cine computed tomography (CT. Videos of the dynamic scans are provided as Graphics Interchange Format (GIF) files A-C.

## CT

CT scans were performed using a 64-MDCT scanner (Light Speed VCT; General Electric Medical Systems, Milwaukee, WI, USA). Low-dose CT protocol for volunteers had the following imaging parameters: 120 kVp, 40 mA, 0.625 mm collimation, 0.5 second gantry rotation, pitch of 1.375, and 10 cm field of view. To reduce radiation exposure, helical scanning was performed in the craniocaudal direction from 2 cm above the aortic arch to 2-3 cm below the carina, corresponding to a length of approximately 8-9 cm [3]. Standard clinical protocol for COPD patients had the following parameters: 80 mA, 120 kVp, 0.625 mm detector collimation, and 0.5 s gantry rotation time. The scan length included the entire lungs [4]. All images were acquired at end-inspiration (TLC) and during forced expiration (SVC).

## Imaging Analysis

MRI and CT images were anonymized and analyzed in random order by thoracic radiologist with 7 year of experience in MRI. Images were analyzed using the "airways stent planning tool" on Myriam platform (Intrasense, Montepellier, France). This tool allows drawing a centerline in the trachea and main stem bronchi both on CT and MR images. Cross-sectional area (CSA), anterior-posterior (AP) and left-right (LR) diameters were taken in seven different positions: 1 cm (T1), 2 cm (T2), 3 cm (T3), 4 cm (T4), 5 cm (T5) above the carina in the trachea and 1 cm below the carina in the right (RMB) and left (LMB) main stem bronchi (Figure 1E). CSA and AP/LR diameters were measured with a hand-tracing tool on axial reformat perpendicular to the trachea centerline. The %Collapse was calculated as follows: $\%CSA=100x[1 - CSA_{FVC}/CSA_i]$ where $CSA_i$ and $CSA_{FVC}$ are the CSAs of the airway lumen at end-inspiration and during FVC, respectively. The % of variation for AP (and LR) diameter between inspiration and expiration was calculated as follows: $\%AP=100x[1-AP_e/AP_i]$ where $AP_i$ and $AP_e$ are the APs of the airway lumen at end-inspiration and -expiration, respectively.

A magnification setting with a zoom factor of 5 was used for central airways measurements. Window setting for MRI was set to obtain the best Contrast-to-Noise ratio (CNR) between tracheal wall and lumen by using an approach similar to chest CT with the standard lung window. Due to the lack of defined window setting for MRI, we set for each patient the window level above the background noise level and the window width approximately two-folds higher than the window level. This method supplies the best CNR between high and low density lung structures, similar to CT using the standard lung window [5]. Window setting for CT were: window length -500 and width 1600. The level of ambient (background) lighting was kept constant during all viewing sessions to ensure consistent viewing conditions.

For the FVC maneuver, the narrowest section of the trachea in forced expiration was determined using the cine-mode tool on the Advantage Windows Server (AWS) imaging platform (General Electric Healthcare, Milwaukee, WI, USA). This cine-mode tool displays longitudinal and perpendicular views of the trachea on a 4D reconstruction platform that allows selecting which one of the 48 volumes showed the greatest tracheal collapse (Figure 2). This "most collapsed" volume was used to draw the measurements previously described with Myrian. For TB and HV maneuvers, the observer used the cine-mode tool to determine all end-inspiratory and end-expiratory phases during these dynamic maneuvers. Then, these multiple end-inspiratory and end-expiratory phases of the TB and HV maneuvers were analyzed with Myrian. In the TB scans, a median of 6 inspiratory (interquartile range, IQR, 4.25-7 phases) and 6 expiratory phases (IQR 4.25-6.75) was recorded and analyzed. In the HV scans, a median of 9 inspiratory (IQR 7.25-11) and 9 expiratory phases (IQR 8-11) was recorded and analyzed. Half of the MRI ($MRI_1$ vs. $MRI_2$) and CT ($CT_1$ vs. $CT_2$) data were analyzed twice 1 month apart for intra-observer variability assessment.

### Mixed model analysis

Data were analyzed using a mixed-effects models to investigate whether there was an association between specific covariates and the outcomes of interest, while accounting for the correlation within the same patients [6]. With the mixed model analysis, we wanted to assess the contribution of %AP and %LR to %CSA.

The outcome for this model was %CSA, while the covariates were: %AP, %LR, the maneuvers (FVC, TB and HV) and the central airways positions (from T1-T5 and RMB-LMB). To compare airways changes during dynamic maneuvers, BH maneuver was used as reference because representing the most standardized procedure. To compare airways changes between the central airways positions, T2 was used as reference instead of T1 to exclude the area next to the carina, which usually shows the largest changes. Statistical analysis was performed with SPSS (version 20.0, SPSS, Chicago, IL, USA) and R (version 3.1.3, the R foundation for statistical computing, Vienna, Austria).

## Bibliography

1. Salamon ER, Lever S, Kuo W, Ciet P, Tiddens HAWM. Spirometer guided chest imaging in children: It is worth the effort. Pediatr Pulmonol 2015;Submitted:1–9.
2. Ciet P, Wielopolski P, Manniesing R, Lever S, de Bruijne M, Morana G, Muzzio PC, Lequin MH, Tiddens H A WM. Spirometer-controlled cine magnetic resonance imaging used to diagnose tracheobronchomalacia in paediatric patients. Eur Respir J 2014;43:115–24.
3. Boiselle PM, O'Donnell CR, Bankier AA, Ernst A, Millet ME, Potemkin A, Loring SH. Tracheal Collapsibility in Healthy Volunteers during Forced Expiration: Assessment with Multidetector CT. Radiology 2009;252:255–262.
4. O'Donnell CR, Bankier AA, O'Donnell DH, Loring SH, Boiselle PM. Static end-expiratory and dynamic forced expiratory tracheal collapse in COPD. Clin Radiol 2014;4:357–362.
5. Teufel M, Ketelsen D, Fleischer S, Martirosian P, Graebler-Mainka U, Stern M, Claussen CD, Schick F, Schaefer JF. Comparison between high-resolution CT and MRI using a very short echo time in patients with cystic fibrosis with extra focus on mosaic attenuation. Respiration 2013;86:302–11.
6. Verbeke, Geert; Molenberghs G. Linear Mixed Models for Longitudinal Data, 1st ed. Springer-Verlag New York; 2000. doi:10.1007/978-1-4419-0300-.

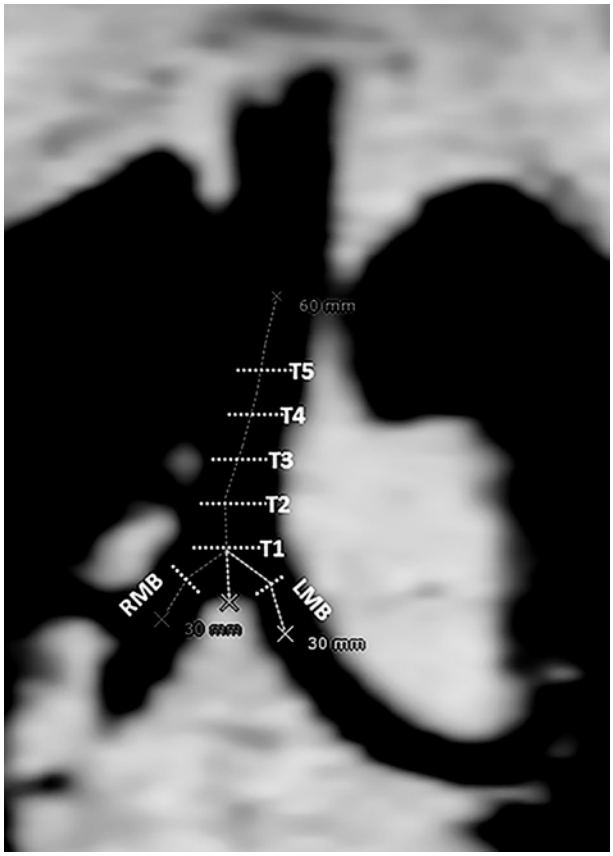


**Figure 1E. Central airways measurements.**

Cross-sectional area (CSA), anterior-posterior (AP) and left-right (LR) diameters were measured at 1 cm (T1), 2 cm (T2), 3 cm (T3), 4 cm (T4) and 5 cm (T5) from carina bifurcation. CSA, AP and LR were also measured at 1 cm below the carina in the right (RMB) and left main bronchus (LMB).

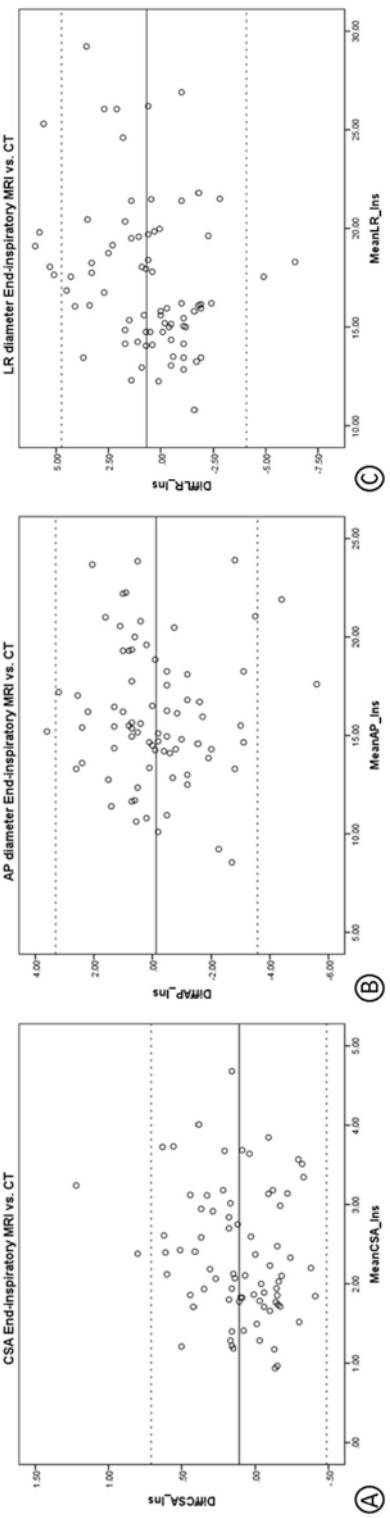


**Figure 2E.** Inter-modality agreement ($MRI_1$ versus $CT_1$) for end-inspiratory measurements.

Bland-Altman plots of a) end-inspiratory cross-sectional area (CSA), b) end-inspiratory anterior-posterior (AP) diameter and c) end-inspiratory left-right (LR) diameter. Ins=inspiratory; DiffCSA_Ins=Difference CSAs end-inspiratory MRI-end-inspiratory CT; DiffAP_Ins=Difference APs end-inspiratory MRI-end-inspiratory CT; DiffLR_Ins=Difference LRs end-inspiratory MRI-end-inspiratory CT; MeanCSA_Ins=[CSA end-inspiratory MRI+CSA end-inspiratory CT]/2; MeanAP_Ins=[AP end-inspiratory MRI+AP end-inspiratory CT]/2; MeanLR_Ins=[LR end-inspiratory MRI+LR end-inspiratory CT]/2. Note that mean differences are close to zero (mean difference CSA=0.11 $cm^2$; AP=-0.13 mm and LR= 0.67 mm) and most of the observations are around the mean.

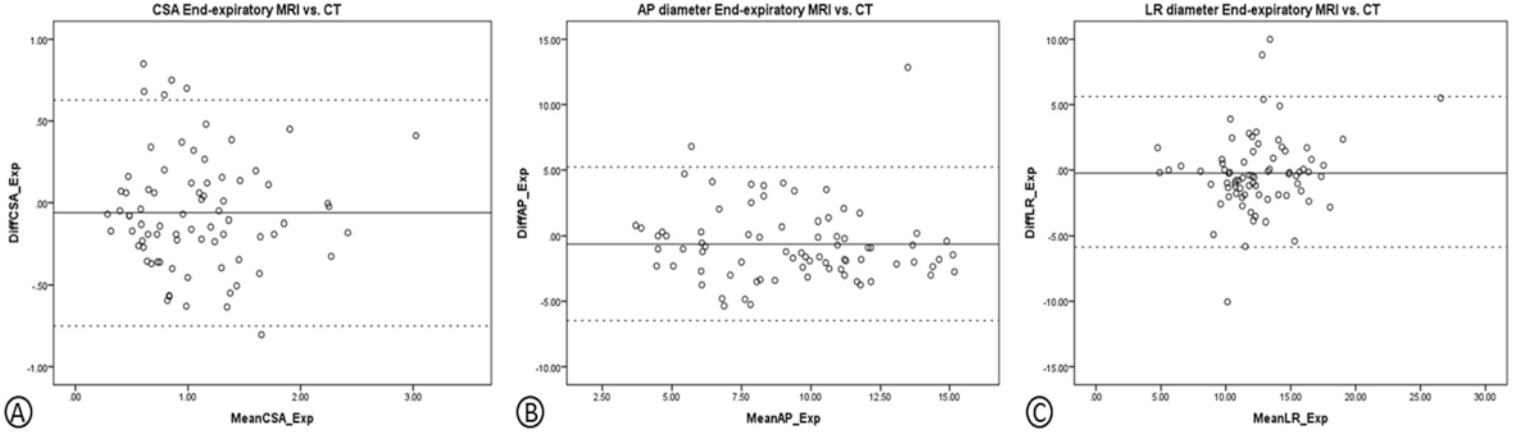


**Figure 3E. Inter-modality agreement ($MRI_1$ versus $CT_1$) for dynamic-expiratory measurements.**

Bland-Altman plots of a) dynamic-expiratory cross-sectional area (CSA), b) dynamic-expiratory anterior-posterior (AP) diameter and c) dynamic-inspiratory left-right (LR) diameter. Exp=Expiratory; DiffCSA_Exp=Difference CSAs end-expiratory MRI-end-expiratory CT; DiffAP_Exp=Difference APs end-expiratory MRI-end-expiratory CT; DiffLR_Exp=Difference LRs end-expiratory MRI - end-expiratory CT; MeanCSA_Exp=[CSA end-expiratory MRI+CSA end-expiratory CT]/2; MeanAP_Exp=[AP end-expiratory MRI+AP end-expiratory CT]/2; MeanLR_Exp=[LR end-expiratory MRI+LR end-expiratory CT]/2. Note that mean differences are close to zero (mean difference CSA=-0.06 $cm^{2,}$ AP=-0.62 mm and LR=-0.24 mm) and most of the observations are around the mean.

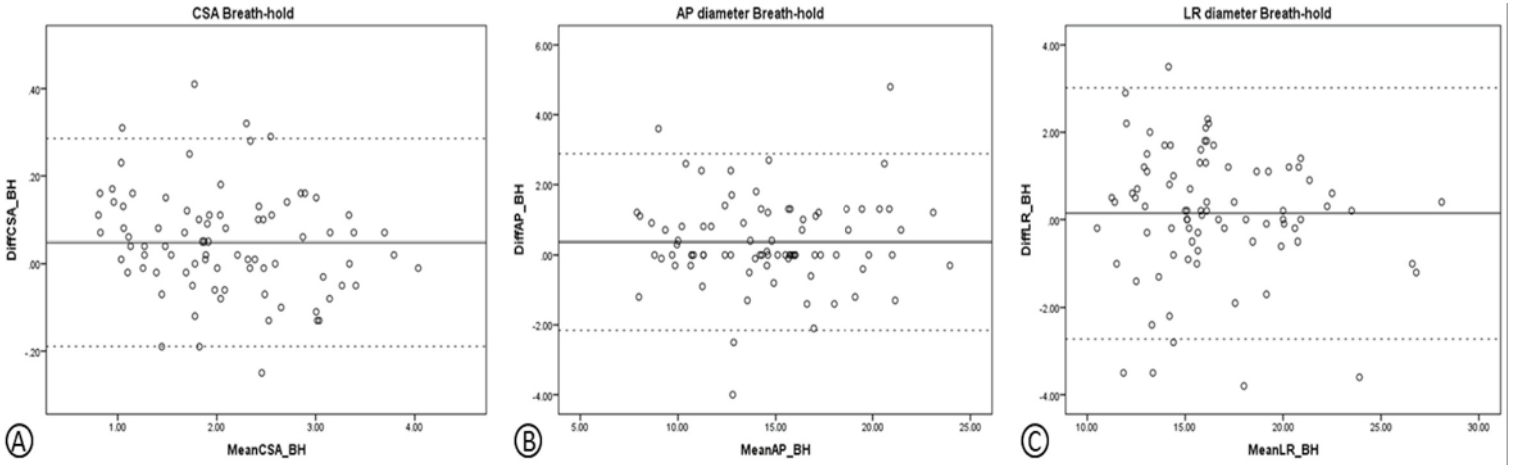


**Figure 4E. Intra-observer agreement ($MRI_1$ versus $MRI_2$) for breath-hold maneuver.**

Bland-Altman plots of breath-hold maneuver: a) cross-sectional area (CSA), b) anterior-posterior (AP) diameter and c) left-right (LR) diameter. BH=breath-hold; DiffCSA_BH=Difference CSAs MRI BH ($MRI_1$ vs $MRI_2$); DiffAP_BH=Difference APs MRI BH ($MRI_1$ vs $MRI_2$); DiffLR_BH= Difference LRs MRI BH ($MRI_1$ vs $MRI_2$); MeanCSA_BH= [CSA BH $MRI_1$+CSA BH $MRI_2$]/2; MeanAP_BH=[AP BH $MRI_1$+AP BH $MRI_2$]/2; MeanLR_BH=[LR BH $MRI_1$+LR BH $MRI_2$]/2. Note that mean differences are close to zero (mean difference CSA=-0.05 $cm^2$, AP=0.36 mm and LR=0.14 mm) and most of the observations are around the mean.

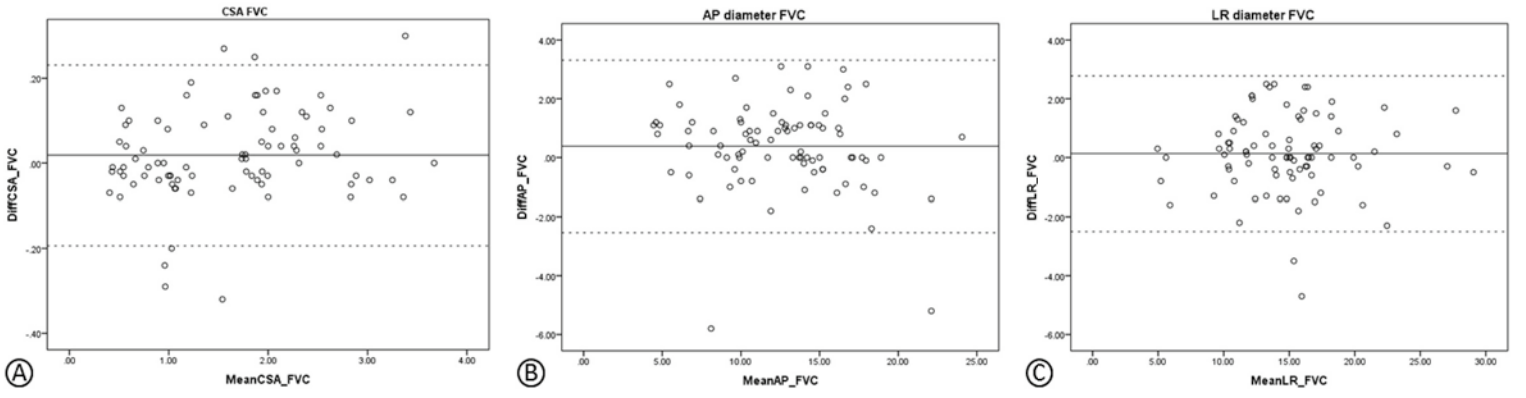


**Figure 5E. Intra-observer agreement ($MRI_1$ versus $MRI_2$) for Forced vital capacity (FVC) maneuver.**

Bland-Altman plots of breath-hold maneuver: a) cross-sectional area (CSA), b) anterior-posterior (AP) diameter and c) left-right (LR) diameter. FVC=forced vital capacity; DiffCSA_FVC=Difference CSAs MRI FVC ($MRI_1$ vs $MRI_2$); DiffAP_FVC=Difference APs MRI FVC ($MRI_1$ vs $MRI_2$); DiffLR_FVC=Difference LRs MRI FVC ($MRI_1$ vs $MRI_2$); MeanCSA_FVC=[CSA FVC $MRI_1$+CSA FVC $MRI_2$]/2; MeanAP_FVC=[AP FVC $MRI_1$+AP FVC $MRI_2$]/2; MeanLR_FVC=[LR FVC $MRI_1$+LR FVC $MRI_2$]/2. Note that mean differences are close to zero (mean difference CSA=0.02 $cm^2$, AP=0.38 mm and LR=0.13 mm) and most of the observations are around the mean.

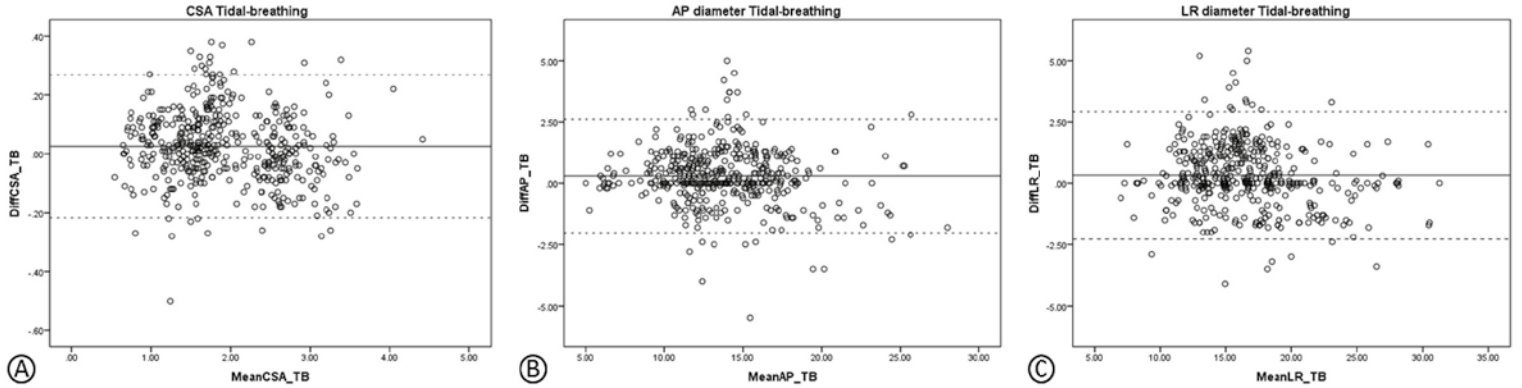


**Figure 6E. Intra-observer agreement ($MRI_1$ versus $MRI_2$) for tidal breathing (TB) maneuver.**

Bland-Altman plots of breath-hold maneuver: a) cross-sectional area (CSA), b) anterior-posterior (AP) diameter and c) left-right (LR) diameter. TB=tidal breathing; DiffCSA_TB=Difference CSAs MRI TB ($MRI_1$ vs $MRI_2$); DiffAP_ TB=Difference APs MRI TB ($MRI_1$ vs $MRI_2$); DiffLR_ TB=Difference LRs MRI TB ($MRI_1$ vs $MRI_2$); MeanCSA_ TB=[CSA TB $MRI_1$+CSA TB $MRI_2$]/2; MeanAP_ TB=[AP TB $MRI_1$+AP TB $MRI_2$]/2; MeanLR_ TB=[LR TB $MRI_1$+LR TB $MRI_2$]/2. Note that mean differences are close to zero (mean difference CSA=0.03 $cm^2$, AP=0.3 mm and LR=0.23 mm) and most of the observations are around the mean.

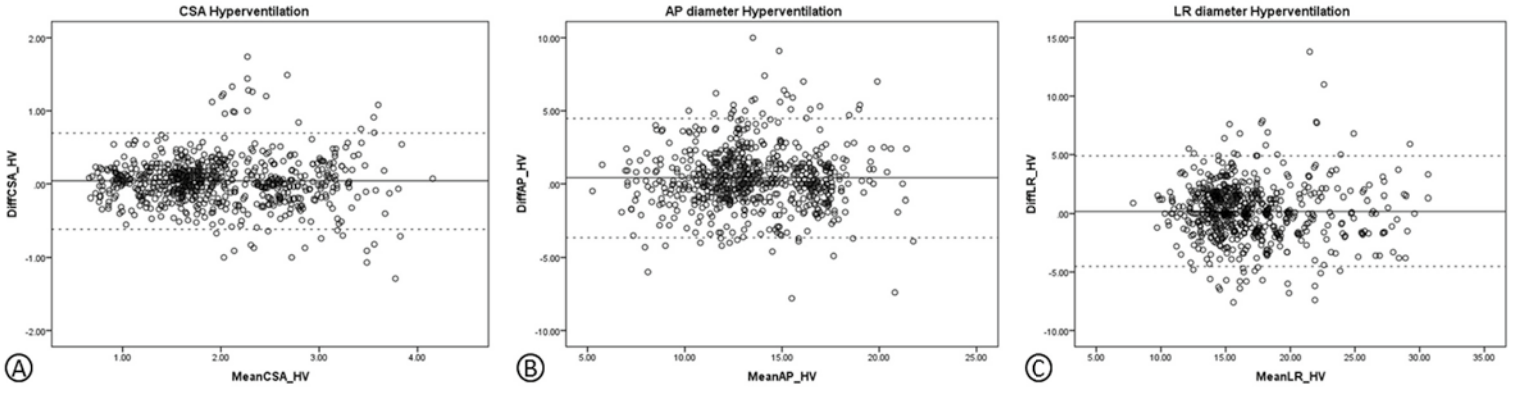


**Figure 7E. Intra-observer agreement ($MRI_1$ versus $MRI_2$) for hyperventilation (HV) maneuver.**

Bland-Altman plots of breath-hold maneuver: a) cross-sectional area (CSA), b) anterior-posterior (AP) diameter and c) left-right (LR) diameter. HV=hyperventilation; DiffCSA_HV=Difference CSAs MRI HV ($MRI_1$ vs $MRI_2$); DiffAP_HV=Difference APs MRI HV ($MRI_1$ vs $MRI_2$); DiffLR_HV=Difference LRs MRI HV ($MRI_1$ vs $MRI_2$); MeanCSA_HV=[CSA HV $MRI_1$+CSA HV $MRI_2$]/2; MeanAP_HV = [AP HV $MRI_1$+AP HV $MRI_2$]/2; MeanLR_ HV=[LR HV $MRI_1$+LR HV $MRI_2$]/2. Note that mean differences are close to zero (mean difference CSA=0.04 $cm^2$, AP=0.4 mm and LR=0.18 mm) and most of the observations are around the mean.

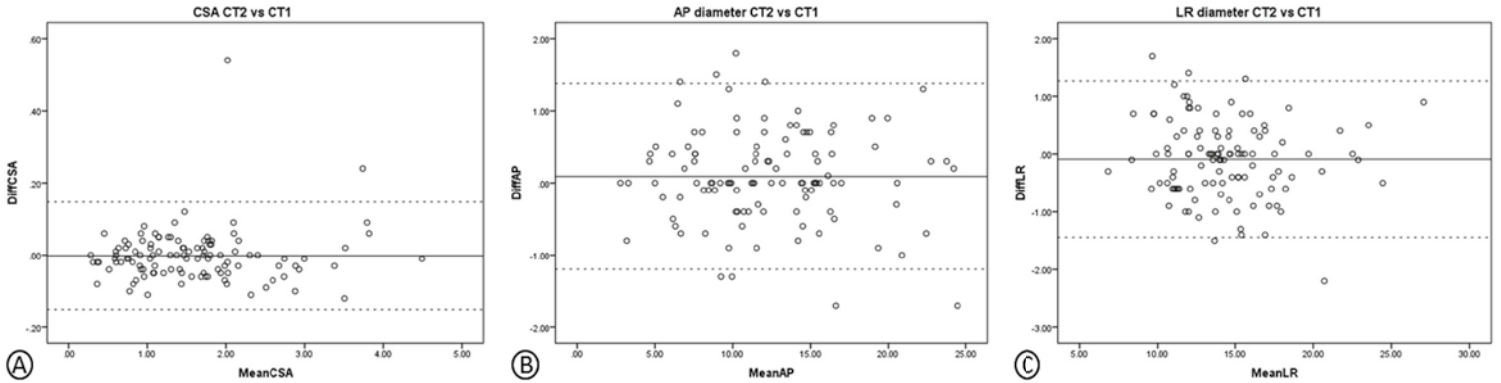


**Figure 8E. Intra-observer agreement CT ($CT_2$ vs. $CT_1$) measurements.**

Bland-Altman plots of CT measurements: a) cross-sectional area (CSA), b) anterior-posterior (AP) diameter and c) left-right (LR) diameter. DiffCSA= Difference CSAs $CT_2$ versus $CT_1$; DiffAP=Difference APs $CT_2$ versus $CT_1$; DiffLR=Difference LRs $CT_2$ versus $CT_1$; MeanCSA=[CSA $CT_2$+CSA $CT_1$]/2; MeanAP=[AP $CT_2$+AP $CT_1$]/2; MeanLR=[LR $CT_2$+LR $CT_1$]/2. Note that mean differences are close to zero (mean difference CSA=-0.0016 $cm^2$, AP=0.09 mm and LR=-0.09 mm) and most of the observations are around the mean.

**Table 2E.** Central airways %collapse per location for breath-hold (BH) maneuver.

| **CONTROLS** | | | | **PATIENTS** | | |
|---|---|---|---|---|---|---|
| **Maneuver** | **Breath-hold maneuver** | | | **Breath-hold maneuver** | | |
| | **Difference %** | | | **Difference %** | | |
| **Location** | *CSA* | *AP* | *LR* | *CSA* | *AP* | *LR* |
| **Trachea 1** | 22.1 (15.5-40.7)% | 15.9 (4.9-30.3)% | 14.5 (-1.4-26.3)% | 18.6 (-7.9; 29.7)% | 18.5 (-0.6; 24.2)% | 3.4 (-16.4; 5.2)% |
| **Trachea 2** | 26.4 (17-34.6)% | 16.4 (11.5-23.5)% | 5 (1.1-23.6)% | 21 (16.5; 21.3)% | 13.3 (4.7; 23.4)% | 13.5 (-15.2; 25.3)% |
| **Trachea 3** | 25.1 (18.3-29.6)% | 14.7 (10.1-21.3)% | 13 (-1.1-20)% | 13.4 (3.8; 18.5)% | 15.5 (0; 19.7)% | -0.7 (-5.3; 4)% |
| **Trachea 4** | 20.5 (15.7-32.6)% | 17.6 (17.1-22.5)% | 12 (4.3-16.5)% | 8.1 (0.4; 11.4)% | 17.8 (11.4; 18.5)% | -0.5 (-0.7; 1.3)% |
| **Trachea 5** | 26.2 (21.1-38)% | 17.6 (9.6-29.3)% | 17.3 (9.1-19.8)% | 27 (10; 29.2)% | 16.2 (12.7; 17.4)% | 24.3 (1.3; 26.3)% |
| **RMB** | 26.8 (7.3-35.3)% | 15 (3.3-25.4)% | 6.1 (-9.1-15.7)% | 22.3 (-22.6; 26.8)% | 16.2 (15.1; 23)% | 17.4 (11; 21.6)% |
| **LMB** | 31.5 (15.3-37.5)% | 15.8 (2.2-23.1)% | 8.3 (-4.9-22.2)% | 16.1 (14.6; 26)% | 18.5 (2.7; 31.2)% | 10.6 (-6.4; 13.8)% |

Trachea 1-5=tracheal points 1 -5 cm above carina, RMB=right main bronchus 1 cm below the carina; LMB=left main bronchus 1 cm below the carina. Data are expressed as median ($1^{st}$- $3^{rd}$ quartiles) for volunteers and as median (min - max) for patients.

**Table 3E.** Central airways %collapse per location for forced vital capacity (FVC) maneuver.

| **CONTROLS** | | | | **PATIENTS** | | |
|---|---|---|---|---|---|---|
| **Maneuver** | **FVC maneuver** | | | **FVC maneuver** | | |
| | **Difference %** | | | **Difference %** | | |
| **Location** | *CSA* | *AP* | *LR* | *CSA* | *AP* | *LR* |
| **Trachea 1** | 50.1 (35.2-70.3)% | 45.4 (33.3-46.6)% | 28.6 (8.7-41)% | 69.1 (66.5; 83.2)% | 28.1 (8.3; 62.5)% | 55.3 (37.5; 63.4)% |
| **Trachea 2** | 49.6 (19.5-68.4)% | 39.6 (19.4-53.7)% | 29.8 (12.6-36.4)% | 77.1 (59.3; 77.6)% | 38.7 (20.1; 68.8)% | 40.2 (37.8; 59.4)% |
| **Trachea 3** | 50.2 (19.8-63.4)% | 35.8 (27.1-57.5)% | 28.5 (3.2-32.4)% | 78.7 (67.8; 80.7)% | 56.1 (54.2; 70.6)% | 34 (29.1; 49.6)% |
| **Trachea 4** | 43.3 (24.4-67.6)% | 35.7 (23-61.4)% | 24.2 (11.7-32.3)% | 76 (68.8; 79.2)% | 56.7 (43.7; 62.6)% | 38.6 (35.8; 59)% |
| **Trachea 5** | 56.3 (22.7-61.5)% | 29.1 (21.1-48.4)% | 27.5 (6.5-42.7)% | 76.5 (66.8; 81)% | 49.7 (41.7; 71.3)% | 37.3 (36.7; 63.4)% |
| **RMB** | 49.5 (40.1-60.8)% | 33.1 (14.1-59.5)% | 21.7 (10.5-41)% | 60.5 (56; 78.5)% | 54.7 (34.2; 63.4)% | 39 (37.8; 47.8)% |
| **LMB** | 58.6 (35.6-64.9)% | 55.3 (25.2-60.3)% | 14.8 (9.8-30.3)% | 65.1 (52.9; 83.2)% | 62.2 (35.5; 67.5)% | 36.5 (32.8; 54.2)% |

Trachea 1-5=tracheal points 1 -5 cm above carina, RMB=right main bronchus 1 cm below the carina; LMB=left main bronchus 1 cm below the carina. Data are expressed as median (1st- 3rd quartiles) for volunteers and as median (min - max) for patients.

**Table 4E.** Central airways %collapse per location for tidal breathing (TB) maneuver.

| **CONTROLS** | | | | **PATIENTS** | | |
|---|---|---|---|---|---|---|
| **Maneuver** | **Tidal-breathing maneuver** | | | **Tidal-breathing maneuver** | | |
| | **Difference %** | | | **Difference %** | | |
| **Location** | *CSA* | *AP* | *LR* | *CSA* | *AP* | *LR* |
| **Trachea 1** | 10.8 (5.4; 12.9)% | 2.9 (-3.9; 4.9)% | 7 (6.4; 12.1)% | 23.7 (22.3; 28.7)% | 8.7 (7; 14.4)% | 15.4 (14.8; 16.7)% |
| **Trachea 2** | 12.4 (7.9; 14.1)% | 4 (1.7; 10.1)% | 4.4 (2.6; 9.7)% | 21.3 (10.3; 39.6.)% | -3 (-3.1; 8.4)% | 12.2 (10.8; 34.8)% |
| **Trachea 3** | 9.7 (5; 11.7)% | 4.4 (2.1; 9)% | 0.1 (-1.8; 4.5)% | 15.6 (13.4; 45.2)% | 7.6 (-1.8; 23.5)% | 11.8 (2.4; 29.8)% |
| **Trachea 4** | 6.6 (2.5; 10.9)% | 5.7 (-1.5; 9.7)% | 2.9 (-1; 6)% | 16.3 (9.3; 39.4)% | 13.1 (12.4; 17.1)% | 12.3 (-1.2; 23.1)% |
| **Trachea 5** | 6.4 (0.5; 12.3)% | 5.7 (3; 8.3)% | 1.7 (-1.8; 4.1)% | 12.3 (9.1; 37.3)% | 11.3 (7; 18.4)% | 1.5 (-2.7; 23.7)% |
| **RMB** | 4.3 (-2.4; 11.7)% | -0.3 (-2.8; 11)% | 0.3 (-1.2; 7.2)% | 19.4 (18.7; 25.8)% | 14.2 (11.5; 16.6)% | 12.1 (8; 16.9)% |
| **LMB** | 12.8 (7.4; 16.9)% | 6.6 (-3.3; 15.2)% | 4.8 (3; 8.4)% | 22 (17.4; 27.6)% | 17.8 (-0.2; 25.2) | 8.1 (2.2; 10.7)% |

Trachea 1-5=tracheal points 1 -5 cm above carina, RMB=right main bronchus 1 cm below the carina; LMB=left main bronchus 1 cm below the carina. Data are expressed as median ($1^{st}$- $3^{rd}$ quartiles) for volunteers and as median (min - max) for patients.

**Table 5E.** Central airways %collapse per location for hyperventilation (HV) maneuver.

| **CONTROLS** | | | | **PATIENTS** | | |
|---|---|---|---|---|---|---|
| **Maneuver** | **Hyperventilation maneuver** | | | **Hyperventilation maneuver** | | |
| | **Difference %** | | | **Difference %** | | |
| **Location** | *CSA* | *AP* | *LR* | *CSA* | *AP* | *LR* |
| **Trachea 1** | 19.9 (12; 26)% | 10.8 (5.3; 21.1)% | 12.6 (6.2; 17.9)% | 28.2 (7.7; 33.2)% | 7.7 (-1.5; 27.1)% | 11.4 (6.9; 20.5)% |
| **Trachea 2** | 14.4 (11.3; 21.8)% | 8.7 (4.5; 14)% | 5.6 (1.4; 11.4)% | 18.7 (-9.8; 34.4)% | 11.2 (3.9; 14)% | 12.8 (-2; 19.2)% |
| **Trachea 3** | 13.1 (9.4; 18.3)% | 11.3 (6.7; 16.1); | 2.7 (1.3; 6.1)% | 17.2 (2.5; 32.1)% | 15.2 (2.4; 17.5)% | 0.2 (-0.7; 12.9)% |
| **Trachea 4** | 12.8 (4.2;17.4)% | 6.9 (3.9; 10.9)% | 2.6 (-2.8; 7.6)% | 4.2 (-2.2; 28.7)% | 4.9 (1.5; 22.8)% | 0.8 (-2.6; 12.1)% |
| **Trachea 5** | 11.6 (4.2; 17)% | 11.8 (5.1; 12.8)% | 4.8 (-0.1; 7)% | 15.1 (2.9; 17.5)% | 13.6 (7.7; 16.7)% | 4.4 (-2.4; 10.9)% |
| **RMB** | 23.5 (18.8; 28.7)% | 12.4 (5.9; 20.7)% | 8.4 (5.5;20.5)% | 26.2 (4.5; 30.8)% | 22.3 (4.1; 24.6)% | 9.9 (5.9; 11.7)% |
| **LMB** | 22.8 (18.5; 27.9)% | 13.1 (8; 15.4)% | 11.5 (7.5; 18.1)% | 9.3 (-8.9; 35.1)% | 17 (-16.7; 29.5)% | 15.1 (-2.1; 19.5)% |

Trachea 1-5=tracheal points 1 -5 cm above carina, RMB=right main bronchus 1 cm below the carina; LMB=left main bronchus 1 cm below the carina. Data are expressed as median (1st- 3rd quartiles) for volunteers and as median (min - max) for patients.

# Part 3

## Diaphragm mechanics using MRI

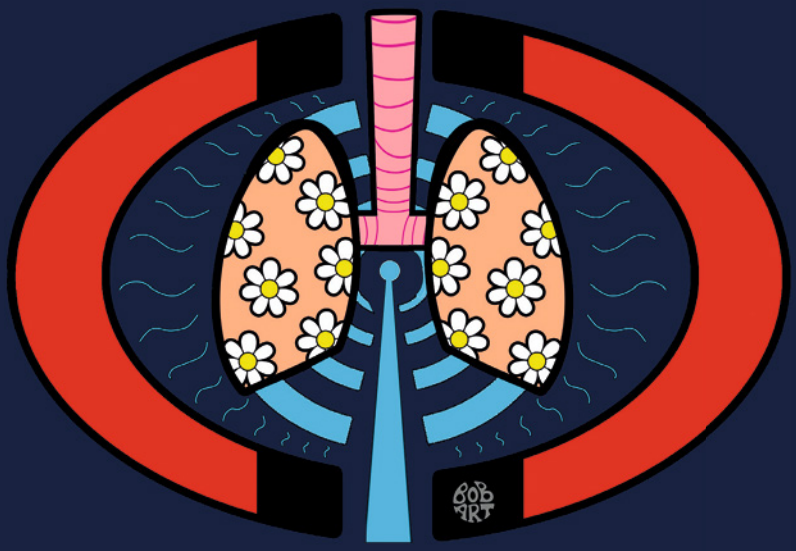

# Chapter 10

## Lung MRI and Impairment of Diaphragmatic Function in Pompe Disease

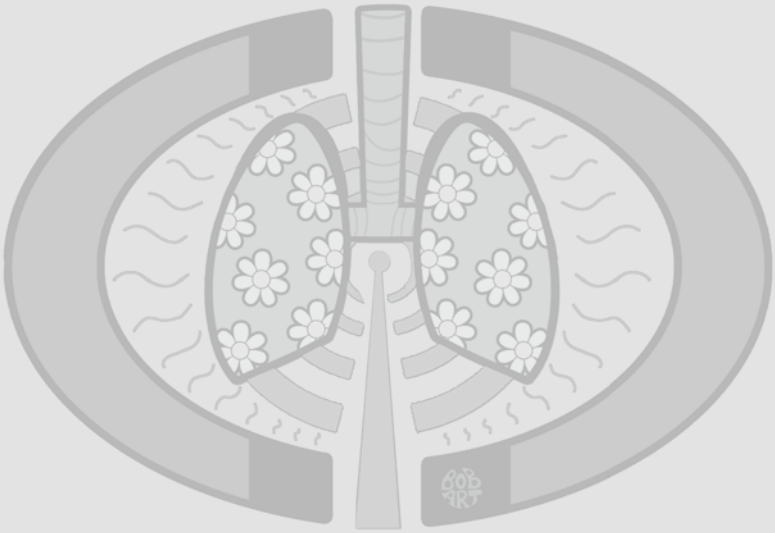

*Ciet P, Wielopolski P, Manniesing R, Lever S, de Bruijne M, Morana G, Muzzio PC, Lequin MH, Tiddens HAHW*

BMC Pulm Med. 2015 May 6;15:54.

## Abstract

**Background:** Pompe disease is a progressive metabolic myopathy. Involvement of respiratory muscles leads to progressive pulmonary dysfunction, particularly in supine position. Diaphragmatic weakness is considered to be the most important component. Standard spirometry is to some extent indicative but provides too little insight into diaphragmatic dynamics. We used lung MRI to study diaphragmatic and chest-wall movements in Pompe disease.

**Methods:** In ten adult Pompe patients and six volunteers, we acquired two static spirometer-controlled MRI scans during maximum inspiration and expiration. Images were manually segmented. After normalization for lung size, changes in lung dimensions between inspiration and expiration were used for analysis; normalization was based on the cranial-caudal length ratio (representing vertical diaphragmatic displacement), and the anterior-posterior and left-right length ratios (representing chest-wall movements due to thoracic muscles).

**Results:** We observed striking dysfunction of the diaphragm in Pompe patients; in some patients the diaphragm did not show any displacement. Patients had smaller cranial-caudal length ratios than volunteers ($p<0.001$), indicating diaphragmatic weakness. This variable strongly correlated with forced vital capacity in supine position ($r=0.88$) and postural drop ($r=0.89$). While anterior-posterior length ratios also differed between patients and volunteers ($p=0.04$), left-right length ratios did not ($p=0.1$).

**Conclusions:** MRI is an innovative tool to visualize diaphragmatic dynamics in Pompe patients and to study chest-walland diaphragmatic movements in more detail. Our data indicate that diaphragmatic displacement may be severely disturbed in patients with Pompe disease.

## Background

Pompe disease (OMIM 232300: acid maltase deficiency or glycogen storage disease type II) is an inherited progressive metabolic myopathy caused by acid α-glucosidase deficiency due to mutations in the acid α-glucosidase (GAA) gene (OMIM 606800) [1,2]. Pulmonary dysfunction caused by progressive weakness of the respiratory muscles is a characteristic feature of the disease [1,3,4]. In patients with the classic infantile form cardiorespiratory failure leads to death within the first year of life [5,6]. In patients with late-onset or non-classic Pompe disease pulmonary dysfunction progresses more slowly. The first sign of respiratory involvement in these patients is decreased pulmonary function in supine position, eventually necessitating respiratory support during sleep. Patients in the end-stage of the disease require continuous respiratory support [7-9]. Weakness of the diaphragm–the main respiratory muscle – is considered to be the major cause of respiratory dysfunction in Pompe disease [3,10]. Although pulmonary function tests (PFTs) may be indicative of diaphragmatic weakness by showing a difference between forced vital capacity (FVC) in sitting and supine position – i.e. postural drop – or by a decreased mean inspiratory pressure (MIP), they provide too little insight in dynamics of the diaphragm [11]. More insight in the function of the diaphragm has become extra relevant since enzyme replacement therapy (ERT) has been available for Pompe disease. While several studies have shown that ERT has positive effects on skeletal muscle function by showing stabilization or improvement of muscle strength or the distance walked in six minutes, the effects on lung function especially in supine position seem to be less pronounced [7,12-16]. In an earlier study that compared the effects of ERT on pulmonary function in sitting and supine positions, we found that 15% of patients were therapy resistant when pulmonary function was measured in sitting position, and that 35% were therapy resistant when it was measured in supine position [13]. Recent MRI sequences and image analysis techniques make it possible to directly assess the individual contribution of respiratory muscles – including the diaphragm – during the breathing cycle [17-22].

The aim of the current study was to determine whether MRI could be used as an innovative tool to gain greater insight into the function of the diaphragm in Pompe disease, and to correlate these data with the results of PFTs.



## Methods

### Study population

All patients with Pompe disease in the Netherlands are referred to Erasmus MC University Medical Centre Rotterdam. For this cross-sectional pilot study we selected ten adult patients with various degrees of respiratory dysfunction. As controls we included six age- and gender-matched volunteers. Informed consent was obtained from all participants. The study protocol was approved by the Medical Ethical Committee at our hospital (Amendment 7 to protocol MEC-2007-103).

## PFT

An MRI-compatible spirometer was used to standardize lung volumes and breathing movements during the MRI (MasterSceen Pneumo spirometer, CareFusion, Houten, the Netherlands). Before MRI, FVC and forced expiratory volume in one second (FEV1) were measured according to ATS/ERS standards [23,24]. Spirometry parameters are expressed in percentages predicted. Postural drop (ΔFVC) was calculated as (FVCsitting-FVCsupine)/FVCsitting *100%. An ΔFVC of more than 25% is thought to reflect diaphragmatic weakness [11,25]. Before MRI, a Dwyer pressure gauge was used according to ATS/ERS standards to measure maximum static inspiratory (MIP) and expiratory pressures (MEP) [26]. Results are expressed in kilopascal (kPa). The carbon dioxide (CO2) fraction in the expired gas was measured with a capnograph (ms-capno, Viasys Healthcare, Wurzberg, Germany) at maximum expiration. In the absence of ventilation irregularities, the expiratory CO2 approximates the arterial CO2 pressure. A daytime expiratory CO2 over 6.0 kPa suggests hypercapnia and chronic alveolar hypoventilation [27].

## MRI and imaging analysis

Scanning was performed with a 3T GE Signa 750 MRI (General Electric Healthcare, Milwaukee, USA) using the whole-body coil for radio-frequency excitation and a 32-channel torso coil for signal reception. First, a 3-plane localizer was performed during a maximum inspiratory movement (i.e. a five-second breath-hold scan); all subsequent volumes imaged were based on this localizer. Second, shimming was performed on this localizer, and shim settings were maintained throughout scanning. To evaluate changes in lung shape and volume, two static scans were acquired. These use two 12-second breath-hold scans covering the entire thoracic region acquired at end-inspiration and end-expiration in a 3D RF-spoiled gradient echo sequence with TR/TE=1/0.5 ms, flip angle 2°, sagittal volume acquisition with 3 mm slice thickness, 1.5 mm slice separation between slices and planar pixel resolution between 1.4x1.4 and 1.5x1.5 $mm^2$. Overall acquisition time per patient was 20 minutes.

Each lung was segmented manually at inspiration and expiration using 3D Slicer (http://www.slicer. org), with segmentation being performed every second slice in the axial plane [28]. A full 3D segmentation was reconstructed by interpolating the individual segmentation slices in the cranial-caudal axis. Using the 3D lung segmentations, the length and volume of each independent lung was estimated along the main axes of the MRI acquisition (cranial-caudal, anterior-posterior and left-right). To cope for variations in lung size due to inter-subject anatomical variations, each length at maximum inspiration was divided by the corresponding length at maximum expiration. Therefore the normalised value is a rate of length increase compared with the expiration point (e.g. a ratio of 1.2 would mean an increase of 20% in length). Because of the assumption that the chest-wall is responsible for changes in volume in the anterior-posterior and left-right directions, and the diaphragm expands the lung in the cranial-caudal directions, it is possible to study the contributions to volume changes of the chest-wall and the diaphragm individually.

### Statistical analysis

Data were analyzed using SPSS version 21 (SPSS, Chicago, IL, USA) and are presented as medians with ranges, or as numbers with percentages. The Mann-Whitney test was used to analyze differences in PFT results and MRI findings between patients and volunteers. The Spearman's correlation coefficient (r) was used to calculate the relationship between PFT outcomes and MRI results in Pompe patients. A p-value <0.05 was considered statistically significant.

## Results

### Study population

Table 1 shows the characteristics of the Pompe patients and the volunteers. All Pompe patients had an acid alpha-glucosidase deficiency and all patients carried the common mutation c.-32-13T>G in one GAA allele and a second pathogenic mutation in the second allele. In five patients this second pathogenic mutation was c.525delT, in two patients c.1548G>A, and the other three patients carried a different second mutation. None of the patients was currently smoking and two patients had smoked in the past. None of the patients or volunteers had co-morbidities that could influence the function of the diaphragm.

**Table 1.** Patient characteristics and PFT results in patients and volunteers.

| | Patients | Volunteers | P-value |
|---|---|---|---|
| **Age (years)** | 46 (32-66) | 43 (27-55) | 0.25 |
| **Gender, (% males)** | 5 (50) | 3 (50) | 1.0 |
| **Height (cm)** | 178 (154-196) | 177 (175-190) | 0.39 |
| **Weight (kg)** | 73 (61-88) | 85 (65-94) | 0.13 |
| **BMI (kg/m²)** | 23.4 (20.6-25.4) | 24.9 (21-25.7) | 0.18 |
| **Duration of the disease (years)** | 16 (9-30) | - | - |
| **Duration of ERT (years)** | 5.5 (0-7) | - | - |
| **Wheelchair-dependent (%)** | 1 (10) | 0 (0) | 0.79 |
| **Ventilator-dependent (%)** | 3 (30) | 0 (0) | 0.37 |
| *Pulmonary function test* | | | |
| **$FVC_{sitting}$ (%)** | 60 (45-84) | 102 (92-111) | 0.001 |
| **$FVC_{supine}$ (%)** | 43 (27-70) | 102 (87-113) | 0.001 |
| **ΔFVC (%)[a]** | 33 (11-44) | 0 (0-10) | 0.001 |
| **$FEV_{1\ sitting}$ (l/s)** | 59 (42-80) | 98 (85-117) | 0.001 |
| **$FEV_{1\ supine}$ (l/s)** | 40 (30-63) | 91 (76-112) | 0.001 |
| **MIP (kPa)** | 6.9 (3.9-8.3) | 8.6 (6.4-11.8) | 0.07 |
| **MEP (kPa)** | 10.0 (6.4-11.8) | 12.5 (10.3-14.2) | 0.02 |

Continuous variables are expressed as median and range, categorical variables as number and percentage. BMI=body mass index, ERT=enzyme replacement therapy, FVC=forced vital capacity, $FEV_1$=forced expiratory volume in one second, MIP=maximum static inspiratory pressure, MEP=maximum static expiratory pressure. [a]ΔFVC is calculated as $(FVC_{sitting}-FVC_{supine})/FVC_{sitting}$ x100%.

## PFT

Table 1 shows PFT in sitting and supine positions. In both these positions, patients had lower median values for FVC and FEV1 than healthy volunteers did (p=0.001). The median ΔFVC was higher in Pompe patients (p=0.001). The median MEP was lower in patients (10.0 kPa) than in volunteers (12.5 kPa, p=0.02). The median MIP showed a trend towards a lower median value for the patients (6.9 kPa) relative to the healthy volunteers (8.6 kPa, p=0.07). Three patients had a expiratory CO2 fraction over 6.0 kPa and two of these patients were ventilator-dependent.

## MRI

Figure 1 shows the line-up during the MRI. Participants were placed in supine position with the MRI-compatible spirometer positioned above them. Figure 2 shows coronal slices through the carina for the breath-hold scans with the corresponding color plots of a Pompe patient and a volunteer. In the Pompe patient there was hardly any displacement of the diaphragm. Additional file 1 in the online data supplement shows the color plots of each individual subject and Additional files 2 and 3 demonstrate two examples of dynamic MRI scans in a healthy volunteer and a patient with Pompe disease.

**Figure 1. Line-up during the MRI Patients were placed in supine position in the MRI scanner with an MRI-compatible spirometer positioned just above the head.**

Figure 3 shows the changes per individual in the three chest-cage directions between inspiration and expiration. In volunteers, the main contributor to the changes in lung volume was the diaphragm (white bars). In most Pompe patients, these changes were due mainly to the thoracic muscles (grey and black bars), but, as Figure 3 shows, these patients had a large variety in diaphragmatic and chest-wall movements. The median cranial-caudal length change, representing diaphragmatic displacement before normalization for lung size, was 82 mm (range 46-90 mm) in volunteers and 28 mm (range 5-49 mm) in patients (p=0.002). The median anterior-posterior length change was 37 mm in volunteers (range 25-42 mm) and 18 mm (range 13-31 mm) in patients (p=0.006); the median left-right length change was 24 mm in volunteers (range 21-34 mm) and 17 mm (10-26 mm) in patients (p=0.02).

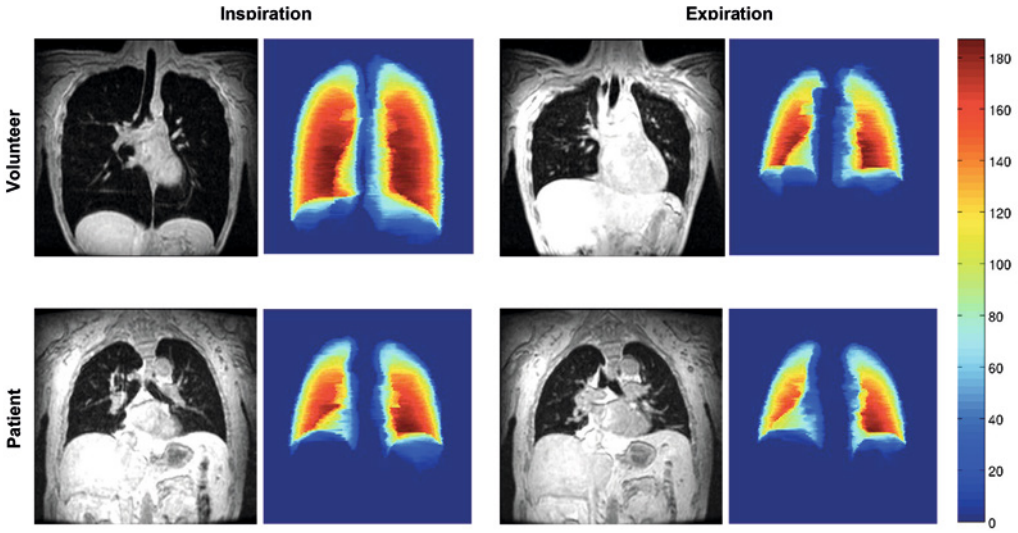


**Figure 2. MR images and color maps at maximum inspiration and expiration MR images during 12-second breath-holds in inspiration and expiration in a patient with Pompe disease and a healthy volunteer.** The color maps represent the thickness of the segmentation in the anterior-posterior axis (red being the thickest and blue being the thinnest). Note the limited increase in vertical length in the Pompe patient relative to the increase in the healthy volunteer.

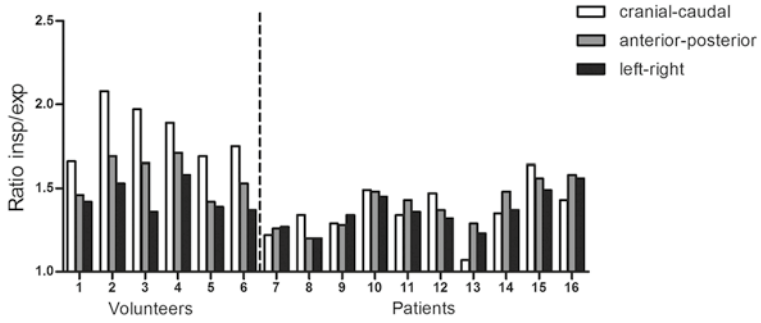


**Figure 3. Ratios between inspiration and expiration in three directions for patients and volunteers measured with MRI.** The length ratios between inspiration and expiration in the cranial-caudal direction (white bars), anterior-posterior direction (black bars) and left-right direction (grey bars) are shown for individual patients and volunteers. Volunteers are numbered 1 to 6 and patients 7 to 16. The length ratios are calculated by dividing the median length during inspiration by the median length during expiration for each axis.

Figure 4 shows the different length ratios after normalization for lung size. The cranial-caudal length ratio between inspiration and expiration (representing diaphragmatic displacement) was lower in Pompe patients (median 1.35, range 1.07-1.64) than in volunteers (median 1.82, range 1.66-2.08) (p=0.001). While the anterior-posterior length ratio was also lower in patients (median 1.40, range

1.20-1.58) than in volunteers (median 1.59, range 1.42-1.71) (p=0.04), the left-right length ratio did not differ significantly between patients (median 1.35, range 1.20-1.56) and volunteers (median 1.41, range 1.36-1.58) (p=0.1). In the three Pompe patients who were ventilator-dependent the cranial-caudal length ratio was lower than in the other Pompe patients (median 1.22 versus 1.43, p=0.02). These ventilator-dependent patients had a longer duration of the disease (median 29 years versus 15 years). There was no correlation between the cranial-caudal length ratio and the duration of ERT.

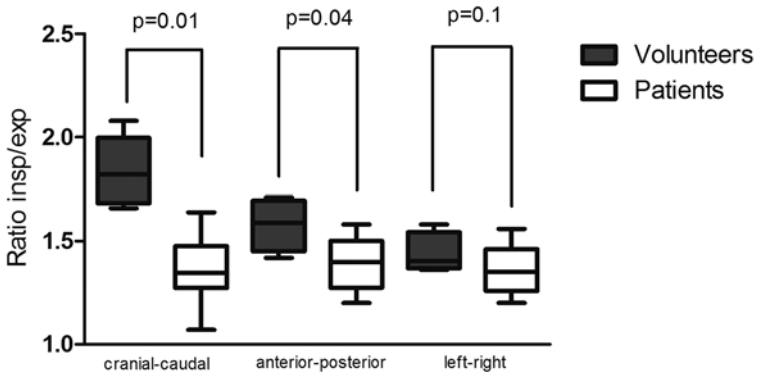


**Figure 4. Median ratios between inspiration and expiration in three directions for both groups.** This figure shows the same ratios as Figure 2, but now for the groups of Pompe patients and volunteers. The box plots represent the median with the range. The Mann-Whitney test was used to calculate the difference in each direction between patients and volunteers.

**Correlation between PFT and MRI**

As Figure 5 shows, ΔFVC and FVC supine were strongly correlated with the cranial-caudal length ratio (r=0.89 and r=0.88, p<0.001) in Pompe patients, but there were no correlation between MIP and the cranial-caudal length ratio (r=0.32, p=0.37), MEP and cranial-caudal length ratio (r=0.23, p=0.53), or FVC sitting and cranial-caudal length ratio (r=0.46, p=0.18). The only significant correlation regarding the anterior-posterior length ratio was with FVC supine (r=0.74, p=0.02).

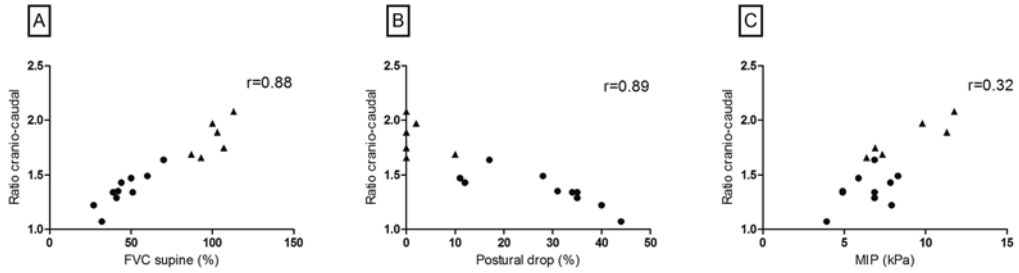


**Figure 5. Correlation between cranial-caudal length ratios and FVC supine (A), postural drop (B) and MIP (C).** The dots represent patients and the triangles volunteers. Spearman's correlation coefficient (r) was used to calculate the correlation between the cranial-caudal length ratio versus FVC in supine position, the postural drop (ΔFVC) and MIP. As these calculations were performed only in the Pompe patients, the volunteers were excluded for these analyses. FVC=forced vital capacity, MIP=maximum static inspiratory pressure.

## Discussion

Our study shows that MRI can be used as an innovative tool to gain greater insight into involvement of the diaphragm in Pompe disease. It was demonstrated that the diaphragmatic function is severely impaired and in some patients there was even hardly any displacement of the diaphragm. To a lesser extent, movement of the anterior chest-wall was reduced. Our results suggest that diaphragmatic displacement measured with MRI is strongly correlated with the postural drop and FVC in supine position measured with common spirometry.

Decreased pulmonary function is an important feature of Pompe disease. Ten or 15 years after onset, half of the adult patients with Pompe disease require ventilator assistance. The main cause of death in this group of patients is respiratory failure, a process in which dysfunction of the diaphragm is considered to play an important role [8,9,29]. Our MRI study suggests that the function of the diaphragm in Pompe disease is more impaired than that of the thoracic musculature. It is not clear how and why the diaphragm muscles are more severely affected than the other respiratory muscles. Our study supports a recent study describing atrophy of the diaphragm and reduced lung height on static MRI and computed tomography scans in patients with Pompe disease. In this latter study semi-quantitative scoring scales were used, and computed tomography was used to measure lung height in one direction [30]. In our study MRI was performed under spirometry control and lung-shape variations were quantified in three directions. This enabled us to show that the cranial-caudal movement related to diaphragmatic function in patients with Pompe disease is impaired more than the anterior-posterior motions of the anterior chest-wall. Similarly, the correlation we found between ΔFVC and FVC in supine position and our MRI results suggest that both these parameters might be used as an indirect tool for determining diaphragmatic function, with the advantage that MRI also visualizes diaphragmatic and chest-wall movements.

A striking finding in our study was that displacement of the diaphragm was extremely impaired in some of the patients, while still residual pulmonary function in supine position was measurable. This could have important consequences when therapy comes in place and might explain why pulmonary function, particularly in supine position, responds poorly to ERT in some of the Pompe patients. Therefore, more studies are required to investigate at what stage the diaphragm and other respiratory muscles become affected in Pompe disease; especially since it has been shown that response to ERT is better in patients who are less severely affected [3,13,31]. Another intriguing question is how MIP and MEP relate to diaphragmatic weakness. It has been hypothesized that these parameters might be better predictors for diaphragmatic weakness than FVC in supine position [30]. Our study implied a weak correlation between MIP or MEP and diaphragmatic displacement. A possible explanation could be that MIP reflects both the strength of the diaphragm and other inspiratory muscles, while the cranial-caudal length ratio only reflects diaphragmatic displacement. In an earlier study we found a positive correlation between FVC in upright position and MIP an MEP [3]. Larger studies are required to explore this relationship in more depth. Comparison of diaphragmatic involvement in patients with Pompe disease to those with other neuromuscular disorders such as Duchenne Muscular Dystrophy might provide insight whether onset and the extend of diaphragmatic involvement is disease specific.

A limitation of our pilot study is that we selected a relatively small number of adult Pompe patients with variable degrees of respiratory dysfunction (FVC in supine position: 27 to 70% of normal). This subset of patients may not be fully representative for the total group of Pompe patients. In subsequent studies also patients with normal or close to normal respiratory function need to be studied to get more insight at what stage of the disease the diaphragm becomes affected. The use of MRI to evaluate diaphragmatic and chest-wall movements has some limitations. Contraindications such as metal implants, invasive ventilation and claustrophobia make it impossible to scan certain patients. Moreover, patients need to be able to perform spirometry in supine position. In next studies it might also be considered to include other techniques to measure lung and respiratory muscle function in addition to spirometry such as sniff nasal inspiratory pressures, transdiaphragmatic pressures or transdiaphragmatic twitch pressures [32]. Prigent *et al* showed that transdiaphragmatic pressures and transdiaphragmatic twitch pressures correlated well with all spirometry volumes and non-invasive maximal pressures in adult patients with Pompe disease [33]. Whether transdiaphragmatic pressure measurements show a better correlation with the cranial-caudal length ratio measured with lung MRI than with spirometry data needs further investigation.

## Conclusions

MRI appears to be an innovative tool to visualize diaphragmatic dynamics in Pompe patients and to study chest-wall and diaphragmatic movements in more detail. Our data indicate that diaphragmatic displacement can be very severely impaired in patients with Pompe disease and might explain why FVC responds poorly to ERT in some of the patients. As MRI adds detailed dynamic and structural information to data obtained by pulmonary function tests, particularly of the diaphragm, it may serve as a valuable tool in providing new insights in when the diaphragm starts to be involved in the disease process and on its responsiveness to therapy. It may also serve as a prognostic tool. More research is warranted to explore these topics.

## Bibliography


1. van der Ploeg AT, Reuser AJ. Pompe's disease. Lancet. 2008;372:1342–53.
2. van der Beek NA, de Vries JM, Hagemans ML, Hop WC, Kroos MA, Wokke JH, et al. Clinical features and predictors for disease natural progression in adults with Pompe disease: a nationwide prospective observational study. Orphanet J Rare Dis. 2012;7:88.
3. van der Beek NA, van Capelle CI, van der Velden-van Etten KI, Hop WC, van den Berg B, Reuser AJ, et al. Rate of progression and predictive factors for pulmonary outcome in children and adults with Pompe disease. Mol Genet Metab. 2011;104:129–36.
4. Pellegrini N, Laforet P, Orlikowski D, Pellegrini M, Caillaud C, Eymard B, et al. Respiratory insufficiency and limb muscle weakness in adults with Pompe's disease. Eur Respir J. 2005;26:1024–31.
5. van den Hout HM, Hop W, van Diggelen OP, Smeitink JA, Smit GP, Poll-The BT, et al. The natural course of infantile Pompe's disease: 20 original cases compared with 133 cases from the literature. Pediatrics. 2003;112:332–40.
6. Kishnani PS, Hwu WL, Mandel H, Nicolino M, Yong F, Corzo D, et al. A retrospective, multinational, multicenter study on the natural history of infantile-onset Pompe disease. J Pediatr. 2006;148:671–6.
7. van der Ploeg AT, Clemens PR, Corzo D, Escolar DM, Florence J, Groeneveld GJ, et al. A randomized study of alglucosidase alfa in late-onset Pompe's disease. N Engl J Med. 2010;362:1396–406.
8. Muller-Felber W, Horvath R, Gempel K, Podskarbi T, Shin Y, Pongratz D, et al. Late onset Pompe disease: clinical and neurophysiological spectrum of 38 patients including long-term follow-up in 18 patients. Neuromuscul Disord. 2007;17:698–706.
9. Gungor D, de Vries JM, Hop WC, Reuser AJ, van Doorn PA, van der Ploeg AT, et al. Survival and associated factors in 268 adults with Pompe disease prior to treatment with enzyme replacement therapy. Orphanet J Rare Dis. 2011;6:34.
10. McCool FD, Tzelepis GE. Dysfunction of the diaphragm. N Engl J Med. 2012;366:932–42.
11. Fromageot C, Lofaso F, Annane D, Falaize L, Lejaille M, Clair B, et al. Supine fall in lung volumes in the assessment of diaphragmatic weakness in neuromuscular disorders. Arch Phys Med Rehabil. 2001;82:123–8.
12. van der Ploeg AT, Barohn R, Carlson L, Charrow J, Clemens PR, Hopkin RJ, et al. Open-label extension study following the Late-Onset Treatment Study (LOTS) of alglucosidase alfa. Mol Genet Metab. 2012;107(3):456–61.
13. de Vries JM, van der Beek NA, Hop WC, Karstens FP, Wokke JH, de Visser M, et al. Effect of enzyme therapy and prognostic factors in 69 adults with Pompe disease: an open-label single-center study. Orphanet J Rare Dis. 2012;7:73.
14. Furusawa Y, Mori-Yoshimura M, Yamamoto T, Sakamoto C, Wakita M, Kobayashi Y, et al. Effects of enzyme replacement therapy on five patients with advanced late-onset glycogen storage disease type II: a 2-year follow-up study. J Inherit Metab Dis. 2012;35:301–10.
15. Schneider I, Hanisch F, Muller T, Schmidt B, Zierz S. Respiratory function in late-onset Pompe disease patients receiving long-term enzyme replacement therapy for more than 48 months. Wien Med Wochenschr. 2013;163:40–4.
16. Strothotte S, Strigl-Pill N, Grunert B, Kornblum C, Eger K, Wessig C, et al. Enzyme replacement therapy with alglucosidase alfa in 44 patients with late-onset glycogen storage disease type 2: 12-month results of an observational clinical trial. J Neurol. 2010;257:91–7.
17. Suga K, Tsukuda T, Awaya H, Takano K, Koike S, Matsunaga N, et al. Impaired respiratory mechanics in pulmonary emphysema: evaluation with dynamic breathing MRI. J Magn Reson Imaging. 1999;10:510–20.
18. Cluzel P, Similowski T, Chartrand-Lefebvre C, Zelter M, Derenne JP, Grenier PA. Diaphragm and chest wall: assessment of the inspiratory pump with MR imaging-preliminary observations. Radiology. 2000;215:574–83.

19. Craighero S, Promayon E, Baconnier P, Lebas JF, Coulomb M. Dynamic echo-planar MR imaging of the diaphragm for a 3D dynamic analysis. Eur Radiol. 2005;15:742–8.

20. Kiryu S, Loring SH, Mori Y, Rofsky NM, Hatabu H, Takahashi M. Quantitative analysis of the velocity and synchronicity of diaphragmatic motion: dynamic MRI in different postures. Magn Reson Imaging. 2006;24:1325–32.

21. Gierada DS, Curtin JJ, Erickson SJ, Prost RW, Strandt JA, Goodman LR. Diaphragmatic motion: fast gradient-recalled-echo MR imaging in healthy subjects. Radiology. 1995;194:879–84.

22. Unal O, Arslan H, Uzun K, Ozbay B, Sakarya ME. Evaluation of diaphragmatic movement with MR fluoroscopy in chronic obstructive pulmonary disease. Clin Imaging. 2000;24:347–50.

23. Miller MR, Hankinson J, Brusasco V, Burgos F, Casaburi R, Coates A, et al. Standardisation of spirometry. Eur Respir J. 2005;26:319–38.

24. Quanjer PH, Stanojevic S, Cole TJ, Baur X, Hall GL, Culver BH, et al. Initiative ERSGLF: multi-ethnic reference values for spirometry for the 3-95-yr age range: the global lung function 2012 equations. Eur Respir J. 2012;40:1324–43.

25. Allen SM, Hunt B, Green M. Fall in vital capacity with posture. Br J Dis Chest. 1985;79:267–71.

26. American Thoracic Society/European Respiratory S. ATS/ERS Statement on respiratory muscle testing. Am J Respir Crit Care Med. 2002;166:518–624.

27. Annane D, Orlikowski D, Chevret S, Chevrolet JC, Raphael JC. Nocturnal mechanical ventilation for chronic hypoventilation in patients with neuromuscular and chest wall disorders. Cochrane Database Syst Rev. 2007. CD001941.

28. Fedorov A, Beichel R, Kalpathy-Cramer J, Finet J, Fillion-Robin JC, Pujol S, et al. 3D Slicer as an image computing platform for the Quantitative Imaging Network. Magn Reson Imaging. 2012;30:1323–41.

29. Hagemans ML, Winkel LP, Van Doorn PA, Hop WJ, Loonen MC, Reuser AJ, et al. Clinical manifestation and natural course of late-onset Pompe's disease in 54 Dutch patients. Brain. 2005;128:671–7.

30. Gaeta M, Barca E, Ruggeri P, Minutoli F, Rodolico C, Mazziotti S, et al. Late-onset Pompe disease (LOPD): correlations between respiratory muscles CT and MRI features and pulmonary function. Mol Genet Metab. 2013;110(3):290–6.

31. Kobayashi H, Shimada Y, Ikegami M, Kawai T, Sakurai K, Urashima T, et al. Prognostic factors for the late onset Pompe disease with enzyme replacement therapy: from our experience of 4 cases including an autopsy case. Mol Genet Metab. 2010;100:14–9.

32. DePalo VA, McCool FD. Respiratory muscle evaluation of the patient with neuromuscular disease. Semin Respir Crit Care Med. 2002;23:201–9.

33. Prigent H, Orlikowski D, Laforet P, Letilly N, Falaize L, Pellegrini N, et al. Supine volume drop and diaphragmatic function in adults with Pompe disease. Eur Respir J. 2012;39:1545–6.

## Supplement

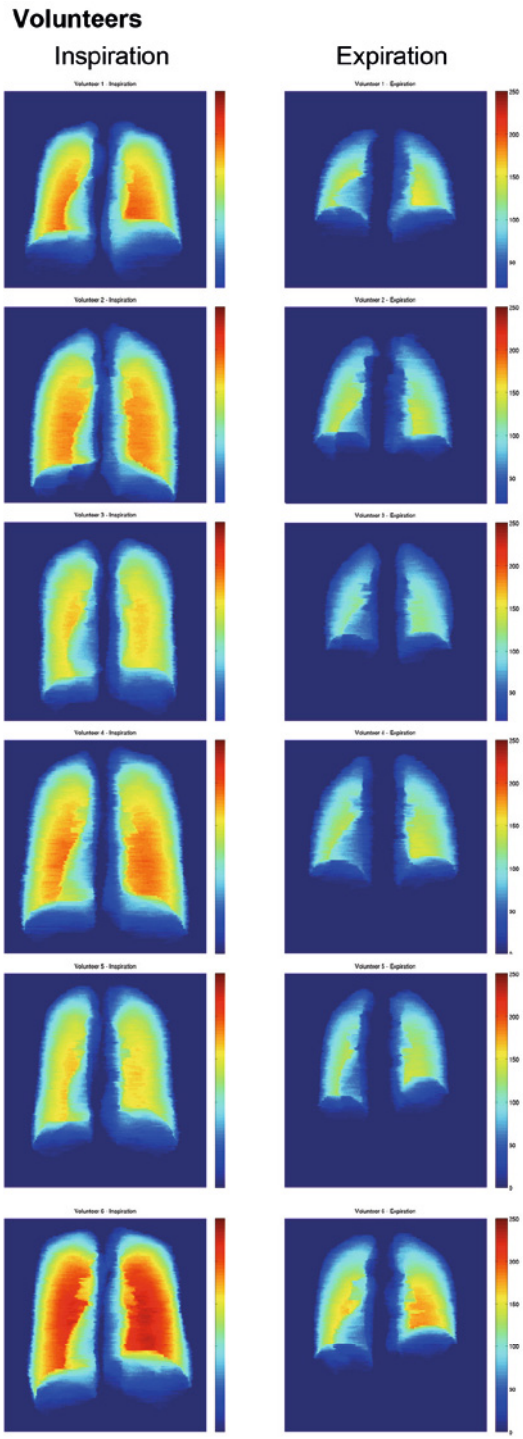

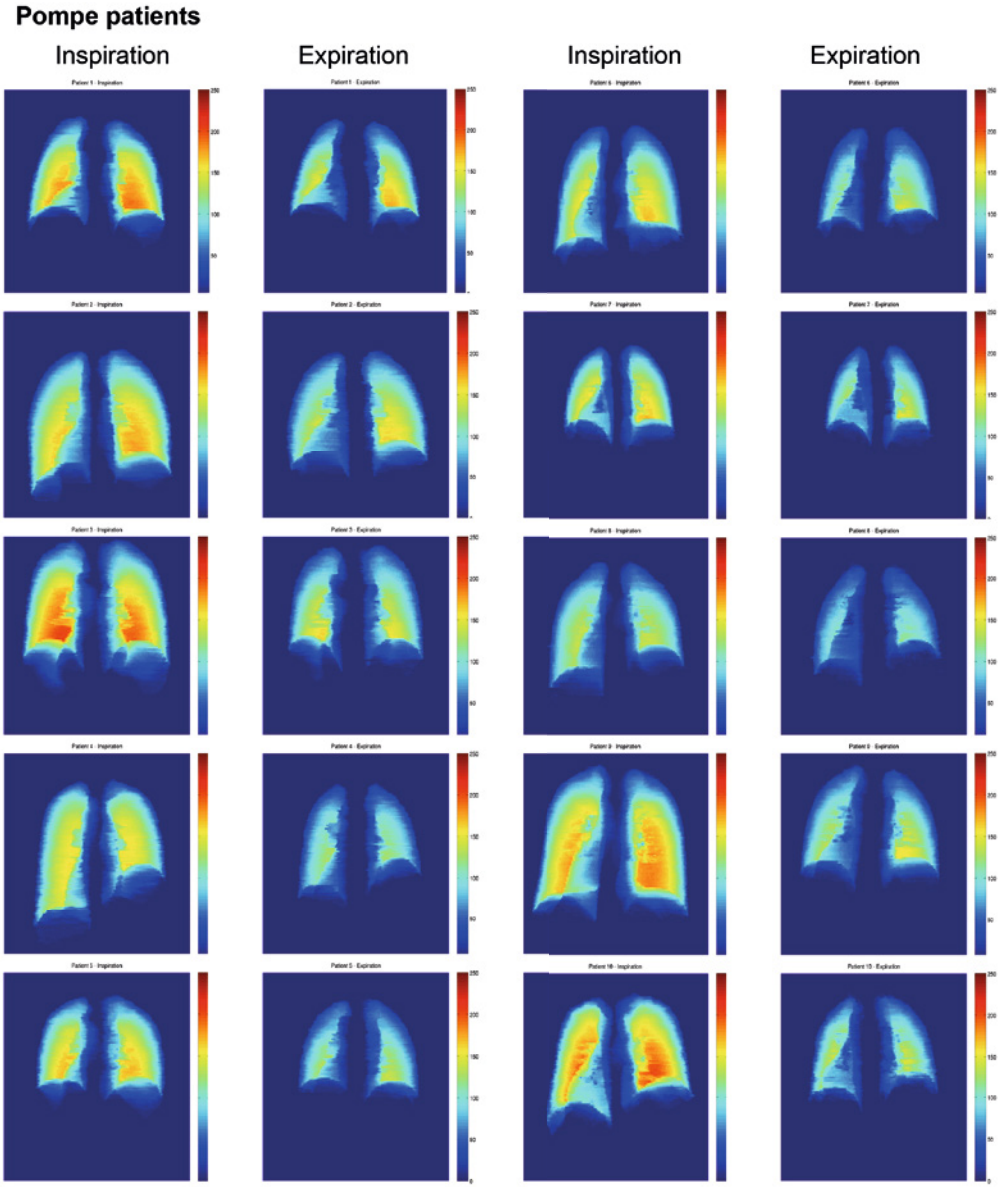
Pompe patients
Inspiration
Expiration
Inspiration
Expiration

# Chapter 11

## Discussion

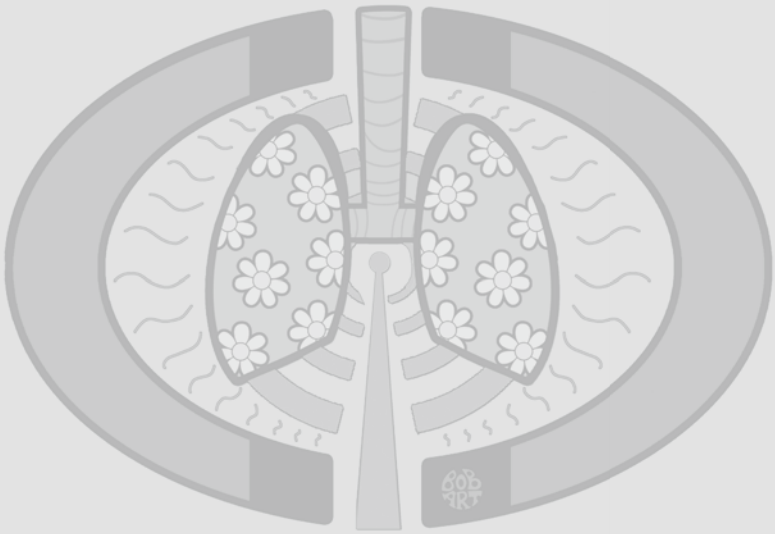

In this thesis, we aimed to use chest Magnetic Resonance Imaging (MRI) as a new technique for thoracic imaging. The core of the thesis consists of the application and development of new MRI protocols for Cystic Fibrosis (CF) lung disease. We also developed innovative applications of chest MRI for the dynamic evaluation of airways and the diaphragm. In this chapter, we discuss the main findings of our studies in the context of the current literature, their implications and the possible future research directions.

## Chest MRI for Morphological Imaging

As described in chapter 2, chest MRI is intrinsically limited by several technical factors which affect image quality [1]. These limitations make comparison with computed tomography (CT) regarding morphological imaging somewhat biased. CT has undoubtedly higher spatial resolution than MRI and shorter acquisition times, which makes it the first choice for thoracic imaging [2]. In addition the long track record of chest CT has made it the current gold standard in clinical practice both as diagnostic and monitoring tool [3-5].

Conversely, chest MRI has been in development for only two decades, after the introduction of new techniques, which allowed to obtain reasonable image quality in acceptable scan time [6]. The major driving force to develop chest MRI is its application for lung diseases requiring repeated imaging and where cumulative radiation dose related to the use of chest CT is considered an important limitation [7,8]. One of these lung diseases is CF, the most common hereditary disorder in Caucasians [9]. Patients with CF suffer of chronic lung infection and inflammation that starts in early childhood [10]. Repeated imaging is needed to efficiently monitor and to direct therapy in CF lung disease [11]. Several studies have shown that CT is more sensitive than pulmonary function tests to detect disease progression in CF [12]. At the same time, it is clear that although small, the risk related to repeated scans cannot be ignored [8]. Some studies in large cohort populations have shown an increased incidence of radiation-induced cancers related to the use of CT imaging [13]. Even though the range of radiation dose registered in these cohort studies is clearly higher than those used in chest CT imaging for CF, the risk cannot be totally eliminated by reducing the dose, due to the stochastic nature of the damage caused by ionizing radiation [8]. Moreover, this risk is even higher in young children, who have higher radiation sensitivity than adults [14].

For these reasons, almost ten years ago the first studies were conducted comparing image quality of chest MRI to CT. In a cross sectional study of Puderbach et al, an MRI protocol using Half-Fourier single-shot turbo spin-echo" (HASTE@Siemens) sequence showed good comparability with CT to detect specific CF lung disease related to morphological findings, such as bronchiectasis, mucus plugging, bullae/cysts, and collapse/consolidation [15]. However, HASTE showed lower ability to correctly classify the severity of bronchiectasis, bronchial wall thickening and trapped air [15]. In a second study conducted by our group using a steady state free precession (SSFP@General Electric)

MRI protocol, similar results were shown [16]. In particular it became clear that there was a systematic underestimation of the severity of lung damage by MRI relative to CT due to poor visualization of peripheral bronchiectasis [16]. Similarly MRI was less sensitive to detect trapped air relative to CT [16]. Rajaram *et al* showed that SSFP MRI was inferior to CT in imaging parenchymal lung disease [17]. One limitation of these studies was the conventional Cartesian k-space acquisition scheme used [18]. Cartesian k-space acquisition schemes are more sensitive to breathing and cardiac artifacts than non-Cartesian (i.e. helicoidal, radial, etc.) acquisition [19]. Non-Cartesian k-space sequences, such as radial (STARVIBE@Siemens) and helical (PROPELLER@General Electric) are characterized by greatly reduced sensitivity to motion compared to previous fast spin-echo and gradient-echo sequences [20].

To test if this new type of sequences are superior to conventional MRI sequences, in the study described in chapter 3, we compared PROPELLER (Periodically Rotated Overlapping ParallEL Lines with Enhanced Reconstruction; BLADE@Siemens) sequence to CT [21]. PROPELLER is a free-breathing Turbo Spin-Echo sequence with non-Cartesian k-space acquisition scheme (helicoidal) [22]. The main finding of our study was that despite this lower sensitivity to motion; PROPELLER MRI was still inferior to CT [23]. In particular, we found that compared to CT, PROPELLR MRI tended to underestimate CF findings for mild CF disease and to overestimate for severe CF disease [23]. A second important positive finding of our study was the high specificity of MRI for CF findings, which justifies its use for short or long term monitoring of specific CF lung disease alteration, such as consolidation, mucus plugs, etc [23].

Recently a multi-sequence MRI protocol including HASTE, BLADE, volumetric interpolated breath-hold examination (VIBE) and time-resolved angiography with stochastic trajectories (TWIST) was compared to CT [24]. This cross sectional study showed good agreement between CT and MRI, although scoring was performed in consensus, and therefore intra- and inter-reader variability were not assessed [24].

To date all the sequences tested so far for CF lung imaging were limited by low signal to noise ratio (SNR) because of long echo times (TE) [1]. To overcome this limitation, ultra-short or zero-TE (UTE/ZTE) sequences (microsecond μs instead of millisecond ms) have been recently developed and tested in CF disease, showing better results compared to conventional sequences [25,26]. Unfortunately, these UTE/ZTE sequences require long acquisitions times, because they are performed under free-breathing conditions; hence reproducibility is affected by patient performance.



It is important to note that, all the aforementioned studies were based on a single center experience. The primary and most obvious limitation of single-center studies is their potentially limited external validity. Especially the clinical value of MRI single centers studies is limited as standardization across MRI vendors and centers is difficult [27]. This lack of standardization still remains the main limitation in the implementation of chest MRI as a tool for routine clinical care [27]. To date no multi-vendor

studies have been published, mostly because of the large variability in MRI performance among vendors or even between similar scanners of the same vendor. In a recent study presented at the International Society of Magnetic Resonance in Medicine (ISMRM), variation up to 40% were registered in SNR for the same sequence (same scan parameters) performed in different scanners [28].

In summary, the continous development of high performance morphological MR sequences for chest MRI has reduced the diagnostic gap to CT. However, to close this gap, a large effort in MRI protocol standardization is needed allowing large cohort multi-centers studies [21].

## Beyond morphological imaging

One of the major advantages of MR over CT is its multi-parametric imaging capability and superior tissue characterization. Different tissue weighting provides a variety of information facilitating lesion characterization [1]. For instance T2-weighted sequences are important to identify fluid-containing structures, such as cysts or pleural effusions, while PD-weighted sequences are appropriate for airway imaging and trapped air assessment [1]. MR allows to obtain important functional information without exposing patients to ionizing radiation. Several MRI techniques can be used to obtain VIPS, i.e. functional information about **V**entilation, **I**nflammation, **P**erfusion, and **S**tructure [21]. The application of these MRI techniques to obtain VIPS information in patients with CF is described in chapters 4-7 of this thesis.

### Assessment of Inflammation with MRI

In chapter 4 and 5, we described the use of Diffusion-Weighted MRI to assess inflammation in patients with CF [29]. Inflammation is a major component of CF lung disease leading to progressive damage of lung structure [30]. The vicious cycle of infection, inflammation and damage determines those structural changes (i.e. bronchiectasis), which facilitate chronicity of infection [31]. CF patients face a state of chronic inflammation that increases during respiratory tract exacerbation (RTE). Different methods to assess lung inflammation have been evaluated so far. Several blood markers have been proposed, but they have shown low sensitivity and low clinical utility. Among pulmonary function tests, Lung Clearance Index (LCI) and Fractional exhaled nitric oxide (FeNO) have been used to assess inflammation [32,33]. However both LCI and FeNO showed high variability and limited ability to provide regional information on inflammation [34,35]. Regarding imaging, PET-CT has been also used to show persistent foci of inflammation in patients with CF, but its use is restricted by high radiation exposure [36]. Therefore, to date no radiation-free techniques were available to quantify and localize lung inflammation.

For the first time, we proposed DW-MRI as possible technique to localize and quantify inflammation in patient with CF [29]. In the first study on DW-MRI (chapter 4), we explored the feasibility of this technique in patients with CF [29]. The major finding of this cross-sectional study performed in a

group of stable patients with CF was that DW-MRI showed foci of high signal intensity ("hotspots") which only in part overlapped with structural lung changes on morphological CT or MRI [29]. We also observed that DW-MRI had a strong correlation with radiological and clinical parameters indicating of CF lung disease severity [29]. In addition, there were significant differences in PFT parameters between patients with and without DW-MRI hotspots [29].

Based on these results, we decided to validate DW-MRI in a cohort of CF patients with and without RTE (chapter 5). The most interesting observation of this study was that DW-MRI could track inflammatory changes over the course of RTE treatment. In patients with RTE, DWI signal at high b values showed an overall significant reduction following antibiotic treatment, while in the control group no significant differences in DWI signal between baseline and follow-up were observed. Interestingly, the morphological score (CF-MRI) was significantly different between the RTE and control groups both at baseline and follow-up. Therefore CF-MRI score was not able to detect patients with RTE. The other important finding was the fair to good accuracy of DW-MRI to differentiate patients with CF treated for a RTE. The final important finding of this study was the low intra- and inter-observer variability of DW-MRI, which supports the robustness of this method in clinical trials focused on RTE treatment.

In these two studies we have shown that DW-MRI could be a useful tool to efficiently localize and quantify inflammation during RTE. The final step to validate our method would be to compare areas with and without DWI signal using broncho-alveolar lavage (BAL) in order to clarify the nature of DWI hotspots.

**Assessment of Perfusion with MRI**

In chapter 6, we studied perfusion in a group of patients with CF. It is well known that structural changes affecting lung ventilation determine a reduction of lung perfusion according to the hypoxic-vasoconstriction reflex. This principle was demonstrated a decade ago by Eichinger *et al*, showing that areas of hypoperfusion matched areas of structural changes using contrast-enhanced MRI (CEMRI). Despite this study, CEMRI was not widely introduced in clinical practice. This likely happened because the technique at that time was not robust. Large variability between observers was a common problem, and only highly trained radiologists could provide reproducible results. Moreover no automated software tools for lung segmentation or perfusion quantification were available. Finally the risk related to contrast administration further reduced the enthusiasm to implement CEMRI in the CF population.



A recent study renewed interest on CEMRI. Wielpütz *et al* showed that hypoperfusion is a common entity in mild CF disease, and that it can be reversed after treatment for RTE exacerbation [37]. The findings of this study supported the use of CEMRI as an imaging biomarker in CF patients. In our CEMRI study in chapter 6, we aimed firstly to study the relationship between hypoperfusion (HP) and trapped air (TA). In addition we evaluated the relation between TA assessed by CEMRI and CT

and PFT. The main finding of our study was that HP was more frequent and severe than TA in patient with early CF disease. We also confirmed that expiratory CT detects more TA than expiratory MRI. From our study it became clear that the term TA is a misnomer, and that hypodense regions on CT and hypo-intense regions on MRI would be better described by the terms low-density region (LDR) and low-intensity region (LIR) respectively.

The higher prevalence of HP compared to TA in CF patients suggests that other factors play a role in addition to the hypoxic-vasoconstriction reflex. One of these factors might be inflammation, as suggested by the findings of Wielpütz *et al*, that lung perfusion improved after RTE treatment [37]. It would be also interesting to investigate whether reversibility of TA/HP is restricted only to mild CF patients or it would occur in more advanced disease as well. These interesting questions will be addressed by studies using CEMRI only after further validation of the technique. A multi-vendor platform as VIPS MRI might help to make CEMRI an important imaging biomarker for CF lung disease [21]. Moreover other non-contrast techniques such as Fourier Decomposition (FD) or Arterial Spin Labeling (ASL) might be further developed in order to obtain information about perfusion without contrast administration [38,39].

**Assessment of Ventilation with MRI**

Ventilation imaging with MR can be performed with several techniques. The most studied technique for ventilation imaging is that with hyperpolarized gas MRI [40]. Hyperpolarized gas MRI uses gaseous contrasts based on helium ($^{3}$He) and xenon ($^{129}$Xe) to provide high resolution images of pulmonary ventilation, microstructure and gas exchange [40]. Despite the great potential of this technique, its high complexity and cost of the noble gasses and the need of dedicated hardware limits its application in clinical practice [41]. A more feasible and promising technique is Oxygen-enhanced MRI, which uses the paramagnetic effect of oxygen to shorten T1 relaxation times obtaining maps of the oxygen distribution in the lung [42,43]. Oxygen-enhanced MRI has been already used and tested in patients with asthma and chronic obstructive pulmonary disease [43,44]. Despite that the technique is cheaper and more available than hyperpolarized gases MRI, it has been not yet transferred in clinical practice because of its long acquisition times (5-30 min) [40]. The most promising technique for ventilation MRI is a non-contrast SSFP-based sequence that provides ventilation and perfusion maps [45]. This technique for ventilation MR imaging technique is FD, a free-breathing technique that does not use gaseous or intravenous contrast agents. FD has been already validated in healthy volunteers and patient with CF [38,46].

In chapter 7 we describe the use of a three-dimensional (3D) version of FD that we developed using the DIfferential Sub-sampling with Cartesian Ordering (DISCO) sequence [47]. The standard FD is based on a bi-dimensional (2D) SSFP sequence [45]. This entails that for covering the entire lung it is necessary to set a multi-slab acquisition, which can last from 3-10 minutes depending on the slab thickness. In our study, we demonstrate that 3D FD with DISCO is feasible and it facilitates the assessment of TA compared to conventional breath-hold expiratory scans. After further optimization

and validation, our 3D FD MRI might be a feasible method to implement in clinical practice for the assessment of lung ventilation.

## MRI to assess central airways mechanics

In chapter 8, we describe a MRI protocol that we developed to assess central airways dynamics [48]. Cine computed tomography (CT. Central airways are routinely assessed with bronchoscopy, but this technique has some disadvantages [49]. Bronchoscopy in children usually requires anesthesia, therefore relevant breathing maneuvers (i.e. forced expiration and coughing) cannot be performed and exact measurements of airway dimensions are difficult [49]. Dynamic evaluation can be performed using computed tomography (CT), but MRI has the advantage to avoid ionizing radiation, which is particularly important for pediatric patients or for those patients who require repeated imaging [50].

In the study described in chapter 8, we showed that cine-MRI is a feasible technique in pediatric patients [48]. By using an MRI compatible spirometer we were able to perform specific breathing maneuvers, such as peak flow or coughing that helped to diagnose tracheomalacia [48]. We think that spirometer controlled cine-MRI has great potential to replace bronchoscopy or cine-CT. To validate this technique, we are currently conducting a study where we will compare sensitivity and specificity of our spirometry-controlled cine-MRI protocols to bronchoscopy for diagnosing tracheomalacia.

In chapter 9, we applied a similar cine-MRI protocol to a cohort of healthy volunteers and patients with COPD to quantify tracheal collapse in different dynamic conditions. We proved that the cine-MRI protocol allows exact measurement of the tracheal collapse in different breathing conditions. Interestingly we found that tracheal collapse in adults varies from 23% in breath-hold condition, to 53% during peak flow expiration, to 12% in free-breathing and to 14 % during hyperventilation. To further optimize this technique, automated segmentation software tool is needed in order to reduce time-consuming post-processing. Moreover, this cine-MRI protocol might be combined with other MRI techniques to characterize airway lesions. By using a multi-parametric MRI protocol with contrast it might be possible to differentiate between benign and malignant airway lesions, avoiding unnecessary diagnostic bronchoscopy and facilitating surgical planning.



## MRI to assess diaphragm mechanics

In chapter 10, we describe the use of MRI to assess diaphragmatic motion [51]. The assessment of the function of the diaphragm is highly relevant for several diseases [52]. Neurological diseases, such as muscular dystrophy or metabolic degenerative disease, can affect diaphragmatic function [53]. Diaphragm is the main inspiratory muscle; therefore its dysfunction leads to respiratory insufficiency [53]. To date, the gold standard to assess diaphragmatic motion has been lung function tests, which

– as previusoly mentioned – are limited by low sensitivity and high variability [54]. Regarding imaging, ultrasound (US) has been the most used technique to assess diaphragmatic motion [55]. In fact compared to MRI, US is cheaper and faster, although it lacks cross-sectional capabilities and it has large variability due to the operator dependency [52,55]. MRI has a great potential to provide a sensitive imaging biomarker of diaphragm motility [56,57].

In our study, we applied a spirometry controlled cine-MRI protocol to assess diaphragm motility in patients with Pompe disease and in a group of healthy volunteers [51]. Pompe disease is a hereditary genetic metabolic disorder, characterized by accumulation of glycogen in the muscles and nerves [58]. This results in progressive muscle weakness, hypotonia, recurrent chest infections and eventually respiratory insufficiency [58]. The enzyme replacement therapy for this disease costs around 23K€ a month [59]. A sensitive tool to assess therapy efficacy on the function of the diaphragm and other respiratory muscles was missing. PFT can be indicative of diaphragmatic weakness by showing a difference between forced vital capacity (FVC) in sitting and supine position or by a decreased mean inspiratory pressure (MIP), but it provides only indirect information on diaphragm mechanics. In our study, we showed that MRI could be a sensitive tool to assess diaphragm mechanics [51]. We demonstrate that the diaphragmatic displacement can be severely impaired in patients with Pompe disease [51]. The second important finding of our study was that Pompe patients could be stratified according the displacement of the diaphragm, which was extremely impaired in some of the patients, while in others some residual function of the diaphragm in supine position was measurable [51]. The main advantage of MRI compared to ultrasound is the superior detailed anatomical information in 3D that can be obtained in dynamic and static conditions. Our MRI protocol has also the advantage that it is combined with the use of the spirometer, enabling to correlate pulmonary function with MRI parameters related to the diaphragm. Combining these parameters may provide new insights in the disease process and on its response to therapy. This method has been recently improved by automated software tools analyzing the motion of the diaphragm and other respiratory muscles. This technique will be used in a longitudinal study where we aim to compare diaphragm and chest wall musculature mechanics in patients with Pompe disease with healthy volunteers. In this study, we will also compare MRI with ultrasound of the diaphragm.

When validated, this technique is likely to become an important diagnostic tool for other diseases, such as congenital diaphragmatic hernia, diaphragm paralysis and other causes of limb-girdle weakness.

## Other directions for future research

In addition to the findings and possible future research directions based on the studies of this thesis, there are several opportunities to further improve the role of thoracic MRI as diagnostic and monitoring tool.

## MRI protocol standardization

As discussed previously, the main reason of the limited use of chest MRI in the clinic is the lack of standardization among MRI vendors and hospitals. Few centers have acquired sufficient experience to routinely introduce chest MRI in clinical practice [27]. Most of pulmonologists are not aware of chest MRI capabilities, and they prefer to rely on CT. Even radiologists find chest MRI difficult and time consuming, mostly because they are not familiar with the technique.

However, with the technological advances achieved over the last decade, chest MRI is now mature to be translated in clinical practice [7,60]. Through an international collaboration, we aim to develop a VIPS chest MRI protocol that will supply information about Ventilation, Inflammation, Perfusion and Structure in one session of maximum half an hour [21]. This protocol will be harmonized among the main MRI vendors (General Electrics, Philips and Siemens). This VIPS platform will be firstly tested for monitoring CF lung disease during a pulmonary exacerbation and later for other chronic lung diseases.

## Other applications of lung MRI in pediatrics

Different chronic lung diseases are suitable to be assessed with thoracic MRI. Bronchopulmonary dysplasia (BPD) is a severe chronic lung condition associated with long-term respiratory sequelae [61]. Chest CT has been used to assess and monitor structural lung changes in BPD [62]. Despite low or ultra-low dose CT protocols developed for BPD, the young age of these patients and the need for repeated imaging are a matter of concern regarding the risk of radiation-induced cancer. MRI as radiation-free technique would allow repeated imaging in BPD patients [62]. Moreover MRI will allow to obtain information about structural lung changes, but also about ventilation and perfusion. This functional information might be relevant to understand pathophysiology of BPD and why some patients evolve to severe obstructive airways disease.

Other diseases that might be studied with MRI are Chronic Obstructive Pulmonary Disease (COPD) and asthma. For parenchymal visualization, ultrashort (UTE) and zero echo-time (ZTE) sequences showed better spatial resolution, signal-to-noise (SNR) and contrast-to-noise ratio (CNR) than conventional sequences [63,64]. Using these sequences, patients with COPD can be differentiated from healthy subjects and classified according disease severity [64]. In fact, with increased COPD grade, the parenchymal signal intensity distribution shifts toward lower signal intensities, so UTE signal can be used to quantify parenchymal tissue destruction and inflammation [64]. These measurements are highly reproducible and usable for longitudinal studies.

Several studies have shown the utility of ventilation imaging with MRI for COPD and asthma [44,65-67]. For example oxygen-enhanced MRI showed higher correlation to PFT and clinical parameters of COPD than CT, with higher potential for more accurate clinical stage classification [66]. Similar results were showed in patients with asthma [68]. Interestingly, to date Fourier Decomposition has not been tested in COPD patients. This technique would have the advantage to supply information about

ventilation and perfusion in a single free-breathing scan without contrast administration. Perfusion biomarkers might become relevant for clinical trials and using Fourier Decomposition would avoid Gadolinium administration, which has been recently debated after evidence of brain Gd deposition [69].

Lung perfusion in COPD and asthma has been extensively investigated with MRI [70-76]. Multiple quantitative and semi quantitative perfusion-derived parameters have been described to classify COPD severity [70-72]. Interestingly MRI appears to be more sensitive than CT in identifying early perfusion abnormalities among controls and mild COPD subjects [72]. Full quantitative analysis of pulmonary microvascular perfusion seems time-consuming and not needed [70]. There is indeed a close correlation between quantitative and semi quantitative perfusion parameters, therefore semi quantitative values may be useful as surrogate markers for regional pulmonary blood flow (PBF) in clinical practice and for follow-up examinations [70].

## Development of Software tools for thoracic MRI

Another important limiting factor for the use of MRI in clinical practice has been the lack of dedicated software tools for automatic analysis of thoracic MRI. To date there are no automatic commercially available segmentation software for lung and airways on MR images. These tools are indispensable to move from qualitative to quantitative imaging. Physicians need to extract meaningful numbers out of the images that can help them to objectively determine disease progression, stability or improvement. Our group is aiming to develop scoring systems for several lung diseases that can be ultimately automated. The biomarkers derived from these software tools will be integrated in the report that accompanies the radiological examination.

## Summary

In this thesis we have shown the multiple capabilities of MRI for lung imaging. Chest MRI is ready to be converted in a unique single session imaging tool that can provide structural and functional information. Several chronic obstructive lung diseases might benefit from the development of the VIPS MRI platform, which will allow new clinical diagnostic scenarios and interventional clinical trials.

## Bibliography


1. Ciet P, Tiddens HAWM, Wielopolski PA, et al. Magnetic resonance imaging in children: common problems and possible solutions for lung and airways imaging. Pediatr Radiol 2015. DOI:10.1007/s00247-015-3420-y.
2. Muller NL. Computed tomography and magnetic resonance imaging: past, present and future. Eur Respir J Suppl 2002; 35: 3s – 12s.
3. Goo HW. Advanced functional thoracic imaging in children: From basic concepts to clinical applications. Pediatr Radiol 2013; 43: 262–8.
4. Lobo L, Antunes D. Chest CT in infants and children. Eur J Radiol 2013; 82: 1108–17.
5. De Wever W, Verschakelen J, Coolen J. Role of imaging in diagnosis, staging and follow-up of lung cancer. Curr Opin Pulm Med 2014; 20: 385–92.
6. Wild JM, Marshall H, Bock M, et al. MRI of the lung (1/3): methods. Insights Imaging 2012; 3: 345–53.
7. Biederer J, Beer M, Hirsch W, et al. MRI of the lung (2/3). Why … when … how? Insights Imaging 2012; 3: 355–71.
8. Kuo W, Ciet P, Tiddens H a WM, Zhang W, Guillerman RP, van Straten M. Monitoring cystic fibrosis lung disease by computed tomography. Radiation risk in perspective. Am J Respir Crit Care Med 2014; 189: 1328–36.
9. Egan ME. Genetics of Cystic Fibrosis: Clinical Implications. Clin Chest Med 2016; 37: 9–16.
10. Spoonhower KA, Davis PB. Epidemiology of Cystic Fibrosis. Clin Chest Med 2016; 37: 1–8.
11. Tiddens HAWM, Rosenow T. What did we learn from two decades of chest computed tomography in cystic fibrosis ? Pediatr Radiol 2014; 44: 1490–5.
12. de Jong P a, Lindblad a, Rubin L, et al. Progression of lung disease on computed tomography and pulmonary function tests in children and adults with cystic fibrosis. Thorax 2006; 61: 80–5.
13. Pearce MS, Salotti J a, Little MP, et al. Radiation exposure from CT scans in childhood and subsequent risk of leukaemia and brain tumours: a retrospective cohort study. Lancet 2012; 380: 499–505.
14. Miglioretti DL, Johnson E, Williams A, et al. The use of computed tomography in pediatrics and the associated radiation exposure and estimated cancer risk. JAMA Pediatr 2013; 167: 700–7.
15. Puderbach M, Eichinger M, Haeselbarth J, et al. Assessment of morphological MRI for pulmonary changes in cystic fibrosis (CF) patients: comparison to thin-section CT and chest x-ray. Invest Radiol 2007; 42: 715–25.
16. Failo R, Wielopolski P a, Tiddens H a WM, Hop WCJ, Mucelli RP, Lequin MH. Lung morphology assessment using MRI: a robust ultra-short TR/TE 2D steady state free precession sequence used in cystic fibrosis patients. Magn Reson Med 2009; 61: 299–306.
17. Rajaram S, Swift AJ, Capener D, et al. Lung morphology assessment with balanced steady-state free precession MR imaging compared with CT. Radiology 2012; 263: 569–77.
18. Paschal CB, Morris HD. K-space in the clinic. J Magn Reson Imaging 2004; 19: 145–59.
19. Hennig J. K-space sampling strategies. Eur Radiol 1999; 9: 1020–31.
20. Wright KL, Hamilton JI, Griswold MA, Gulani V, Seiberlich N. Non-Cartesian parallel imaging reconstruction. J Magn Reson Imaging 2014; 40: 1022–40.
21. Tiddens HAWM, Stick SM, Wild JM, et al. Respiratory tract exacerbations revisited: Ventilation, inflammation, perfusion, and structure (VIPS) monitoring to redefine treatment. Pediatr Pulmonol 2015; 50: S57–65.
22. Hirokawa Y, Isoda H, Maetani YS, Arizono S, Shimada K, Togashi K. Evaluation of motion correction effect and image quality with the periodically rotated overlapping parallel lines with enhanced reconstruction (PROPELLER) (BLADE) and parallel imaging acquisition technique in the upper abdomen. J Magn Reson Imaging 2008; 28: 957–62.
23. Ciet P, Serra G, Bertolo S, et al. Assessment of CF lung disease using motion corrected PROPELLER MRI: a comparison with CT. Eur Radiol 2015; published online May 30. DOI:10.1007/s00330-015-3850-9.

24. Renz DM, Scholz O, Böttcher J, et al. Comparison Between Magnetic Resonance Imaging and Computed Tomography of the Lung in Patients With Cystic Fibrosis With Regard to Clinical, Laboratory, and Pulmonary Functional Parameters. Invest Radiol 2015; 50: 21–4.

25. Dournes G, Menut F, Macey J, et al. Lung morphology assessment of cystic fibrosis using MRI with ultra-short echo time at submillimeter spatial resolution. Eur Radiol 2016. DOI:10.1007/s00330-016-4218-5.

26. Dournes G, Grodzki D, Macey J, et al. Quiet Submillimeter MR Imaging of the Lung Is Feasible with a PETRA Sequence at 1.5 T. Radiology 2015; 276: 258–65.

27. Ackman JB. A practical guide to nonvascular thoracic magnetic resonance imaging. J Thorac Imaging 2014; 29: 17–29.

28. Keenan K, Stupic K, Boss M, et al. Multi-site, multi-vendor comparison of T1 measurement using ISMRM/NIST system phantom. In: International Society of Magnetic Resonance in Medicine (ISMRM). 2016: #3290.

29. Ciet P., Serra G., Andrinopoulou E.A., Bertolo S., Ros M., Catalano C., Colagrande S., Tiddens H.A. MG. Diffusion weighted imaging in cystic fibrosis disease: beyond morphological imaging. Eur Radiol.

30. Nichols DP, Chmiel JF. Inflammation and its genesis in cystic fibrosis. Pediatr Pulmonol 2015; 50 Suppl 4: S39–56.

31. Cohen-Cymberknoh M, Kerem E, Ferkol T, Elizur A. Airway inflammation in cystic fibrosis: molecular mechanisms and clinical implications. Thorax 2013; 68: 1157–62.

32. Belessis Y, Dixon B, Hawkins G, et al. Early cystic fibrosis lung disease detected by bronchoalveolar lavage and lung clearance index. Am J Respir Crit Care Med 2012; 185: 862–73.

33. Keen C, Gustafsson P, Lindblad a, Wennergren G, Olin a-C. Low levels of exhaled nitric oxide are associated with impaired lung function in cystic fibrosis. Pediatr Pulmonol 2010; 45: 241–8.

34. Wagener JS, Elkin EP, Pasta DJ, et al. Pulmonary function outcomes for assessing cystic fibrosis care. J Cyst Fibros 2015; 14: 376–83.

35. Horsley A, Wild JM. Ventilation heterogeneity and the benefits and challenges of multiple breath washout testing in patients with cystic fibrosis. Paediatr Respir Rev 2015; 16: 15–8.

36. Amin R, Charron M, Grinblat L, et al. Cystic Fibrosis: Detecting Changes in Airway Inflammation with FDG PET/CT. Radiology. 2012; 264: 868–75.

37. Wielpütz MO, Puderbach M, Kopp-Schneider A, et al. Magnetic Resonance Imaging Detects Changes in Structure and Perfusion, and Response to Therapy in Early Cystic Fibrosis Lung Disease. Am J Respir Crit Care Med 2014; : 1–49.

38. Bauman G, Puderbach M, Heimann T, et al. Validation of Fourier decomposition MRI with dynamic contrast-enhanced MRI using visual and automated scoring of pulmonary perfusion in young cystic fibrosis patients. Eur J Radiol 2013; 82: 2371–7.

39. Schraml C, Schwenzer NF, Martirosian P, et al. Non-invasive pulmonary perfusion assessment in young patients with cystic fibrosis using an arterial spin labeling MR technique at 1.5 T. MAGMA 2012; 25: 155–62.

40. Fain SB, Korosec FR, Holmes JH, O'Halloran R, Sorkness RL, Grist TM. Functional lung imaging using hyperpolarized gas MRI. J Magn Reson Imaging 2007; 25: 910–23.

41. Lilburn DML, Pavlovskaya GE, Meersmann T. Perspectives of hyperpolarized noble gas MRI beyond 3He. J Magn Reson 2013; 229: 173–86.

42. Jakob PM, Wang T, Schultz G, Hebestreit H, Hebestreit A, Hahn D. Assessment of human pulmonary function using oxygen-enhanced T(1) imaging in patients with cystic fibrosis. Magn Reson Med 2004; 51: 1009–16.

43. Stadler A, Stiebellehner L, Jakob PM, et al. Quantitative and o(2) enhanced MRI of the pathologic lung: findings in emphysema, fibrosis, and cystic fibrosis. Int J Biomed Imaging 2007; 2007: 23624.

44. Zhang W-J, Niven RM, Young SS, Liu Y-Z, Parker GJM, Naish JH. Dynamic oxygen-enhanced magnetic resonance imaging of the lung in asthma—Initial experience. Eur J Radiol 2015; 84: 318–26.

45. Bauman G, Puderbach M, Deimling M, et al. Non-contrast-enhanced perfusion and ventilation assessment of the human lung by means of fourier decomposition in proton MRI. Magn Reson Med 2009; 62: 656–64.

46. Lederlin M, Bauman G, Eichinger M, et al. Functional MRI using Fourier decomposition of lung signal: reproducibility of ventilation- and perfusion-weighted imaging in healthy volunteers. Eur J Radiol 2013; 82: 1015–22.

47. Saranathan M, Rettmann DW, Hargreaves BA, Clarke SE, Vasanawala SS. DIfferential subsampling with cartesian ordering (DISCO): A high spatio-temporal resolution dixon imaging sequence for multiphasic contrast enhanced abdominal imaging. J Magn Reson Imaging 2012; 35: 1484–92.

48. Ciet P, Wielopolski P, Manniesing R, et al. Spirometer-controlled cine magnetic resonance imaging used to diagnose tracheobronchomalacia in paediatric patients. Eur Respir J 2014; 43: 115–24.

49. Williamson JP, James a L, Phillips MJ, Sampson DD, Hillman DR, Eastwood PR. Quantifying tracheobronchial tree dimensions: methods, limitations and emerging techniques. Eur Respir J 2009; 34: 42–55.

50. Boiselle PM, Ernst A. Recent advances in central airway imaging. Chest 2002; 121: 1651–60.

51. Wens SC, Ciet P, Perez-Rovira A, et al. Lung MRI and impairment of diaphragmatic function in Pompe disease. BMC Pulm Med 2015; 15: 54.

52. Kharma N. Dysfunction of the diaphragm: imaging as a diagnostic tool. Curr Opin Pulm Med 2013; 19: 394–8.

53. Nason LK, Walker CM, McNeeley MF, Burivong W, Fligner CL, Godwin JD. Imaging of the diaphragm: anatomy and function. Radiographics 2012; 32: E51–70.

54. Pacia EB, Aldrich TK. Assessment of diaphragm function. Chest Surg Clin N Am 1998; 8: 225–36.

55. Chavhan GB, Babyn PS, Cohen R a, Langer JC. Multimodality imaging of the pediatric diaphragm: anatomy and pathologic conditions. Radiographics 2010; 30: 1797–817.

56. Eichinger M, Tetzlaff R, Puderbach M, Woodhouse N, Kauczor H-U. Proton magnetic resonance imaging for assessment of lung function and respiratory dynamics. Eur J Radiol 2007; 64: 329–34.

57. Unal O, Arslan H, Uzun K, Ozbay B, Sakarya ME. Evaluation of diaphragmatic movement with MR fluoroscopy in chronic obstructive pulmonary disease. Clin Imaging 2001; 24: 347–50.

58. Pellegrini N, Laforet P, Orlikowski D, et al. Respiratory insufficiency and limb muscle weakness in adults with Pompe's disease. Eur Respir J 2005; 26: 1024–31.

59. Kanters T a, Hoogenboom-Plug I, Rutten-Van Mölken MPMH, Redekop WK, van der Ploeg AT, Hakkaart L. Cost-effectiveness of enzyme replacement therapy with alglucosidase alfa in classic-infantile patients with Pompe disease. Orphanet J Rare Dis 2014; 9: 75.

60. Biederer J, Mirsadraee S, Beer M, et al. MRI of the lung (3/3)-current applications and future perspectives. Insights Imaging 2012; 3: 373–86.

61. Lal CV, Ambalavanan N. Biomarkers, Early Diagnosis, and Clinical Predictors of Bronchopulmonary Dysplasia. Clin Perinatol 2015; 42: 739–54.

62. Walkup LL, Woods JC. Newer Imaging Techniques for Bronchopulmonary Dysplasia. Clin Perinatol 2015; 42: 871–87.

63. Ohno Y, Nishio M, Koyama H, et al. Pulmonary 3 T MRI with ultrashort TEs: influence of ultrashort echo time interval on pulmonary functional and clinical stage assessments of smokers. J Magn Reson Imaging 2014; 39: 988–97.

64. Ma W, Sheikh K, Svenningsen S, et al. Ultra-short echo-time pulmonary MRI: Evaluation and reproducibility in COPD subjects with and without bronchiectasis. J Magn Reson Imaging 2015; 41: 1465–74.

65. Ohno Y, Hatabu H, Takenaka D, Van Cauteren M, Fujii M, Sugimura K. Dynamic oxygen-enhanced MRI reflects diffusing capacity of the lung. Magn Reson Med 2002; 47: 1139–44.

66. Ohno Y, Iwasawa T, Seo JB, et al. Oxygen-enhanced Magnetic Resonance Imaging versus Computed Tomography. Am J Respir Crit Care Med 2008; 177: 1095–102.

67. Kruger SJ, Nagle SK, Couch MJ, Ohno Y, Albert M, Fain SB. Functional imaging of the lungs with gas agents. J Magn Reson Imaging 2015; : n/a – n/a.

68. Ohno Y, Nishio M, Koyama H, et al. Asthma: Comparison of Dynamic Oxygen-enhanced MR Imaging and Quantitative Thin-Section CT for Evaluation of Clinical Treatment. Radiology 2014; 273: 132660.

69. Murata N, Gonzalez-Cuyar LF, Murata K, et al. Macrocyclic and Other Non–Group 1 Gadolinium Contrast Agents Deposit Low Levels of Gadolinium in Brain and Bone Tissue. Invest Radiol 2016; 00: 1.

70. Hueper K, Parikh M a, Prince MR, et al. Quantitative and semiquantitative measures of regional pulmonary microvascular perfusion by magnetic resonance imaging and their relationships to global lung perfusion and lung diffusing capacity: the multiethnic study of atherosclerosis chronic obstructi. Invest Radiol 2013; 48: 223–30.

71. Hueper K, Vogel-Claussen J, Parikh M a., et al. Pulmonary Microvascular Blood Flow in Mild Chronic Obstructive Pulmonary Disease and Emphysema. The MESA COPD Study. Am J Respir Crit Care Med 2015; 192: 570–80.

72. Fan L, Xia Y, Guan Y, et al. Capability of differentiating smokers with normal pulmonary function from COPD patients: a comparison of CT pulmonary volume analysis and MR perfusion imaging. Eur Radiol 2013; 23: 1234–41.

73. Xia Y, Guan Y, Fan L, et al. Dynamic Contrast Enhanced Magnetic Resonance Perfusion Imaging in High-Risk Smokers and Smoking-Related COPD: Correlations with Pulmonary Function Tests and Quantitative Computed Tomography. COPD J Chronic Obstr Pulm Dis 2014; 11: 510–20.

74. Sergiacomi G, Taglieri A, Chiaravalloti A, et al. Acute COPD exacerbation: 3 T MRI evaluation of pulmonary regional perfusion – Preliminary experience. Respir Med 2014; 108: 875–82.

75. Bryant M, Ley S, Eberhardt R, et al. Assessment of the relationship between morphological emphysema phenotype and corresponding pulmonary perfusion pattern on a segmental level. Eur Radiol 2015; 25: 72–80.

76. Jobst BJ, Triphan SMF, Sedlaczek O, et al. Functional Lung MRI in Chronic Obstructive Pulmonary Disease: Comparison of T1 Mapping, Oxygen-Enhanced T1 Mapping and Dynamic Contrast Enhanced Perfusion. PLoS One 2015; 10: e0121520.

# Chapter 12

## Summary

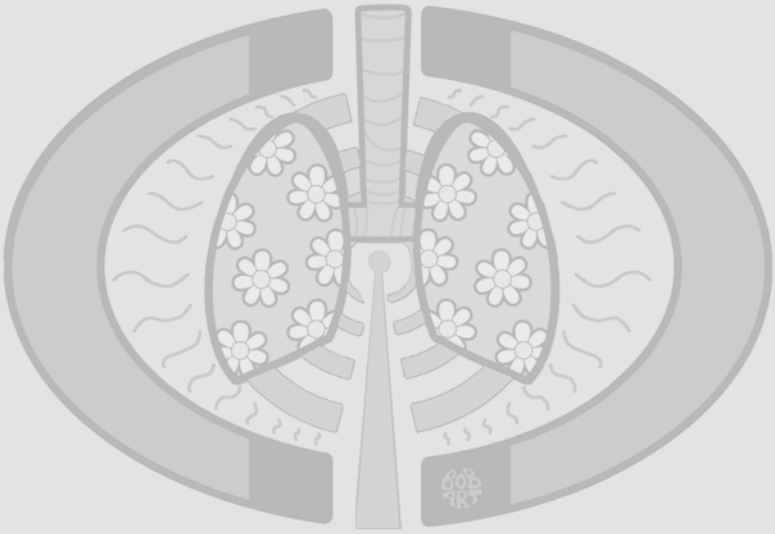

**Chapter 1** contains a general introduction to thoracic MRI and describes the aims of the studies included in this thesis.

**Chapter 2** is a state-of-the-art review about thoracic MRI, especially focused on children. It sets the stage for the studies performed in this thesis by describing the most common MRI acquisition techniques, their problems and the possible solutions to make chest MRI feasible in children.

The studies described from *chapter 3 to chapter 7* are the core of this thesis and consist of the application and development of new MRI protocols for monitoring Cystic Fibrosis (CF) lung disease. CF lung disease requires repeated imaging in order to assess disease progression. To reduce cumulative dose related to CT imaging, MRI has been proposed as a safe radiation-free alternative.

In **chapter 3**, we describe a study comparing chest MRI to CT to monitor CF lung disease using PROPELLER MRI, a sequence with reduced sensitivity to motion artifacts. We found that motion correction in PROPELLER MRI does not improve assessment of CF lung disease compared to CT. However, the good inter- and intra-observer agreement and the high specificity suggest that PROPELLER MRI can play a role in the short-term follow-up of CF lung disease (i.e. pulmonary exacerbations).

In chapter 4 and 5, we describe the use of diffusion-weighted MRI (DW-MRI) as possible tool to monitor and quantify lung inflammation during respiratory tract exacerbation (RTE) in patients with CF. **Chapter 4** represents a cross-sectional study where we explored the feasibility of DW-MRI to assess inflammatory lung changes in patients with CF. We observed that the areas of increased DW-MRI signal ("hotspots") only partly overlapped structural abnormalities on morphological CT or MRI. In addition, DW-MRI scores strongly correlated with radiological and clinical indicators of CF lung disease severity. Significant differences in pulmonary function ($FEV_1$) were found between patients without and with DW-MRI hotspots. Finally, we found that the amount of mucus in the lungs of patients with CF was the best predictor of restricted diffusion.

**In Chapter 5** we describe a longitudinal DW-MRI study, where we applied our DW-MRI protocol to a group of CF patients with and without respiratory tract exacerbation (RTE). This study demonstrated that DWI score and Apparent Diffusion Coefficient (ADC) detected the clinical changes of patients with CF treated for a RTE with fair to good accuracy. Moreover, DWI score and ADC were strongly correlated with symptom scores and spirometry measures in these patients.

In **chapter 6** we describe the use of contrast enhanced MRI (CEMRI) in a group of CF patients to assess the relationship between hypoperfusion (HP) and trapped air (TA). We compared the amount of TA quantified by CT, MRI and pulmonary function tests (PFT) with the amount of HP quantified with MRI. Our study demonstrated that HP was more frequent and its volume larger than TA quantified by MRI. Interestingly the volume of TA measured with MRI was similar to that quantified by PFT,

but smaller than TA on CT. Our findings showed that HP contributes importantly to regions often described in radiology reports as ”trapped air” or as “mosaic pattern” on CT. Therefore, we propose that these terms could be better replaced by low-density region (LDR) for CT and low-intensity region (LIR) for MRI respectively.

In **chapter 7** we describe an upgraded three-dimensional (3D) version of Fourier Decomposition (FD) technique, an MRI method for ventilation and perfusion imaging. We showed that both Cartesian and non-Cartesian K-space acquisition schemes enable 3D FD ventilation maps. Despite that the temporal resolution of our protocol was not sufficient to obtain 3D perfusion maps, 3D FD enabled a faster and more comprehensive assessment of trapped air compared to conventional 2D and 3D breath-hold scans. This method might be applied in critically ill or non-collaborative patients to perform ventilation imaging with MR.

Chapters 8-10 describe the use of MRI to assess airways and diaphragm in dynamic conditions (cine-MRI). In **chapter 8**, we described a new MRI protocol to assess tracheobronchomalacia (TBM) in pediatric patients. This feasibility study showed that cine-MRI has great potential to replace bronchoscopy or cine-CT in pediatric patients, so limiting the burden of invasive procedures or radiation exposure. In **chapter 9** we used the same MRI protocol as described in chapter 8 to assess tracheal collapse in a group of healthy volunteers and patients with saber-sheath TBM. We showed that MRI allows to assess tracheal collapse in different breathing conditions, such as peak flow, tidal breathing and hyperventilation maneuvers. Significant differences in tracheal collapse were found between volunteers and TBM patients for all three breathing maneuvers.

In **chapter 10**, we described the use of MRI to assess diaphragmatic impairment in a group of patients with Pompe disease, a glycogen storage disease that affected nerves and muscles. Using a spirometry controlled cine-MRI protocol we assessed diaphragm motility in patients with Pompe disease and a group of healthy volunteers. We demonstrated that the diaphragmatic displacement in patients with Pompe disease was severely impaired compared to healthy volunteers. We also demonstrated that Pompe patients could be stratified according the displacement of the diaphragm, which function was extremely impaired in some of the patients, while in others some residual function of the diaphragm in supine position was measurable. The higher sensitivity of our MRI method compared to PFT and ultrasound could provide new insights in the disease process of Pompe disease and on its response to therapy.

The findings of the studies included in the thesis are discussed in **chapter 11** along with their implications and future research directions.

# Chapter 13

## Samenvatting

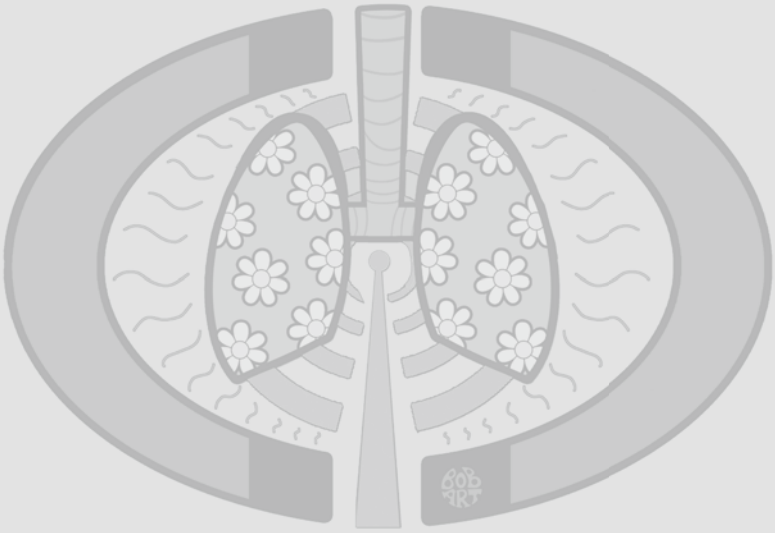

**Hoofdstuk 1** geeft een algemene introductie over de long MRI als stralingsvrij alternatief voor de long CT. De doelen van de studies die in dit proefschrift staan worden beschreven.

**Hoofdstuk 2** is een state-of-the-art review over long MRI, vooral voor kinderen. Deze review geeft een achtergrond van de studies in dit proefschrift en beschrijft de meest gebruikte MRI-technieken, hun problemen en de mogelijke oplossingen om long MRI bij kinderen mogelijk te maken.

De studies beschreven in *hoofdstuk 3 t/m 7* zijn de kern van dit proefschrift en beschrijven de ontwikkeling en het gebruik van nieuwe MRI protocollen voor Cystic Fibrosis (CF) longziekte. Voor CF longziekte is het belangrijk om regelmatig en met veilige en gevoelige radiologische methoden de voortgang van de longziekte te bewaken.

In **hoofdstuk 3** vergelijken we de gevoeligheid van PROPELLER MRI met CT om CF longziekte op te sporen. PROPELLER MRI zou minder gevoelig zijn voor storing door beweging. We vonden PROPELLER MRI in vergelijking met CT toch minder goed om CF longziekte te monitoren. Wel was er een goede inter- en intra-observer overeenkomst en was er een hoge specificiteit van PROPELLER MRI om longafwijkingen bij CF op te sporen. Dit suggereert dat MRI een rol zou kunnen spelen in de korte-termijn follow-up van CF longziekte, bijvoorbeeld bij toename van long problemen (exacerbaties).

In hoofdstuk 4 en 5 beschrijven we het gebruik van diffusie-weighted MRI (DW-MRI) als techniek voor het opsporen en kwantificeren van ontsteking tijdens exacerbaties bij patiënten met CF. **Hoofdstuk 4** beschrijft ons cross-sectionele onderzoek waarin we de uitvoerbaarheid van DW-MRI hebben onderzocht om ontsteking in de longen bij patiënten met CF op te sporen. We hebben waargenomen dat gebieden met een verhoogd DW-MRI signaal ("hotspots") slechts gedeeltelijk overlappen met structurele afwijkingen op CT of MRI. Verder was er een duidelijke samenhang tussen de DW-MRI scores met radiologische en klinische kenmerken van CF longziekte. Significante verschillen in longfunctie werden gevonden tussen patiënten zonder en met DW-MRI hotspots. Uiteindelijk vonden we dat de hoeveelheid slijm in de luchtwegen van patiënten met CF de beste voorspeller was van de ernst van de ontsteking.

**Hoofdstuk 5** beschrijft ons DW-MRI vervolgonderzoek, waar we het DW-MRI protocol bij een groep van CF-patiënten met en zonder exacerbatie hebben getest. Deze studie toonde aan dat we met de DWI score en de apparent diffusie coëfficiënt (ADC) de klinische veranderingen bij patiënten met CF behandeld voor een exacerbatie met een redelijke tot goede nauwkeurigheid konden volgen. Verder kwamen de DWI score en ADC goed overeen met symptoomscores en longfunctiemetingen bij deze patiënten.

In **hoofdstuk 6** beschrijven we het gebruik van contrast enhanced MRI (CEMRI) bij een groep CF-patiënten om de relatie te bestuderen tussen longdoorbloeding en toegankelijkheid van de kleine luchtwegen (= Trapped air: TA). We vergeleken de hoeveelheid TA gemeten met CT, MRI en longfunctietesten met de longdoorbloeding gekwantificeerd met MRI. Onze MRI studie toonde dat het gebied met een verminderde longdoorbloeding groter was dan het trapped air gebied. De hoeveelheid TA gemeten met MRI kwam goed overeen met die gemeten met longfunctietesten. TA volume gemeten met MRI was kleiner dan dat gemeten met CT. Onze bevindingen tonen aan dat verminderde longdoorbloeding bijdraagt aan gebieden die in radiologierapporten worden aangeduid als "trapped air" of als "mozaïek patroon" op CT. Daarom stellen we voor dat deze termen beter kunnen worden vervangen door lage dichtheid regio (LDR) voor CT en lage intensiteit regio (LIR) voor MRI.

In **hoofdstuk 7** beschrijven we een verbeterde drie-dimensionale (3D) versie van Fourier Decomposition (FD) techniek, een MRI methode om ventilatie en doorbloeding met MRI zichtbaar te maken. Deze methode kan bij ernstig zieke of niet-cooperatieve patiënten worden toegepast.

In **hoofdstuk 8-10** beschrijven we het gebruik van cine-MRI voor de dynamische beoordeling van luchtwegen en het middenrif. In **hoofdstuk 8** beschrijven we een nieuw dynamisch MRI-protocol voor de beoordeling van centrale luchtweg stabiliteit bij kinderen. Deze studie toonde aan dat cine-MRI waarschijnlijk belastende kijkingrepen kan vervangen bij kinderen voor de beoordeling van luchtwegen. In **hoofdstuk 9** gebruikten we het cine-MRI protocol om de luchtwegstabiliteit bij een groep gezonde vrijwilligers en bij volwassen patiënten met slappe centrale luchtwegen te beoordelen. Duidelijke verschillen in luchtwegstabiliteit werden gevonden tussen vrijwilligers en patiënten.

In **hoofdstuk 10** beschrijven we het gebruik van MRI om de functie van het middenrif te beoordelen in een groep van patiënten met de ziekte van Pompe, een stofwisselingsziekte die zenuwen en spieren aantast. Tijdens gecontroleerde ademhalingsmanoeuvres beoordeelden wij de bewegelijkheid van het middenrif bij patiënten met de ziekte van Pompe en bij een groep gezonde vrijwilligers. We tonen aan dat de functie van het middenrif bij patiënten met de ziekte van Pompe ernstig verminderd was ten opzichte van de gezonde vrijwilligers. Deze methode kan ons helpen om het ziekteproces bij de ziekte van Pompe beter te begrijpen en om het effect van enzymtherapie beter te beoordelen.

De bevindingen van de studies in dit proefschrift worden besproken in hoofdstuk 11, samen met hun betekenis voor de gezondheidszorg en toekomstige onderzoeksrichtingen.

# List of Publications

## Manuscripts based on this thesis

### Chapter 2

**Ciet P**, Tiddens HA, Wielopolski PA, Wild JM, Lee EY, Morana G, Lequin MH. Magnetic resonance imaging in children: common problems and possible solutions for lung and airways imaging. Pediatric Radiology 2015 Dec;45(13):1901-15.

### Chapter 3

**Ciet P**, Serra G, Bertolo S, Spronk S, Ros M, Fraioli F, Quattrucci S, Assael MB, Catalano C, Pomerri F, Tiddens HA, Morana G. Assessment of CF lung disease using motion corrected PROPELLER MRI: a comparison with CT. European Radiology 2016 Mar;26(3):780-7.

### Chapter 4

**Ciet P**, Serra G, Andrinopoulou ER, Bertolo S, Ros M, Catalano C, Colagrande S, Tiddens HA, Morana G. Diffusion weighted imaging in cystic fibrosis disease: beyond morphological imaging. European Radiology 2016 Feb 12.

### Chapter 5

**Ciet P**, Bertolo S, Ros M, Andrinopoulou ER, Tavano V, Lucca F, Feiweier T, Krestin GP, Tiddens HAWM, Morana G. Quantification of Lung Inflammation in Cystic Fibrosis during Respiratory Tract Exacerbation using Diffusion-Weighted Magnetic Resonance Imaging. (Submitted)

### Chapter 6

**Ciet P**; Wielopolski P; Li S; Andrinopolou EA, van Der Wiel E; Morana G, Tiddens HAWM. Mosaic pattern in Cystic Fibrosis lung disease: trapped air or hypoperfusion? (Submitted)

### Chapter 7

**Ciet P**; Bos AC, Wielopolski P, Hernández-Tamames JA, de Bruijne M, Tiddens HAWM, Perez-Rovira A. Three-dimensional Fourier Decomposition lung Magnetic Resonance Imaging with Cartesian and Differential Sub-sampling Cartesian Ordering (DISCO) techniques? (Submitted)

### Chapter 8

**Ciet P**, Wielopolski P, Manniesing R, Lever S, de Bruijne M, Morana G, Muzzio PC, Lequin MH, Tiddens HA. Spirometer-controlled cine magnetic resonance imaging used to diagnose tracheobronchomalacia in paediatric patients. European Respiratory Journal. 2014 Jan;43(1):115-24

**Chapter 9**

Ciet P, Boiselle PA, Bankier AA, Heidinger B, O'Donnel C, Andrinopolou EA, Alsop D, Litmanovich DE. Cine-MRI of Tracheal Dynamics in Healthy Volunteers and Patients with Tracheomalacia. (In preparation)

**Chapter 10**

Wens SC, **Ciet P**, Perez-Rovira A, Logie K, Salamon E, Wielopolski P, de Bruijne M, Kruijshaar ME, Tiddens HA, van Doorn PA, van der Ploeg AT. Lung MRI and impairment of diaphragmatic function in Pompe disease. BMC Pulmonary Medicine. 2015 May 6;15:54

## Other manuscripts

- Amin R, Charron M, Grinblat L, Shammas A, Grasemann H, Graniel K, **Ciet P**, Tiddens H, Ratjen F. Cystic fibrosis: detecting changes in airway inflammation with FDG PET/CT. Radiology. 2012 Sep;264(3):868-75.
- Liszewski MC, Hersman FW, Altes TA, Ohno Y, **Ciet P**, Warfield SK, Lee EY. Magnetic resonance imaging of pediatric lung parenchyma, airways, vasculature, ventilation, and perfusion: state of the art. Radiology Clinic North America. 2013 Jul;51(4):555-82.
- **Ciet P**, Litmanovich DE. MR safety issues particular to women. Magnetic Resonance Imaging Clinic North America. 2015 Feb;23(1):59-67.
- Baez JC, **Ciet P**, Mulkern R, Seethamraju RT, Lee EY Pediatric Chest MR Imaging: Lung and Airways. Magnetic Resonance Imaging Clinic North America. 2015 May;23(2):337-49.
- Baez JC, Seethamraju RT, Mulkern R, **Ciet P**, Lee EY. Pediatric Chest MR Imaging: Sedation, Techniques, and Extracardiac Vessels. Magnetic Resonance Imaging Clinic North America. 2015 May;23(2):321-35.
- Tiddens HA, Stick SM, Wild JM, **Ciet P**, Parker GJ, Koch A, Vogel-Claussen J. Respiratory tract exacerbations revisited: ventilation, inflammation, perfusion, and structure (VIPS) monitoring to redefine treatment. Pediatric Pulmonology. 2015 Oct;50 Suppl 40:S57-65.
- Tepper LA, **Ciet P**, Caudri D, Quittner AL, Utens EM, Tiddens HA. Validating chest MRI to detect and monitor cystic fibrosis lung disease in a pediatric cohort. Pediatric Pulmonology. 2016 Jan;51(1):34-41.
- **Ciet P**, Boiselle PM, Michaud G, O'Donnell C, Litmanovich DE. Optimal imaging protocol for measuring dynamic expiratory collapse of the central airways. Clinic Radiology. 2016 Jan;71(1):e49-55
- van Mastrigt E, Logie K, **Ciet P**, Reiss IK, Duijts L, Pijnenburg MW, Tiddens HA. Lung CT imaging in patients with bronchopulmonary dysplasia: A systematic review. Pediatr Pulmonol. 2016 May 5.

- Rutten M, **Ciet P**, van den Biggelaar R, Oussoren E, Langendonk JG, van der Ploeg AT, Langeveld M. Severe tracheal and bronchial collapse in adults with type II mucopolysaccharidosis. Orphanet Journal of Rare Disease. 2016 Apr 26;11:50.
- Salamon E, Lever S, Kuo W, **Ciet P**, Tiddens HA. Spirometer guided chest imaging in children: It is worth the effort!. Pediatr Pulmonol. 2016 Jun 6.
- Mogalle K, Perez-Rovira A, **Ciet P**, Wens SC, van Doorn PA, Tiddens HA, van der Ploeg AT, de Bruijne M. Quantification of Diaphragm Mechanics in Pompe Disease Using Dynamic 3D MRI. PLoS One. 2016 Jul 8;11(7):e0158912.

## Book Chapters and Monographs

- European Respiratory Society (ERS) handbook of Paediatric Respiratory Medicine – **Ciet P**, M van Straten, Tiddens HA. Computed tomography. 2013. ISBN 9781849840392
- **Ciet P**, Heidinger B, D Litmanovich – Trachea and Bronchi – Problem Solving in Chest Imaging – Elsevier (In press)

# Acknowledgments/Dankwoord

Finally the thesis is ready! I say this with emphasis, because a lot of things happened since I started my PhD. I moved to the Netherlands, then to USA then back to the Netherlands. My beautiful wife gave me two amazing children, I learned a third language and now finally I have finished my PhD, so this is the moment to thank all people who contributed to this journey towards my PhD.

Eindelijk is de thesis klaar! Ik zeg dit met nadruk, omdat er veel is gebeurd sinds ik mijn Phd startte. Ik verhuisde naar Nederland, toen naar Amerika en weer terug naar Nederland. Mijn fantastische vrouw heeft mij twee prachtige kinderen gegeven, ik heb een nieuwe taal geleerd en nu heb ik eindelijk mijn proefschrift klaar. Dus dit is het moment om alle mensen te bedanken die hebben bijgedragen aan mijn proefschrift.

Ten eerste mijn promoteren, die mij de mogelijkheid gaven dit boekje te maken. Professor Dr. H.A.W.M Tiddens, beste Harm (Beste baas), ik heb je ontmoet in 2009, toen ik je van de luchthaven van Venetië naar het Treviso ziekenhuis bracht. Ik herinner me dat we de hele reis in het Engels met elkaar spraken, wat in die periode nog een beetje moeilijk was voor mij, want mijn niveau was nog erg basic. Ik werd direct gegrepen door je enorme enthousiasme en passie voor onderzoek. Dit enthousiasme heeft me altijd geïnspireerd en bevorderd in mijn persoonlijke ontwikkeling. Bedankt voor je begeleiding in dit gehele traject, voor jouw hulp om me te concentreren op belangrijke dingen en om me het gevoel te geven onderdeel te zijn van jouw familie. Dit ook dankzij jouw vrouw Rosaria, voor de verschillende diners en feesten, die mij en mijn familie het gevoel hebben gegeven meer vrienden dan collega's te zijn. Grote dank ook aan je dochters (Chiara en Elena), die mij en mijn vrouw wat vrije tijd hebben gegeven door op te passen op onze kinderen.

Prof G. P. Krestin, beste Gabriel, bedankt voor de onderzoeksmogelijkheden die u mij hebt geboden binnen uw afdeling hier in Rotterdam. Bedankt voor het ondersteunen van mijn fellowship in de Verenigde Staten en mij te helpen bij het leren van deze nieuwe taal. Ik wil je ook graag bedanken voor de geboden mogelijkheid van de kinderradiologie-opleiding, waaraan ik in januari zal beginnen. Het is voor mij een eer te werken binnen uw afdeling, één van de beste radiologie-afdelingen binnen Europa en in de hele wereld.

Dr Giovanni Morana, dear Gianni thanks for your support. You have been my first mentor since my residency training and you are the person who believed in me and gave the opportunity to achieve this PhD. You transmitted me your passion for Magnetic Resonance Imaging and your comments and suggestions have been always determinant to finalize the projects described in this thesis. I will always be grateful.

Prof Dr Johan de Jongste, beste Johan bedankt voor je kritische blik op mijn onderzoek projecten, je ervaring in kinderlongziekten was altijd bepalend om mij belangrijk opmerkingen te kunnen geven. Dank ook voor de bereidheid om plaats te nemen in de kleine en grote commissie.

Prof Dr Mathias Prokop, Prof Dr Irwin Reiss en Prof Dr Edmond Rings bedankt voor het plaatsnemen in de kleine commisie. Prof Dr Juan Hernandez-Tamamez,, Dr Menno van der Eerden, Dr. Jan von der Thusen en Dr Giovanni Morana bedankt voor het plaatsnemen in de grote commisie.

Tijdens mijn promotie was ik regelmatig op de afdeling Radiologie aanwezig, vooral in het Sophia op afdeling Kinderradiologie. Hier zou ik graag de volgende mensen bedanken die steeds voor me klaar stonden:
Dear Dr Piotr Alfred Wielopolski, o querido Piotr, I do not know if I have to thank you in English or Spanish, considering our "language-switching brainstorming sessions" where we discussed about lung MRI in 2-3 languages. Without your support, this thesis could not have been possible; your contribution has been crucial. A large part of my knowledge in lung MRI has been absorbed by your incredible experience in this difficult topic. I really enjoyed and I am still enjoying working with you and I consider you not just a colleague, but also a real friend.
Dr Jacqueline van Holten, Dr Nanko de Graaf, Dr Annick Davos, Dr Simone Ter Host, Dr Josephine Bomer, Prof Dr Morteza Meradij en Dr Marjolein Dremmen bedankt dat jullie mij steeds hielpen in het integratieproces van de klinische activiteiten binnen de afdeling Kinderradiologie.
Dr Marteen Lequin bedankt voor de input voor het review artikel waar jij senior-auteur van bent. Ook voor je uitleg en antwoorden op mijn radiologische vragen.
Ik wil ook graag de kinderradiologie baliemedewerkers in het Sophia bedanken, Roland Margreet en Edith. Ik heb veel praktische hulp gekregen bij het inplannen van alle long MRI scans.
Ik wil oog graag de afdeling Medische beeldvorming (Biomedical Imaging Groep Rotterdam) bedanken waar ik met plezier heb samengewerkt met Ass. Prof. Dr. Marleen de Bruijne, Ass. Prof Dr Stephan Klein, Dr Jean-Marie Guyader, Dr Adria Perez-Rovira. Querido Adria, me he encantado trabajar contigo y poder hablar de nuestros proyectos de investigación en español. Te voy a echar de menos in Rotterdam seguramente.

Andere mensen van de Radiologie afdeling die van belang zijn geweest om dit proefschrift af te ronden zijn Dr Marcel van Straten, Silvia Bruiniks, Hanneke Muharam – Kamminga, Mika Vogel, Mart Rentmeester en alle MRI en CT laboranten. Een speciaal bedankt aan de medewerkers van de Research Office en dan met name Linda Everse en Jolanda Meijer. Ook bedankt aan de medewerkers van het imaging trialbureau en de secretaresse van radiologie-afdeling voor alle antwoorden op alle praktische vragen die ik had.

Dr Ieneke Hartmann, beste Ieneke bedankt voor alles wat je me geleerd hebt over thoracale ziekten, voornamelijk in mijn eerste periode in Rotterdam. Ik wil ook je bedanken dat jij mij wilde helpen om de thorax radiologie opleiding te bekrachtiging door NVvR.

I would like to thanks the entire group of the chest section at Beth Israel Deaconess Medical Center (BIDMC) in Boston, a group of outstanding thoracic radiologists and researchers.

Firstly, Ass. Prof Dr Diana Litmanovich, dear Diana thanks for your support before, during and after the fellowship program; I always felt that I could discuss with you any problem openly. It was also nice to collaborate with you to several research projects.

Prof Dr Alexander Bankier, dear Alex thanks for all teaching moment in the reading room and for the scientific inputs in the research projects I conducted at BIDMC. A big thanks also goes to your wife Francesca for the exquisite dinners at your place and to your daughter Miriam for babysitting Agata in Boston.

Prof Dr Phillip Boiselle, dear Phil I would like to thank you for all teaching moments in the reading room. I really enjoyed working with you on those Fridays morning, especially when you gave me so many precise references and explanations for the thoracic findings we were describing in the reports. Thanks as well for your important contribution in the COPD MRI project.
Dr Paul Spirn, dear Paul I would never forget all your mentoring during the first period of my fellowship in Boston. I really enjoyed all moments I spent with you in the reading room learning the importance of a properly written report. Your quote "a radiologist is known by his reports" has become one of my preferred adage.

I want to thank Prof Dr Ronald Eisenberg and Dr Janneth Romero for their tutoring during the fellowship. I would like to thank also Prof Dr David Alsop, Dr Fotini Kourtedelis and all research assistants for your support in the COPD MRI project.

A special thanks goes to Mario Silva. Caro Mario avere trascorso l'anno con te a Boston è stato molto bello. Poter chiacchierare un po' in Italiano dopo lunghe giornate di lavoro, uscire assieme per andare a vedere le partite dei Boston Celtics o per far una corsetta lungo il Charles river sono stati momenti importanti del mio periodo a Boston che non dimenticherò mai. Anche se lontano, ti considero più che un amico, ed insieme con Monica (e Agata) siete diventati oramai parte della nostra "famiglia".

A big thanks goes to Benedikt Heidinger, it was a lot of fun working with you. Dear Bene thanks for helping me with the MRI projects and for all time spent together in Boston. I would like to thank also Maria Elena Occhipinti and Meredith Cunningham for the research collaboration during my fellowship and for the assistance in submitting papers.

Prof Dr Edward Lee, dear Edward thanks for giving me the opportunity to work with you at the Boston Children's Hospital. During my rotation there, I learned a lot from your great knowledge in Pediatric thoracic radiology. I also enjoyed working with you to several research projects. I hope this fruitful collaboration will continue.

A big thanks goes to all friends/family we made in Boston: Lina&Enders, Francesca&Ivan, Stefania&Mario and Lucy&Andreas. The time spent together with our children was great and a lot of fun.

Het kinderlongziektenteam van het Erasmus MC Sophia, beste Marielle, Hettie, Sanne, Suzanne, Saskia, Isme bedankt voor alle input tijdens de researchbesprekingen op de vrijdagmiddag. Lieve Lisbeth bedankt voor het introduceren van mij in het Generatie R project, waarvan ik hoop dat het een begin zal zijn van een lange samenwerking.

Verder wil ik graag de kinderlongziekten "familie" bedanken. Ik zeg familie, want ik heb mij altijd gevoeld als onderdeel van een uitstekende groep die niet alleen samenwerkt maar elkaar ook helpt wanneer dat nodig is. In deze groep is er een waardevol persoon die alle problemen kan oplossen, dat is Els van der Wiel. Beste Els bedankt voor het beantwoorden van alle praktische dingen, je bent een voorbeeld voor de METC! Je was altijd aanwezig wanneer dat nodig was, ik ben je ergje jeje dankbaar Ik wil ook de groep van longfunctielaboranten bedanken (Sandra, Laura, Cheyenne en Sunny), zonder jullie hulp zou het niet mogelijk zijn geweest voor geen spirometrie gecontroleerde MRI. Ook de CF verpleegkundigen (Evelien, Jorien, Annelies) en de kinderlongartsen van de Kinderhaven wil ik graag bedanken voor het helpen van het vinden van de patiënten voor mijn laatste studie.

Dan wil ik mijn directe collega's Daan, Marije, Esther, Leonie, Aukje, Jennifer, en Wieying bedanken voor de gezelligheid en het meedenken met de dagelijkse problemen in het leven van een promovendus. Hartelijke dank ook aan Irma Stok-Beckers, beste Irma bedankt voor het oplossen van alle praktische dingen en voor het altijd vinden van 30 minuten tijd in de drukke agenda van de baas om een afspraak te maken.

Ook bedankt aan mijn docente Chrisje, je geduld en flexibiliteit hielpen me de tijd te vinden om onze Nederlandse lessen te plannen en om deze taal snel te leren.

I cannot forget the two "Aussie" girls whom I had the opportunity to work with. Dear Karla and Elizabeth it was nice not just working with you but also hanging out for a chat or a beer. Thanks especially to Liz, who helped me several times to review the grammar of my articles.

Gracias también a Karla Graniel, ha sido un placer trabajar contigo y lo siento mucho que has debido marcharte.

Un ringraziamento enorme va anche all'intero dipartimento di Radiologia di Treviso, dove è iniziato questo lungo dottorato. Grazie Silvia e Mirco per il vostro aiuto nel condurre diversi studi presentati in questa tesi, e per tutti i momenti extra lavorativi che hanno saldato la nostra amicizia. Un grazie anche a tutti i radiologi del dipartimento (Addonisio, Cancian, Cugini, Ballestriero, Dorigo, Granieri,

Cultrera, Latorre, etc.), da cui ho imparato molto durante le rotazioni diagnostiche della scuola di specialità.

Vorrei ringraziare anche i miei tutor durante la specialità a Padova, in particolare Prof Dr Giampiero Feltrin e Prof Dr Piercarlo Muzzio per avermi dato la possibilità di effettuare la fellowship di ricerca a Rotterdam durante la scuola di specialità. Un grazie anche agli altri membri del Dipartimento di Radiologia di Padova, Ass. Prof Dr Stramare Roberto, Prof Dr Diego Miotto, Prof Dr Leopoldo Rubaltelli, Dr Talenti, Dr Fitta', Dr Torraco, Dr Tregnaghi, Dr Motta, etc.

I want to thank as well all people encountered in my stay here in Rotterdam. First of all who gave us a shelter, initially meant for a short stay and for a single person to become a place for two people and a kid. Dear Cesare and René, we really enjoyed to stay in the house of the "red kimono".

Devo ora ringraziare tutta la comunità di expat italiani che hanno reso speciale la nostra permanenza a Rotterdam. Grazie a Gianluca e Carmen per le cene e le numerose serate organizzate. Grazie a Francesca, Marialuisa, Alessandro e Veronica, Alessandro e Gaia, Alexia, Antonio, Valerio e Valentina, Federico, Marta, Giulia, Salvatore, Guido, Brunella, etc. I momenti trascorsi assieme ci hanno fatto sentire un po' a casa, come se fossimo ancora in Italia.

Un grazie anche gli amici di lunga data come Gabriel, Mauro e Carmelina che in questi anni all'estero hanno trovato il tempo di venirci a visitare.

Vorrei ringraziare le mie sorelle (Alessia, Sabrina, Paola) e i miei nipoti (Cristiana, Serena, Elisa & Co) per aver fatto da corrieri di provviste Italiane in Olanda, specialmente di Prosecco e Grappe.

Un grazie a Mauro, Silvia e Claudia per averci aiutato nei numerosi traslochi in giro per il mondo.

Un grazie anche a miei genitori, Papà Luigi e Mamma Leonora. Anche se non capite molto la mia scelta di stare qui a Rotterdam, specie per tutte le offerte ricevute dall'Italia, vi ringrazio di avermi sempre sostenuto e aiutato nel mio percorso formativo e lavorativo. Vi ho sempre sentiti al mio fianco e se ho ottenuto questo PhD lo devo anche a voi, grazie! Anche se lontano, io per voi ci sarò sempre.

Un grazie alla mia principessina Agata, che con la sua allegria ed energia mi fa passare ogni malumore. Un grazie all'ultimo arrivato, Carlo, i tuoi sorrisi sono così disarmanti che vedendoli mi dimentico di tutto il resto.

Last but not least, un grazie enorme va alla mia bellissima moglie Laura, una persona speciale che ha reso tutto questo possibile. Se tu non avessi assecondato (o forse il verbo più giusto qui è sopportato) le mie ambizioni lavorative non avrei mai raggiunto questi obiettivi. Sei sempre stata presente nei momenti di sconforto o quando avevo bisogno di un consiglio. Mi hai perdonato quando ho esagerato nel lavoro, tornando a casa tardi la sera o lavorando nei weekend. Mi hai seguito ovunque ti abbia portato, da Padova a Rotterdam, da Rotterdam a Boston e ritorno. Per questo mi sento la persona più fortunata al mondo ad averti al mio fianco e posso francamente dire che questo dottorato è anche tuo. Ti amo.

# Summary of PhD training and related activities

| | |
|---|---|
| Name PhD student: **Pierluigi Ciet** | PhD period: |
| Erasmus MC Department: | September 2011- December 2015 |
| 1. Radiology | |
| 2. Pediatric Pulmonology | Promoters: |
| Research School: | – Prof. Dr. H.A.W.M. Tiddens |
| National Institute of Health Sciences in Rotterdam (NIHES) | – Prof. Dr. G.P. Krestin |

**1. PhD training**

| | Year | Workload (Hours/ECTS) |
|---|---|---|
| **Research skills** | | |
| – Statistics: | | |
| – Introduction to clinical research | 2011 | 1 |
| – Biostatistics for clinicians | 2011 | 1.5 |
| – Methodology | | |
| – Course NIH grant writing, Erasmus MC | 2012 | 1.5 |
| – CITI exam | 2013 | 2 |
| – Basic human subjects protection | | |
| – Conflict of interest | | |
| – Health Information Privacy and Security (HIPS) | | |
| **In-dept courses** | | |
| – Applied MR Techniques, Advanced Course (ESMRMB) | 2011 | 1.5 |
| – International society of Magnetic Resonance in Medicine (ISMRM) – Italian Chapter | 2012 | 1 |
| **Seminars and workshops** | | |
| – "Preparing for the first early pulmonary intervention studies in infants and preschool children with Cystic Fibrosis". European Respiratory Society (ERS) research seminar. | 2011 | 0.5 |
| – Media Contacts for Researchers | 2014 | 0.5 |

| | Year | Workload (Hours/ECTS) |
|---|---|---|
| **(Inter)national conferences** | | |
| NACFC (North America Cystic Fibrosis Congress) 2011 (2 Posters) | 2011 | 1 |
| RSNA (Radiological Society of North America) 2011 (2 oral presentations, Awarded Research Trainee Prize) | 2011 | 1 |
| ECR (European Congress of Radiology) 2011 (2 oral presentations) | 2011 | 1 |
| ESTI 2012 (European Society of Thoracic Imaging (oral presentation) | 2012 | 1 |
| RSNA (Radiological Society of North America) 2012 (Poster) | 2012 | 1 |
| ECR 2013 (European Congress of Radiology) (Oral presentation) | 2013 | 1 |
| ECPR (European Conference of Pediatric Radiology) 2013 (Invited Speaker) | 2013 | 1 |
| RSNA (Radiological Society of North America) 2013 (Oral Presentation) | 2013 | 1 |
| RSNA (Radiological Society of North America) 2014 (Poster) | 2014 | 1 |
| ECFS (European Cystic Fibrosis Society) 2015 (Invited Speaker) | 2015 | 1 |
| **Medical Board Certification** | | |
| Educational Commission for Foreign Medical Graduates(ECFMG) certificate | 2012-2013 | 30 |
| **Didactic Skills** | | |
| – Radiology resident morning conferences | 2013-2014 | 2 |
| – Master Student Supervision | 2015 | 3 |
| **Other activities** | | |
| – Friday Pediatric Pulmonology clinical conference (Sophia) | 2013-2015 | 5 |
| – Research meeting (every Friday) | 2011-2015 | 4 |
| – PhD lunch meeting (biweekly) | 2011-2015 | 3 |
| – Peer review for articles for scientific journals | 2011-2015 | 3 |
| **Total** | | **70.5** |

# About the Author

Pierluigi Ciet was born on April 25th 1980 in Asolo, Treviso, Italy. He graduated in 1999 from the secondary school at Liceo Scientifico Primo Levi, and in the same year, he started his medical training at the Faculty of Medicine and Surgery of the University of Padova, Italy.

During his medical training, he participated in the European Erasmus exchange student program and he attended from 2004-2005 the Faculty of Medicine and Surgery of Oviedo, Spain. In 2006, he received his master degree of medicine (grades 106/110). His master's thesis was awarded with the "Guerrino Lenarduzzi" prize from the Venetian Institute of Science, Letters and Arts as best regional master's thesis in radiology.

After passing the Italian national board examination in 2007, he started his residency program at the Department of Radiology of Padova (heads Prof Dr Giampiero Feltrin and Prof Dr Pier Carlo Muzzio). In 2009, during his residency program, he completed a research fellowship at the Department of Pediatric respiratory Medicine, Sophia Children's Hospital -Erasmus Medical Centre, where he conducted a research project about chest MRI in cystic fibrosis under the supervision of Prof Dr Harm AWM Tiddens.

In 2011 he completed his radiology residency training and graduated cum laude. In the same year, he started his PhD program at the Department of Radiology and Department of Pediatric Respiratory Medicine and Allergology of the Erasmus Medical Centre working at the projects described in this thesis. During his PhD, Pierluigi successfully passed the United Stated Medical License Examination (USMLE) and in 2013 he obtained the Educational Commission for Foreign Medical Graduates (ECFMG) certificate. From June 2013 till September 2014, he interrupted his PhD program to complete the clinical fellowship of Cardiothoracic Imaging at the Beth Israel Deaconess Medical Center (head Prof Dr Alexander Bankier, fellowship's director Prof Dr Diana Litmanovich), Harvard Medical School, Boston, USA.

After the fellowship, he returned to Rotterdam to finalize his PhD program. Since January 2015, in addition to his MRI research he started to work clinically in the Pediatric Radiology Department and in the Lung Analysis laboratory of the Erasmus Medical Centre Sophia Children's Hospital.

Dr Ciet is married with dr Laura Serra, and they have two children Agata (28-12-2011) and Carlo (18-02-2016).

# Abbreviations

| | | |
|---|---|---|
| 2D | = | bi-dimensional |
| 3D | = | three-dimensional |
| ADC | = | apparent diffusion coefficient |
| AF | = | acceleration factor (parallel imaging) |
| AP | = | anterior-posterior diameter |
| ARC | = | Autocalibrating Reconstruction for Cartesian imaging |
| ASL | = | arterial spin-labeling |
| ASSET | = | Array coil Spatial Sensitivity Encoding |
| BAL | = | bronchoalveolar lavage |
| BH | = | breath-hold |
| BMI | = | body mass index |
| BW | = | bandwidth |
| CEMRI | = | contrast enhanced MRI |
| CF | = | cystic fibrosis |
| CF-CT | = | cystic fibrosis computed tomography score |
| CF-MRI | = | cystic fibrosis magnetic resonance imaging score |
| CNR | = | contrast-to-noise ratio |
| COPD | = | chronic obstructive pulmonary disease |
| CPAM | = | congenital lung airway malformations |
| CPAP | = | Continuous Positive Airway Pressure |
| CS | = | compress sensing |
| CSA | = | cross-sectional area |
| CT | = | computed tomography |
| CT-BE | = | computed tomography bronchiectasis score |
| CT-Mucus | = | computed tomography mucus plugging score |
| CXR | = | chest x-ray |
| DCE | = | dynamic contrast-enhanced imaging |
| DISCO | = | DIfferential Subsampling with Cartesian Ordering |
| DW-MRI | = | diffusion weighted MRI |
| ECG | = | electro-cardiogram |
| EPI | = | echo planar imaging |
| ERT | = | enzyme replacement therapy |
| EVC | = | expiratory vital capacity |
| FA | = | flip angle |
| FD | = | Fourier decomposition |

| | | |
|---|---|---|
| $FEF_{25-75}$ | = | forced expiratory flow at 25-75% of the pulmonary volume |
| FeNO | = | fraction of exhaled Nitric Oxide |
| $FEV_1$ | = | forced expiratory volume in 1 second |
| FOV | = | field-of-view |
| FRC | = | functional residual volume |
| FS | = | fat saturation |
| FVC | = | forced vital capacity |
| GBCA | = | gadolinium based contrast agents |
| GRAPPA | = | GeneRalized Autocalibrating Partial Parallel Acquisition |
| GRE | = | gradient echo |
| HP | = | hypoperfusion |
| HP-MRI | = | hyperpolarized gas MRI |
| HV | = | hyperventilation |
| ICC | = | intra class correlation coefficients |
| IVC | = | inspiratory vital capacity |
| kV | = | kilovolt |
| LAR | = | low-attenuation region |
| LCI | = | lung clearance index |
| LIR | = | low-intensity region |
| LMB | = | left main bronchus |
| LR | = | left-right diameter |
| mA | = | milliampère |
| mAs | = | milliampere * seconds |
| MDCT | = | multi-detector computed tomography |
| MEP | = | maximum static expiratory pressure |
| MIP | = | maximum static inspiratory pressure |
| MPR | = | multi-planar reformat |
| MRA | = | Magnetic resonance Angiography |
| MRI | = | magnetic resonance imaging |
| NEX | = | number of excitation |
| OE-MRI | = | oxygen enhanced MRI |
| PD | = | proton density |
| PET | = | positron emission tomography |
| PEX | = | pulmonary exacerbation score |
| PFT | = | pulmonary function test |
| PROPELLER | = | periodically rotated overlapping parallel lines with enhanced reconstruction |
| RMB | = | right main bronchus |
| ROI | = | region-of-interest |

RTE = respiratory tract exacerbation
RV = residual volume
SAR = Specific Absorption Rate
SE = spin echo
SENSE = SENSitivity Encoding
SL = slice thickness
SNR = signal-to-noise ratio
SPGR = spoiled gradient echo
SSFP = steady state free precession
STIR = short tau inversion recovery
T = Tesla
T1 = relaxation time 1 (Spin–lattice relaxation)
T2* = T2 star relaxation time
T2 = relaxation time 2 (Spin-spin relaxation time)
TA = acquisition time
TA = trapped air
TB = tidal breathing
TBM = tracheobronchomalacia
TE = echo time
TLC = total lung capacity
TOF = time-of-flight
TR = repetition time
TRICKS = Time Resolved Imaging of Contrast KineticS
TrueFISP = True fast imaging with steady state precession
TSE = turbo spin-echo
UTE = ultra-short echo time sequence
ZTE = zero echo time sequence